I. REGIONAL VARIATIONS IN UPPER MANTLE COMPRESSIONAL VELOCITIES BENEATH SOUTHERN CALIFORNIA

II. POST-SHOCK TEMPERATURES: THEIR EXPERIMENTAL DETERMINATION, CALCULATION, AND IMPLICATIONS

Thesis by

Susan Ann Raikes

In Partial Fulfillment of the Requirements

for the Degree of

Doctor of Philosophy

California Institute of Technology

Pasadena, California

1978

(Submitted May 23, 1978)

ACKNOWLEDGEMENTS

Throughout my stay at Caltech, I have benefitted greatly from the help, advice and support of Professors Hiroo Kanamori and Thomas Ahrens. I would also like to thank everyone at the Seismological Laboratory, but especially David Hadley, Gregory Lyzenga, Raymond Jeanloz and Drs. Christine Powell and Ian Jackson, for many interesting and helpful discussions.

The experiments in the second part of my thesis could not have been carried out without the able technical assistance of the staff of the Helen and Roland Lindhurst Laboratory of Experimental Geophysics -- Messrs. Harold Richeson, David Johnson, Epaprodito Gelle and Ron Smith -- or of the machine shop -- Messrs. Elmer Steffensen, Richard Wickes and Charles Hudson; I am most grateful for their help and patience. The expertise of Mr. Victor Nenow and Mr. Wayne Miller was invaluable in developing the electronic equipment used in the experiments.

For their assistance in the preparation of this thesis, I would like to thank Mrs. Janet Boike, who typed the manuscript, and Mr. Laszlo Lenches and Mr. Joe Galvan, who drafted most of the figures.

Finally, I would like to thank all of my friends for their help and encouragement -- if I were to name all those to whom I am indebted, this would be the longest section of my thesis.

During part of my tenure as a graduate student I was supported by a Fluor Fellowship and I also received an I.B.M. Special Summer Fellowship. Various sections of the work in the first part of my thesis were supported by the National Science Foundation Earth Sciences Division under grant no. DES75-03643, and by the United States Geological Survey under contracts

14-08-0001-15893 and 14-08-0001-16711. The second part was carried out under NASA grant NGL 05-002-105.

ABSTRACT

The establishment in Southern California of a large seismographic network provides an unique opportunity for studying the seismic velocity variations within a tectonically active region that includes a major plate boundary, whose surface expression is the San Andreas Fault. In the first part of this thesis, the compressional velocity within the upper mantle beneath Southern California is investigated through observations of the dependence of teleseismic P-delays at all stations of the array on the distance and azimuth to the event. The variation of residuals with azimuth was found to be as large as 1.3 sec at a single station; the delays were stable as a function of time, and no evidence was found for temporal velocity variations related to seismic activity in the area. These delays were used in the construction of models for the upper mantle P-velocity structure to depths of 150 km, both by ray tracing and inversion techniques. The models exhibit considerable lateral heterogeneity including a region of low velocity beneath the Imperial Valley, and regions of increased velocity beneath the Sierra Nevada and much of the Transverse Ranges. These changes are attributed to variation in the degree of partial melting within the upper mantle; their relationship to, and implications for, regional tectonics are discussed in the final chapter of this section.

One of the major uncertainties in the interpretation of shock wave data is the temperature reached under shock compression and subsequent release. The second half of this thesis describes the development of a technique for the experimental determination of post-shock temperatures,

and its application to several metals and silicates shocked to pressures in the range 5 to 30 GPa. The technique utilises an infra-red radiation detector to determine the brightness temperature of the free surface of the sample after the shock wave has passed through it, and has yielded highly reproducible results that are consistent for the wavelength ranges 4.5 to 5.75 and 7 to 14μ. The comparison of these results with values calculated using conventional theories provides some insight into the thermal processes occurring in shock waves. In particular, the measured temperatures are generally higher than those calculated; this is attributed to elasto-plastic effects in metals, and is probably associated with strength effects in silicates, both of which are commonly ignored in the calculation of theoretical temperatures. The implications of these observations for the interpretation of shock-induced metamorphism and impact phenomena, and for the application of shock-wave data to the interpretation of the behaviour of silicates within the earth's mantle, are discussed in the final chapter.

TABLE OF CONTENTS

Table of Contents - continued

Part I - continued

PART I

REGIONAL VARIATIONS IN UPPER MANTLE COMPRESSIONAL VELOCITIES BENEATH SOUTHERN CALIFORNIA

Chapter 1

INTRODUCTION

Southern California is a region containing a number of markedly different tectonic regimes, including an extension of the active zone of rifting in the Gulf of California into the Imperial Valley, and a major transform plate boundary whose surface expression is the San Andreas Fault. It is perhaps reasonable to expect that these surface features are accompanied by structural variations at depth within the crust or upper mantle. The U.S.G.S.-Caltech Seismographic Network, comprising over a hundred stations, provides an unique opportunity for gathering travel time data relevant to an investigation of these regions. In this study, the azimuthal dependence of teleseismic P-residuals for stations in this network is determined and used to infer lateral variations in the compressional velocity beneath Southern California.

1.1. A Brief Survey of Regional Tectonics and Geology

The geology of Southern California is extremely varied and complex, and it is beyond the scope of this work to attempt to describe it in any detail. However, a brief review of a few of the main features within the various regional subdivisions, especially those that might be associated with velocity changes at depth within the crust and upper mantle, is appropriate. These features may include centres of vulcanism, for Spence (1974) found evidence from teleseismic residuals for an upper mantle velocity anomaly associated with the Silent Canyon Volcanic Centre in Nevada, the plate boundary itself, which must extend to the base of the lithosphere (and indeed, the San Andreas Fault has been

shown to persist to depths ∿75 km in Central California (Husebye et al., 1976; Peake and Healy, 1977)), and areas of geothermal activity. Large velocity anomalies associated with the last named have been reported; for example for Yellowstone (Iyer et al., 1974; Iyer, 1975; Hadley et al., 1976), and Long Valley (Steeples and Iyer, 1976). Also, since thermal perturbations in the upper mantle decay slowly (on a time scale of tens of millions of years), the plate tectonic history of the region should be taken into account. For example, Solomon and Butler (1974) found evidence from teleseismic travel times for a "dead slab", or fragment of the formerly subducted Farallon plate, beneath Oregon and Northern California.

A reconstruction of the Cenozoic plate tectonic history of the Western United States was made by Atwater (1970) based on the magnetic lineations of the Eastern Pacific. Her model, which assumes a constant rate of 6 cm/yr between the Pacific and (fixed) North American plates is illustrated in Figure 1-1; between 20 m.y. and the present 4 cm/yr are assumed to be taken up by near-coastal faults such as the San Andreas, and the remaining 2 cm/yr further inland. The basic history as it affects Southern California is as follows: prior to 38 m.y. ago, there was an active subduction zone off the coast, with the Farallon plate dipping beneath North America, and intermediate vulcanism was prevalent throughout the western United States. About 32 m.y. ago, the Farallon plate started to break up off Baja California, and thereafter pieces of the ridge began colliding with the trench. By 24 m.y. the Farallon plate between the Mendocino and Murray fracture zones had disappeared, and the relative motion was taken up at the hot, soft,

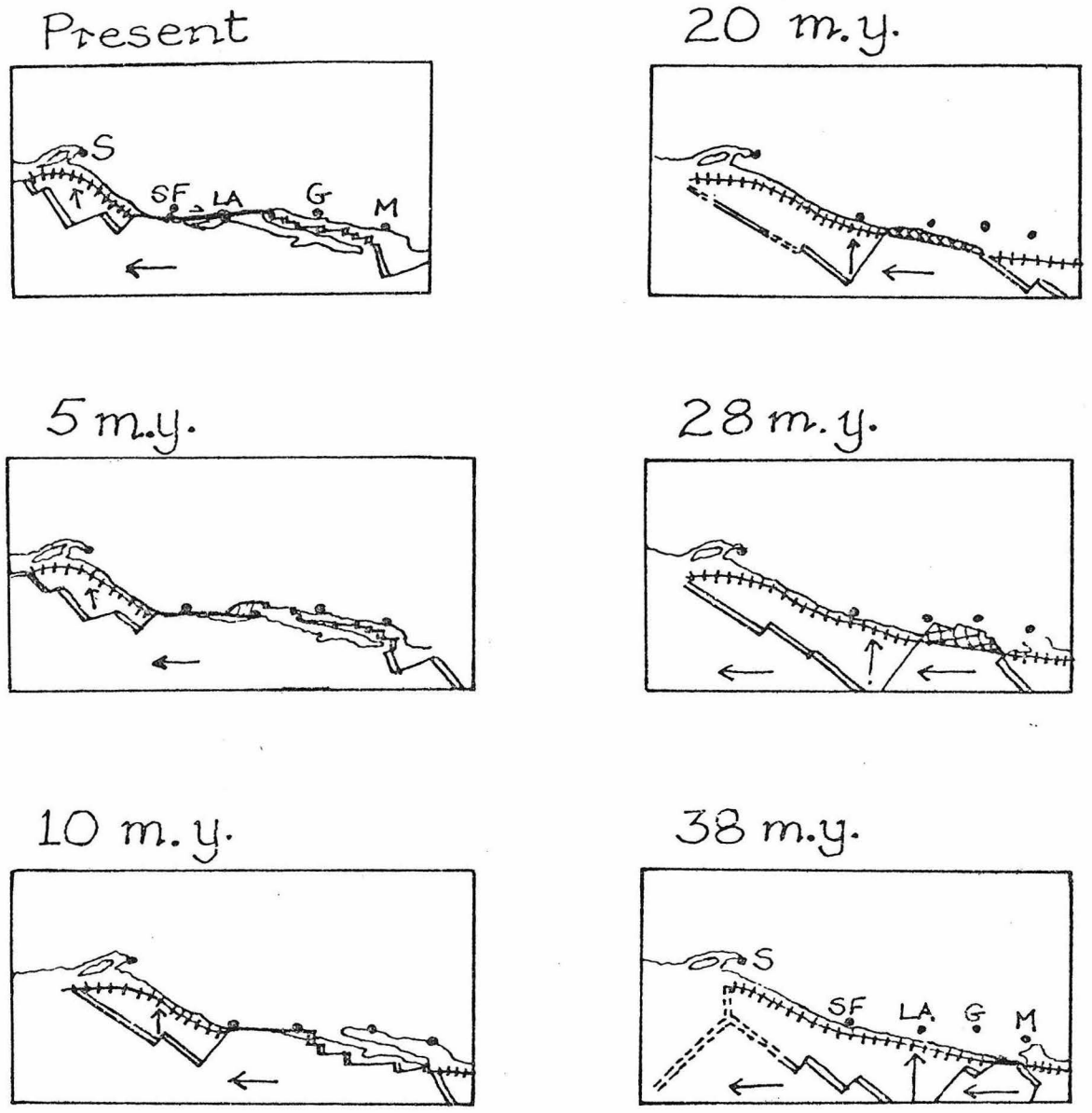

Figure 1-1. Reconstruction of the Cenozoic plate tectonic history of the western United States (after Atwater, 1970). S = Seattle, S.F. = San Francisco, L.A. = Los Angeles, G = Guaymas, M = Mazatlan
═══ = ridge, ┼┼┼┼┼┼┼ = trench,
——— = transform fault.

ocean-continent boundary. Subduction ceased off Southern California between this time and ∿20 m.y. ago, when the region between the Mendocino and Murray fracture zones lay offshore; by this time the ocean-continent boundary had cooled and gained in strength, and the relative plate motion was transmitted inland and accommodated on various faults. The San Andreas fault has had an offset of 350 km since 23.5 m.y. ago, about 275 km of which is post-Miocene (e.g., Huffman, 1970). Between 20 m.y. and 5 m.y. ago, cessation of subduction proceeded northwards, and the San Andreas and Basin and Range systems presumably extended coastward to connect into the Baja margin system. The subduction of the trailing (western) edge of the Farallon plate between the Mendocino and Murray fracture zones some 20 m.y. ago was followed by an outbreak of basaltic vulcanism in the Channel Islands, Santa Ynez and Santa Monica mountains, and the extensional stress field that existed until spreading ceased off western Baja California was presumably responsible for the inception of formation of the Los Angeles basin (Campbell and Yerkes, 1976). About 5 m.y. ago, the ridge off western Baja California "jumped" to a weaker inland zone, and the Gulf of California started to open. The San Andreas then had to bend inland to connect into the new extensional boundary, in such a way that oblique compression began in the Transverse Ranges (Crowell, 1968).

Figure 1-2 is a highly simplified map of the geology of Southern California. The seismographic network extends from the Southern Coast Ranges and Sierra Nevada in the north to the Imperial Valley in the south.

The major features of the Sierra Nevada and the Peninsular Ranges

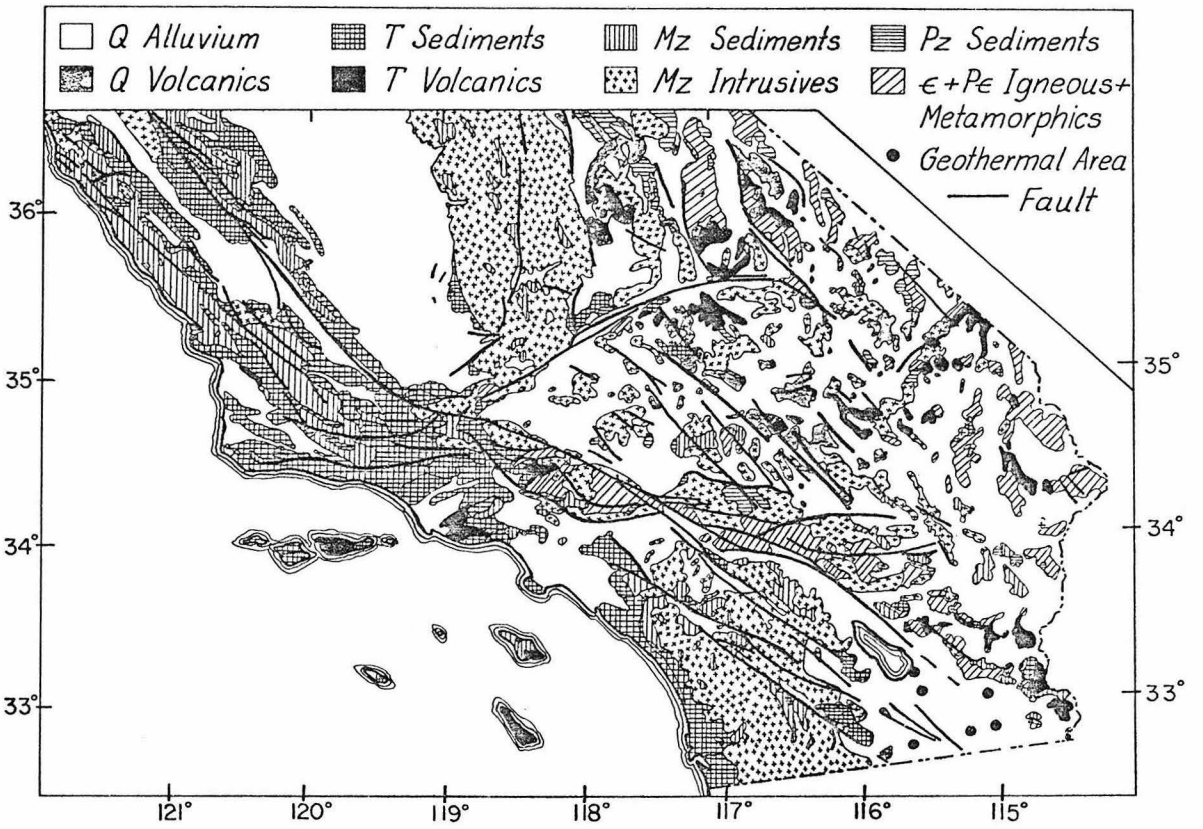

Figure 1-2. Simplified geological map of Southern California.

are large Mesozoic batholiths, which are examples of the continental margin calc-alkaline plutonism common in much of the circum-Pacific area. (The Southern California batholith appears somewhat less potassic than the Sierra Nevada, however (Larsen, 1948).) The origin of the Sierra Nevada batholith is believed to be deep, 30 to 50 km, (Bateman and Wahraftig, 1966), and an upper mantle origin has been suggested for the Sierra Nevada uplift (Crough and Thompson, 1977). Heat flow within the Sierra Nevada is remarkably low, and has been associated with changes within the upper mantle beneath this region (Roy et al., 1972). Uplift in the northern Sierra Nevada took place predominantly between 7.4 and 2.3 m.y. ago, but on the southeastern front most activity has taken place in the last 3 m.y. and displacement continues.

Development of the offshore borderland apparently began in the Mesozoic, and reached its peak in the Miocene after the cessation of subduction, but is still proceeding; it is characterised by basins, vulcanism, high heat flow and folding and faulting (Kraus, 1965; Doyle and Bandy, 1972).

The Salton Trough from Banning Pass to the Gulf of California is an area of current extension in an approximately east-west direction associated with predominantly north-northwest trending right lateral strike slip faults having a characteristic *en-echelon* pattern, and is viewed as a continuation on to the continent of the active spreading centre in the Gulf of California (see, e.g., Biehler et al., 1964). This is an area of crustal thinning and, especially in the Imperial Valley, high tectonic activity, as is indicated by the seismicity:

there have been nine earthquakes of magnitude 6 or greater since 1918, and numerous earthquake swarms. The heat flow in the region is generally high, and there are several localised geothermal areas (see Figure 1-2). Cenozoic sediments within the deep basin of the Imperial Valley reach a maximum thickness of about 6.4 km.

The Mojave Desert may be divided into two distinct units: the western part, or Antelope Valley, and an eastern part. The latter contains fewer faults, is currently less seismically active, and has more widespread vulcanism. In particular, quaternary vulcanism only occurs east of the boundary, which is in the region of the Pisgah-Calico-Lenwood fault system. The north eastern Mojave and the Owens Valley area may be considered as part of the extensional Basin, and Range Province. There is also geothermal activity in the Owens Valley, particularly near Coso at the southern end, and in Long Valley at the northern end.

Running east-west across the general northwesterly tectonic grain of the entire west coast are the Transverse Ranges, through which the San Andreas fault cuts obliquely between the San Bernardino and San Gabriel mountains without significantly offsetting the surface topography. The current style of faulting in this region is predominantly left-lateral east west strike slip and thrust faulting giving rise to earthquakes such as the San Fernando and Point Mugu events, but the surface geology is extremely complicated. East of Cajon Pass the southern boundary of the Transverse Ranges is marked by southward thrusting of crystalline rocks over young gravels along the Banning Fault (Allen, 1957). In the area of Lucerne Valley at the northern

boundary, the crystalline rocks are again thrust over younger sediments (alluvium), this time in a northerly direction (Dibblee, 1964). Although the thrust faulting is similar to the eastern and western Transverse Ranges, the general tectonic style is somewhat different. In the western part, large deep basins which are currently subsiding, such as the Los Angeles Basin (Yerkes et al., 1965) and the Ventura-Santa Barbara channel (Vedder et al., 1965), suggest vertical tectonics with great uplift and subsidence occurring in the same region. This is hard to reconcile with the gravity data, which do not show evidence of any changes in crustal thickness beneath the Los Angeles basin or San Gabriel Mountains (McCulloh, 1960; Biehler, 1976, personal communication).

On the basis of these observations, one might expect to find deep velocity variations associated with the Sierra Nevada, the Imperial Valley, and the San Andreas fault. An additional contrast between the velocities beneath the eastern and western parts of the Mojave Desert is also possible, as is some feature that might explain the tectonics of the Transverse Ranges.

1.2. Previous Studies of Seismic Velocities in Southern California

Until the recent massive expansion of the Southern California Seismograph Network, there was little opportunity of making a detailed study of regional velocity variations. Early investigations consisted largely of studies of travel times from local earthquakes (e.g., Gutenberg, 1944, 1951, 1952; Richter, 1950), a number of seismic refraction experiments (e.g., Roller and Healy, 1963) and analysis of surface wave phase velocities using the few existing stations (e.g., Press, 1956). Some

of the results are summarised below.

Seismic refraction studies in the Southern California borderland (Shor and Raitt, 1956) provided good information on the transition from a thin (~12 km) oceanic crust off the Patton escarpment to a thicker continental crust of about 20 km beneath San Clemente Island and finally about 30 km at the coast. The crustal velocities generally showed three layers beneath the sediments, the top having a velocity of 5 to 5.8 km/s, the middle (where present) one of about 6.2 km/s and the lowest a velocity of 6.8 km/s; P_n velocities were about 8.2 km/s. Further refraction measurements along the coast of California, consisting of two reversed profiles between Los Angeles and San Francisco (Healy, 1963) also had a P_n velocity of 8.2 km/s along the southern portion of the profile, but there was no evidence for an intermediate crustal layer and the crustal velocity was found to be 6.1 km/s. For a one layer crust, the thickness at Los Angeles was estimated at 35 km, which is slightly high compared with more recent measurements, as is the value of P_n.

A long reversed refraction profile was run from Santa Monica to Lake Mead in 1961 (Roller and Healy, 1963). The crustal thickness along this line was found to be about 29 km at Santa Monica Bay, 36 km beneath the Transverse Ranges, 26 km beneath the Mojave Desert and 30 km beneath Lake Mead. The P_n velocity was found to be 7.8 km/s, and the crust beneath the low velocity surface material to have a velocity of 6.1 to 6.2 km/s, with an intermediate layer of 6.8 to 7.0 km/s material.

Press (1956) studied the crustal structure in Southern California using the phase velocity of Rayleigh waves. He found crustal thicknesses

of 30 to 35 km beneath the Transverse and Peninsular Ranges, considerable thickening to about 48 km beneath the southern Sierra Nevada and thinning offshore by an amount similar to that deduced from refraction profiles. Crustal thickening of a similar amount beneath the Sierra Nevada was also reported by Thompson and Talwani (1964) from refraction studies. In a compilation of gravity, seismic retraction and phase velocity data, Press (1960) proposed a model for the crust of the California-Nevada region which consisted of two layers beneath the sediments. The upper layer, presumably of granitic rock, was 23 km thick and had a velocity of 6.11 km/s, and the second gabbroic-ultramafic layer had a velocity of 7.66 km/s and a thickness of 26 km, being in turn underlain by an ultramafic layer of velcoity 8.11 km/s, and this model was long used in the location of local earthquakes. Press associated the velocity of 8.11 km/s with P_n, giving an apparent crustal thickness of at least 49 km which is at variance with the values determined from surface wave data alone. However, an alternative explanation, which he was reluctant to adopt, was that P_n was in fact 7.77 km/s, which implied that the 8 km/s layer was at a depth of at least 90 km. This interpretation is in better agreement with later refraction data.

Since the expansion of the Southern California array, a considerable amount of travel time data has been accumulated allowing a more detailed examination of regional velocity variations. Refraction profiles utilising blasts at a number of local quarries and at the Nevada Test Site reveal that the crustal thickness through much of Southern California lies in the range 30 to 35 km, and the P_n velocity is 7.8 km/s which is typical of tectonically active areas such as the Basin and Range

Province. A representative crustal model (Kanamori and Hadley, 1975) has a 4 km thick 5.5 km/s layer underlain successively by 7.8 km of material with a velocity 6.3 km/s and a 5 km 6.8 km/s layer, and is similar to that of Roller and Healy (1963). Further refraction profiles are described by Hadley and Kanamori (1977) who report upper crustal velocities of 6.1 km/s (Carrizo Plains, Salton Trough) to 6.3 km/s (Imperial Valley). An intermediate branch with a velocity of 6.7 to 7.0 km/s was also found, although it was not observed as a first arrival, and P_n was generally determined at 7.8 km/s, although a value of 8.0 km/ was found from NTS through the eastern Mojave Desert. Crustal thicknesses were again found to be about 32 km, and there was no evidence for crustal thickening under the Transverse Ranges. Within the Mojave Desert, the intermediate layer (6.7 km/s) was found to be only ∿5 km thick as opposed to ∿15 km in the Transverse and Peninsular Ranges. Refraction profiles have also been carried out in the Imperial Valley (e.g., Biehler et al., 1964); the crustal thickness at the southern end of the Salton Sea is 20 km (Fuis, 1976, personal communication).

The crustal structure is thus remarkably uniform throughout much of Southern California, with little variation in crustal thickness. (except for thinning offshore and in the Imperial Valley, and thickening beneath the Sierra Nevada) and in P_n velocity, although regional variations do exist in the thickness of the intermediate layer.

Investigations of deeper structure have been less numerous, and the depth extent of the 7.8 km/s (P_n) layer is not known although it must be at least 20 km to be observed at such great distances. In the light of recent measurements confirming the value of P_n velocity to be 7.8 km/s

Press's (1960) alternative model (which implied that if this were the case, then a velocity of 8 km/s would not be reached until depths of at least 90 km within the California-Nevada region) may be relevant. Studies of body wave travel times (Archambeau et al., 1969) and waveform (Helmberger, 1973) and Rayleigh dispersion (Biswas and Knopoff, 1974) indicate that within the Basin and Range Province the low P_n velocity of 7.8 km/s may persist to depths of 150 km or more.

A study of teleseismic residuals (Raikes, 1976) demonstrated the existence of regions of increased mantle velocity beneath the Sierra Nevada and the Transverse Ranges, and because of the lack of further constraints, a simple model was proposed in which these two regions were continuous, and located at depths of 100 to 200 km, being possibly related to a local thinning of the low velocity zone. However, the addition of further data (Hadley and Kanamori, 1977) showed that the Transverse Ranges anomaly was a separate and distinct entity, and was associated with a locally observed refractor at a depth of $\sim$50 km having a velocity of 8.3 km/s. It is the aim of this study to provide more detailed models of upper mantle velocity variations throughout Southern California.

1.3. The Array

The Southern California array started by the California Institute of Technology in the 1930's, and expanded during the 1960's, has recently, as a result of co-operation with the United States Geological Survey, grown at an almost exponential rate. There are currently some one hundred and twenty short period instruments operating throughout the

various regions of Southern California, and the distribution of those stations used in this study is shown in Figure 1-3. The composition of the network has not been fixed during the period of this study, however, as stations are often removed or installed.

The stations operated originally by Caltech have been telemetered to Pasadena, and recorded on 16 mm develocorder film since 1972; these stations have a peak response at around 5 Hz (0.2 sec) and are located at strategic points throughout Southern California with a concentration in the vicinity of the Los Angeles Basin. Stations installed by the U.S.G.S. are also telemetered to Pasadena and recorded on develocorder film; their peak response is around 10 to 15 Hz. Of the sub-arrays operated by the U.S.G.S., the Santa Barbara net was the earliest to be installed, in 1969, in the general area of the Santa Barbara Channel and Ventura Basin. The Imperial Valley net was established in early 1973, and has recently been expanded, and stations were added throughout the Mojave Desert in 1974, although some of the eastern stations have now been withdrawn. Extensive coverage of the San Gabriel and San Bernardino Mountains and the northern Peninsular Ranges was provided by the installation of the San Bernardino networks (now operated by Caltech, as is the Santa Barbara net) which was started in early 1975, and has continued until recently. The newest array is that in the Carrizo Plains area, which was installed during the latter half of 1976.

The most recent development in the Southern California array is the use of a computer to monitor continuously incoming digital data from all stations, and record earthquakes detected by a certain number of stations; this is described in detail by Johnson (in preparation), and is known

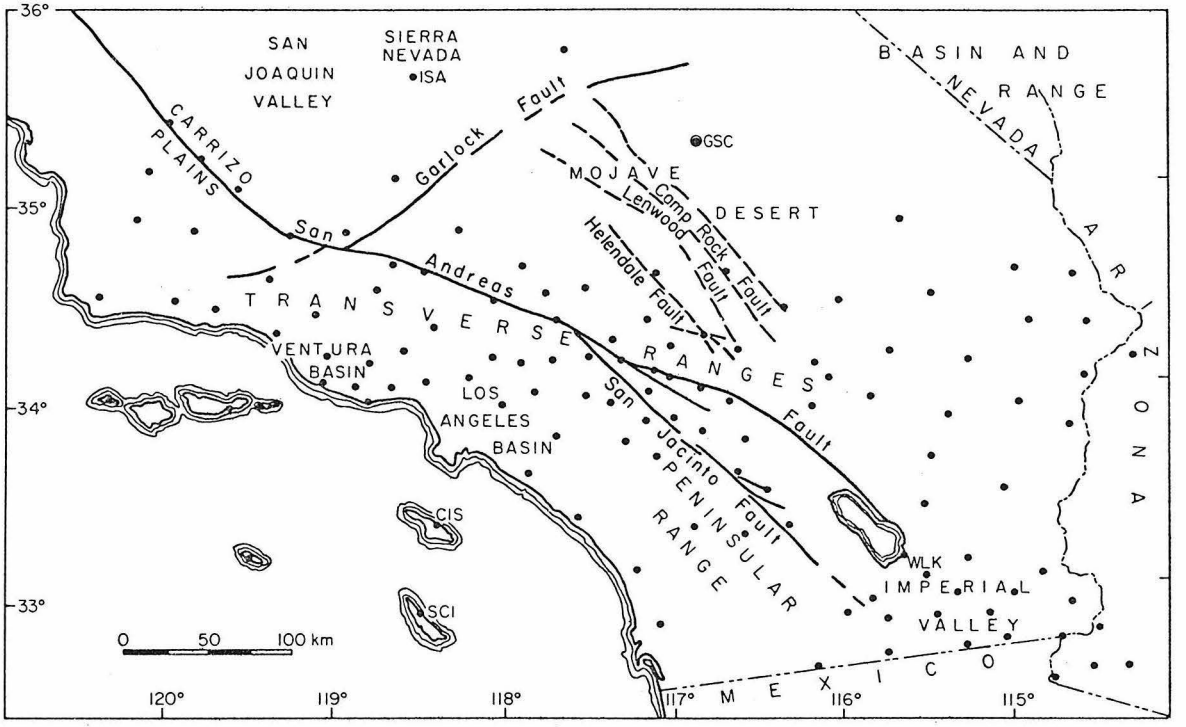

Figure 1-3. Map of the main topographic regions in Southern California showing the distribution of the stations (solid circles) of the U.S.G.S.-Caltech seismograph network used in this study.

as the CEDAR system. Although most of the arrival times used in this study were read from develocorder records, advantage was taken of the availability of this high quality digital data for some of the events occurring in late 1976 and 1977.

Chapter 2

METHOD OF INVESTIGATION

The method chosen for investigation of lateral variations of lower crustal and uppermost mantle compressional velocity structure within Southern California was to study the variation of teleseismic P-delays as a function of source azimuth (and distance) for all the stations of the array. This technique has been used by a number of authors investigating regional velocity variations: for example, it was used to infer fluctuations in the depth and thickness of the low velocity zone in Northern California (Bolt and Nuttli, 1966; Nuttli and Bolt, 1969) and the existence of a high-velocity dipping slab beneath northern Nevada (Koizumi et al., 1973). A variation of the technique, in which the dependence of residuals from an earthquakes the study region were analysed as a function of receiver azimuth and distance, was used by Spence (1974) to investigate the upper mantle structure beneath the Nevada Test Site, and by Engdahl (1975) to delineate variations in velocity beneath the Tonga-Fiji arc. The data produced by such studies are often amenable to analysis by inversion techniques such as the one developed by Aki and co-workers, and applied to residuals from arrays such as NORSAR (Aki etaal., 1977), LASA (Aki et al., 1976), Central California (Husebye et al., 1976), one in the Lesser Himalayas (Menke, 1977), and Hawaii (Ellsworth and Koyanagi, 1977). Models resulting from such analyses may then be compared with surface geology and tectonics in an effort to obtain a fuller understanding of the processes occurring near the surface of the earth.

2.1. The Method of Residuals

The P-wave travel time, T^A, from an earthquake to a station A may be expressed as a sum of contributions from near-source, near-receiver and other path effects:

$$T^A = T_S^A + T_P^A + T_R^A \qquad (1)$$

Here T_S^A is the travel time through the near source structure, T_R^A that through near receiver structure, and T_P^A the contribution from the rest of the path. If the theoretical travel time with respect to some standard earth model is T^O, then the residual, or delay, at the station A with respect to that model is

$$t^A = T^A - T^O = \delta_S^A + \delta_P^A + \delta_R^A + E^A \qquad (2)$$

where δ refers to the difference in travel time from the standard, and the subscripts S, P, and R refer to the source, path and receiver contributions as before. E^A is a (small) term representing the error introduced by mislocation of the event. In order to minimise the effects of path, source structure and mislocation, and facilitate comparison of residuals from different events and source regions, it is common to normalise the residuals in some way. This may be done by subtracting the residual at a single station, or the average residual for all stations in the array. In the former case, the expression for the relative residual becomes

$$t_A = t^A - t^B = (\delta_S^A - \delta_S^B) + (\delta_P^A - \delta_P^B) + (\delta_R^A - \delta_R^B) + (E^A - E^B) \qquad (3)$$

Provided that the distance between the stations A and B is not large, and the earthquake sufficiently distant, the separation of the rays to A and B will be small except in the vicinity of the stations. Unless

there are large changes in velocities over small distances along the remainder of the path, (3) then reduces to

$$t_A = \delta_R^A - \delta_R^B + \text{small error} \qquad (4)$$

except where there are large mislocations. If the structure below B is known, the structure beneath A can be determined by observing the variations in the relative residuals with distance and azimuth to the event. (Alternatively, if neither structure is known, the variation of the structure beneath A relative to that beneath B may be investigated.) The degree to which the structure can be resolved depends on the distribution of the events and stations used.

2.2. Determination of Residuals for the Caltech Array

Signals from the stations of the U.S.G.S.-California Institute of Technology Southern California Seismograph Network (Figure 2-1) are telemetered to a central location and recorded on film; many of the stations have been operational since 1974.

Arrivals were read at as many stations as possible for teleseisms of magnitude 5.5 or greater occurring in the distance range 45-95° (except for 3 events occurring in the range 30-45°), mainly at depths of 50 km or more, during the period March 1974 to October 1977. The magnitude and depth (and to a certain extent the distance) restrictions were introduced to ensure clear arrivals at the majority of stations, and only those events with unambiguous first arrivals were retained in this study; a typical record section is shown in Figure 2-2. Figure 2-3 shows the distribution of events (but not all events are plotted):

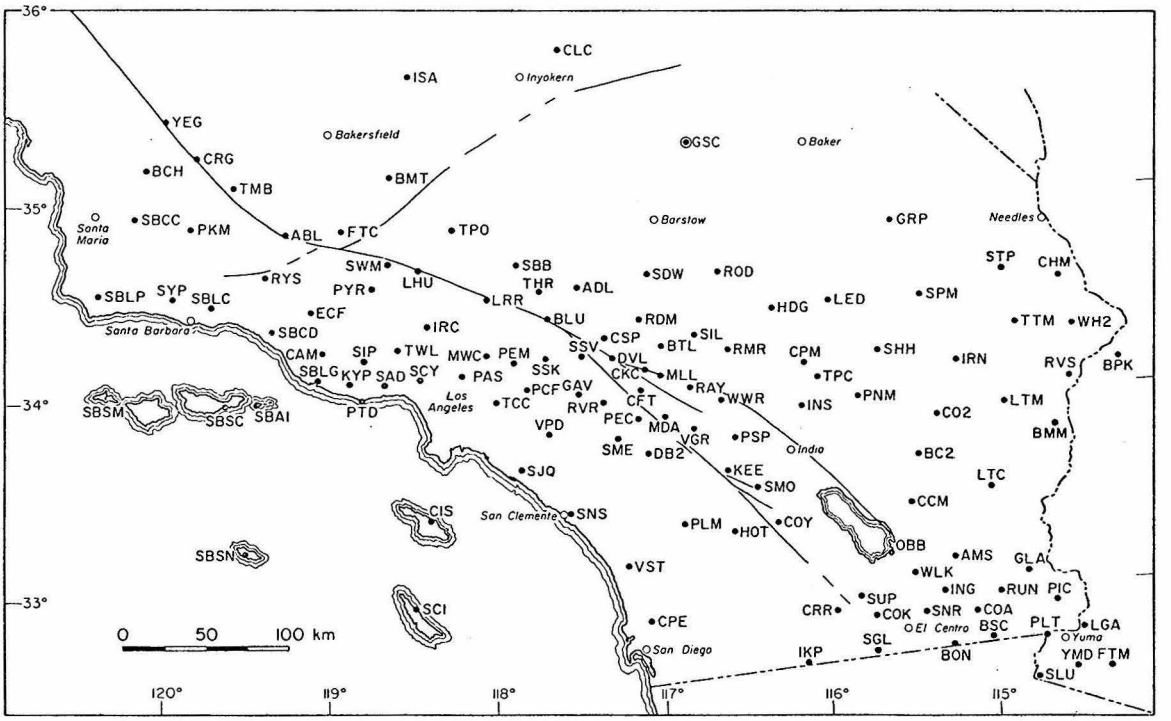

Figure 2-1. Stations used in this study.

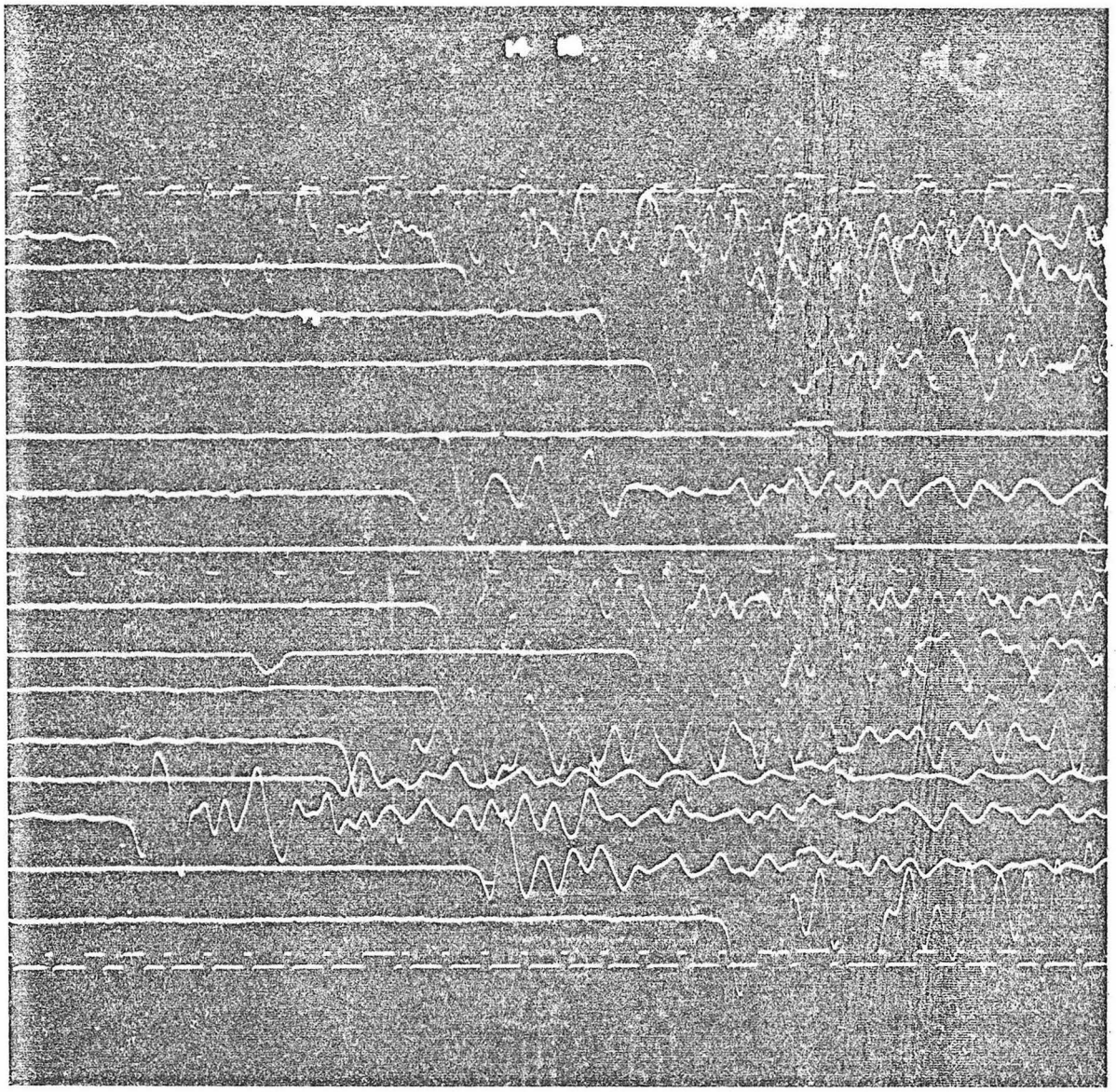

Figure 2-2. Typical develocorder record section: first arrivals at stations of the C.I.T. tele-net from an event, magnitude 6.0 in Fiji, which occurred at a depth of 440 km on 25th November 1976. The traces are, from top to bottom, WWV time, SYP, ISA, CLC, GSC, (SBB missing), CSP (dead), RVR, reference, PEC, TPC, PLM, VST, CPE, SCI, IKP, GLA, WWV time.

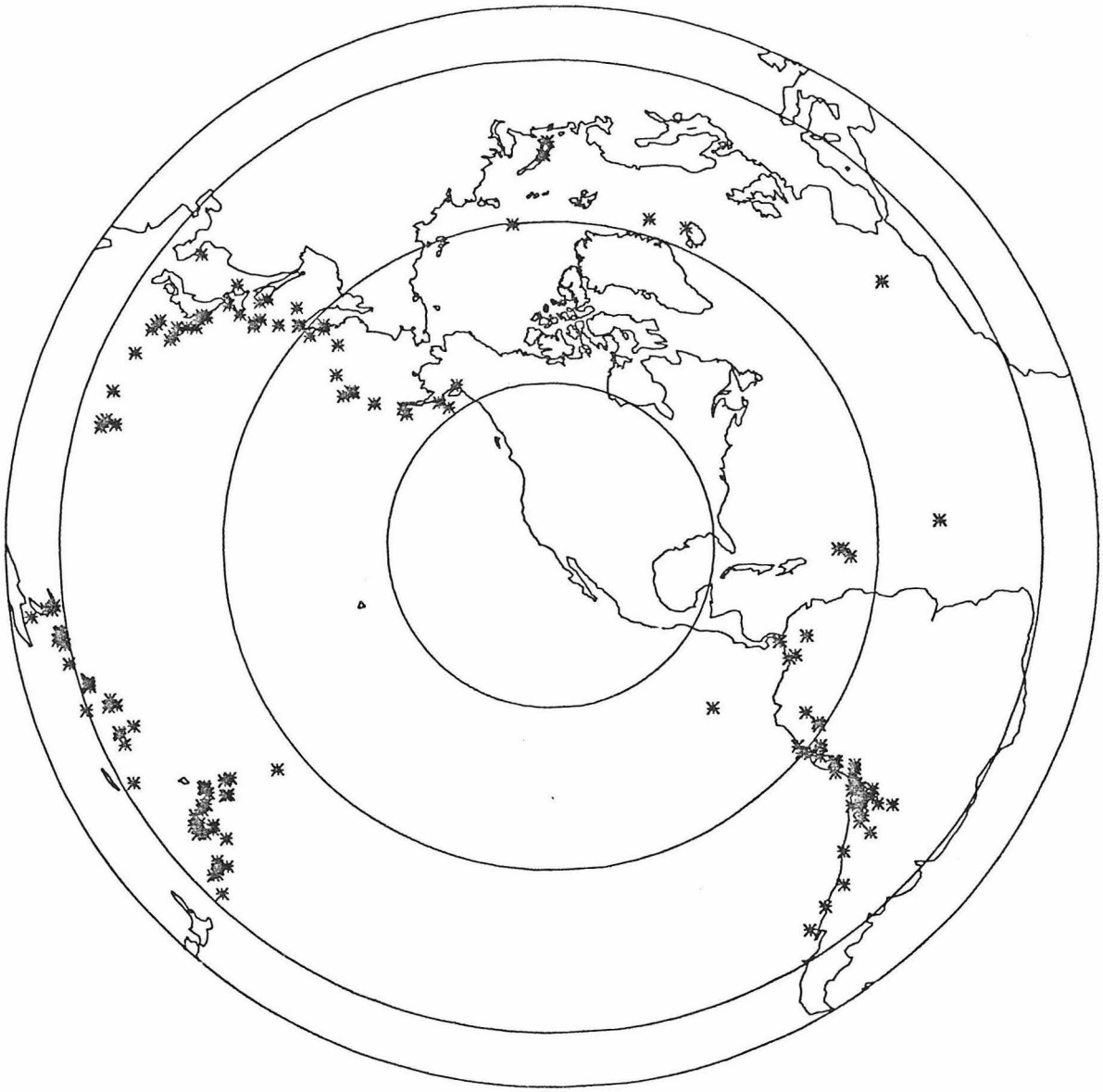

Figure 2-3. Distribution of events used in this study. The map is centred at PAS, and the three inner circles are drawn at distances of 30°, 60° and 90°.

azimuthal coverage is fairly good except for the azimuth ranges 5-90° (few clear recordings of first arrivals from events in Europe and the North Atlantic) and 150-280° (no suitable events between southern South America and northern New Zealand). (A complete list of the events used may be found in Table 3-2.)

For most events, the first arrivals were read from 16 mm develocorder film at a scale of 1 cm per second; the films each contain about 14 stations plus simultaneously recorded WWVB time traces at top and bottom. Estimated reading accuracy varied from .05 to .1 sec depending on the station. (This is actually an estimate of the consistency of the readings rather than the accuracy of determinations of the actual arrival time. The latter is not important in relative residuals provided the same feature is always identified as the first arrival.) In many recent studies, (visual) correlation techniques have been applied, and a prominent peak or zero crossing timed instead of the first arrival. Whilst this is a useful method for earthquakes with emergent first arrivals, it was not used in this study because it was felt that variations in instrument response from station to station, and at a given station as a function of time, would result in increased scatter in residuals if the "arrival" times were so determined. Some arrival times for events in late 1976 and 1977 were read from the high quality digital data recorded by the CEDAR System (Johnson,in preparation).

The theoretical arrival times for each event were calculated using the U.S.G.S. hypocentral location and the Jeffreys-Bullen travel-time tables; corrections were made for the earth's ellipticity (although the relative variation in this over Southern California would be negligible)

and the station elevation. Residuals were calculated relative to the J-B arrival time at each station, and these then normalised by subtracting the residual at Goldstone (GSC). This was chosen as the normalising station because it received clear arrivals for the majority of events, and was furthest from any likely perturbing structure. The average residual over all stations recording an event was not used, because this is highly dependent on the number and location of the receivers; as this changes from event to event, it makes comparison of residuals normalised in this way difficult.

2.3. Sources of Error

The basis of this technique is the assumption that the variation in relative residuals arises largely from velocity structure immediately beneath the array. In this section the effects of other contributions which may bias the relative residuals and lead to errors in the velocity models are discussed.

a. Station elevation correction

The station elevation correction Δt_H applied to the J-B travel times is determined from the expression

$$\Delta t_H = (h/v)\cos\Theta \qquad (5)$$

where: h = station height (km)

v = velocity of uppermost crust

Θ = angle of incidence of ray at surface.

In this study, a crustal velocity of 5 km/s was used, and the height correction was generally $\sim$.1 sec, although for the highest station

(BTL, elevation 2.5 km) it reached a maximum of .5 sec. (Figure 2-4 shows a simplified elevation map of the network.) The major source of error lies in the assumption that the surface velocity is 5 km/s. If this is as much as 2 km/s too high, then the correction may be underestimated by up to .3 sec. In general, however, the error is likely to be less than .1 sec, except for the highest stations. Errors could arise from the use of the value of Θ determined from the J-B value of ray parameter (= $dT/d\Delta$). In this case, the values of $dT/d\Delta$ actually observed are very close to those given by the J-B tables, as is discussed later in this chapter. The average deviation from the theoretical value is ±.05 sec/degree, with a maximum of ±.2 sec/degree, which leads to negligible changes in the height correction.

b. Normalisation

Reading errors for the normalising station will, of course, add to the error in relative residuals at the other stations. For this reason it is especially important to choose as reference station one which generally records non-ambiguous first arrivals. Since the estimated reading error is $\sim$±.05 sec, the error in relative residual is $\sim$±.1 sec.

Structure beneath the normalising station will not cause errors in the relative delays, but can lead to misleading changes in their absolute level. This problem will be discussed when the residual data are presented in the next chapter.

c. Mislocation of the source

In any analysis of errors due to event mislocation, the prime

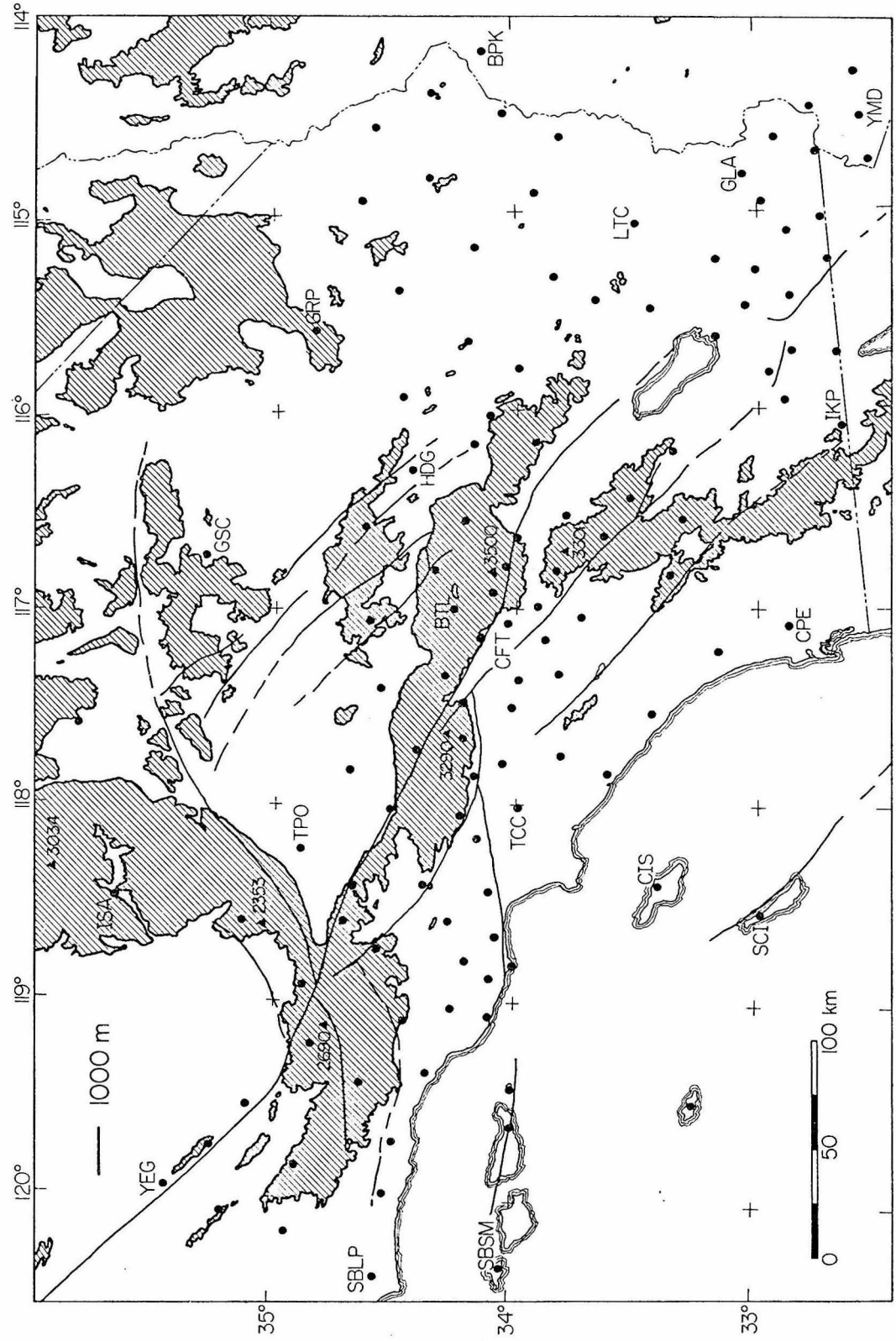

Figure 2-4. Simplified elevation map of the network. Stations are indicated by solid circles and areas higher than 1000 m are shaded.

question is how large the mislocation is likely to be. U.S.G.S. hypocentral co-ordinates for the size of event and source regions concerned have an estimated accuracy of one to two tenths of a degree (they are given to three decimal places), but this is probably an underestimate for shallow events where source structure can lead to large systematic mislocations of up to 100 km. (However, these mislocations will, to a certain extent, compensate for the effects of structure near the source.) Systematic errors can also be caused by the distribution of stations, and location technique, as can be seen by comparing U.S.G.S. and ISC locations; this is shown in Figure 2-5 for events during the period January to June, 1974. The ISC tends to locate events in the South and North Pacific further east than does the U.S.G.S., but these effects are only of the order of two-tenths of a degree.

Additional information on possible event mislocations, and on structure near the source or the receiver, can be obtained by investigating the event locations as determined by the Caltech array. The most convenient way of comparing the two locations is in an array diagram such as that of Figure 2-6, which shows the difference between the observed and predicted values of azimuth and $dT/d\Delta$ for the events used in this study. These vectors are extremely small -- the mean of the absolute value of the difference is 0.05 sec/degree in $dT/d\Delta$, and 0.81° in azimuth, while the mean values of the differences are 0.02 sec/degree and 0.38°. This implies that, in general, the effects of source mislocation should not be severe, and also that there are no large regional trends in velocity structure beneath the array. The largest deviations in azimuth are observed for events in the Solomon

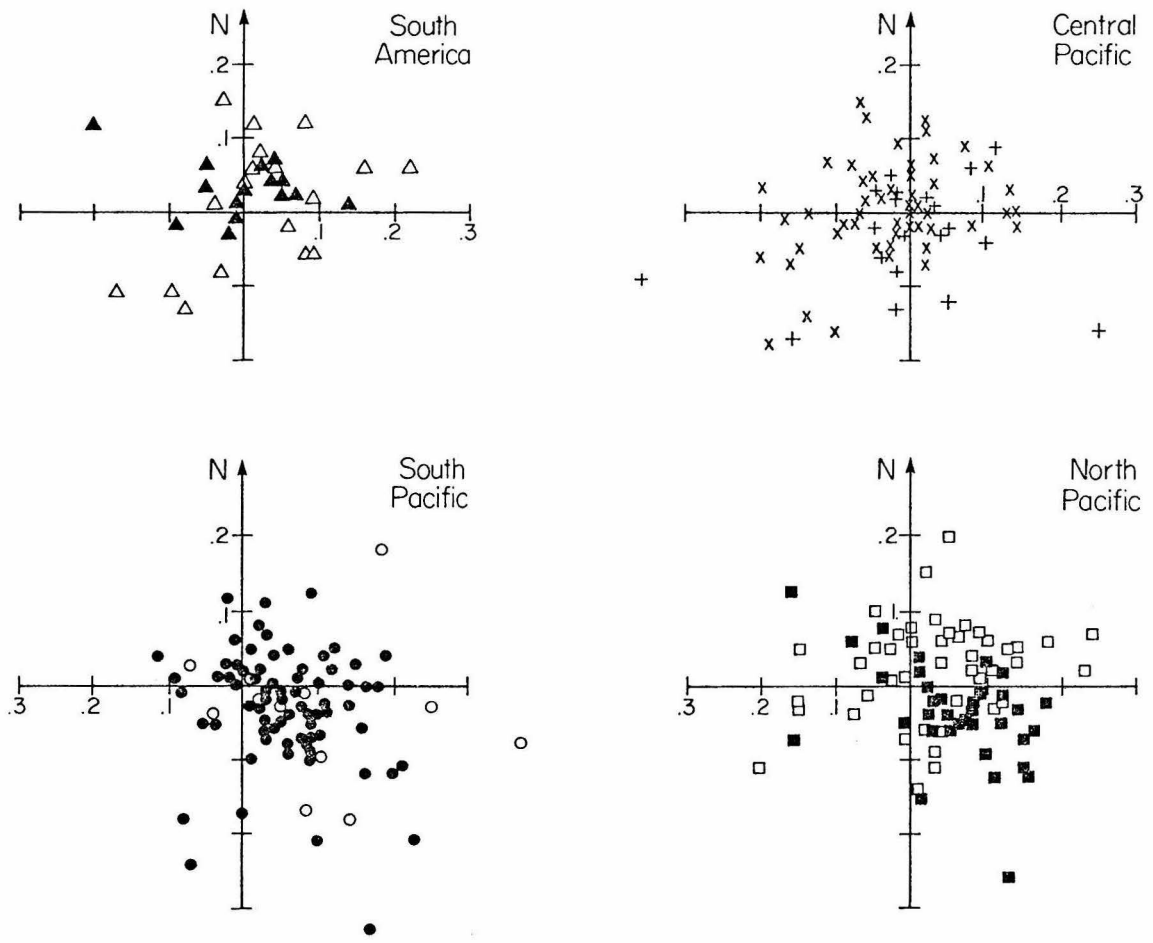

Figure 2-5. Comparison of I.S.C. locations of earthquakes with magnitude $\geq$ 5.5 with those given by the U.S.G.S. for various source regions. The events occurred in the period January to June 1974, and in each case the I.S.C. location is plotted relative to the U.S.G.S. one. In a,b and d solid symbols are events deeper than 65 km; in c these are shown by "+" signs.

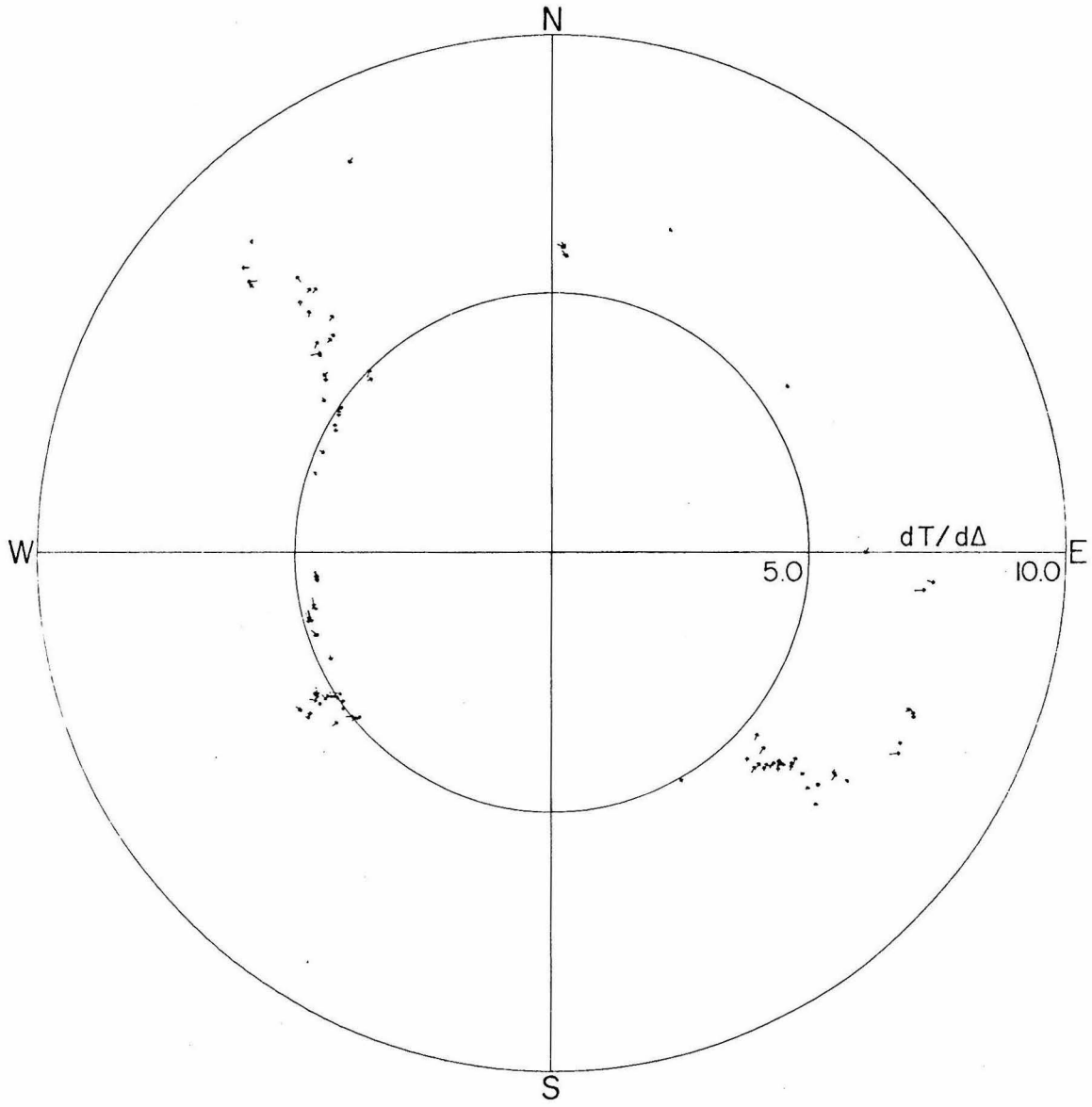

Figure 2-6. The Caltech array diagram. Each vector represents one event; the tail corresponds to the observed azimuth and dT/dΔ and the head to the theoretical values given by the U.S.G.S. location and the J-B tables.

Island-New Hebrides region, and are probably due to structure in the source region (Powell, 1976). The largest differences in $dT/d\Delta$ occur for events in the Leeward Islands. (A detailed analysis of the Caltech array diagram and its implications is given in Powell and Raikes, 1978.) Note that errors in the origin time do not affect relative residuals.

The problem of interpretation of relative residuals is described in detail by Engdahl et al. (1977). Mislocation errors are highly dependent on the station separation, and will become progressively worse with increasing station distance from the normalising station, as is shown in Table 1 of Engdahl et al. For the Caltech array, the maximum station separation is ∿370 km, and the largest difference in distance to a single event is ∿3°. Table 2-1 shows the distribution of stations as a function of distance from GSC.

Errors in the depth of the event of up to ±100 km (depending on depth) have little effect on relative residuals. The maximum change in relative residual δ_{ij} due to an epicentral mislocation of M° may be calculated from the following expression due to Engdahl et al.

$$\delta_{ij} = \pm M \sqrt{(p_i \cos\theta_i - p_j \cos\theta_j)^2 + (p_i \sin\theta_i - p_j \sin\theta_j)^2} \qquad (6)$$

where: p = slowness, sec/degree

θ = azimuth, degree

and the subscripts i, j refer to the two stations

For a mislocation of 0.3°, and a difference in distance from the event to the two stations of 3°, this yields a maximum error of ∿0.1 sec for the distance and azimuth range covered in this study. Similar values were also obtained by systematic mislocation of events in the various

Table 2-1

DISTRIBUTION OF STATIONS

Distance from GSC	Number of Stations
0 - 50 km	0
50 - 100 km	4
100 - 150 km	21
150 - 200 km	32
200 - 250 km	28
250 - 300 km	22
300 - 350 km	10
350 - 400 km	3

source regions.

Random mislocations of events would thus be manifest as scatter of about ±.1 sec (maximum) in the relative residuals for a given source region. (Actually, the observed scatter was small, providing another argument in support of small mislocations.) If a large systematic bias of location exists for a given source region because of the distribution of receivers used to locate the event, or source structure, the resulting shift of residuals would be hard to detect, as it would not cause scatter of residuals, but would result in an error which would change gradually across the array and could be as much as two or three tenths of a second. (Mislocations of up to 100 km may occur for shallow events because of structure near the source.) In such a case, it would probably be hard to construct a velocity model which could explain the relative residuals for all source regions.

d. Effect of structure in the source region and along the ray path.

All the events used in this study, with the exception of the Novaya Zemlya explosions, occurred at major plate boundaries, which might be expected to have complex velocity structures. In particular, the majority of events occurred in subduction zones, and were not restricted to those occurring at the greatest depths, so the effects of the structure of the dipping slab could affect the residuals. (See, e.g., Engdahl, 1975.) Table 2-2 shows the results of some calculations to see how the take-off angle or the source varies as the result of a 3° difference to the receiver, which is the maximum for GSC and any other station. The average difference is 1.07°, which may be an overestimate,

Table 2-2

CHANGE IN TAKE-OFF ANGLE AT SOURCE FOR 3° DIFFERENCE IN DISTANCE

Source Depth (km)	Velocity (km/s)	40°	50°	60°	70°	80°	90°
100	8.0	8.2 8.1	7.6 7.3	6.8 6.5	6.0 5.85	5.3 5.0	4.7 4.5
		0.22	*1.50*	*0.94*	*0.69*	*1.35*	*0.89*
300	8.6	8.1 8.0	7.4 7.2	6.65 6.45	6.0 5.8	5.2 5.05	4.6 4.5
		0.62	*1.16*	*1.10*	*1.06*	*.77*	*0.5*
500	9.8	8.0 7.8	7.3 7.1	6.6 6.4	5.9 5.6	5.2 4.9	4.6 4.6
		1.67	*1.41*	*1.40*	*1.97*	*2.08*	*0*

The two figures in ordinary script are the J-B values for $dT/d\Delta$ at $\Delta°$ and $(\Delta+3)°$, the one in italics is the change in take-off angle, in degrees.

since the values of $dT/d\Delta$ used were taken from the (unsmoothed) J-B tables, where they are only given to 0.1 sec/deg. (The velocities are from Bullen Model A, which was derived from the J-B tables.) This is a small change, so the paths to the two stations will not be far apart; since the velocity heterogeneity associated with plate boundaries is probably of fairly limited extent, the changes in relative residuals should be small. In addition, since the structure changes with depth, and events from a number of depths in a given source region were used, the effect of source structure should show up as scatter in the residuals, and be minimised by including, or averaging over, a variety of depths.

The rays to the receiver network diverge as they get further from the event, but the effect of the different paths should be removed by taking the residuals with respect to some standard earth model prior to normalisation. However, any model merely represents an average structure, and lateral heterogeneities in the real earth may lead to changes in travel times and hence errors in the residuals. For the distance range used, the rays lie largely within the lower mantle, which is relatively homogeneous, and free from sharp velocity discontinuities. (Indeed, a study of equation of state fits to the velocity and density profiles of recent earth models by Butler and Anderson (1977) showed that in the depth ranges 1246 to 1546 km and 1771 to 2521 km the mantle could be considered homogeneous and adiabatic.)

Table 2-3 lists the variation in bottoming depth for a 3° difference in source-station separation. The mean difference is slightly less than 100 km, with a corresponding difference in velocity of $\sim$.12 km/s. (The

Table 2-3

VARIATION IN BOTTOMING DEPTH OF RAYS
FOR A 3° DIFFERENCE IN SOURCE-STATION SEPARATION

(Model QM3, Hart, 1977)

Δ_1 deg.	Δ_2 deg.	h_{max_1} km	h_{max_2} km	δh km	δv km/s
95	92	2833	2768	65	.04
90	87	2704	2590	114	.12
85	82	2498	2367	131	.12
80	77	2278	2154	124	.13
75	72	2082	1975	107	.13
70	67	1889	1776	113	.13
65	62	1696	1604	92	.10
60	57	1543	1448	95	.12
55	52	1387	1305	82	.11
50	47	1246	1157	89	.13
45	42	1097	1016	81	.14
40	37	962	893	69	.13

separation of the rays will, of course, increase on the way from the deepest point to the station.) If lateral heterogeneities exist along the path, their effect will in general be large only if they have a wavelength close to the separation of the rays, except if their boundaries are fairly sharp and the direction of the rays happens to coincide with the boundary. A study by Dziewonski et al. (1977) found only large scale (∿1000 km) heterogeneities within the lower mantle beneath 1200 km, although these increased in number near the core-mantle boundary, which could affect the residuals for events in the "Central" Pacific.

One form of lateral inhomogeneity that could perhaps cause significant errors in residuals is variation in the depth of discontinuities within the lower mantle from that given by the earth model. Although such "transition" zones are usually fairly broad within the lower mantle, it is possible that the rays to a station and the normalising station could bottom on opposite sides of the discontinuity, and because the rays are near horizontal for some distance, small changes in velocity could lead to appreciable changes in arrival time. In particular, Whitcomb and Anderson (1970) found evidence for discontinuities at depths of 940 km and 1250 km from reflected P'P' phases. Johnson (1969) found an increased gradient at 1540 km, and possible increased gradients at 1910 km and 2370 km; the latter two, however, lie within the homogeneous region of Butler and Anderson (1977), and may thus be of only localised importance. These discontinuities would principally affect rays from distances less than 40°, ∿50° and ∿60°, or events in northern South America and the northern Japan-Kuril Island-Aleutians arcs. (The

possible discontinuities at 1910 km and 2370 km would be of importance for events at ∿75° and ∿85°, or events in the South Pacific, and Mariana-Bonin Islands regions.)

The discussion of deep structure beneath "hot spots" or "mantle plumes" has occupied much space in the literature. One hot spot that appears to stand the test of time is that beneath Hawaii, and in view of the suggested depth extent of the anomaly (e.g., Anderson, 1975), it should be noted that rays from the Solomon Islands pass directly beneath the island (Figure 2-7). Even if changes of velocity with depth are small, and the lateral spread of rays from a given event inconsiderable, the structure could cause greater scatter in residuals for events in the "Central" Pacific (New Hebrides-Santa Cruz Island-Solomon Islands), as could structure in the source region itself (Powell, 1976).

The separation of ray paths is greatest within the upper mantle close to the network, and errors may arise from heterogeneity here, but not in the area immediately beneath the array that is being studied. Although the rays are steeper here, and the path length in a given depth range small, the heterogeneities are on a smaller scale, and may cause non-negligible errors in relative residuals. Particular structures that could give rise to changes include the ocean to continent transition (Pacific to North America), although unless this extends to depths in excess of 200 km, only the stations nearest to the Patton escarpment should be affected, and deep structure beneath the Gulf of California spreading centre. As can be seen from Figure 2-7, paths from South America to the network closely parallel the latter structure.

Figure 2-7. Ray paths for typical events in the major source regions studied.

Although it is hard to assess accurately the magnitude of errors due to structure along the path, other than immediately beneath the network, it should be small except for the stations furthest from Goldstone, and will tend to be decreased by averaging over a distance and azimuth range. The effects of specific structures (such as the Gulf of California) may show up as an azimuth range where the residuals for a group of stations are inconsistent with those from other azimuths.

e. Choice of earth model

Residuals in this study were calculated with respect to the Jeffreys-Bullen travel time tables. These are also used in the location of the events by the U.S.G.S., and it was felt that the choice of J-B as reference tables would be more self-consistent. The residuals were fairly evenly distributed about zero (in general, $-1.5 \text{ sec} < \delta t < 1.5 \text{ sec}$), and although this is not a significant argument in favour of the use of J-B tables, it is perhaps interesting to note that Johnson (1969) found the mean residual at the Tonto Forest Seismological Observatory, for events at similar distances to those in this study, to be .95 sec, which was attributed to crust and upper mantle structure beneath the observatory.

Errors in relative residuals will arise if the "shape" of the travel time curve is wrong -- that is to say, the slope, or $dT/d\Delta$, does not vary with distance the way it should. A baseline shift, such as the 1.5-2 sec difference between the Herrin (1968) tables and J-B (see e.g., Carder et al., 1966; Sengupta and Julian, 1976), will be removed by normalisation, and have no effect on relative residuals. The

differences between travel time tables become increasingly important as the station separation increases, as this means there is a greater probability of the reference station lying in a region of small variation, and the other station in a range where variations are large (or vice versa). Table 2-4 illustrates the differences to be expected between relative residuals calculated with respect to J-B and Herrin as reference times. The last column ($d\Delta t_{H-JB}$) gives the value of the J-B residual minus the Herrin residual for the case where the reference station is 3° closer to the event. The effect is complicated, and can, in a few cases, exceed 0.2 sec, although this is for the greatest station separation. Since the events used were, in general, at depths greater than 50 km, the average change at depths of 125 km or more was calculated, and was found to be $\lesssim$0.1 sec for all distances. A better approach is to consider individual source regions for Novaya Zemlya, Southern South America and Japan-Kuril Islands events. Herrin residuals should be $\sim$0.17, $\sim$0.15 and $\sim$0.10 sec more negative for stations further from the event than GSC, although in the latter case the large variation in event depth makes generalisation difficult. Herrin residuals for the Leeward Islands would be more positive for stations further away than GSC by about 0.2 sec. The maximum effect for other azimuths should in general be less than 0.1 sec.

The question of which velocity model is correct is unanswerable, since both models may be unrepresentative of the real earth, and which comes closer may be a function of distance. In a study of surface foci travel times, Carder et al. (1966) found prominent departures from J-B in the neighbourhood of 30° and 60°. Sengupta and Julian (1976) made

Table 2-4

EFFECT OF EARTH MODEL ON RELATIVE RESIDUALS

Source Depth, km	Distance Δ°	J-B d(dT/dΔ) sec/degree	J-B Δt sec	Herrin d(dT/dΔ) sec/degree	Herrin Δt sec	$d\Delta t_{H-JB}$ sec
0	40	.1	24.6	.21	24.61	.01
	50	.3	22.7	.21	22.42	-.28
	60	.2	20.2	.19	20.29	.09
	70	.3	18.0	.25	18.17	.17
	80	.2	15.7	.24	15.86	.16
	90	0	13.8	.08	13.9	.17
125	40	.2	24.5	.20	24.44	-.06
	50	.3	22.5	.21	22.27	-.23
	60	.3	20.1	.19	20.18	.08
	70	.2	17.8	.24	18.04	.24
	80	.3	15.6	.25	15.75	.15
	90	.2	13.9	.08	13.94	.04
250	40	.2	24.3	.21	24.25	-.05
	50	.25	22.1	.21	22.10	0
	60	.2	19.8	.19	20.04	.24
	70	.2	17.9	.23	17.9	0
	80	.2	15.5	.26	15.62	.12
	90	.1	13.9	.07	13.9	0
450	40	.2	24.0	.21	23.89	-.11
	50	.3	21.9	.21	21.79	-.11
	60	.2	19.7	.20	19.80	.10
	70	.2	17.5	.21	17.65	.15
	80	.2	15.3	.27	15.39	.09
	90	0	13.8	.05	13.85	.05
650	40	.1	23.5	.20	23.39	-.11
	50	.2	21.4	.21	21.39	-.01
	60	.2	19.3	.19	19.48	.18
	70	.2	17.2	.20	17.37	.17
	80	.1	15.1	.24	15.09	-.01
	90	0	13.8	.04	13.79	-.01

$d(dT/d\Delta)$ = Difference in ray parameter for 3° difference in distance

$\Delta t = t_{\Delta+3} - t$ = Difference in travel time for a 3° difference in distance.

$d\Delta t_{H-JB}$ = Difference between relative J-B and Herrin residuals, where reference station is 3° closer to the event.

a careful analysis of travel times from deep earthquakes compared to a number of standard tables. Although there were still noticeable differences, they concluded that for distances less than 80°, the shape of the Herrin curve gave a better fit to their data than J-B.

A comparison of the observed values of $dT/d\Delta$ for the events used, obtained by fitting a plane wave to the arrival times for the Southern California network, and those predicted by the J-B and Herrin tables and model QM3 (Hart, 1977) does not give any clear indication which (if any) of these models is best. The differences between the models are similar to the scatter in the data, which are in any case rather sparse. Figure 2-8 shows the observed values (corrected to surface focus by ray tracing) and those of the three models mentioned above. For distances less than 60° there are very few data, but J-B does not give a noticeably worse fit than the other two; indeed, it may be slightly better. For distances in the range 60-80° the Herrin values are closer to those observed for South American events; and J-B values to North Pacific ones. Beyond 85° J-B is slightly better, but there appear to be changes in slope at $\sim$80° and $\sim$85° not well matched by any of the models shown. Since it seems that no one model gives an appreciably better fit to the observations over the whole distance and azimuth range, the choice of J-B times as standard is probably not unreasonable, and should not lead to substantial errors in either the relative residuals or the velocity models derived to explain them. (Note, though, that Herrin does fit the South American events better, so the J-B residuals for the Imperial Valley area may be slightly too negative for this azimuth.)

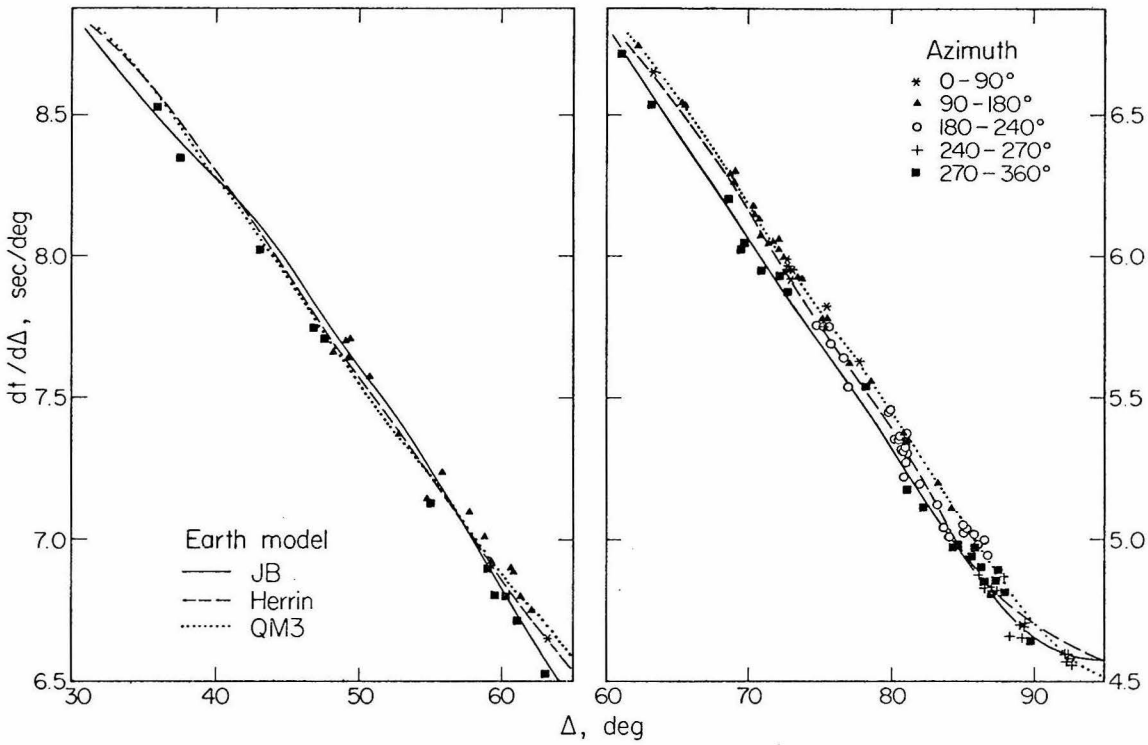

Figure 2-8. Observed values of dT/dΔ (corrected to surface focus) for the events used in this study compared with the theoretical curves for the J-B and Herrin tables and model QM3.

f. Summary

Errors in relative residuals will be most severe for stations furthest from GSC, where they may reach 0.2-0.3 sec. Random errors, which cause scatter in the residuals from a given source region, may arise from mislocation of the event, reading errors and heterogeneity along the ray path. Such effects are expected to be less than 0.2 sec even for those stations furthest from the reference station, and this is substantiated by the magnitude of the scatter observed. Systematic errors due to inaccurate height corrections, large ($\sim$100 km) event mislocations (due to structure in the source region), specific structures along the ray path, and the choice of travel time tables may be larger, and are harder to estimate. They will in general cause inconsistent residual variations for groups of stations on the periphery of the array, and this will be discussed further in Chapter 5.

Chapter 3

THE OBSERVATIONS AND THEIR IMPLICATIONS

An initial investigation of the relative residuals for twelve stations of the Southern California network revealed a marked dependence on azimuth, with variations of up to 1.2 sec at a single station. Figure 3-1 presents these data, which were obtained for events during the period 1972 to early 1976; variations are typical of those observed throughout the array.

The study was then extended to the whole array, as listed in Table 3-1, and the events used, which occurred in the period 1974-1977, are listed in Table 3-2. Since the array has changed markedly as a function of time during this period, some stations record relatively few arrivals (for example, the Carrizo Plains network began operation in mid-1976), and at other stations, notably some in the Imperial Valley, few arrivals were of sufficient quality to be retained. The mode of presenting the data used in Figure 3-1 illustrates well the type of azimuthal variation observed, but is not the most convenient way to show data for the whole array, especially for those stations with few first arrivals. Instead, contour maps of average residuals for a given source region were used to give a clear picture of the variation of relative residuals. However, since this study is aimed at determining the upper mantle structure, the effects of sediments would obscure the pattern due to deeper structure. The relative residuals were thus corrected, as far as possible, for sediment and crustal thickness. (It should be emphasised, however, that these corrections are only approximate, and errors will produce misfits

Figure 3-1. The azimuthal variation of residuals for selected stations. In each plot the polar angle is the azimuth of approach, and the radius is proportional to the normalised residual. Each point represents the mean residual for events in a 2^{o} azimuth window and the distance range indicated by the symbol.

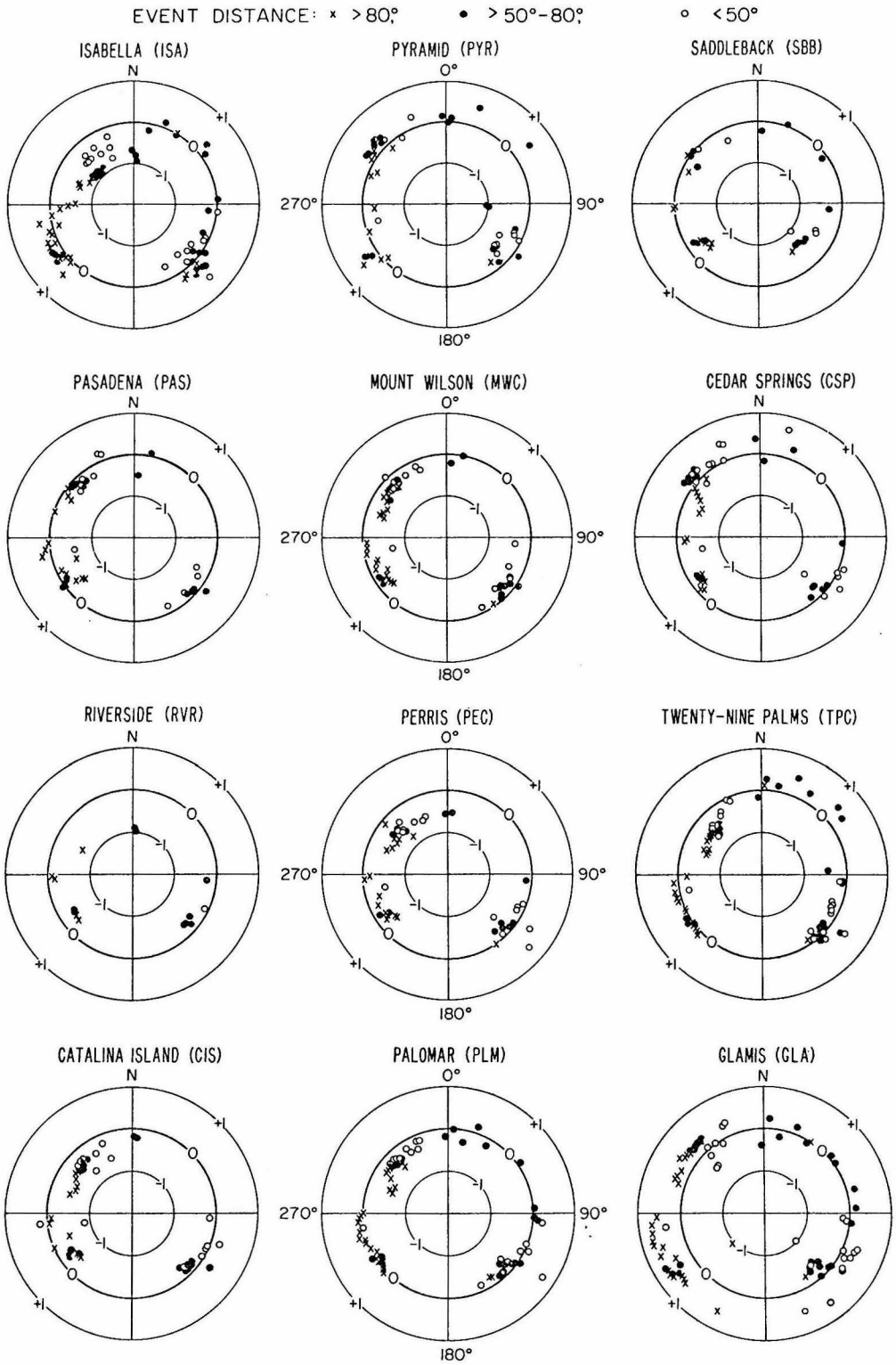
OBSERVED P-DELAYS IN SECONDS
(NORMALISED WITH RESPECT TO GOLDSTONE)
EVENT DISTANCE: × >80° • >50°-80° ○ <50°
ISABELLA (ISA)
PYRAMID (PYR)
SADDLEBACK (SBB)
PASADENA (PAS)
MOUNT WILSON (MWC)
CEDAR SPRINGS (CSP)
RIVERSIDE (RVR)
PERRIS (PEC)
TWENTY-NINE PALMS (TPC)
CATALINA ISLAND (CIS)
PALOMAR (PLM)
GLAMIS (GLA)
N
0°
90°
180°
270°
+1
-1

Table 3-1

LOCATIONS OF STATIONS USED IN THIS STUDY

STATION	LAT		LONG		ELEV	STATION	LAT		LONG		ELEV
	DEG	MIN	DEG	MIN	KM		DEG	MIN	DEG	MIN	KM
SYP	34.	31.63	-119.	58.67	1.30	ISA	35.	39.80	-118.	28.40	0.83
CLC	35.	49.00	-117.	35.80	0.77	GSC	35.	18.10	-116.	48.30	0.99
SBB	34.	41.30	-117.	49.50	0.85	CSP	34.	17.87	-117.	21.33	1.27
RVR	33.	59.60	-117.	22.50	0.26	PEC	33.	53.50	-117.	9.60	0.62
TPC	34.	6.35	-116.	2.92	0.76	PLM	33.	21.20	-116.	51.70	1.69
VST	33.	9.40	-117.	13.90	0.11	CPE	32.	52.80	-117.	6.00	0.21
SCI	32.	58.80	-118.	32.80	0.22	IKP	32.	38.93	-116.	6.48	0.96
GLA	33.	3.10	-114.	49.60	0.63	SNS	33.	25.90	-117.	32.90	0.19
SJQ	33.	37.20	-117.	50.70	0.16	CIS	33.	24.40	-118.	24.20	0.48
VPD	33.	48.90	-117.	45.70	0.18	TCC	33.	59.67	-118.	0.77	0.30
MWC	34.	13.40	-118.	3.50	1.73	PAS	34.	8.95	-118.	10.29	0.31
SCY	34.	6.37	-118.	27.25	0.29	TWL	34.	16.70	-118.	35.67	0.38
IRC	34.	23.40	-118.	24.00	0.58	PYR	34.	34.08	-118.	44.50	1.25
SWM	34.	43.00	-118.	35.00	1.22	JUN	34.	28.18	-117.	52.67	1.21
THR	34.	33.19	-117.	43.10	1.02	CKC	34.	8.18	-117.	10.48	0.55
MLL	34.	5.48	-116.	56.18	1.51	CFT	34.	2.11	-117.	6.66	0.67
MDA	33.	54.78	-116.	59.97	0.84	RAY	34.	2.18	-116.	48.67	2.34
WWR	33.	59.51	-116.	39.36	0.70	VGR	33.	49.91	-116.	48.55	1.48
DB2	33.	44.10	-117.	3.72	0.63	PSP	33.	47.63	-116.	32.93	0.19
KEE	33.	38.30	-116.	39.19	1.37	SMO	33.	32.15	-116.	27.70	2.44
COY	33.	21.84	-116.	18.63	0.21	HUT	33.	18.84	-116.	34.89	1.97
LRR	34.	31.50	-118.	1.70	0.91	TPO	34.	52.70	-118.	13.80	0.80
BLU	34.	24.32	-117.	43.52	1.88	AUL	34.	33.38	-117.	25.02	0.90
SDW	34.	36.55	-117.	4.45	1.18	ROM	34.	24.00	-117.	11.10	1.43
PEM	34.	10.04	-117.	52.18	0.50	PCF	34.	3.19	-117.	47.44	0.16
BTL	34.	15.43	-117.	0.29	2.53	SIL	34.	20.87	-116.	49.64	1.73
SSK	34.	12.97	-117.	41.32	1.76	SSV	34.	12.46	-117.	29.98	1.61
GAV	34.	1.35	-117.	30.74	0.19	OVL	34.	12.02	-117.	19.71	0.60
SME	33.	49.36	-117.	21.32	0.49	STP	34.	34.27	-114.	50.88	0.63
TTM	34.	20.12	-114.	49.65	1.10	CHM	34.	33.18	-114.	34.32	0.94
WH2	34.	18.87	-114.	24.55	1.24	BPK	34.	7.48	-114.	12.58	0.50
RVS	34.	2.08	-114.	31.08	0.68	LTM	33.	54.90	-114.	55.10	0.74
BMM	33.	45.40	-114.	35.14	0.56	HSP	32.	44.81	-115.	33.71	-.01
PIC	32.	54.85	-114.	38.59	0.26	LGA	32.	45.58	-114.	29.57	0.07
FTM	32.	33.29	-114.	20.01	0.26	YMD	32.	33.28	-114.	32.68	0.08
RMR	34.	12.77	-116.	34.52	1.70	HDG	34.	25.73	-116.	18.30	1.35
CPM	34.	9.24	-116.	11.80	0.94	INS	33.	56.14	-116.	11.66	1.70
PNM	33.	58.64	-115.	48.05	1.15	LED	34.	28.06	-115.	56.19	0.85
SHH	34.	11.26	-115.	39.27	1.12	GRP	34.	48.26	-115.	36.27	1.24
SPM	34.	28.32	-115.	24.16	0.91	PIU	34.	44.42	-115.	15.64	1.21
IRN	34.	9.60	-115.	11.04	0.98	CO2	33.	50.83	-115.	20.68	0.28
BC2	33.	39.42	-115.	27.67	1.18	LTC	33.	29.34	-115.	4.20	0.46
ROD	34.	37.78	-116.	36.29	1.29	SBCC	34.	56.38	-120.	10.32	0.61
SBLP	34.	33.57	-120.	24.02	0.13	SBSM	34.	2.24	-120.	21.01	0.17
SBLC	34.	29.79	-119.	42.81	1.19	SBSC	33.	59.68	-119.	37.99	0.46
SBAI	34.	0.80	-119.	26.23	0.11	SBSN	33.	14.68	-119.	30.38	0.26
ECF	34.	27.48	-119.	5.44	0.97	SBCO	34.	22.12	-119.	20.63	0.21
CAM	34.	15.27	-119.	2.00	0.27	SBLG	34.	6.87	-119.	3.85	0.41
SIP	34.	12.24	-118.	47.94	0.70	KYP	34.	6.11	-118.	52.77	0.70
SAD	34.	4.86	-118.	39.90	0.73	PTO	34.	0.25	-118.	48.38	0.04
CJP	34.	10.92	-118.	59.19	0.50	CLP	34.	5.33	-118.	57.85	0.50
OBB	33.	10.04	-115.	38.20	-.06	AMS	33.	8.48	-115.	15.25	0.14
CCM	33.	25.75	-115.	27.88	0.49	COT	33.	18.29	-115.	21.20	0.28
WLK	33.	3.08	-115.	29.44	-.05	SUP	32.	57.31	-115.	49.43	0.22
CRR	32.	53.18	-115.	58.10	0.10	CUK	32.	50.95	-115.	43.61	-.01
SGL	32.	38.95	-115.	43.52	0.11	ING	32.	59.30	-115.	18.61	-.00
SNR	32.	51.71	-115.	26.21	-.03	COA	32.	51.81	-115.	7.36	-.03
RUN	32.	58.32	-114.	58.63	0.15	BGN	32.	41.67	-115.	16.11	0.01
BSC	32.	41.67	-115.	16.11	0.01	BCK	32.	43.49	-115.	2.64	0.04
PLT	32.	43.87	-114.	43.76	0.06	SLU	32.	30.10	-114.	46.64	0.04
LHU	34.	40.30	-118.	24.70	1.04	YEG	35.	26.18	-119.	57.56	0.94
CRG	35.	14.53	-119.	43.40	1.20	BCH	35.	11.10	-120.	5.05	1.14
PKM	34.	53.75	-119.	49.13	1.70	TMB	35.	5.24	-119.	32.08	1.02
ABL	34.	51.05	-119.	13.25	1.98	RYS	34.	38.60	-119.	21.10	1.84
BMT	35.	8.15	-118.	35.81	1.24	FTC	34.	52.25	-118.	53.51	0.92

Table 3-2

U.S.G.S. HYPOCENTRAL PARAMETERS

FOR EVENTS USED IN THIS STUDY

LOCATION	DATE	TIME			LAT		LONG		DEPTH	MAG
		H	M	S	DEG	MIN	DEG	MIN	KM	
N CHILE	JAN02 74	10	42	29.9	-22.	30.00	-68.	24.00	105.	6.4
PERU COAST	JAN05 74	8	33	50.7	-12.	18.00	-76.	24.00	98.	6.3
GALAPAGOS	JAN07 74	2	18	50.7	0.	0.0	-91.	30.00	0.	5.4
NWE HEBRIDES	JAN10 74	8	51	13.3	-14.	24.00	166.	54.00	34.	6.7
KERMADEC	JAN15 74	8	32	14.0	-30.	54.00	-178.	54.00	114.	5.6
MARIANAS	JAN25 74	20	28	13.0	18.	54.00	145.	30.00	141.	5.9
SOLOMON IS	JAN31 74	23	30	5.3	-7.	30.00	155.	54.00	34.	6.0
KURIL IS	MAR11 74	11	37	33.5	48.	18.00	153.	12.00	169.	5.9
S FIJI	MAR23 74	14	28	35.4	-23.	54.00	179.	48.00	535.	6.1
ANDREANOF	MAR27 74	16	28	47.3	50.	6.00	-179.	42.00	37.	5.6
KODIAK	MAR29 74	21	56	35.3	57.	36.00	-153.	54.00	44.	5.7
SOUTH PERU	APR27 74	6	1	47.3	-15.	0.0	-72.	12.00	113.	5.8
MARIANAS	MAY01 74	15	22	24.7	18.	18.00	145.	12.00	455.	5.5
HONSHU	MAY05 74	14	19	12.0	37.	42.00	141.	42.00	48.	5.6
MARIANAS	MAY11 74	6	14	8.6	19.	42.00	147.	18.00	6.	6.4
TONGA	JUN04 74	4	14	15.9	-15.	48.00	-175.	6.00	276.	6.0
NEW BRITAIN	JUN27 74	7	46	11.9	-4.	42.00	152.	30.00	70.	6.1
KERMADEC	JUL02 74	23	26	26.6	-29.	6.00	-176.	0.0	0.	6.8
PANAMA-COLOMBIA	JUL13 74	1	18	22.8	7.	42.00	-77.	42.00	12.	6.4
PAN-COLOMBIA	JUL14 74	2	13	50.4	7.	42.00	-77.	36.00	15.	5.9
PERU-BRAZIL	AUG09 74	4	53	30.9	-8.	18.00	-74.	18.00	159.	5.6
FIJI ISLANDS	AUG10 74	11	22	26.4	-21.	24.00	-179.	12.00	602.	5.5
ANDREANOF	AUG13 74	3	46	20.3	51.	30.00	-178.	6.00	52.	5.8
COLOMBIA	AUG24 74	2	47	30.1	4.	18.00	-76.	54.00	84.	5.9
HONSHU	AUG25 74	1	18	39.9	32.	0.0	142.	18.00	0.	5.9
NOV ZEMLYA	AUG29 74	9	59	55.5	73.	24.00	55.	6.00	0.	6.4
LEEWARD IS	SEP07 74	19	40	52.2	15.	6.00	-60.	36.00	58.	5.7
JUJUY ARG.	SEP16 74	0	38	15.3	-23.	54.00	-65.	30.00	280.	5.6
HONSHU	SEP27 74	3	10	7.9	33.	36.00	141.	6.00	46.	5.8
LEEWARD IS	OCT08 74	9	50	58.1	17.	18.00	-62.	0.0	47.	6.6
KURIL IS	OCT09 74	7	32	2.2	44.	42.00	150.	6.00	49.	6.3
FIJI REGION	OCT21 74	4	12	29.4	-17.	54.00	-178.	36.00	602.	6.0
NOVAYA ZEMLYA	NOV02 74	4	59	56.7	70.	48.00	54.	6.00	0.	6.7
TONGA	NOV02 74	22	19	5.2	-15.	12.00	-174.	6.00	97.	5.6
ANDREANOF	NOV11 74	5	17	51.0	51.	36.00	-178.	6.00	68.	5.8
SOUTH FIJI	NOV12 74	6	29	21.1	-23.	54.00	-177.	36.00	196.	5.6
SOUTH HONSHU	NOV29 74	22	5	22.4	30.	42.00	138.	18.00	419.	6.1
PERU-BRAZIL	DEC05 74	11	57	31.3	-7.	42.00	-74.	30.00	162.	6.0
NEAR ALEUTIANS	DEC25 74	2	49	13.0	51.	42.00	174.	36.00	40.	5.7
SOUTH ALASKA	DEC29 74	18	25	0.7	61.	36.00	-150.	30.00	67.	5.6
MARIANAS	JAN01 75	14	16	1.0	21.	36.00	142.	54.00	313.	5.6
KERMADEC	JAN12 75	17	47	23.5	-33.	30.00	-178.	6.00	23.	5.8
FOX ALEUTIANS	JAN13 75	9	19	10.3	52.	12.00	-171.	6.00	42.	5.7
TONGA	JAN17 75	9	30	42.3	-17.	54.00	-174.	30.00	153.	5.8
JAPAN	JAN20 75	17	31	10.6	35.	0.0	142.	12.00	28.	5.9
NEW BRITAIN	FEB07 75	4	51	44.0	-7.	18.00	149.	30.00	33.	6.3
ANDREANOF	FEB22 75	8	36	7.4	51.	24.00	-179.	6.00	48.	6.3
SOUTH FIJI	FEB22 75	22	4	37.7	-24.	54.00	-179.	6.00	375.	6.2
NORTH CHILE	FEB26 75	20	14	59.6	-19.	48.00	-69.	18.00	82.	5.7
FIJI	FEB27 75	18	42	53.7	-17.	54.00	-178.	36.00	586.	5.9
CENTRAL CHILE	MAR13 75	15	26	42.5	-29.	54.00	-71.	18.00	4.	6.2

Table 3-2 (continued)

LOCATION	DATE	TIME H	M	S	LAT DEG	MIN	LONG DEG	MIN	DEPTH KM	MAG
CATAMARCA	MAR25 75	6	41	33.0	-28.	0.0	-66.	42.00	178.	5.9
NEW BRITAIN	APR09 75	6	26	22.2	-4.	0.0	152.	42.00	113.	6.3
UNIMAK	APR11 75	10	47	15.3	54.	6.00	-163.	12.00	20.	5.5
PERU	APR12 75	15	33	8.6	-14.	48.00	-72.	42.00	81.	5.9
JAN MAYEN	APR16 75	1	27	18.7	71.	30.00	-10.	24.00	13.	6.1
HONSHU	MAY04 75	9	31	59.2	37.	8.00	142.	5.00	23.	5.8
CHILE	MAY10 75	14	27	37.2	-38.	12.00	-73.	24.00	2.	7.8
GULF ALASKA	MAY25 75	19	4	34.4	57.	22.50	-150.	7.13	33.	5.6
N ATLANTIC	MAY26 75	9	11	51.5	35.	59.80	-17.	38.93	33.	6.7
N ATLANTIC	MAY26 75	20	19	35.2	36.	1.70	-17.	35.28	33.	5.6
SOUTH FIJI	MAY29 75	6	42	12.8	-22.	26.30	179.	31.60	616.	5.6
PERU-BOLIVIA	JUN05 75	20	29	37.6	-16.	30.00	-69.	12.00	196.	5.5
FIJI	JUN06 75	1	8	41.1	-20.	36.00	-179.	12.00	658.	6.0
CHILE-ARG	JUN14 75	10	40	21.2	-35.	12.00	-70.	42.00	97.	5.7
HONSHU	JUN14 75	23	36	27.7	36.	16.70	143.	25.73	19.	6.1
NEW HEBRIDES	JUN18 75	16	32	29.1	-13.	43.90	161.	11.28	201.	5.5
JAPAN SEA	JUN29 75	10	37	41.4	38.	45.50	129.	59.40	560.	6.2
SOUTH HONSHU	JUL08 75	22	46	19.2	32.	48.00	142.	12.00	49.	6.0
PERU-BOLIVIA	JUL12 75	6	47	37.5	-17.	10.00	-69.	21.00	156.	5.5
SOLOMON IS	JUL20 75	23	5	18.8	-6.	34.80	154.	39.07	50.	6.2
SOLOMON IS	JUL21 75	2	39	1.2	-6.	54.50	155.	20.00	95.	6.1
SOLOMON ISE	JUL22 75	22	26	39.0	-7.	6.00	155.	34.32	70.	5.5
SOUTH FIJI	JUL24 75	19	1	42.6	-23.	28.60	-179.	46.50	579.	5.6
SOUTH ALASKA	AUG02 75	10	18	17.9	53.	23.20	-161.	29.10	33.	5.8
JAPAN SEA	AUG06 75	21	37	39.7	43.	54.00	139.	16.00	230.	5.6
JUJUY, ARG	AUG10 75	10	25	43.3	-22.	38.90	-66.	35.33	166.	6.2
PERU COAST	AUG11 75	10	39	18.8	-11.	44.00	-77.	45.00	74.	5.6
KOMANDORSKY	AUG15 75	7	28	18.9	54.	52.60	167.	50.70	4.	6.0
NORTH PERU	AUG16 75	0	53	53.7	-5.	22.60	-76.	4.57	123.	5.7
FIJI	AUG20 75	20	18	50.9	-20.	24.00	-178.	23.00	559.	5.7
NOVAYA ZEMLYA	AUG23 75	8	59	57.9	73.	22.10	54.	38.47	0.	6.4
KAMCHATKA	AUG23 75	13	51	24.1	54.	44.50	160.	3.15	141.	5.9
HOKKAIDO	OCT02 75	11	6	46.5	43.	11.90	145.	53.17	75.	5.8
CHILE-ARG	OCT10 75	13	13	9.4	-25.	5.50	-68.	4.40	96.	5.5
NOVAYA ZEMLYA	OCT18 75	8	59	56.3	70.	50.40	53.	41.40	0.	6.3
NOVAYA ZEMLYA	OCT21 75	11	59	57.3	73.	21.10	55.	5.22	0.	6.5
NORTH CHILE	OCT28 75	6	54	22.4	-22.	51.70	-70.	3.45	38.	5.9
HOKKAIDO	OCT30 75	1	41	31.5	42.	0.40	142.	40.10	59.	5.8
FIJI ISLANDS	NOV01 75	6	14	55.5	-18.	28.00	-177.	51.50	424.	5.8
SANTA CRUZ	NOV08 75	11	0	24.5	-10.	57.50	166.	5.58	74.	5.7
SEA OF OKHOTSK	NOV11 75	4	25	32.3	46.	40.40	145.	28.90	355.	5.5
SOUTH FIJI	NOV19 75	6	18	33.9	-24.	3.00	179.	4.80	555.	5.8
KAMCHATKA	NOV19 75	11	6	27.5	54.	21.60	161.	18.10	62.	6.2
NORTH CHILE	DEC06 75	22	47	30.4	-23.	49.40	-68.	49.40	82.	5.4
PERU	DEC11 75	20	17	8.1	-11.	33.30	-74.	33.10	98.	6.0
SANTA CRUZ IS	DEC19 75	2	14	29.6	-11.	45.20	164.	48.23	33.	6.0
OKHOTSK	DEC21 75	10	54	17.7	51.	56.40	151.	34.60	554.	6.0
PERU	JAN05 76	2	31	36.3	-13.	17.30	-74.	53.90	95.	6.0
PERU-BOLIVIA	JAN06 76	23	54	22.2	-17.	55.00	-69.	28.92	76.	5.6
NEW HEBRIDES	JAN09 76	23	54	35.6	-15.	45.50	167.	52.10	168.	6.1
KERMADEC	JAN24 76	21	48	25.9	-28.	38.10	-177.	35.58	78.	6.2

Table 3-2 (continued)

LOCATION	DATE	TIME			LAT		LONG		DEPTH	MAG
		H	M	S	DEG	MIN	DEG	MIN	KM	
SOUTH HONSHU	JAN27 76	23	28	20.9	31.	23.20	138.	3.20	394.	5.0
SOUTH FIJI	FEB03 76	12	27	30.1	-25.	8.20	179.	41.60	477.	5.8
TONGA	FEB03 76	18	3	52.0	-18.	6.50	-175.	1.90	212.	5.9
CHILE-BOLIVIA	FEB05 76	9	53	11.7	-21.	42.10	-68.	13.30	98.	5.8
BONIN IS	FEB14 76	10	50	22.2	26.	33.50	140.	16.50	548.	5.5
SOUTH FIJI	FEB14 76	11	22	17.4	-23.	11.50	-177.	24.90	232.	5.9
NORTH CHILE	FEB18 76	18	3	22.7	-22.	30.80	-68.	36.80	111.	5.4
SOLOMON IS	FEB22 76	18	28	58.3	-6.	18.80	154.	46.70	56.	5.9
NORTH CHILE	FEB27 76	3	36	13.6	-19.	28.50	-69.	3.90	103.	5.5
SOLOMON IS	MAR01 76	19	48	3.5	-9.	16.00	157.	16.60	25.	5.8
SOLOMON IS	MAR02 76	10	51	9.6	-6.	16.90	154.	47.82	61.	5.7
NEW HEBRIDES	MAR04 76	2	50	0.5	-14.	44.60	167.	6.23	90.	6.4
SOLOMON IS	MAR08 76	4	39	55.9	-10.	42.00	165.	0.0	47.	6.1
LEEWARD IS	MAR10 76	9	4	58.8	16.	48.00	-61.	6.00	54.	5.8
N COLOMBIA	MAR13 76	21	44	41.3	6.	48.50	-72.	57.97	165.	5.4
KERMADEC	MAR24 76	4	46	4.4	-29.	53.20	-177.	52.40	33.	6.4
SANTA CRUZ	MAR25 76	16	10	48.5	-11.	56.40	-166.	12.20	59.	5.8
KURIL IS	MAR29 76	19	48	39.8	46.	0.90	149.	30.35	162.	5.5
N COLOMBIA	APR01 76	19	21	14.4	6.	46.90	-72.	59.28	160.	5.2
MARIANAS	APR07 76	7	10	15.8	17.	37.20	145.	33.00	217.	5.7
FIJI	APR10 76	17	12	9.0	-17.	36.00	-178.	30.00	557.	6.0
CHILE-ARG	APR18 76	19	40	20.5	-25.	50.20	-68.	46.44	113.	5.6
KERMADEC	MAY05 76	4	52	51.2	-29.	45.00	-177.	48.00	33.	6.4
SOLOMON IS	MAY09 76	20	44	44.7	-7.	27.20	154.	37.80	34.	5.8
PERU	MAY15 76	21	55	56.2	-11.	36.00	-74.	30.00	33.	6.3
N ATLANTIC	MAY14 76	6	25	34.4	10.	46.90	-43.	29.90	33.	5.6
PERU COAST	MAY18 76	2	2	15.5	-16.	49.60	-72.	42.12	65.	5.4
COLOMBIA	MAY19 76	4	7	15.8	4.	27.80	-75.	47.00	157.	5.9
SANTA CRUZ IS	MAY19 76	19	7	17.2	-12.	47.60	169.	14.10	647.	5.2
TONGA	MAY20 76	4	59	47.1	-15.	56.20	-175.	5.60	292.	5.5
PERU	MAY23 76	16	32	33.0	-10.	29.00	-78.	19.30	73.	5.9
SOUTH CHILE	MAY30 76	3	8	54.2	-41.	38.20	-75.	24.70	28.	6.0
JAPAN	JUN04 76	4	23	32.4	38.	18.90	142.	40.00	21.	5.7
NORTH CHILE	JUN04 76	23	39	36.0	-23.	6.10	-68.	32.50	101.	5.4
SOLOMON IS	JUN05 76	8	20	7.2	-10.	5.20	161.	0.70	61.	6.2
TONGA	JUN18 76	1	45	37.3	-24.	48.80	-175.	21.36	33.	5.6
SOUTH JAPAN	JUN25 76	7	47	46.3	29.	54.80	138.	34.90	433.	5.5
NEW BRITAIN	JUN27 76	21	14	48.3	-5.	7.80	151.	37.09	119.	5.6
OKHOTSK	JUL10 76	11	37	12.8	47.	51.50	145.	43.10	387.	5.8
NEW HEBRIDES	AUG02 76	10	55	25.9	-20.	36.50	169.	16.43	52.	6.1
N CHILE COAST	AUG20 76	6	54	11.3	-20.	24.70	-69.	59.60	81.	5.6
SOLOMON IS	SEP04 76	11	41	59.7	-10.	14.80	161.	5.60	83.	5.6
S BOLIVIA	SEP06 76	23	58	2.2	-21.	19.60	-66.	18.07	188.	5.5
KURIL IS	SEP22 76	0	16	8.2	44.	52.80	149.	13.50	64.	6.1
NOVAYA ZEMLYA	SEP29 76	2	59	57.4	73.	24.20	54.	49.02	0.	5.8
SOLOMON IS	OCT12 76	0	40	52.9	-10.	27.20	161.	17.70	106.	5.9
KAMCHATKA	NOV17 76	5	33	34.6	50.	59.00	156.	13.38	112.	5.5
KURIL IS	NOV24 76	16	9	15.4	52.	1.20	160.	39.00	33.	5.8
FIJI	NOV25 76	14	6	35.4	-19.	29.90	-177.	42.30	442.	6.0
FIJI	NOV27 76	4	0	9.7	-17.	51.20	-178.	48.66	576.	5.5
CHILE-BOLIVIA	NOV30 76	0	40	57.8	-20.	31.20	-68.	55.14	82.	6.5

Table 3-2 (concluded)

LOCATION	DATE	TIME H	M	S	LAT DEG	MIN	LONG DEG	MIN	DEPTH KM	MAG
CHILE-BOLIVIA	DEC03 76	5	27	31.7	-20.	32.30	-68.	37.52	71.	5.4
CHILE-BOLIVIA	DEC04 76	12	32	29.6	-20.	22.90	-68.	31.86	72.	5.6
BONIN IS	DEC12 76	1	8	50.1	28.	2.60	139.	34.50	491.	5.9
TONGA	DEC15 76	7	10	27.8	-17.	19.10	-173.	59.64	79.	5.5
CHILE-BOLIVIA	DEC17 76	20	23	6.2	-20.	54.70	-68.	27.36	57.	5.6
VOLCANO IS	DEC22 76	1	1	41.0	23.	17.80	143.	43.27	49.	5.8
CHILE-BOLIVIA	DEC28 76	13	52	2.7	-20.	25.20	-68.	51.60	100.	5.7
FIJI	JAN21 77	6	11	5.6	-18.	0.80	-178.	22.74	604.	5.8
ARGENTINA	FEB04 77	7	46	36.6	-24.	39.60	-63.	3.00	600.	6.2
KAMCHATKA	FEB13 77	5	51	45.3	54.	3.60	158.	38.04	167.	5.0
SOUTH HONSHU	FEB18 77	20	51	29.8	33.	4.30	140.	49.00	42.	6.0
FIJI	MAR08 77	3	2	32.8	-17.	50.30	-178.	42.60	571.	5.3
NORTH KOREA	MAR09 77	14	27	53.6	41.	36.40	130.	52.70	528.	5.9
COLOMBIA	MAR23 77	2	11	22.7	6.	43.80	-73.	1.20	250.	5.8
PERU-BRAZIL	APR09 77	4	4	12.5	-10.	0.50	-71.	10.86	564.	5.9
KURIL IS	APR10 77	8	31	33.4	44.	28.20	147.	32.97	84.	5.4
FIJI IS	APR14 77	4	5	31.2	-17.	39.50	-178.	39.10	535.	5.2
FIJI	MAY15 77	23	12	53.6	-19.	7.90	-177.	40.32	499.	5.5
NEW HEBRIDES	MAY18 77	6	43	21.1	-18.	59.70	169.	11.64	217.	5.2
FIJI	JUN03 77	14	33	7.0	-18.	56.40	-177.	37.98	573.	5.3
NEW BRITAIN	JUN05 77	15	19	13.7	-4.	33.30	151.	57.36	150.	5.4
MARIANAS	JUN09 77	13	27	12.3	13.	9.20	144.	27.48	97.	5.2
TONGA PREL	JUN22 77	12	8	28.3	-23.	11.40	-175.	55.20	33.	7.2
NOVAYA ZEMLYA	SEP01 77	2	59	57.5	73.	22.60	54.	34.86	0.	5.7
E RUSSIA	SEP09 77	2	35	12.1	43.	33.60	133.	15.60	550.	5.2
PERU	OCT08 77	3	3	38.3	-10.	37.20	-73.	39.00	100.	5.6
FIJI REGION	OCT18 77	23	24	39.6	-17.	40.80	-178.	48.00	600.	5.9
SANTIAGO CEL E	OCT22 77	17	57	17.2	-28.	9.60	-63.	0.60	630.	6.2

when the data are modelled.)

3.1. Corrections for Crustal and Sediment Thickness

A list of the corrections used may be found in Table 3-3.

a. Moho depth

Data from a variety of sources including gravity surveys and seismic refraction profiles indicate that through much of Southern California the depth to Moho is 30-35 km (see, e.g., Kanamori and Hadley, 1975; Hadley and Kanamori, 1977). In particular, the Transverse Ranges have no crustal root, nor is there significant downwarping beneath the deep Los Angeles and Ventura basins. However, there is evidence for crustal thinning offshore (Shor and Raitt, 1956; Press, 1956) and beneath the Imperial Valley (Biehler et al., 1964; Fuis, 1976, personal communication), and thickening beneath the Sierra Nevada (Press, 1956; Thompson and Talwani, 1964). Corrections for crustal thickness were calculated on the basis of a lowermost crustal velocity of 6.7 km/s and a P_n velocity of 7.8 km/s (Hadley and Kanamori, 1977).

The correction at SCI and CIS was estimated at -0.2 sec, based on a crustal thinning of 10 km; no correction was made at SBSN because the station is located on sediments of unknown thickness which will tend to cancel the effect of the crustal thinning.

In the Imperial Valley the crustal thickness is approximately 20 km, but it increases away from the axis of the valley. The crustal correction used was again -0.2 sec.

The depth to Moho beneath ISA is not precisely defined by seismic data. Thompson and Talwani (1964) suggest that the Sierran root extends

Table 3-3

SEDIMENT AND CRUSTAL THICKNESS CORRECTIONS

Corrections are subtracted from observed relative residuals.

Station	T_{SED} sec	T_{MOHO} sec	TOTAL sec
CIS		-0.2	-0.2
SCI		-0.2	-0.2
ISA		-0.3	-0.3
OBB	(0.2)	-0.2	0
WLK	0.7	-0.2	0.5
ING	0.5	-0.2	0.3
COA	0.55	-0.2	0.35
BON	0.8	-0.2	0.6
BCK	0.65	-0.2	0.45
COK	0.65	-0.2	0.45
RUN	0.25	-0.2	0.10
SNR	0.75	-0.2	0.55
SLU	0.55	-0.2	0.35
HSP	0.75	-0.2	0.55
SGL	0.2	-0.2	0
PLT		-0.2	-0.2
GLA		-0.5	-0.05
SUP			-0.10
CRR			-0.05
AMS			-0.15
YMD	0.35	-0.15	0.20
LGA	0.20	-0.15	0.05
FTM		-0.10	-0.10
PIC			0.0
TCC	0.35		0.35
VPD	0.40		0.40
SJQ	0.45		0.45
SNS	0.30		0.30
TWL	0.40		0.40
CAM	0.50		0.50
SBCD	0.20		0.20
ECF	0.15		0.15
ADL	0.40		0.40

to depths of more than 40 km, and Press (1976) found it to be ∿50 km from surface wave dispersion measurements; the correction applied at ISA was 0.3 sec, equivalent to a 15 km crustal thickening. (This is probably appropriate for rays entering the crust under the High Sierra to the north, but may be ∿0.1 sec too high for rays from the south.)

No attempt was made to include azimuthally varying corrections: the maximum difference in distance between the points at which the rays to a given station enter the crust is approximately 25 km, and so the changes should not be large except in regions of steep dip on the Moho, such as the boundaries of the Imperial Valley.

b. Sediment corrections

There are three main areas in the array where sediment corrections are important: the Imperial Valley, the Los Angeles Basin, and the Ventura Basin. Some of the other stations, such as those lying between the San Andreas and San Jacinto Faults (e.g., CKC, MLL, CFT), may also require corrections, but no good data on sediment thicknesses were available outside the three major areas, and so none was made. It must be emphasised that all corrections are approximate, and errors will show up as stations where the residuals do not fit into the general pattern.

Imperial Valley:

Sediment corrections were based on the refraction profiles in Kovach *et al.* (1962), Biehler *et al.* (1964), and some recent data (Fuis, 1976, personal communications); the Valley contains up to 6 km of sediments. The station at Obsidian Buttes (OBB) is located on the

volcanic butte and requires no sediment correction; however, there is evidence of low crustal velocities in this region, and so a correction of 0.2 sec, cancelling the Moho term, was applied. (For stations at the edge of the Valley, sediment thickness is harder to assess, and the corrections are an estimate of the combined effects of sediment and Moho depth.)

Los Angeles Basin:

Corrections to stations in the Los Angeles Basin were based on sediment thicknesses derived from gravity data (McCulloh, 1960), oil company well log velocity data, and empirical delays observed from local earthquakes. They are essentially similar to those used by Hadley and Kanamori (1977). A correction was also introduced at SNS -- the magnitude (0.3 sec) is somewhat arbitrary since there are only limited data in this region and it is based largely on measurements in the nearby San Clemente oil field (Lang, 1972; Higgins, 1958) and the geologic map of the area (Morton, 1974).

Ventura Basin:

Sediment thicknesses for stations in the Santa Barbara network were derived from oil field data (Higgins, 1958), and sections appearing in Vedder et al. (1969), Yeats (1976), and in the Preliminary Report on the Continental Borderland, MF 624. Corrections were deemed necessary at SBCD (located on soft sediment near Casitas Lake), ECF and CAM. The latter is sitting on ∿20,000 feet of sediments of which ∿5,000 feet are quaternary.

3.2. The Observations

The relative residuals observed in this study are summarised in Figure 3-2, which consists of ten contour maps of average relative residuals, corrected for crustal and sediment thickness, for various source regions. Each station for which data were available for a given region is indicated by a black circle, and for most stations and source regions the value of residual used in constructing these maps was the average for at least five events. The main features will now be discussed for the different source locations progressing clockwise from the north.

Figure 3-2a shows the residuals for Russian nuclear explosions at Novaya Zemlya. The most noticeable points are the extremely negative residual at ISA (which may be ∿0.1 sec too low if the crustal thickness was overestimated), somewhat negative residuals in the eastern Mojave desert, and a broad region of positive residuals to the south of the Salton Sea, with the highest residuals occurring in two groups, one close to the axis of the Imperial Valley, and one at its western margin. The residuals for the two most northern stations in the Carrizo Plains are also markedly negative. The most obvious feature is the strong east-west trending zone of negative residuals to the south of the Transverse Ranges, where the delay reaches -1.0 sec. The "pinching out" of this anomaly at the eastern end of the Santa Barbara Channel is probably exaggerated: it is controlled by the residual at PTD, which is located on sediment, but has not been corrected for this. The correction needed is probably ∿0.2 sec, but no good estimates of sediment thickness at this location were found.

Figure 3-2. (a to j; the following 10 pages.)
Contour maps of mean relative residuals, corrected for known crustal structure, for the major source regions studied. The stations are shown as solid circles, the contours are labelled in tenths of a second and the contour interval is 0.2 sec.

Key to shading:

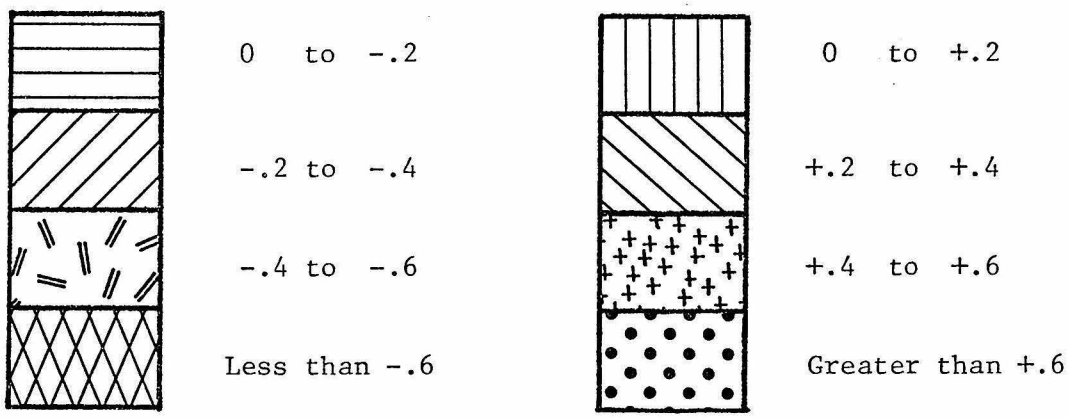

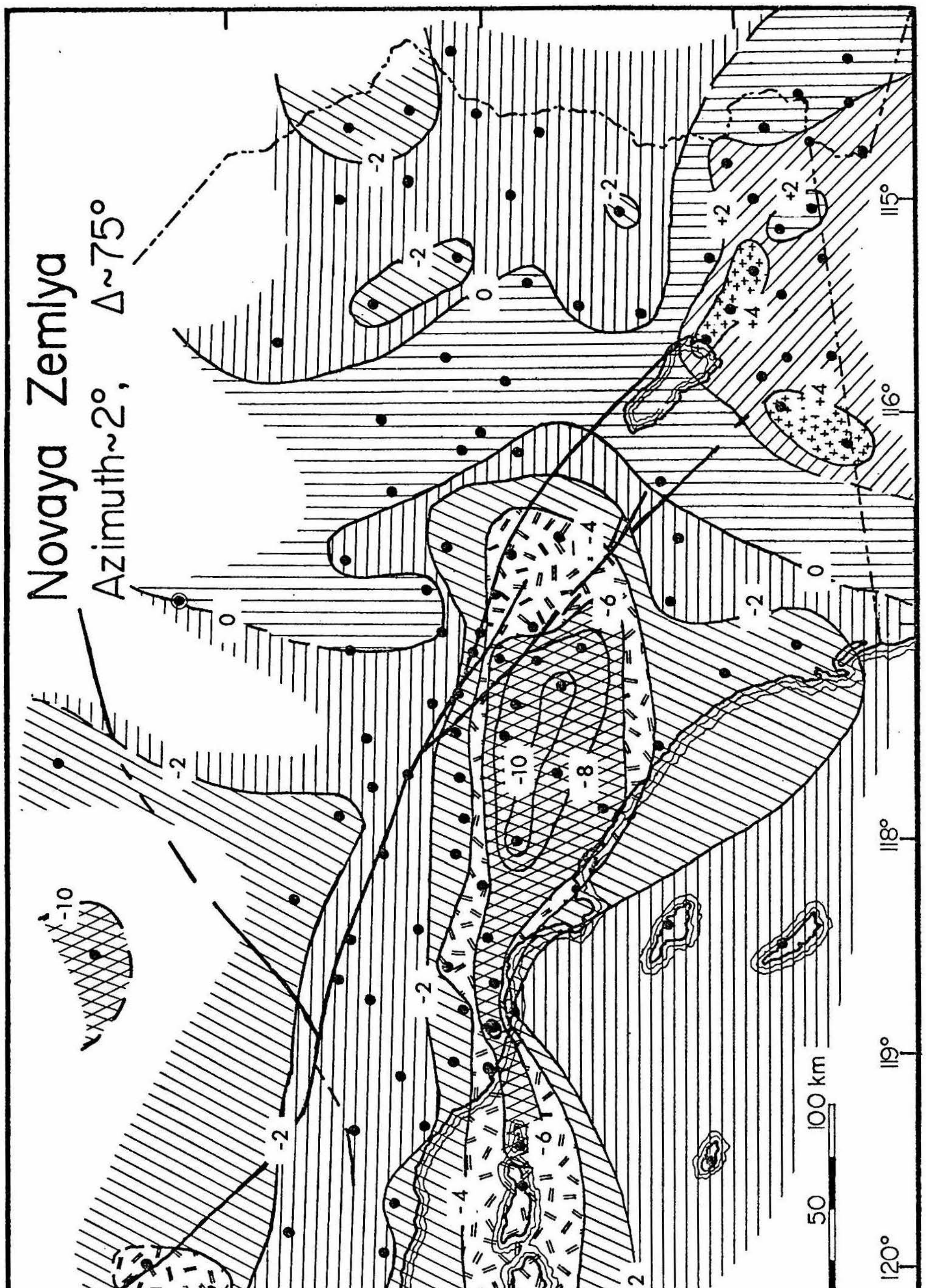
Novaya Zemlya
Azimuth~2°, Δ~75°
36°
35°
34°
33°
115°
116°
118°
119°
120°
0 50 100 km
-10
-8
-6
-4
-2
0
+2
+4

Figure 3-2 (a).

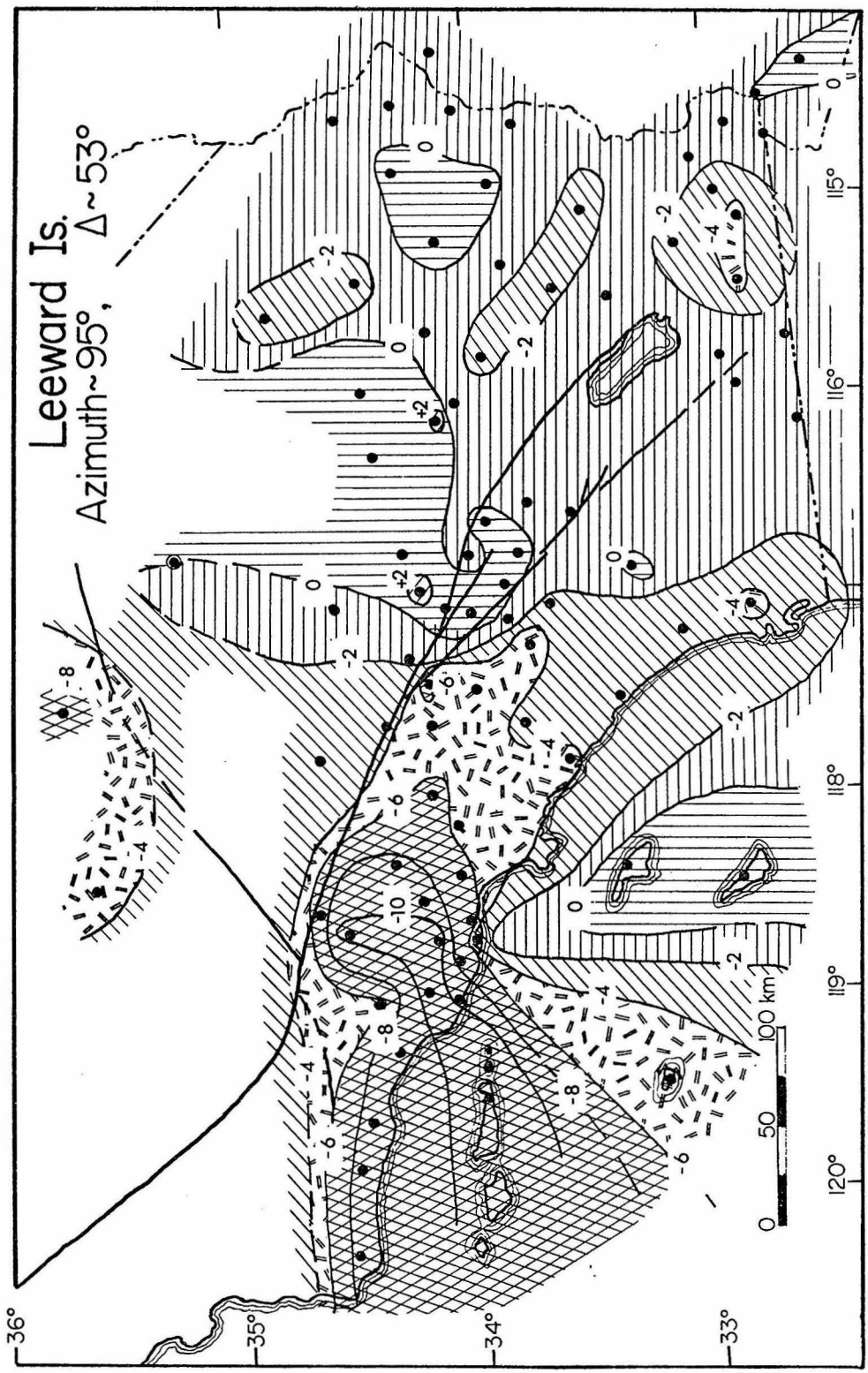
Leeward Is.
Azimuth~95°,
Δ~53°
36°
35°
34°
33°
115°
116°
118°
119°
120°
0
50
100 km

Figure 3-2 (b)

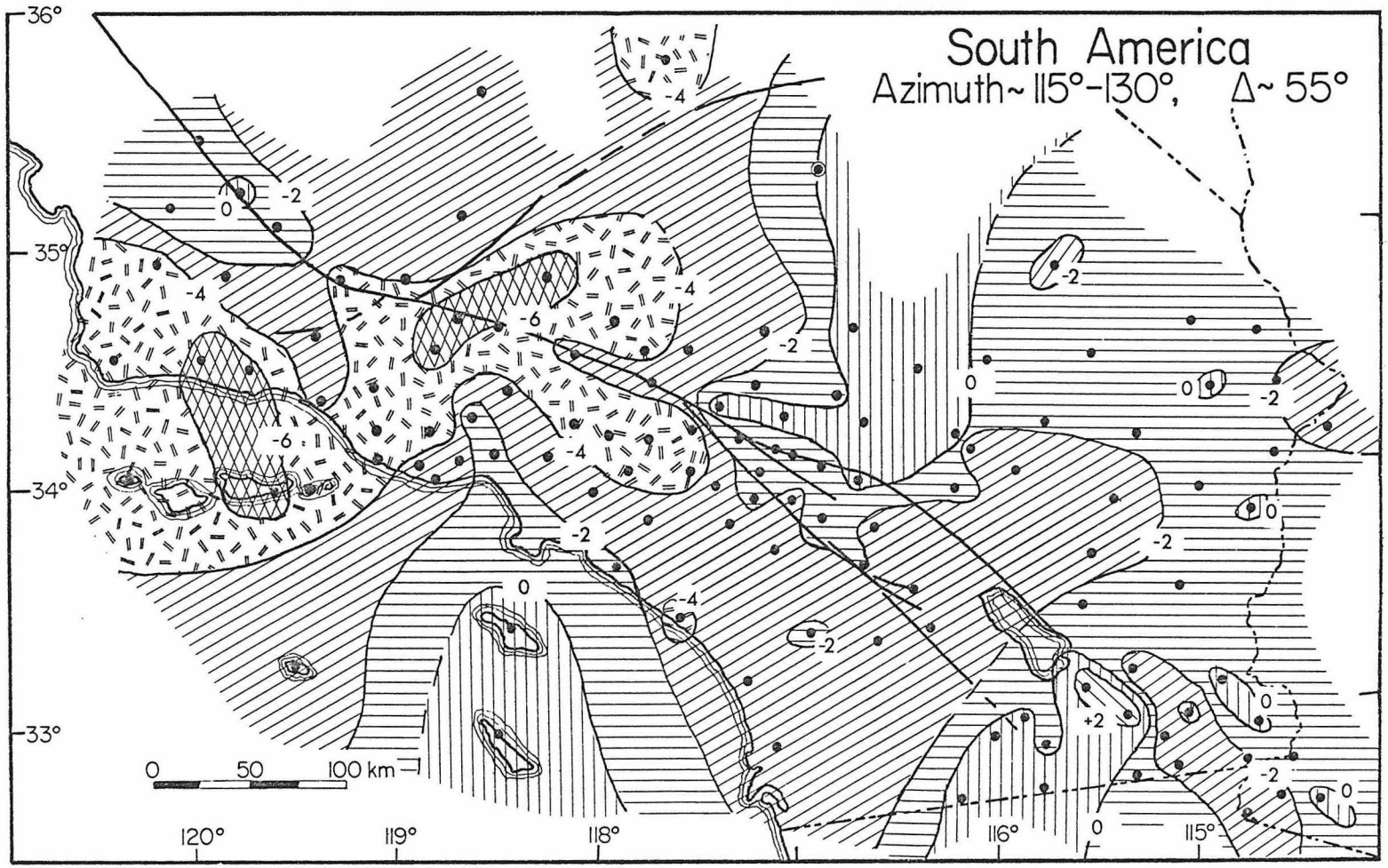
South America
Azimuth~ 115°-130°, Δ~ 55°
36°
35°
34°
33°
120°
119°
118°
116°
115°
0 50 100 km
-4
-2
0
-6
+2

Figure 3-2 (c).

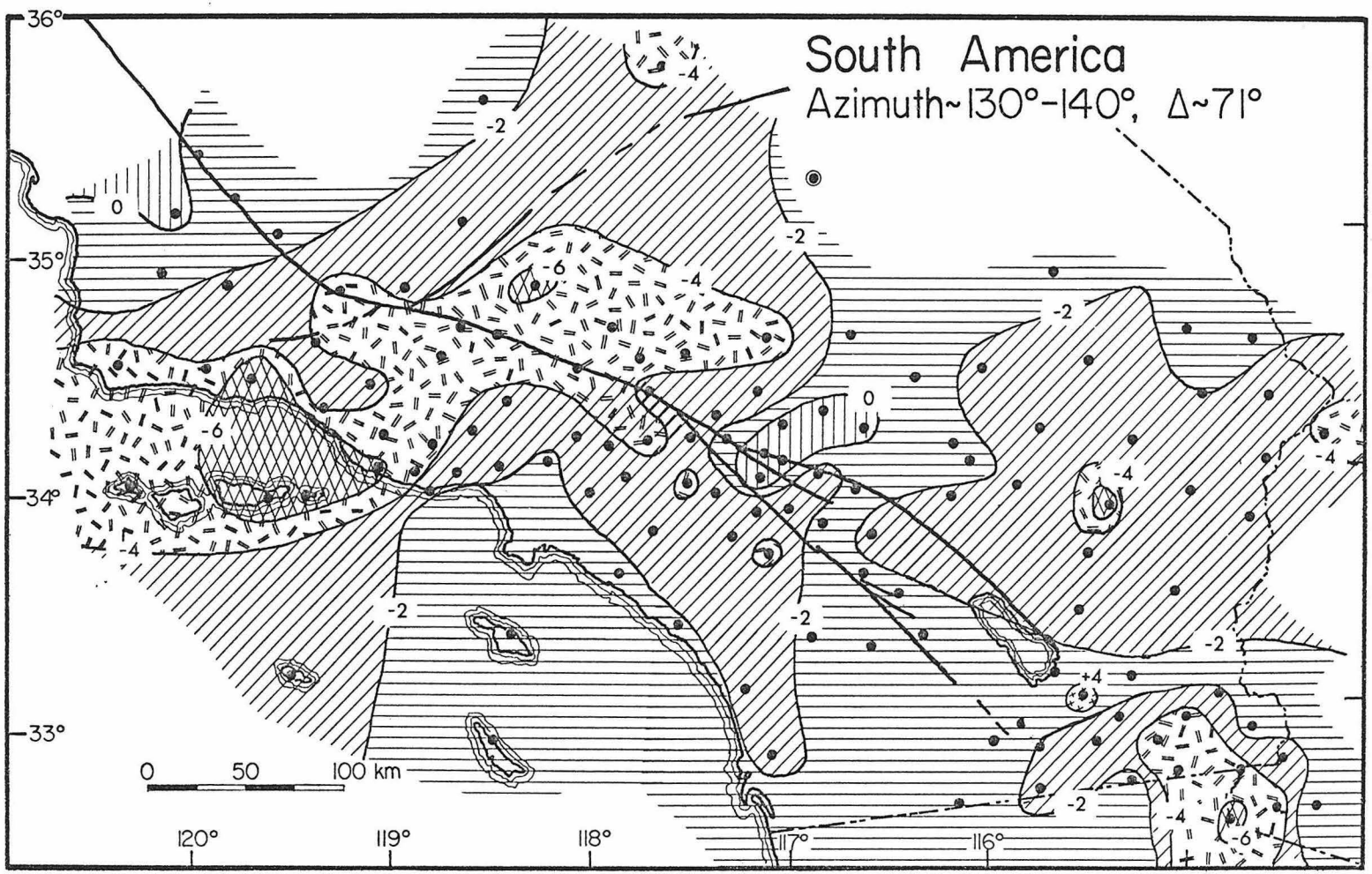
South America
Azimuth~130°-140°, Δ~71°
36°
35°
34°
33°
120°
119°
118°
117°
116°
0
50
100 km
-2
-4
-6
0
+4

Figure 3-2 (d).

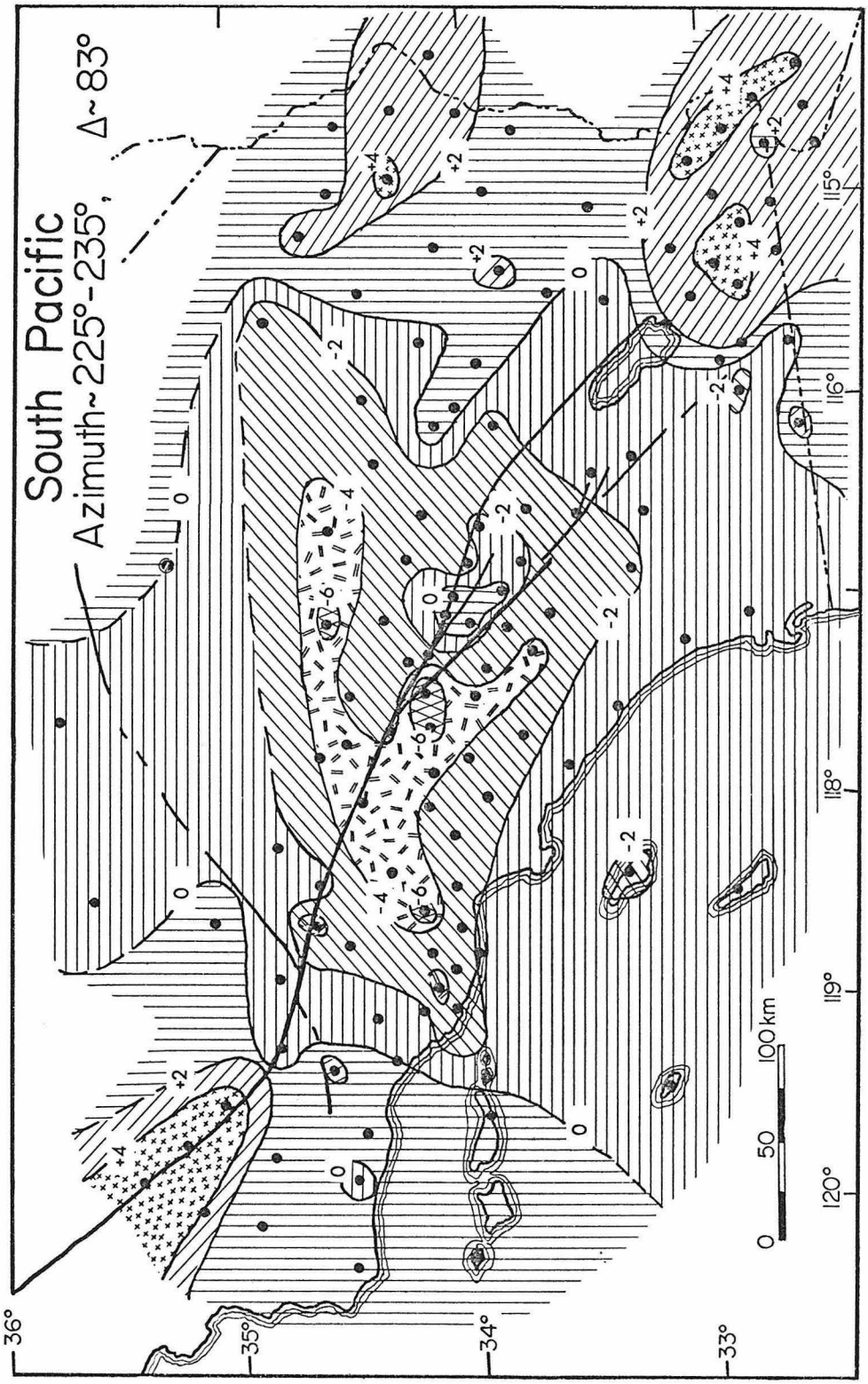
South Pacific
Azimuth~225°-235°, Δ~83°
36°
35°
34°
33°
115°
116°
118°
119°
120°
0
50
100km

Figure 3-2 (e).

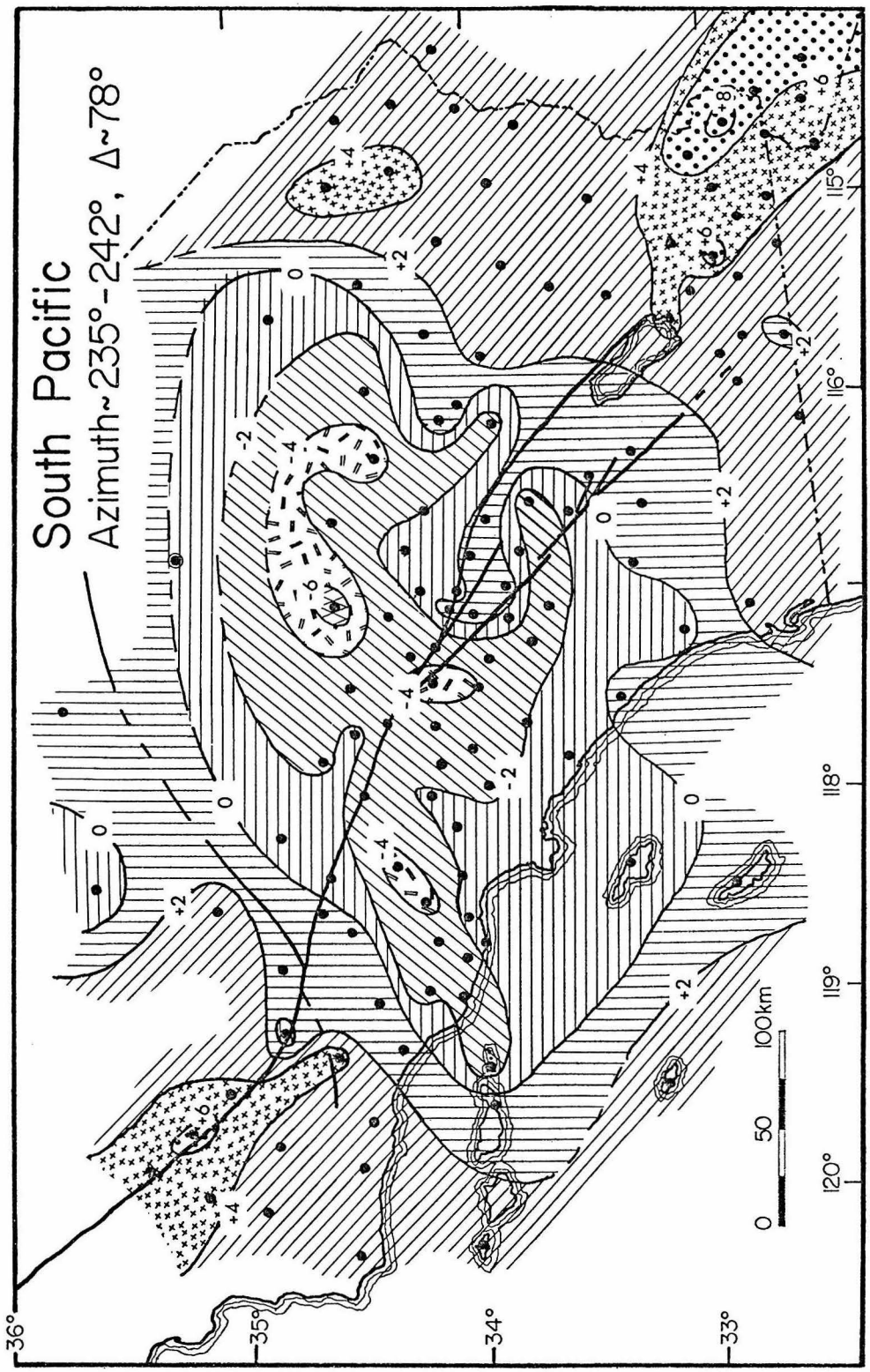
South Pacific
Azimuth~235°-242°, Δ~78°
36°
35°
34°
33°
115°
116°
118°
119°
120°
0
50
100km

Figure 3-2 (f).

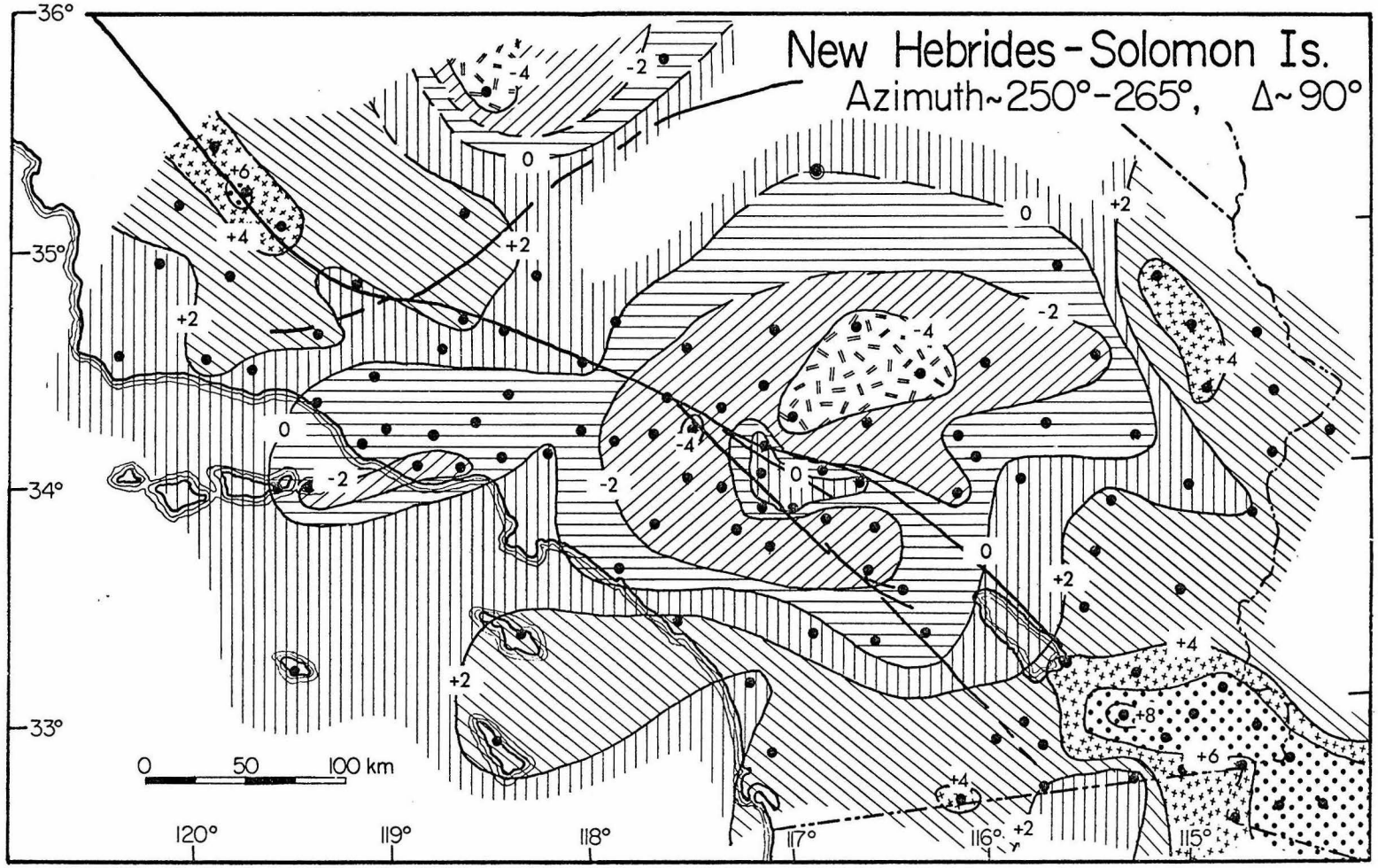
New Hebrides - Solomon Is.
Azimuth~250°-265°, Δ~90°
36°
35°
34°
33°
120°
119°
118°
117°
116°
115°
0 50 100 km

Figure 3-2 (g).

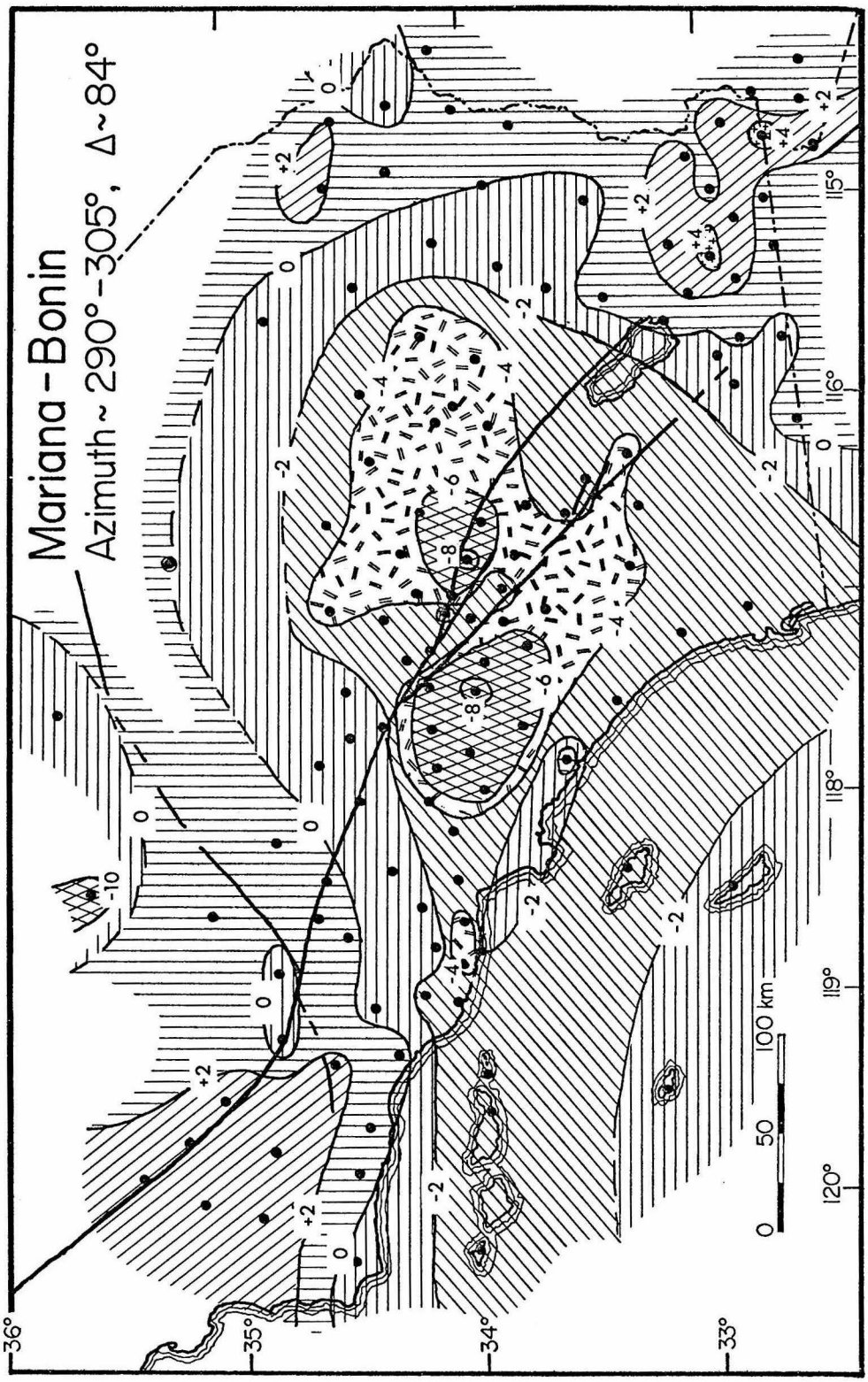
Mariana-Bonin
Azimuth ~ 290°-305°, Δ~84°
36°
35°
34°
33°
115°
116°
118°
119°
120°
0
50
100 km

Figure 3-2 (h).

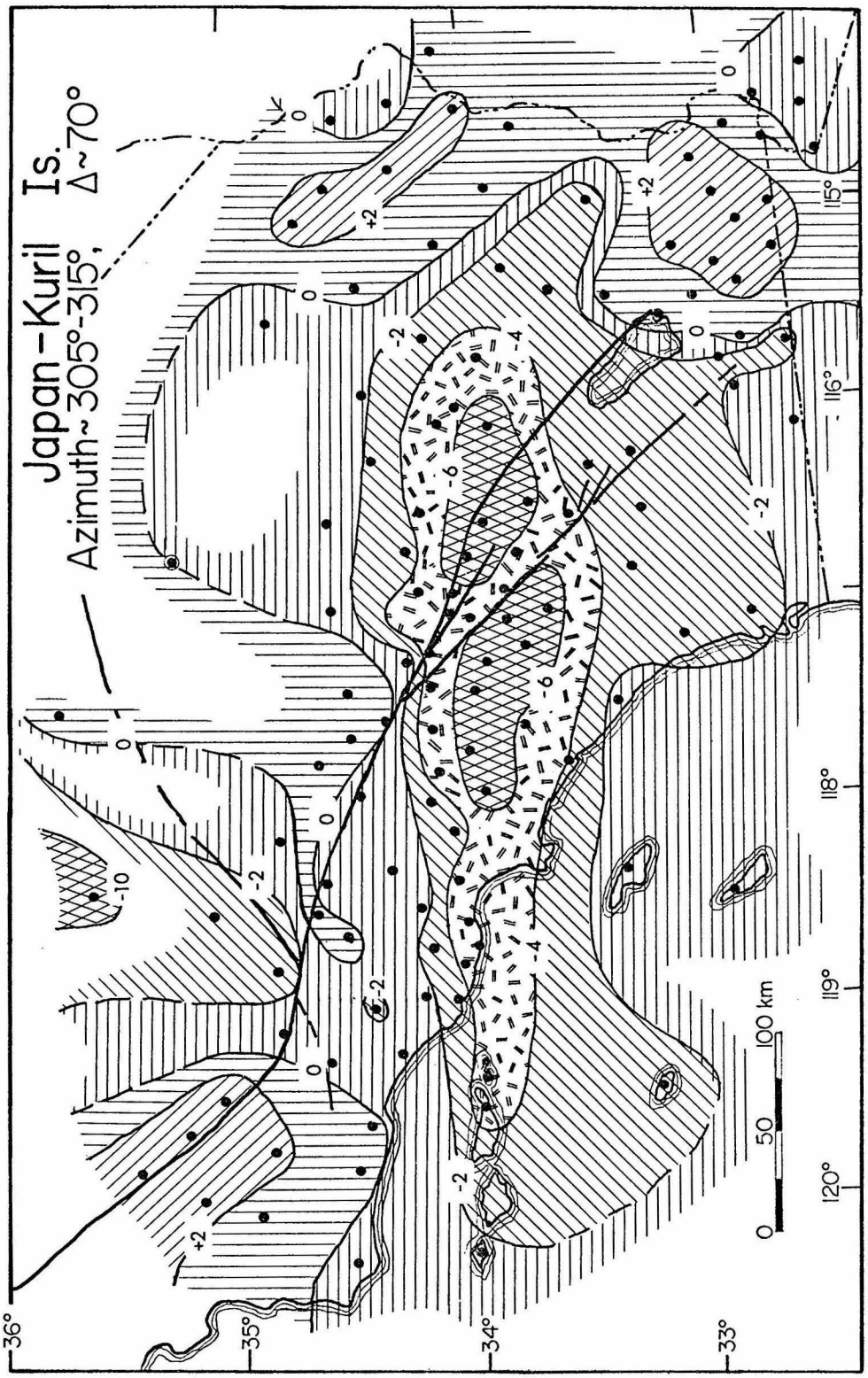
Japan-Kuril Is.
Azimuth~305°-315°; Δ~70°
36°
35°
34°
33°
115°
116°
118°
119°
120°
0
50
100 km
+2
0
-2
-4
-6
-10

Figure 3-2 (i).

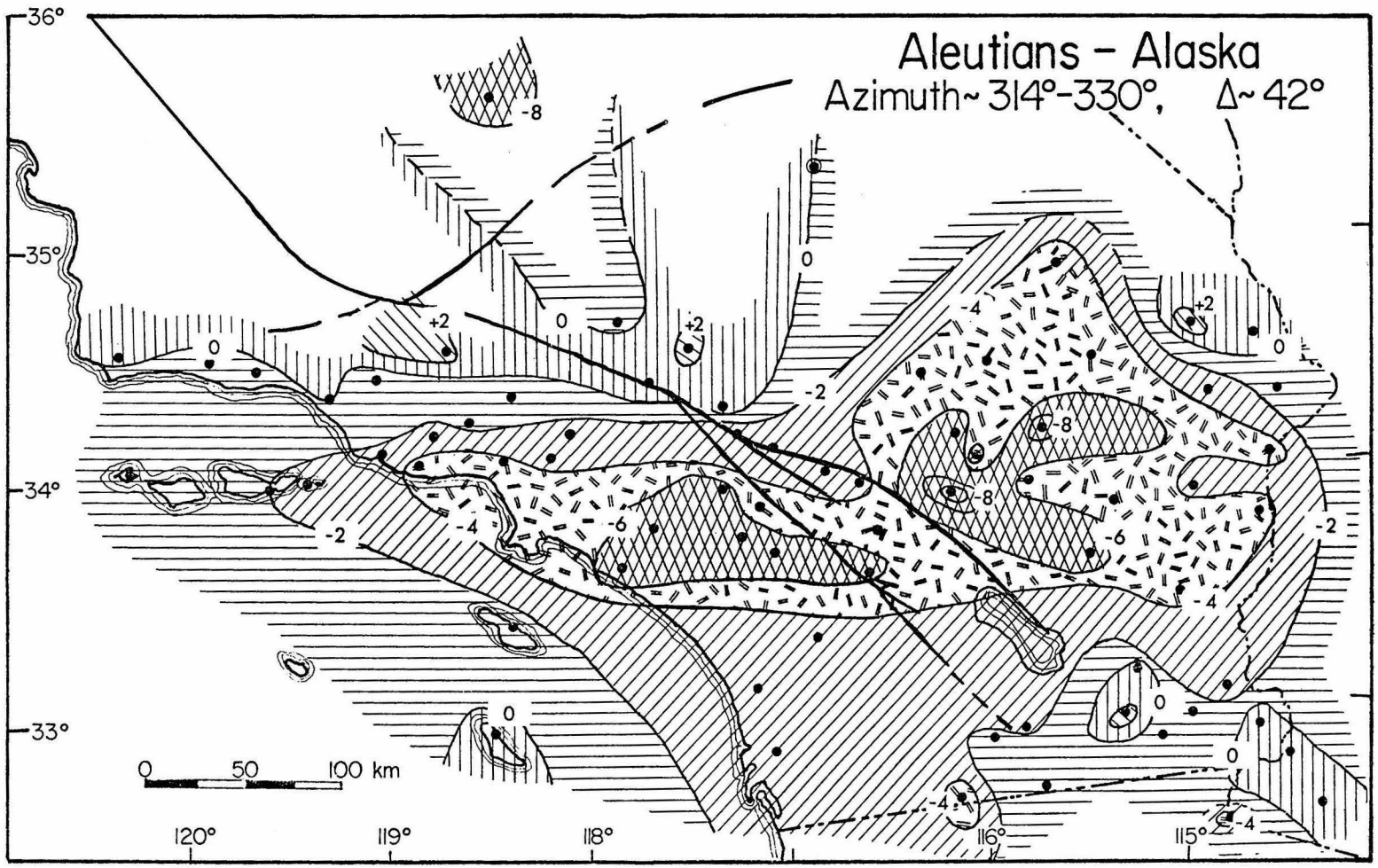
Aleutians – Alaska
Azimuth~ 314°-330°, Δ~ 42°
36°
35°
34°
33°
120°
119°
118°
116°
115°
0 50 100 km
-8
+2
0
-2
-4
-6

Figure 3-2 (j).

Arrivals were read for events in Jan Mayen, Iceland and the North Atlantic, but contour maps for these sources are not included, because they are based on single events recorded at relatively few stations, and the arrivals were somewhat more emergent than those generally retained in this study. In addition, the patterns seemed to change rather rapidly with small changes in azimuth, and without better data it is hard to assess the significance of these changes. However, the pattern observed for Jan Mayen, azimuth ∿20°, was very similar to that shown in Figure 2-3a for Novaya Zemlya, although the residual at ISA was much less negative, the maximum negative delay in the Transverse Ranges was -0.69 sec, and a region of positive residuals exceeding 0.4 sec appeared in the region of TPC, HDG and CPM. In fact, the whole pattern appeared to be shifted to more positive values, as would be the case if the arrival at GSC was early. The opposite effect is apparent for the residuals observed from the Icelandic event, at 26° azimuth, for which the pattern is shifted to more negative values. There is again a marked, approximately east-west trending belt of negative residuals largely to the south of the junction of the San Andreas and San Jacinto faults, which reaches a maximum advance of 1.0 sec at VPD. The eastern Mojave is also extremely early, reaching a peak value of -0.8 sec at WH2. Contours for the event in the North Atlantic at an azimuth of ∿55° are not well controlled, but there are negative (∿-0.2 sec) regions in the eastern Mojave, and in the general area of the Transverse Ranges, Los Angeles Basin and northernmost Peninsular Ranges, where the values are generally ∿-0.3 sec. The lowest values observed were -0.54 sec at IRC and -0.47 sec at SME.

The Imperial Valley is slightly slow for both Jan Mayen and the North Atlantic, but fast for Iceland.

The contour map for events in the Leeward Islands (azimuth ∿95°) is shown in Figure 3-2b: there were only three events, and as two of those were in 1974, many stations only recorded one arrival. ISA is still fast, but CLC is notably faster. A marked negative region extends over the western Transverse Ranges and Santa Barbara Channel; peak values in excess of -1.0 sec were found at Santa Cruz and Anacapa Islands (SBSC and SBAI). The Imperial Valley is now also fast. (If the residuals were calculated with respect to Herrin tables, the negative values of the southern Mojave desert and Imperial Valley would largely disappear. However, the westernmost stations such as SBLP would have slightly more negative residuals.)

The patterns for events in northern and southern South America (Figures 3-2c, d) are similar, with the most negative residuals occurring in a north-east-south-west trending zone extending from the westernmost Santa Barbara Channel to the Antelope Valley. A prominent feature is the area of negative residuals found in the eastern Imperial Valley in Figure 3-2c; for southern South America (Chile, Argentina) residuals for most of the Imperial Valley are negative, but this is especially true for the south-eastern corner (e.g., -0.7 sec at SLU). Although the Imperial Valley stations are at the periphery of the array, and far from GSC and thus subject to greater errors, this change from positive to negative residuals is probably real and significant. However, there is some indication of a trend in residuals across the array of the type that would be caused if the wavefront were incident at a greater

angle than expected. This is equivalent to a decrease in apparent velocity for waves from South American events, which has been reported for other arrays in North America (Powell, 1976), and may thus be a source or path effect.

Residuals for events in the south-western quadrant -- the South and "Central" Pacific, Figures 3-2e, f and g -- are fairly similar, and are appreciably more positive than those for other azimuths. This can be explained if the arrivals at GSC are slightly ($\sim$0.2 sec) early for events in these regions. There is still a negative area associated with the Transverse Ranges, now centred to the north, and slightly east, of the San Gabriel Mountains. The Imperial Valley is once more slow, with the areas of most positive residuals elongated parallel to the Valley axis, and located to the east of it. The eastern Mojave is also slow, as are the Carrizo Plains stations. There is also an "island" of positive residuals in the region of the junction of the San Andreas and San Jacinto faults: as mentioned in the previous section, a number of the stations controlling this region, notably CKC, CFT and MLL, are sited on sediments but have not been corrected for this, and so are expected to have more positive residuals than the surrounding stations that are located on bedrock. There is also evidence (Hadley and Combs, 1974) that crustal velocities are slow in this region.

Figures 3h and i are again very similar, as might be expected, but there are subtle differences reflecting the change in azimuth and distance to events in the Marianas-Bonin and Japan-Kuril arcs. Both show markedly negative (<-1.0 sec) residuals at ISA, northwest trending zones of slightly positive residuals in the Carrizo Plains and in the

vicinity of STP and TTM in the Mojave, although the easternmost Mojave is slightly negative. Imperial Valley stations have positive residuals for events in these source areas. There are also zones of negative residuals trending roughly east-west and centred just south of Cajon Pass. The most negative regions are split in two by the San Andreas-San Jacinto junction area, but as pointed out before, this is controlled largely by stations that probably require sediment corrections; the areas are not apparently offset by the faults, however. Among the subtle differences are the fact that this anomaly is centred slightly further to the south for the Japan-Kuril events, and the appearance of slightly negative residuals at the southernmost end of the Imperial Valley, also for the Japan-Kuril source region.

Events in Alaska and the Aleutians tended to have rather emergent first arrivals -- there have been few large deep events recently -- and so Figure 3-2j is based on relatively few arrival times. Since the events are close, they are also more prone to errors from source structure, mislocation, and lateral heterogeneity along the travel path which are not so well removed by normalisation. Nevertheless, the pattern observed is very similar to that for events in Japan and the Kuril Islands, although the negative "Transverse Ranges" anomaly is slightly more negative, centred further south-east, and extends further into the eastern Mojave.

Figure 3-3 is a similar contour map using the residual data of Hadley and Kanamori (1977) for the phase PKP from an event that occurred at a depth of 620 km in the Java Trench on January 23rd, 1976. Rays for this phase from this event, at a distance of $\sim$120°, are nearly

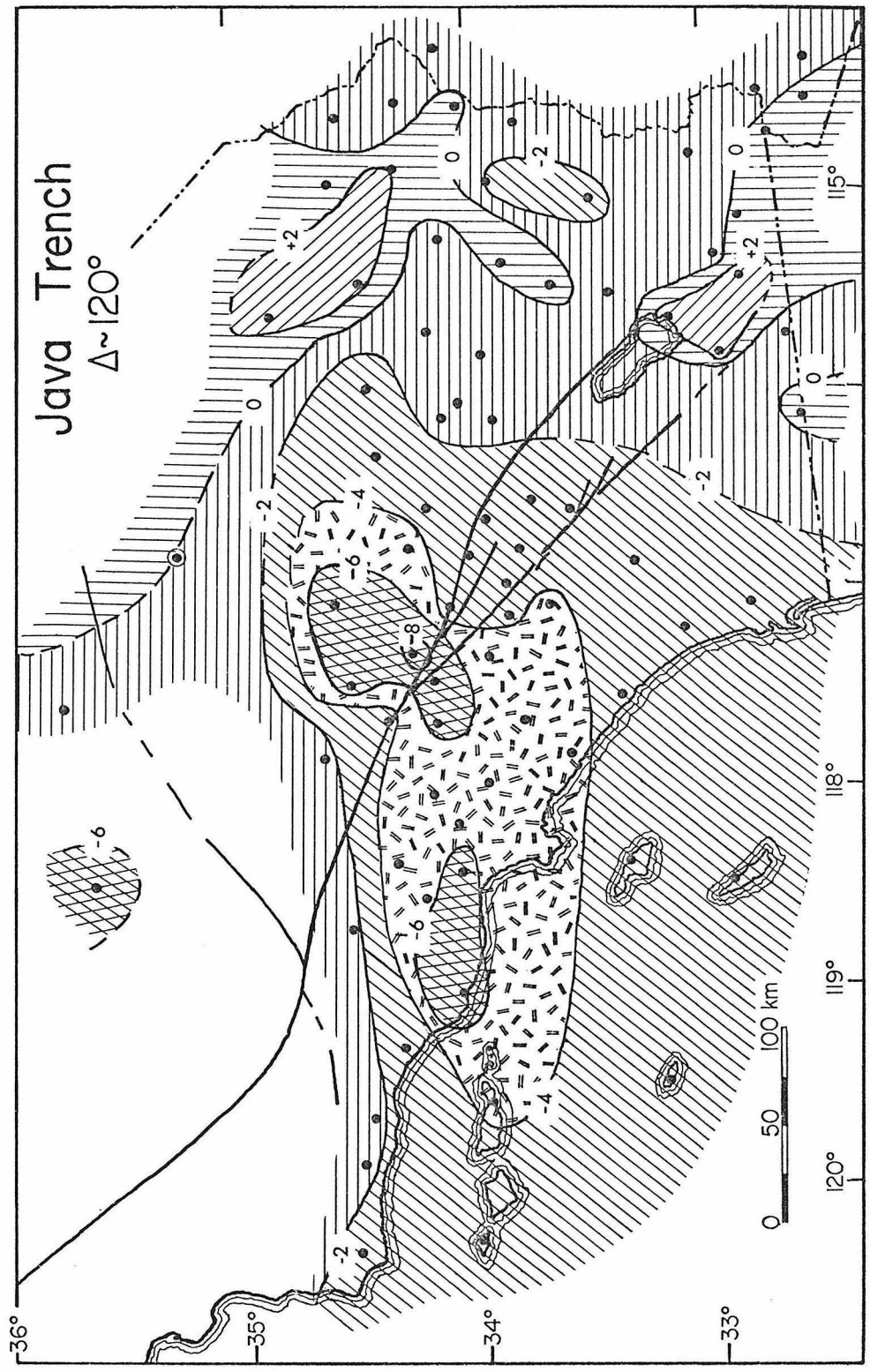

Figure 3-3. Contour map of corrected relative residuals for the Java Trench event studied by Hadley and Kanamori (1977). Shading as in Figure 3-2.

vertically incident, and the residuals thus represent structure directly beneath each station. It is obviously very similar to those observed for the other regions, in particular the northern Pacific and Novaya Zemlya. (The negative residual at ISA may be up to 0.2 sec too low owing to overcorrection for crustal thickness.) An approximately east-west trending negative area now coincides with much of the Transverse Ranges, and there is also a region of positive residuals in the Imperial Valley similar to that observed at other azimuths. (A complete list of the residuals will be found in Table 5-3.)

3.3. Implications of the Observed Variations for Structure Beneath the Array

It is apparent from the considerable variation of the observed relative residuals that there must be marked lateral heterogeneity in compressional velocity beneath the array. In particular, there must be high velocities under the Sierra Nevada, easternmost Mojave desert, and the Transverse Ranges to account for the negative residuals at stations in those regions, and low velocities beneath the Imperial Valley giving rise to the positive residuals. Areas of low velocity must also exist in the Carrizo Plains, and the east-central Mojave desert. The magnitude of the residuals, which can be as high as 0.9 sec, or as low as -1.2 sec, and their azimuthal variations, which reaches a maximum of 1.3 sec, require that the sources of the travel time anomalies be within the upper mantle.

Variations in crustal thickness are insufficient to explain these residuals: a relative residual of only -0.5 sec would imply a crustal

thinning of about 25 km relative to the reference station, and such a change could not go undetected in local gravity and seismic refraction data. Furthermore, since the residuals change rapidly with azimuth to the event, such thinning would have to take place over quite short distances. Consider the case of SBB, where residuals from the South Pacific and South America are -0.3 to -0.5 sec, but residuals from the Central Pacific are about zero; since the points at which the rays from these events cross the Moho are not more than 30 km apart, crustal thinning of 15 to 25 km would have to occur over this distance. Changes in crustal velocity (and expecially in sediment thickness, since the rays travel almost vertically through soft sediments, and the closeness of the paths could not lead to large azimuthal variation of delays) are also ruled out by the rapid azimuthal changes in residuals, and by their magnitude. A residual of -0.5 sec would require that the average crustal velocity was changed from $\sim$6.3 km/s to $\sim$7.2 km/s, which is ruled out by seismic refraction data and travel times for local earthquakes.

The velocity anomalies giving rise to the residual variation must thus lie within the upper mantle beneath the array, but their depth remains to be determined. In an earlier study based on the data of Figure 3-1, a simple model was constructed in which the variations were caused by a high velocity region oriented approximately parallel to the North America-Pacific plate boundary, and lying at depths of 100 to 200 km (Raikes, 1976). This zone extended from the Sierra Nevada to the northern end of the Salton Sea, with a velocity increase of 0.45 km/s in the north decreasing southwards, although the zone broadened in an east-west direction beneath the Transverse Ranges, which also had a

slightly higher velocity increase. It was suggested that this zone might be related to the plate tectonic history of the region, and the "dead slab" found in Oregon and northern California by Solomon and Butler (1974), or consist of a thinning of the low velocity zone beneath the region. The presence of a region of low velocity at ∿50 km below the Imperial Valley was also proposed to explain the residuals at GLA.

However, the addition of further stations made it clear that the Sierran and Transverse Ranges anomalies are distinct, and that the changes probably occur at shallower depths. There is little control over the depth of the Sierran anomaly because ISA is on the periphery of the array, but the shift of the negative residuals resulting from the high velocity region beneath the Transverse Ranges may be used to estimate the depth extent of this anomaly. Figure 3-4 shows a section through Cajon Pass area (where the most negative residuals are observed for the Java Trench event of Figure 3-3) in a north-west-south-east direction, which corresponds to the axis along which rays travel from Japan and the Kuril Islands or South America to the array. Rays from these regions to CSP (the station with the lowest [or "maximum"] residuals for vertically incident rays), from South America to TPO (the lowest residual for that azimuth) and from Japan to RAY (earliest station along the section for that azimuth) are sketched. The latter rays would intersect at a depth of ∿155 km, close to the axis of the Java Trench anomaly, which suggests that the region of high velocity may extend to ∿150 km, compared with the "normal" mantle beneath GSC. Note that this figure also illustrates why the velocity changes must be subcrustal:

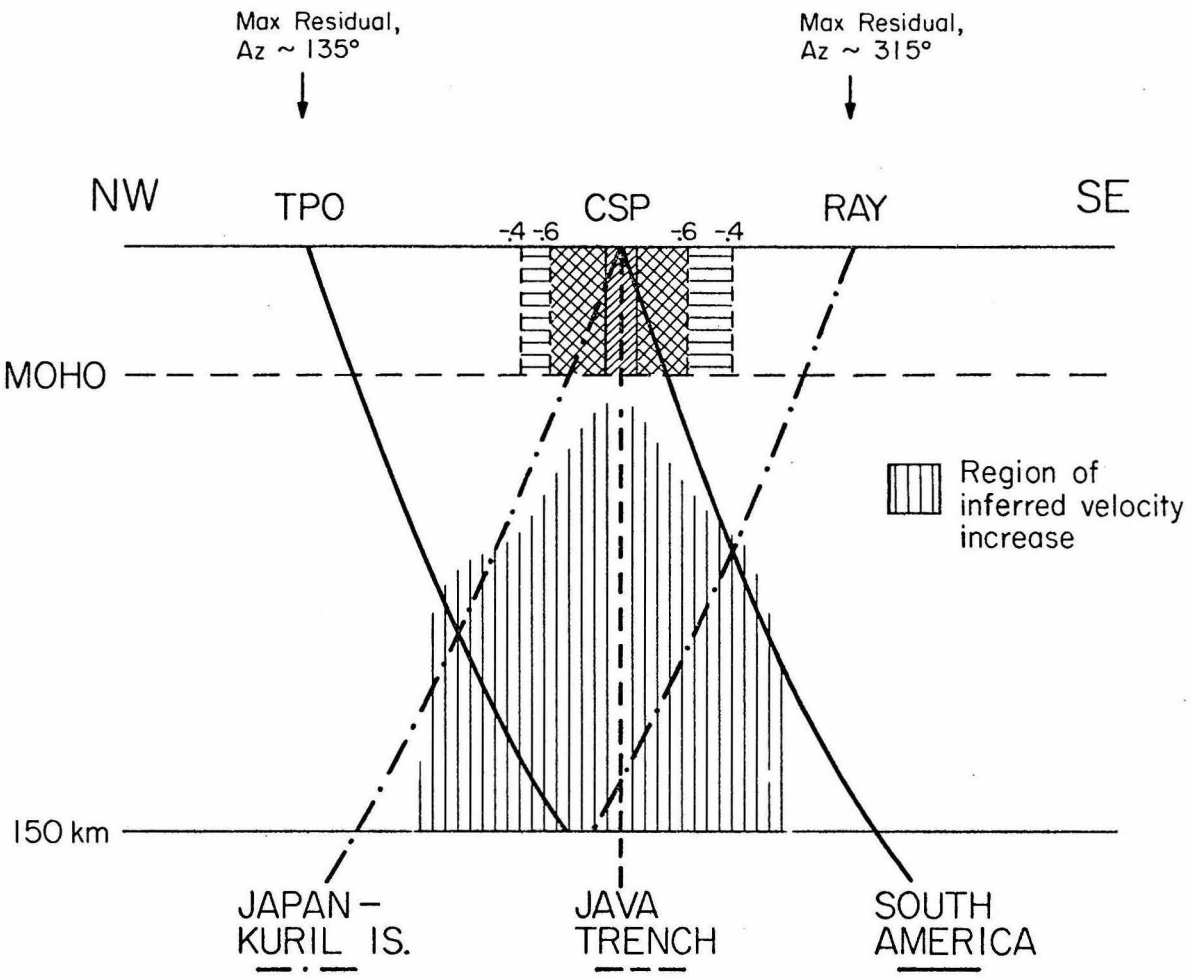

Figure 3-4. NW-SE cross section through the Cajon Pass area. Incoming rays from events in the Java Trench, South America and Japan-Kuril Islands region are shown, and the region of inferred velocity increase in the upper mantle is shaded. Also shown as shaded regions in the crust, are the contours of residuals for the Java Trench event.

the contours of residuals from the Java Trench event are projected on to the crustal section beneath CSP, which would clearly have strongly negative residuals for all three indicated ray paths if the anomaly lay in the crust. Likewise, RAY would be only slightly negative for the South American and Japanese events. (TPO did not record the PKP phase so no conclusion may be made regarding its behaviour.)

As the P_n velocity beneath this area is known to be 7.8 km/s, and if the top of the velocity anomaly reaches 50 km depth, as seems likely, the inferred velocity change would be $\sim$.5 km/s, and the region beneath the Transverse Ranges have a velocity of $\sim$8.3 km/s. This accords well with the observations of Kanamori and Hadley (1977) who found a refractor having a velocity of 8.3 km/s at about 40 km depth beneath the Transverse Ranges from studies of travel time data from two local earthquakes, and used the Java Trench event to estimate the extent of this horizon. Of course, the velocity contrast and depth extent of the anomaly were estimated by assuming that the upper mantle velocity beneath GSC remained constant at 7.8 km/s. This may be rather low for depths of $\sim$150 km, although GSC lies on the edge of the Basin and Range Province, and inversion of both body-wave (Archambeau et al., 1969) and Rayleigh wave (Biswas and Knopoff, 1974) data suggest that within this province the P_n velocity of 7.8 km/s may indeed extend to at least this depth. One remarkable fact about this anomaly is that it appears to extend across the San Andreas Fault, at a depth of 50 km, and yet not be offset by it; this was discussed by Hadley and Kanamori (1977), and has important implications for the tectonics of the region. If the negative residuals at ISA are caused by a similar velocity

contrast, and there is to be no conflict with the known Moho depth of ∿50 km north of there, then the Sierran anomaly must extend to a depth of ∿200 km. This high velocity material may be related to the low heat flow observed within the Sierra Nevada, which was explained by Roy et al. (1972) in terms of the absence of a partial melt (low velocity) zone at similar depths.

The variation of residuals in the Imperial Valley, especially the very positive ones to the east of the Valley for events in the South and Central Pacific, suggests that much of the valley may be underlain at depths of about 50 to 80 km by low velocity material. Such a model would be compatible with the presence of partial melt related to the high heat flow, geothermal activity, and the extension of the active spreading centre from the Gulf of California into this region. However, the rapid change to strongly negative residuals for azimuths between 90 and 140° requires that there be a region of increased velocity under south-west Arizona, or northern Mexico, at depths sufficient to explain this. It is also possible that for rays from events in southern South America, for which the most negative residuals occur, the influence of structure beneath the plate boundary in the Gulf of California, which the paths closely parallel, is also a contributing factor.

In summary, the azimuthal variation of teleseismic residuals at stations of the Southern California network provides evidence for regions of decreased velocity beneath the Imperial Valley, consistent with the high heat flow there, and the Carrizo Plains, and regions of increased velocity beneath the Sierra Nevada, the easternmost Mojave,

south-western Arizona or northern Mexico, and much of the Transverse Ranges. The latter is a major ridge-like structure, which extends to depths of ∿150 km, and is apparently continuous across the San Andreas Fault. Detailed models for the upper mantle velocity structure will be derived in Chapter 5 and their implications discussed in Chapter 6.

Chapter 4

TEMPORAL DEPENDENCE OF RESIDUALS

The occurrence of seismic velocity changes prior to, and presumably associated with, earthquakes has been documented by a number of authors (see, for example, Savarensky, 1968; Semenov, 1969; Aggarwal et al., 1973; Whitcomb et al., 1973; Ohtake, 1973; Wyss and Johnston, 1974; and Johnston, 1978). The investigation of temporal variations in velocity in a tectonically active area is thus of value, both as a possible means of predicting future earthquakes, and in order to establish a "background" level of fluctuations not associated with large earthquakes. Furthermore, the use of residual variations to infer velocity structure is dependent on the stability of those residuals as a function of time; if large fluctuations take place, then the structure inferred from a data base covering only a short time interval (in general 2-3 years for stations in Southern California) may not be wholly representative of the actual structure. It is thus important to investigate possible travel time fluctuations for representative stations within the array.

The U.S.G.S.-Caltech Southern California Seismograph Network provides a good source of such travel-time data, particularly since 1972 when develocorder recording was introduced, allowing greater measurement accuracy. In addition, the presence of large changes in elevation in the vicinity of Palmdale (Castle et al., 1976) makes this an area of special interest, with regard to the possible occurrence of a large earthquake in the future.

Previous searches for possible precursory velocity changes in California have met with limited success. Cramer (1976) was unable to

detect any significant variations prior to the 1974 Thanksgiving Day (Hollister) earthquake, and Bolt (1977) and Cramer et al. (1977) found no changes in travel-time from Nevada test site blasts to Oroville (ORV) prior to the 1975 Oroville earthquake. However, Cramer et al. (1977) reported a .1 sec delay in residuals at ORV for Novaya Zemlya explosions prior to the Oroville event. Small changes in P-velocity have been resolved in studies of travel times from quarry blasts in Southern California: Kanamori and Hadley (1975) reported changes of ∿3%, and Kanamori and Fuis (1976) observed variations of ∿1% prior to the 1975 Galway Lake and Goat Mountain earthquakes. However, Whitcomb et al. (1973) found a change of 10% in Vp/Vs and ∿19% in Vp prior to the 1971 San Fernando earthquake, and Stewart (1973) concluded from data obtained from local and teleseismic events that a change of up to 30% in Vp may have occurred in the source region of the 1973 Point Mugu earthquake. Changes of 10-20% were also observed in the vicinity of Riverside during the period 1964-1969 by Kanamori and Chung (1974), but they concluded that this was not obviously related to seismic activity in the area.

A study of the temporal dependence of teleseismic residuals during the period 1972-1976 was made for 13 stations in Southern California, including six in the vicinity of the Palmdale uplift. Local earthquake residuals were also investigated for seven of the stations, and the variation of teleseismic residuals listed in the International Seismological Centre monthly reports for PAS during the period 1964-1971 analysed in an attempt to extend the data base to a period including a significant earthquake, the San Fernando event of February 9th, 1971, M_L=6.4.

4.1. Method and Observations

Teleseismic residuals have been used to investigate premonitory velocity changes by a number of authors, including Wyss and Johnston (1974) and Cramer (1976). This method, which is discussed in detail by Engdahl et al. (1977), has the advantage that the locations of the sources used, and hence the theoretical travel times, do not depend on a detailed knowledge of local structure in the area of the study, as is the case when local earthquakes are used. However, the effects of source mislocation and inhomogeneities along the travel path can cause considerable scatter, and must be minimised by normalisation. This is usually achieved by taking relative residuals with respect to one or more of the stations studied, or by averaging.

The locations of the stations used in this study are shown in Figure 4-1, together with approximate contours of elevation in the vicinity of Palmdale, as reported by Castle et al. (1976). (The region of uplift is, in fact, oriented parallel to the inferred mantle velocity anomaly (Figure 5-1), and close to its northern boundary.) Throughout this period, the stations studied recorded on 16 mm develocorder film; the method of determining residuals was the same as that described in Chapter 2, and Goldstone (GSC) was again chosen as the normalising station. Any temporal variations at GSC would, of course, show up as changes at all the other stations. The effects of normalisation and sources of error in the residuals are also discussed in Chapter 2; the maximum effect on residuals for events used in this study is estimated at .1 sec. (The distribution of events used is similar to that shown in Figure 2-3; however, residuals from events closer than 45° were

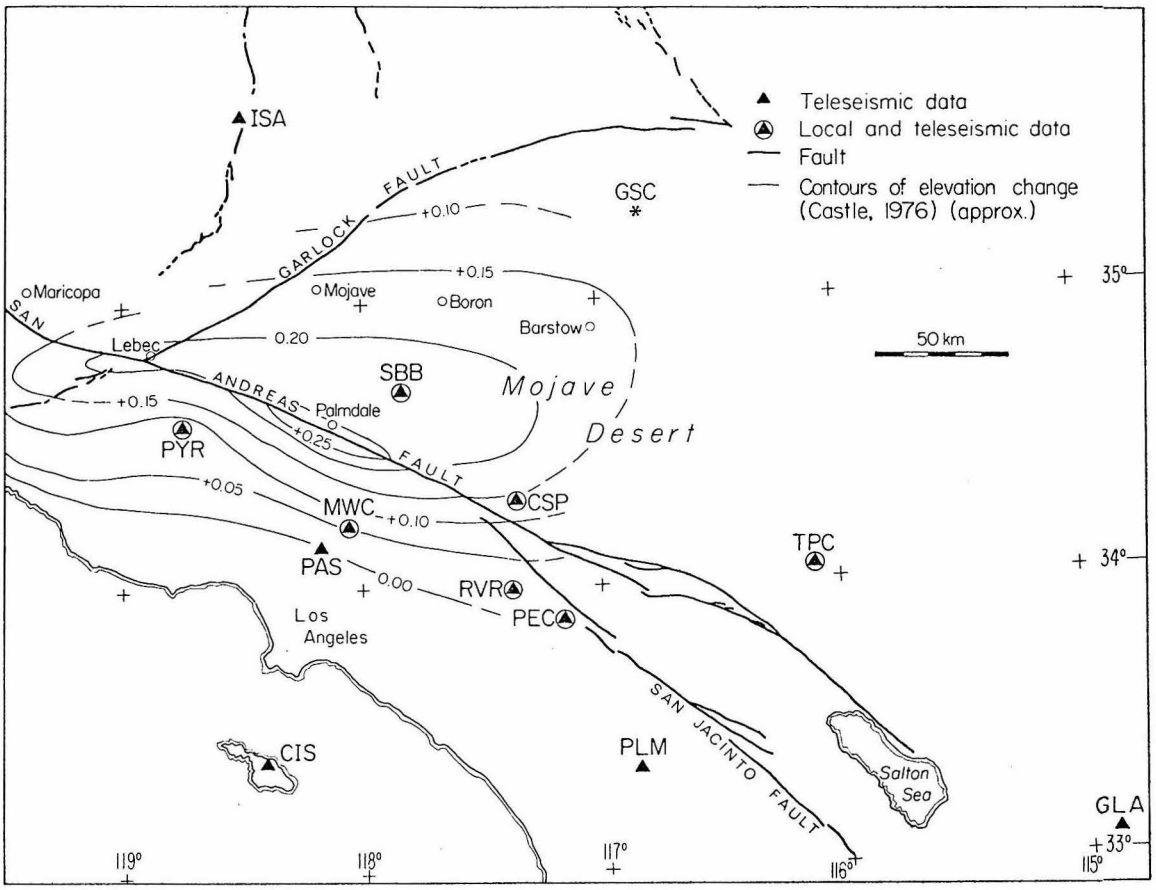

Figure 4-1. Stations used in the study of temporal variation of residuals. Also shown are the contours of the "Palmdale Bulge" reported by Castle et al. (1976).

discarded since they are more prone to error resulting from source structure, mislocation, and choice of earth model. In addition, data from such areas as Iceland and the Mid-Atlantic ridge were not used, because events with clear first arrivals at Southern California stations are uncommon in those areas.)

A further problem arises in the use of teleseismic residuals for investigating temporal velocity changes in Southern California, namely the effect of the marked azimuthal dependence of the residuals due to the local upper mantle structure. This makes it difficult to compare directly data from different source regions, and the use of techniques such as averaging can lead to spurious apparent variations. This is illustrated in Figure 4-2 for the case of GLA. Two commonly used techniques, the calculation of six-monthly means and moving-window averages, were applied to normalised residuals which were uncorrected for the source region. These techniques were then applied to the same set of residuals, but corrected for azimuthal dependence as described below. The results are shown in Figure 4-2a and b. In each case, the uncorrected residuals show a distinct maximum in early 1972, and a minimum in early 1975, whereas the corrected residuals show very little variation, even when a single source area is considered (Figure 4-2c). However, the mean standard deviation of a single six-month or 20 event sample is .38, and hence the peaks at .35 sec (or .39σ from the mean) and minimum at .15 sec (or .21σ from the mean) are not really significant, although they certainly look more imposing than the fluctuations of .01 sec or less for the corrected residuals. (Similarly, the peak of .42 sec and minimum of .09 sec in the 20 event windowed averages are not

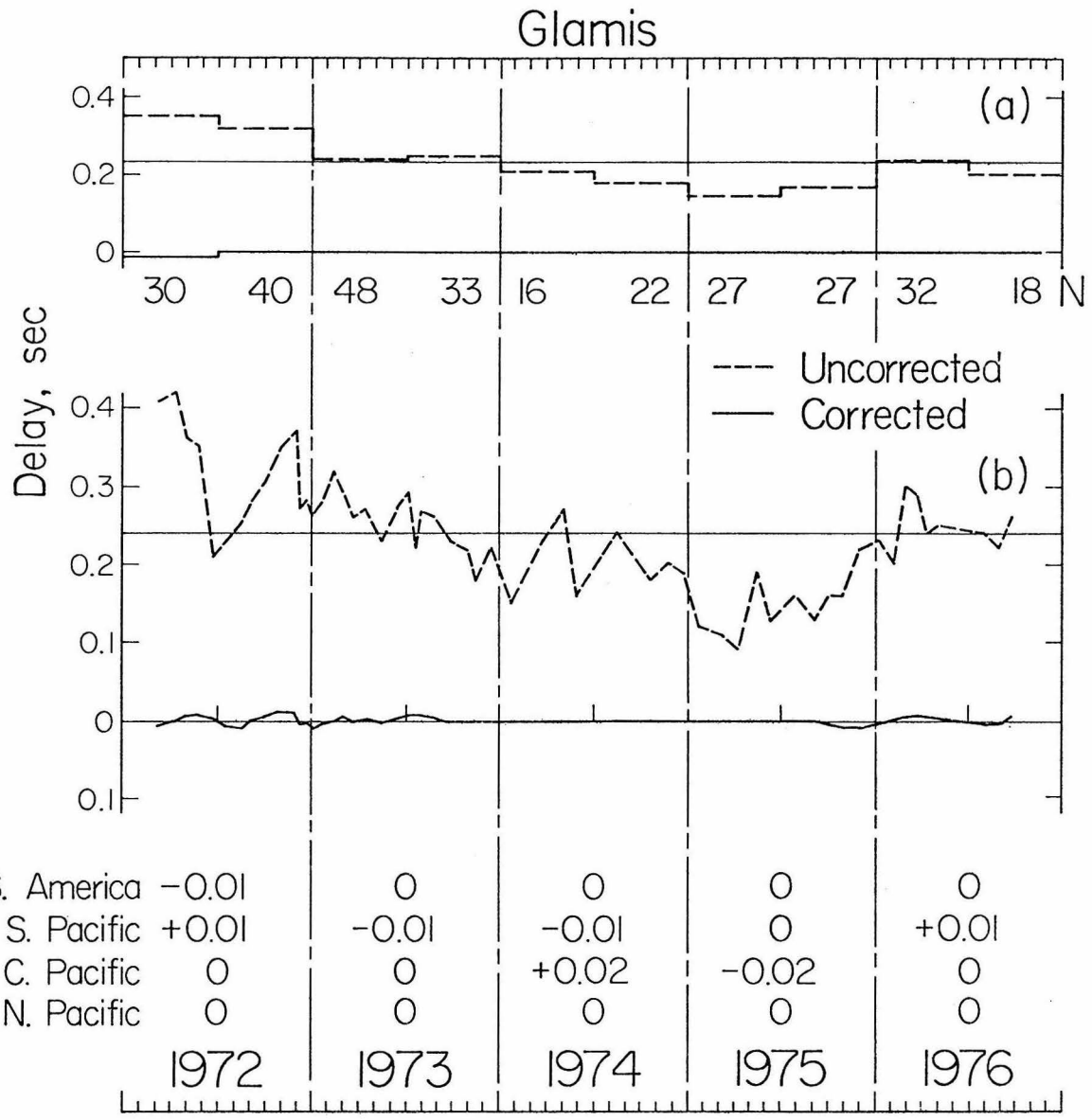

Figure 4-2. Variation of residuals at GLA:
a) Six monthly means for residuals corrected and uncorrected for azimuthal effects. N = number of events.
b) 20 event stepped by 5 moving window averages of the residuals at GLA.
Also listed are the mean annual residuals corrected for azimuthal effects, for events in a single source area.

significant being .47σ and .39σ from the mean respectively.)

The standard deviation was used as a test of significance, rather than the standard error in the mean, because the azimuthal variation of residuals constitutes a source of non-random errors. Had the standard error in the mean of ∿.08 been used, the minima would have been judged insignificant, but the maxima significant at the 2 to 5% levels.

The effects of azimuthal dependence of residuals may be minimised by considering only events within a small distance and azimuth window (approximately 5 to 10° in each). However, if only a single source region is used, the temporal and spatial resolution may be seriously impaired. For consideration of overall velocity changes, it is convenient to correct the residuals from a number of windows by calculating a mean value for events within a single distance-azimuth window, which must contain at least 5 events, and subtracting this from the normalised residual. The residuals from a number of azimuths may then be plotted on a single graph; decreases in velocity show up as periods of increased corrected residuals. Values of the mean residuals for the principal azimuth-distance windows are listed in Table 4-1.

The corrected relative residuals for the stations studied are plotted in Figures 4-3 and 4-4. The 2σ bars indicate the average over all azimuths of the scatter observed in a single distance-azimuth window, and are similar to those expected from reading error alone. It is estimated, on the basis of these errors, that a change in residual of .15 sec lasting for at least six months would be clearly resolved by this method; this corresponds to a velocity change of 9% over a path length of 10 km with a mean velocity of 6 km/s. (A change of .1 sec,

Figure 4-3. Variation of residuals at ISA, PYR, SBB, PAS, MWC and CSP as a function of time. The residuals have been normalised with respect to GSC, and corrected for azimuthal effects. The 2σ bars represent twice the standard deviation expected for a single azimuth-distance window.

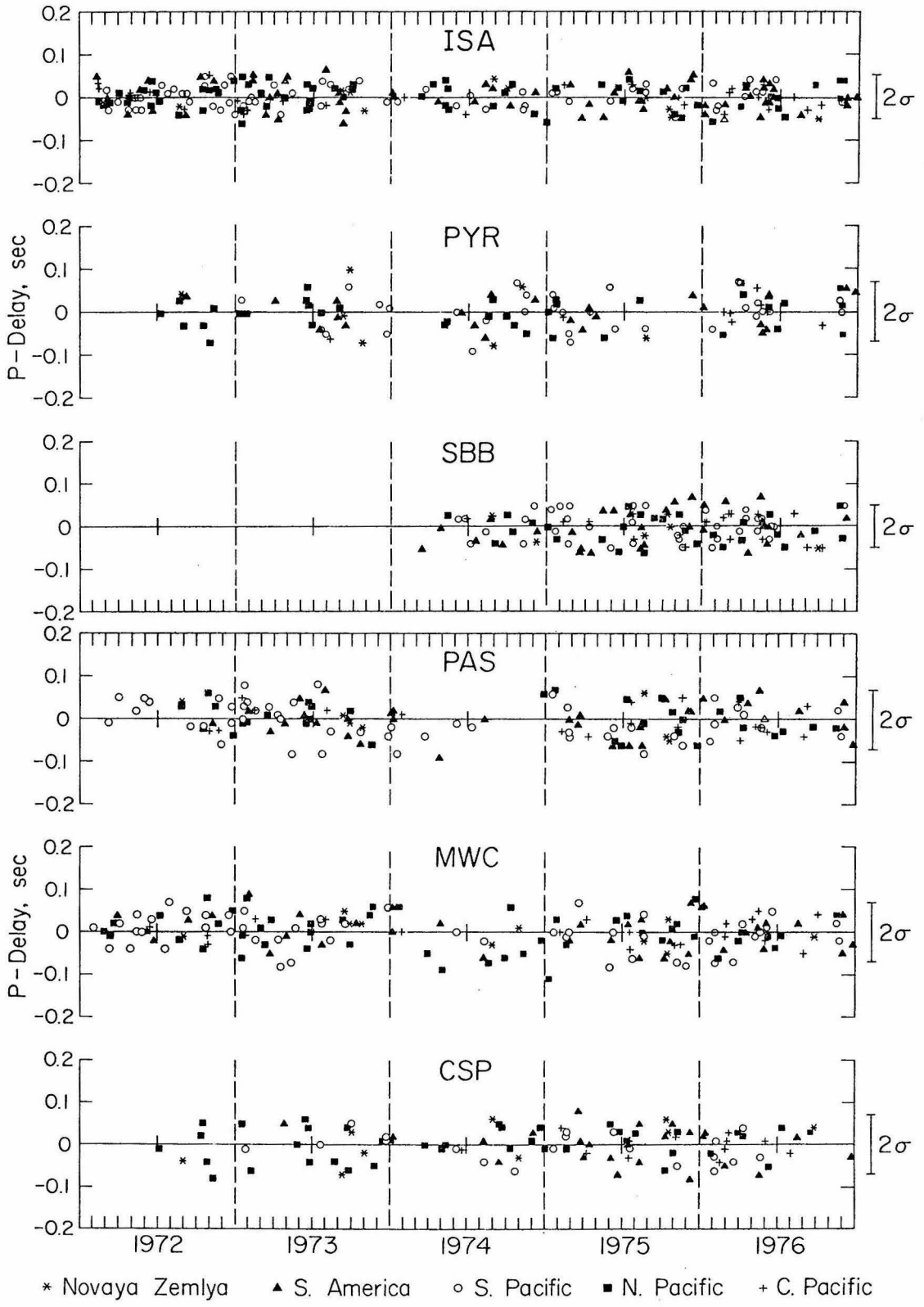
ISA
PYR
SBB
PAS
MWC
CSP
P-Delay, sec
0.2
0.1
0
-0.1
-0.2
2σ
1972
1973
1974
1975
1976
* Novaya Zemlya
▲ S. America
○ S. Pacific
■ N. Pacific
+ C. Pacific

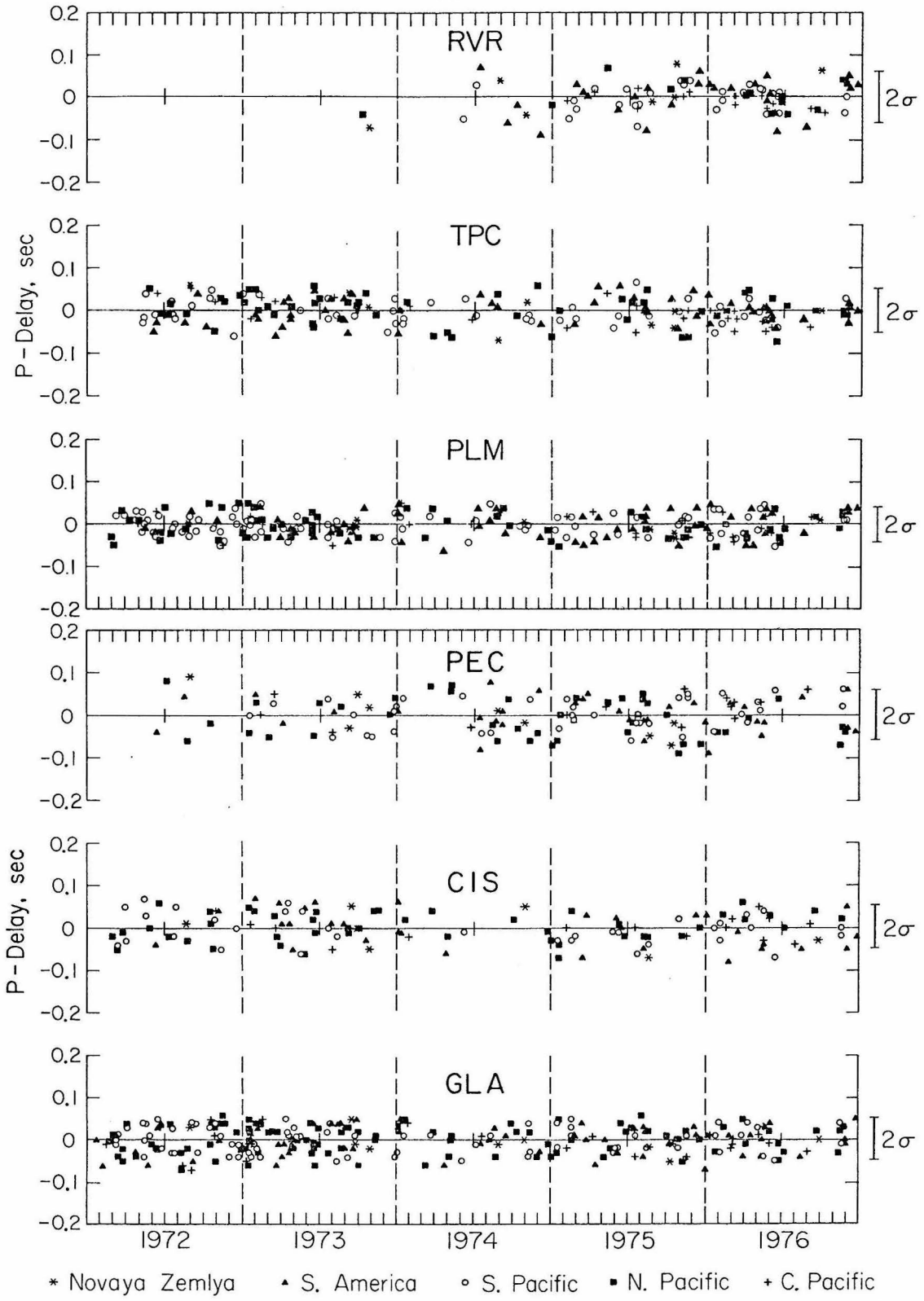

Figure 4-4. Variation of residuals at RVR, TPC, PLM, PEC, CIS, and GLA. Notation as in Figure 4-3.

or 6%, would be barely detectable within the scatter.) The six-monthly means for corrected residuals at each station are plotted in Figure 4-5; also listed is the mean standard deviation, $\bar{\sigma}$, for a six-month sample of events. The deviations from the mean, zero, are in general less than $.5\bar{\sigma}$ and only exceed this on four occasions, reaching $.75\bar{\sigma}$ (.03 sec) at PAS in early 1972, $.70\bar{\sigma}$ (.035 sec) at PEC and $.67\bar{\sigma}$ (-.02 sec) at TPC in early 1974, and $.75\bar{\sigma}$ (-.03 sec) at MWC in late 1974. (These variations are found to be significant only at about the 10% level using the standard error in the mean.)

During the period 1972-1976 no significant changes in teleseismic residuals were observed at any of the stations monitored, although there may be small changes ($\sim$.05 to .1 sec, or a 3-6% velocity change) similar to those reported by Kanamori and Hadley (1975) within the expected scatter.

4.2. Discussion

The absence of any significant changes in teleseismic residuals during the period studied must now be considered in terms of the seismicity of the region and the origins and nature of possible velocity changes. Various formulae have been derived linking the duration of the anomalous period T and the magnitude M of the associated earthquake. Whitcomb *et al.* (1973) proposed the relationship

$$\log_{10} T \text{ (days)} = .68M - 1.31 \qquad (1)$$

and Rikitake (1975) deduced an average relationship from a variety of precursor data

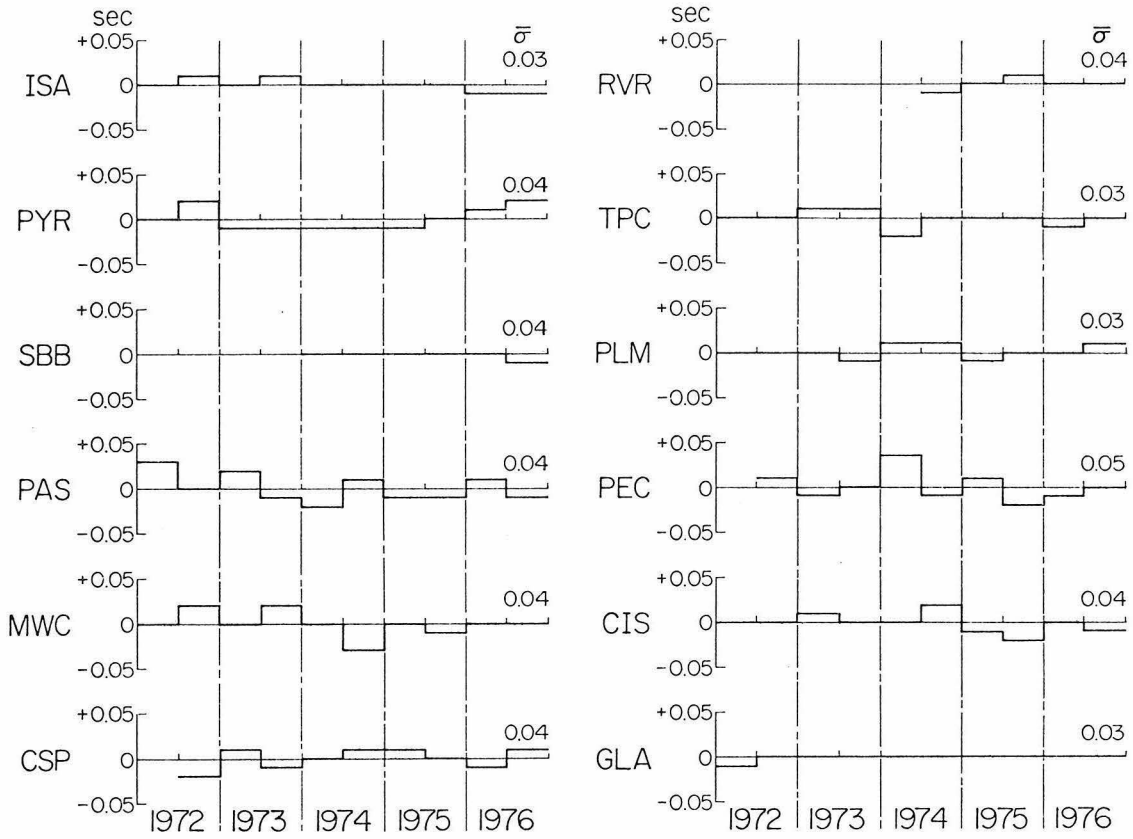

Figure 4-5. Six monthly means of corrected normalised residuals at the stations studied. The values of $\bar{\sigma}$ are the mean standard deviation in a single six month period.

$$\log_{10} T \text{ (days)} = .76M - 1.83 \qquad (2)$$

Since, in the previous section, it was estimated that a period of anomalous velocity must last at least six months to be clearly detectable, these relationships may be used to convert this into a lower magnitude detection limit, yielding values of 5.25 and 5.4 using (1) and (2) respectively.

However, these limits are in no sense absolute: relations (1) and (2) were derived empirically for earthquakes largely of the thrust type, and it has been suggested (Whitcomb et al., 1974; Whitcomb, 1976) that the precursor duration may be longer for earthquakes not having a thrust mechanism. In particular, Whitcomb et al. (1974) reported an anomaly lasting 1.8 years that was apparently associated with a magnitude 4.0 earthquake.

In addition, Anderson and Whitcomb (1975) proposed a relationship between the size of the anomalous region L, and the magnitude M of the ensuing earthquake, namely

$$\log L \text{ (km)} = .26M + .46 \qquad (3)$$

which for the magnitude limits derived above from (1) and (2) gives anomalous regions of diameter 73.1 and 66.8 km respectively. The estimated detection limit may thus be re-expressed as a magnitude $5(\pm\sim.5)$ earthquake occuring within 70 km of a station. Larger earthquakes will, of course, be resolvable at greater distances: for example, a magnitude 6 earthquake would have an associated anomalous area of diameter 105 km according to (3).

A limitation on the usefulness of teleseismic rays in investigation of crustal velocity changes is imposed because of their steepness of incidence. In this study the rays enter the crust at, at most, 20 km from the station, and will only sample velocities within this radius. Consequently, for an earthquake occurring more than about 20 km from a station, teleseismic rays pass only through the edges of the anomalous region, where the velocity change may be lower, causing a smaller change in travel-time. This would result in a smaller "detection radius" than the 70 km derived above, and suggests that for purposes of earthquake prediction a combination of teleseismic and (the more scattered) "local" residual data would be more useful.

Locations of earthquake of magnitude 4.5 and greater occurring in Southern California during the period 1972-1976 are plotted in Figure 4-6. Seismicity has been relatively low during this time, and there are few events sufficiently close to any of the stations that they might be expected to give rise to detectable anomalies. The largest earthquake during this period, a magnitude 5.9 (M_L) at Point Mugu on February 21st, 1973, occurs somewhat early to have been "predicted" using this data set, and is too far from PYR to produce a resolvable anomaly based on Stewart's (1973) estimate of 10 km for the size of the anomalous zone. The other earthquakes that might have been preceded by observable anomalies are the Galway Lake event of June 1st, 1975, which is close to the detection limit for TPC, CSP, and PEC, and the Goat Mountain shocks of November 15th and December 14th, 1975, which are rather small, but fairly close to TPC. None of these gave rise to a strongly visible anomaly, although there is a faint suggestion of a velocity

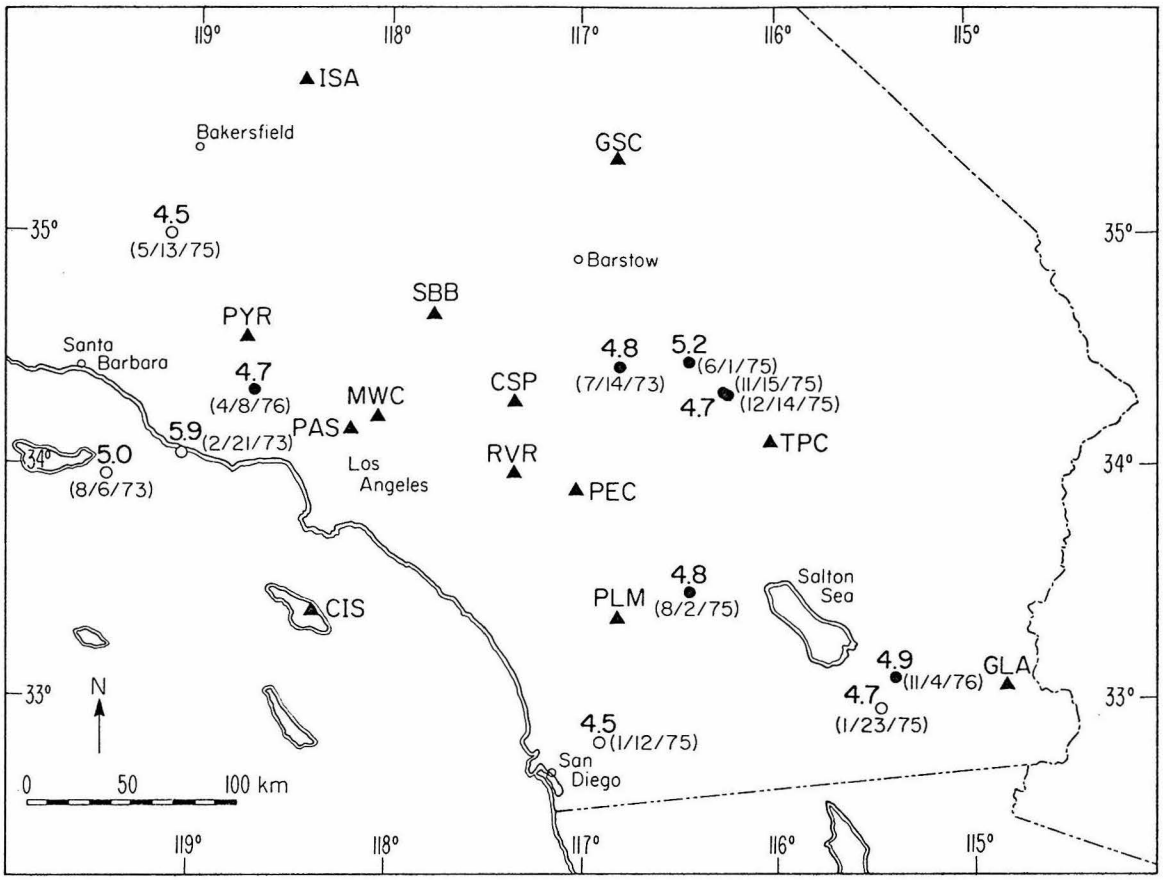

Figure 4-6. Earthquakes of magnitude 4.5 or greater occurring in Southern California during the study period. Open circles denote those events that are outside the "detection radius" described in the text.

increase in late 1975 for paths from the North Pacific to TPC. The Anza earthquake of August 1975 produced no resolvable change at PLM, and the April 1976 Newhall event produced no change at PYR, although there may be a small velocity increase near MWC in late 1975-early 1976. In addition, there appear to be no changes associated with the spreading and deflation of the Palmdale Bulge reported by Castle et al. (1977).

One possible reason for the lack of residual changes is that there have been no large earthquakes sufficiently close to any of the stations monitored, or, indeed, in the time period of the study. The San Fernando earthquake of February 9th, 1971, M_L = 6.4, occurred ∿40 km to the north-west of PAS, and was reportedly preceded by premonitory velocity changes (Whitcomb et al., 1973). In an attempt to see if any variations in teleseismic residual preceded this event, the residuals listed in the ISC Bulletin for teleseismic arrivals at PAS from events in the distance range 45-95°, and at depths greater than 65 km, were analysed for the period 1964-1971. Since these arrivals were read from paper records and cannot be normalised to minimise source and path erorrs (there was no nearby station that reported continuously to the ISC during this period) the data are much more scattered. Events having residuals greater than ±2 sec were discarded since it was felt, on the basis of residuals determined from develocorder records, that these represented either a severe mislocation or a bad reading error. Six-month averages and 60 event stepped by 20 moving window averages were calculated, and are plotted in Figure 4-7. The scatter in the residuals was extremely high, the mean standard deviation of a sample being .70 sec, and they had not been corrected for the azimuthal dependence of residuals

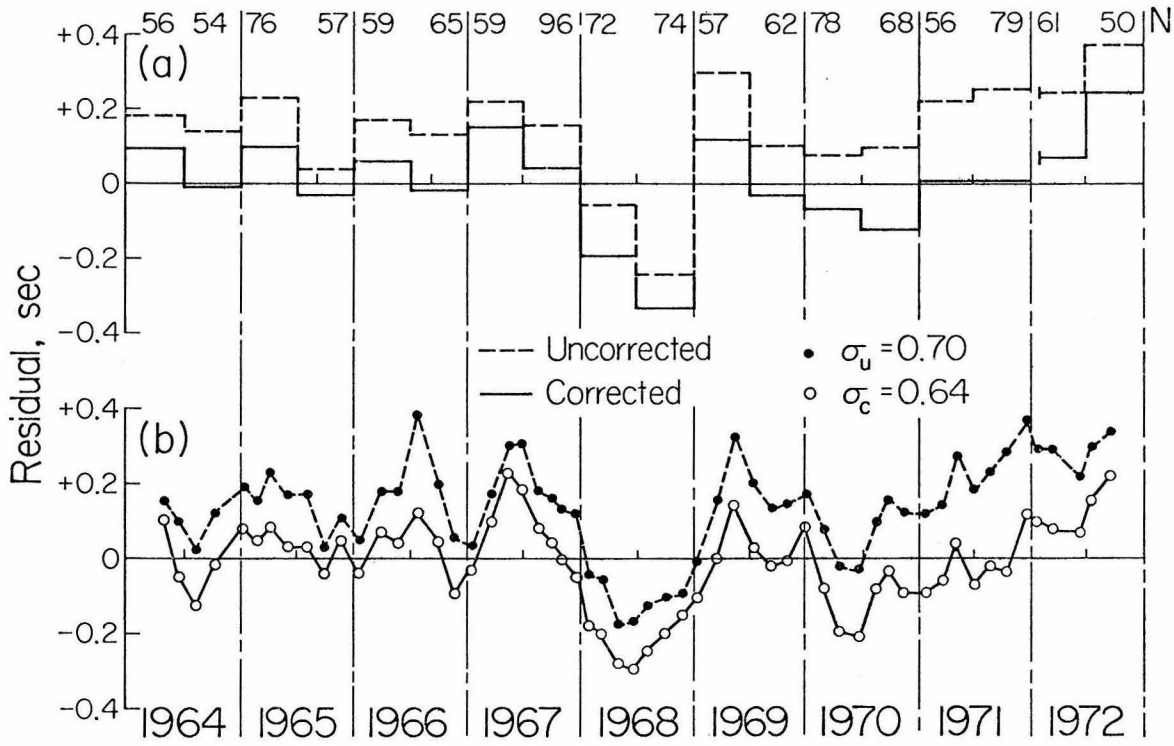

Figure 4-7. Variation of residuals at PAS as listed by the I.S.C. bulletin for the period 1964-1972. Only events with magnitudes greater than 5.5 at distances over 45° were used. Also shown are the variations of residuals corrected for possible azimuthal effects.
a) Six monthly mean (N = number of events).
b) 60 event stepped by 20 moving window average.

at PAS, nor for possible systematic mislocations or travel time errors for a given source region. In an effort to minimise the scatter by removing systematic effects, the data were divided into 14 source regions, and distance-azimuth mean residuals calculated and used to correct the data in a manner similar to that described in the previous section. The corrected averages are also shown in Figure 4-7 -- the main result has been to shift the mean to zero, but the standard deviation is only slightly reduced to .64 sec. This suggests that the main source of scatter may be random errors, and that the value of the mean is significant. In this case, the standard error in the mean, S, should be used to test the significance of variations in the six-monthly and moving window means. The values of S range from .06 to .10 for six-monthly and 60 event averages. The 1968 minimum in residuals of -.33 sec ($.52\sigma_c$ or $\sim 3.5S$) for six monthly averages and -.29 sec ($.45\sigma_c$ or $3.0S$) for 60 event averages is thus significant at the 1% level. The highest means prior to the San Fernando earthquake occur in early 1967 -- a maximum of .15 in the six monthly mean and of .23 in the 60 event average, which are significant at the 5% level. However, there appears to be no convincing pattern of a decrease in velocity followed by a return to normal prior to the earthquake: on the contrary, there is a decrease four years prior to the event followed 3 years before by a marked increase, and then the residuals fluctuate reaching another maximum in late 1972, eighteen months after the earthquake.

Observations of local earthquake residuals are subject to much greater scatter, presumably due to complex local structure and difficulties

of location, but appear to exhibit greater velocity fluctuations. Whitcomb (1976) observed a decrease in Vp/Vs determined from local earthquakes during 1974 and early 1975, followed by a return to normal. He concluded that, based on current theories, a magnitude 5.5 to 6.5 earthquake should occur in the areas of Southern California where the anomalous velocity ratio was observed. However, this conclusion later proved incorrect, as the velocity ratio decreased again after the occurrence of a magnitude 4.7 earthquake near Newhall in April 1976. Of the stations used in this study, SBB is on the north-eastern boundary of Whitcomb's prediction area, PYR near the western margin, and MWC and PAS in the south-eastern quadrant. No changes in teleseismic residuals clearly corresponding to his anomaly are seen at SBB or PYR, although there may be minor velocity increases at PAS and MWC for events from the South Pacific in early and late 1975 respectively. (However, the latter occurs too late to be associated with Whitcomb's anomaly.) Figure 4-8 shows plots of smoothed residuals from local earthquakes at seven of the stations used in this study. In this case the residuals are those determined by the Hypo 71 location programme used in the location of the earthquake from the arrival time data, and they have been smoothed by applying the weighted exponential filter described by Whitcomb (1976). There are apparent decreases in residuals at PEC in early 1974, at TPC in 1974-1975 and at CSP in early 1975, and an apparent increase MWC in mid 1974. However the magnitudes of these changes are small, and they do not appear to correlate well with earthquake occurrence or with the small changes in teleseismic residuals (in particular MWC has a minimum mean teleseismic residual in late 1974).

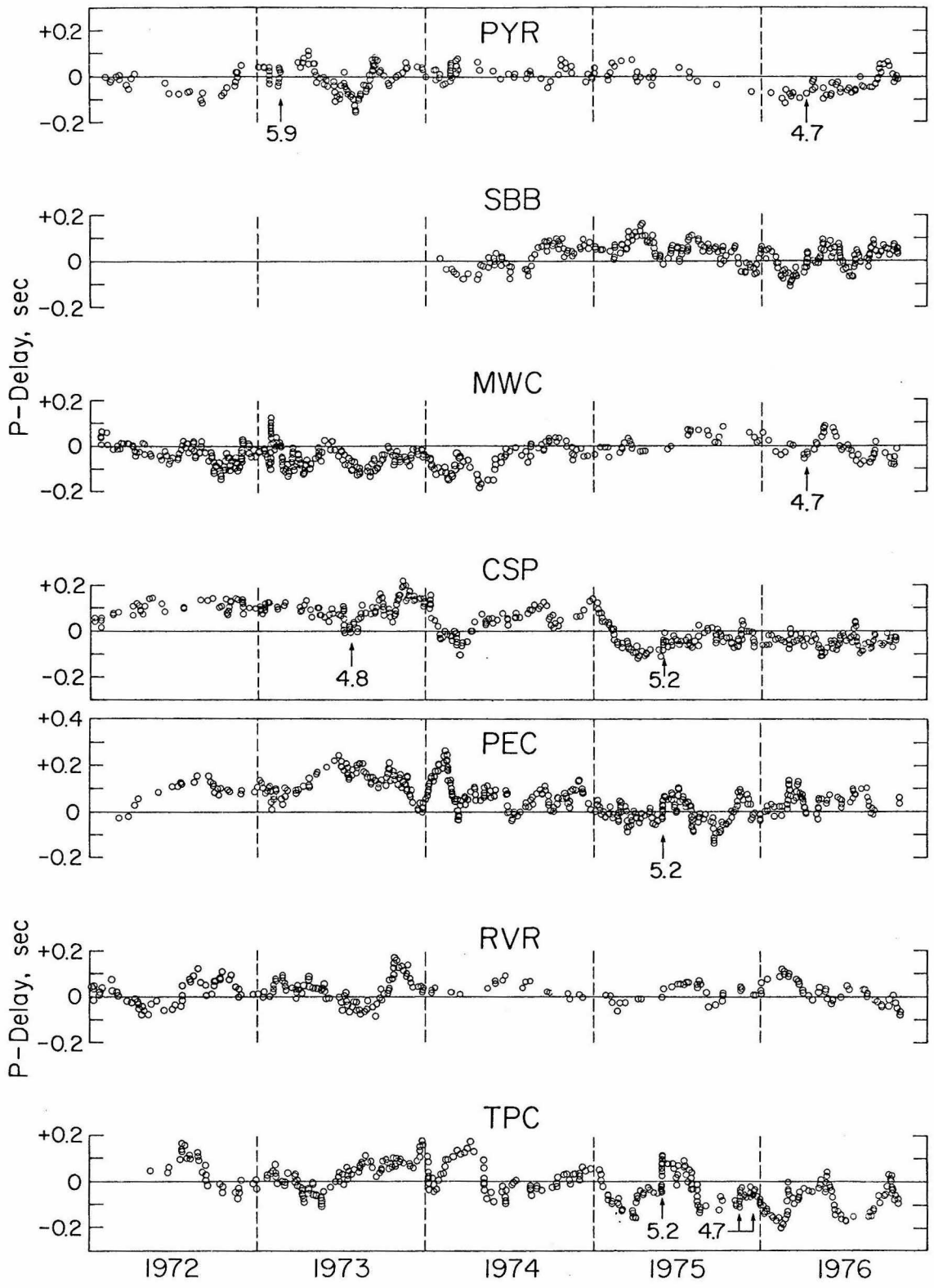

Figure 4-8. Variation of smoothed local residuals for PYR, SBB, MWC, CSP, PEC, RVR and TPC.

A detailed analysis of the variation of residuals from local earthquakes for all stations of the U.S.G.S.-Caltech Southern California Seismograph Network is presented by Powell and Whitcomb (1977). They conclude that during the time period 1972-1976 there are no significant variations in "local" residuals that can be related to the occurrence of earthquakes.

Discrepancies between local and teleseismic residual variations are not unexpected: the former depend strongly on the stations and local structural model used in the location of the earthquake. Furthermore, the teleseismic waves travel steeply through the crust, and if the anomaly is confined to a narrow depth range, it may be poorly sampled by teleseismic rays whereas those from a local earthquake have a long travel path in the anomalous region. The orientation of the cracks that are thought to give rise to the velocity variations is also important. Not only does it give rise to horizontal anisotropy (Whitcomb, 1976), but if the cracks are vertical they will have little effect on the travel times of the nearly vertically incident teleseismic waves. An investigation of variations of seismic velocities in dilatant rock (Gupta, 1973a, b) showed that for areas of strike slip faulting the decrease in compressional velocity is greatest for near horizontal paths; this is also the case for normal faulting. However, for thrust faulting, which is common in the Transverse Ranges, the maximum velocity change is observed for near vertical ray paths, and thus teleseismic residuals should be more affected than local ones. The size of the cracks may also contribute to their differing effect on teleseismic and local waves: small cracks will have a larger effect

on the velocity of the higher frequency, shorter wavelength, P-waves from local earthquakes.

4.3. Conclusions

Teleseismic residuals monitored at 13 stations in Southern California from 1972 to 1976 show no significant variations when normalised to minimise common source and propagation effects, and corrected for their dependence on the azimuth of the event. The absence of clearly resolvable variations may be largely due to the low seismicity in the area during this period. Alternatively, it may imply that the only velocity changes taking place were small (such as might be associated with vertically oriented or small cracks) or limited to a narrow depth range in the crust and thus poorly sampled by teleseismic waves. However, the absence of significant changes in residuals from local earthquakes (Powell and Whitcomb, 1977) supports the idea that only small velocity changes have taken place during this period.

On the basis of these data, and the apparent non-variation of residuals from June 1974 to June 1977 at all the stations used in the study of the azimuthal dependence of residuals, there appears to be no reason to think that the models derived for the upper mantle structure beneath Southern California in Chapter 5 have been significantly biassed due to temporal instability of (crustal) velocities.

Chapter 5

MODELS FOR THE UPPER MANTLE VELOCITY STRUCTURE BENEATH SOUTHERN CALIFORNIA

Two main methods have been used to infer crustal and upper mantle velocity variations from teleseismic residual data. The first involves the use of ray tracing to delineate the region and magnitude of the velocity anomaly, and has been used by Spence (1974) in a study of the Silent Canyon volcanic centre in Nevada, and by Steeples and Iyer (1976) in a study of Long Valley. The second approach, developed more recently by Aki and co-workers (e.g., Aki et al., 1976, 1977) utilises sophisticated inversion techniques to solve for the velocity variations beneath the network studied. In this chapter, the relative merits of these techniques, as they apply to the determination of the upper mantle structure beneath Southern California, will be discussed, and velocity models derived to account for the observed azimuthal dependence of residuals.

5.1. Choice of Modelling Technique

The large quantity of data amassed for the Southern California network during this study makes it impractical to carry out precise ray tracing for each station and every event; in addition, the structure is extremely complex, and it would be hard to incorporate the rapid changes into a systematic numerical ray tracing programme. However, within a given source region the residuals change only slowly, and the mean delay at any station is not only representative of the delay for a single event in the region, but is also less likely to be

biassed by the effects of source structure or mislocation. It was therefore decided to use the mean residual at every station and the ray paths for an "average" event in each source region to infer the local velocity variations. The details of this technique, and the assumptions involved will be discussed in the next section. Among the advantages of this technique are that it permits the use of all stations, even those with relatively few first arrivals, the available constraints provided by seismic refraction data are readily introduced, and the reliability of each residual used can be assessed individually. It does have the disadvantages that the small variations of residual with distance or azimuth within a given source region are ignored, although these appear, in general, to be comparable to the expected scatter and simplifying assumptions are necessary.

The use of the inversion method provides a direct way of determining velocity perturbations within a number of rectangular blocks into which the region under study is subdivided, and each event is considered separately. However, the size of the Southern California network means that the horizontal dimensions of the blocks used cannot be less than $\sim$50 km if the problem is to remain within the handling capability of the computer. This will lead to horizontal smoothing of velocity anomalies. In addition, because of the distance range of the earthquakes used ($\sim$35-95°) the rays are all fairly steeply incident, and the vertical resolution is also impaired. A particular problem encountered when applying this technique to the data for Southern California is the difficulty of finding an optimum combination of events and stations. The network coverage has been changing rapidly during

the period of study, so that some stations, although reliable, have too few first arrivals to be useful in the inversion (without undue increase in the size of the data matrix), and it is hard to find a large number of events where all the reliable stations were operating simultaneously. Nevertheless, the method was applied to a modified data set, and the results are discussed in section 5.3. A comparison of the models derived by the ray tracing and inversion is also presented in that section.

5.2. Models Derived by Ray Tracing

Ray paths were calculated for an "average" event in each source region using the Jeffreys velocity model (which yields travel times similar to those given by the J-B tables). The velocities for the uppermost layers of this model are listed in Table 5-1 (a), together with typical crust and upper mantle velocities for the Transverse Ranges and Mojave Desert (Hadley and Kanamori, 1977). Table 5-1 (b) shows the results of ray tracing calculations for the models listed in Table 5-1 (a) and a variety of take-off (or incidence) angles. The variations in epicentral distance, delta, for different models for a given take-off angle are small (except for Model IV), comparable to the variations in distance within a given source region, and the upper mantle paths are also very close. Model IV shows the effect of a slower surface velocity: even a relatively small decrease can cause a marked lowering of the incidence angle at the surface for a given epicentral difference, although the upper mantle ray path is little changed.

Table 5-1

RAY PATHS FOR DIFFERING UPPER MANTLE STRUCTURE

a) Models for compressional velocity in km/s.

Depth	I Jeffreys	II Transverse Ranges	III Mojave	IV Modified Mojave
0	5.57	5.5	5.5	5.0
5		6.2	6.2	6.2
15	6.5	6.7		
26			6.7	6.7
30	7.8	7.8	7.8	7.8
45		8.2		
96	8.0	8.25	8.0	8.0
160	8.2	8.28	8.2	8.2
223	8.33	8.33	8.33	8.33

Velocity changes in the crust and at the Moho are discontinuous, as is the one at 45 km in Model II. The remainder are changes in gradient but not jumps in velocity.

b) Horizontal distance in km taken to reach a given depth for various take-off angles.

T.O.A.°	Depth		I	II	III	IV
24.5		Δ°	40.1	38.3	38.2	27.8
	15		7	7.5	8*	8.5*
	30		16.5	16	16	17
	45		31.5*	28	32*	37*
	96		63	68	65	76
	160		114	121.5	117	133.5
	223		166	176	170	201
22.5		Δ°	50.3	49.1	49.1	35.8
	15		6	7	7*	8*
	30		14.5	15	14	16
	45		29*	25	29*	33*
	96		56	61	58	66.5
	160		101	107	104	119
	223		147	155	151	175
20		Δ°	60.8	59.7	59.7	50.7
	15		5	6	6*	7*
	30		13	13	12	14
	45		25*	21	25*	28*
	96		49	52	50	57
	160		87	92	89	101
	223		126	132	129	147

Table 5-1(b) (continued)

T.O.A.°	Depth, km		I	II	III	IV
18		Δ	68.8	67.9	67.8	60.2
	15		5	5	5.5*	6*
	30		11.5	11	11	12
	45		22*	19	22*	24.5*
	96		43	46	44	49.5
	160		76	80	78	88
	223		111	116	113	128
15.5		Δ	80.3	79.8	79.7	71.8
	15		4	4.5	5*	5*
	30		10	10	9	10
	45		19*	16	19*	21*
	96		36	38	37	41
	160		64	67	65	73
	223		93	96	95	106
13.5		Δ	92.4	89.0	88.9	81.9
	15		3.5	4	4*	4*
	30		8	8	8	9
	45		16*	14	16*	18*
	96		31	33	32	35
	160		55	58	56	62
	223		79	83	81	90

* ___values interpolated.

In Chapter 3, it was argued that the velocity contrast giving rise to the "Transverse Ranges anomaly" must persist to depths of ∿150 km, and that, if the velocity within the mantle beneath GSC was 7.8 km/s down to this depth, then the velocity in the anomalous zone was ∿8.3 km/s, which is consistent with the refraction data of Hadley and Kanamori (1977). The value of 7.8 km/s for the P-wave velocity at 150 km is not unreasonable for the Basin and Range Province (e.g., Biswas and Knopoff, 1974; Archambeau et al., 196), and GSC is close to the boundary of this region. However, this velocity may be rather low, and changing this assumption would naturally cause the estimates of the velocity contrast (and its extent) to vary. Two basic models were derived for the upper mantle P-velocity structure beneath Southern California: in the first it was assumed that a constant velocity contrast was responsible for the varying residuals, and in the second, a constant depth range of contrast was used. A comparison of the two interpretations is given in Table 5-2.

In Model 1, it was assumed that a constant contrast between 7.8 and 8.3 km/s gave rise to the observed variation of residuals, and this was used to calculate the path lengths in the region of increased velocity that would be required to generate the measured delays at each station. These were then converted to vertical distances using the ray paths appropriate to each source region; the "bottom" of the anomalous region was fixed at 150 km, and the inferred depths to the top of the high velocity zone plotted on a map of the network at the points vertically above the places where the rays cross the upper boundary of the 8.3 km/s layer. A contour map of the depth to the high velocity

Table 5-2

COMPARISON OF THE TWO MODELS

USED TO INTERPRET THE RELATIVE RESIDUALS

Residual, sec	Path length in region of increased velocity, km	Percentage velocity increase for 100 km path
-1.0	130	8.5
-0.9	117	7.5
-0.8	104	6.7
-0.7	91	5.8
-0.6	78	4.9
-0.5	65	4.1
-0.4	52	3.2
-0.3	39	2.4
-0.2	26	1.6
-0.1	13	.8
0	0	0

region was then constructed. Whilst this model provides a good description of the Transverse Ranges structure, it has limitations elsewhere. The predicted depths to the top of the 8.3 km/s layer north of ISA are in conflict with the known Moho depth, suggesting that the velocity contrast involved must either be higher, or persist to greater depths. For stations with positive residuals, the model predicts that a velocity of 8.3 km/s is not reached until depths in excess of 150 km; this can give rise to conflicts in residuals because a velocity anomaly at this depth can cause delays at relatively large distances. This problem was not very severe in the Eastern Mojave or the westernmost stations, which have positive residuals for rays incident from the west, but produced inconsistencies in the Imperial Valley where the residuals change rapidly from station to station. In the last case, the azimuthal and spatial variation of the residuals suggested a shallow low velocity region, and so it was decided to model the behaviour of the 8.3 km/s layer by relying largely on data from the outlying stations, and use the stations in the valley to determine the velocity decrease in a region from 30 to 50 km depth which was required to produce the observed delays. This second model was calculated in a manner similar to that used in constructing Model 2.

Model 2 was derived by assuming that a velocity change over the whole depth range 50-150 km gave rise to the observed residual variation. The ray paths calculated for each source region were used to determine the path length in this region, and this was used, together with the observed delays, to estimate the percentage velocity change in the region. These changes were then plotted on a map of Southern

California at the points vertically above the places where the appropriate rays pass through the midpoint (100 km) of the layer, and a contour map of percentage velocity change constructed.

The model derived by the first method is shown in Figure 5-1; north-south and east-west cross-sections through the Transverse Ranges are shown in Figure 5-2. The features of this model include five major regions where the boundary of the 8.3 km/s layer is depressed below 150 km: the northern Salton Trough-Southern Mojave Desert, the southern offshore borderland, the continental margin, the northern Carrizo Plains area (where the depths exceed 175 km) and the north-eastern Mojave Desert. The 8.3 km/s layer comes within 50 km of the surface north of ISA, in the vicinity of CSP and close to SBLG, and there is an approximately east-west trending ridge of high velocity material beneath much of the Transverse Ranges. This last structure is similar to that reported by Hadley and Kanamori (1977), although it would be more compatible with the refraction data if the top of the high velocity region was close to 50 km over a greater east-west distance. This might be achieved by varying the location of the bottom of the region as well as the top, or by changing the contrast as a function of depth. Beneath the Imperial Valley, velocities of 8.3 km/s should be reached at $\sim$135 km, with a shallowing to the south-east which is in part responsible for the negative residuals observed from South American events. Figure 5-3 shows the decrease in velocity between 30 and 80 km required to produce the observed residual variation. The lowest velocities are mainly confined to the centre of the valley, although there is a very slow region to the north of IKP. The maximum

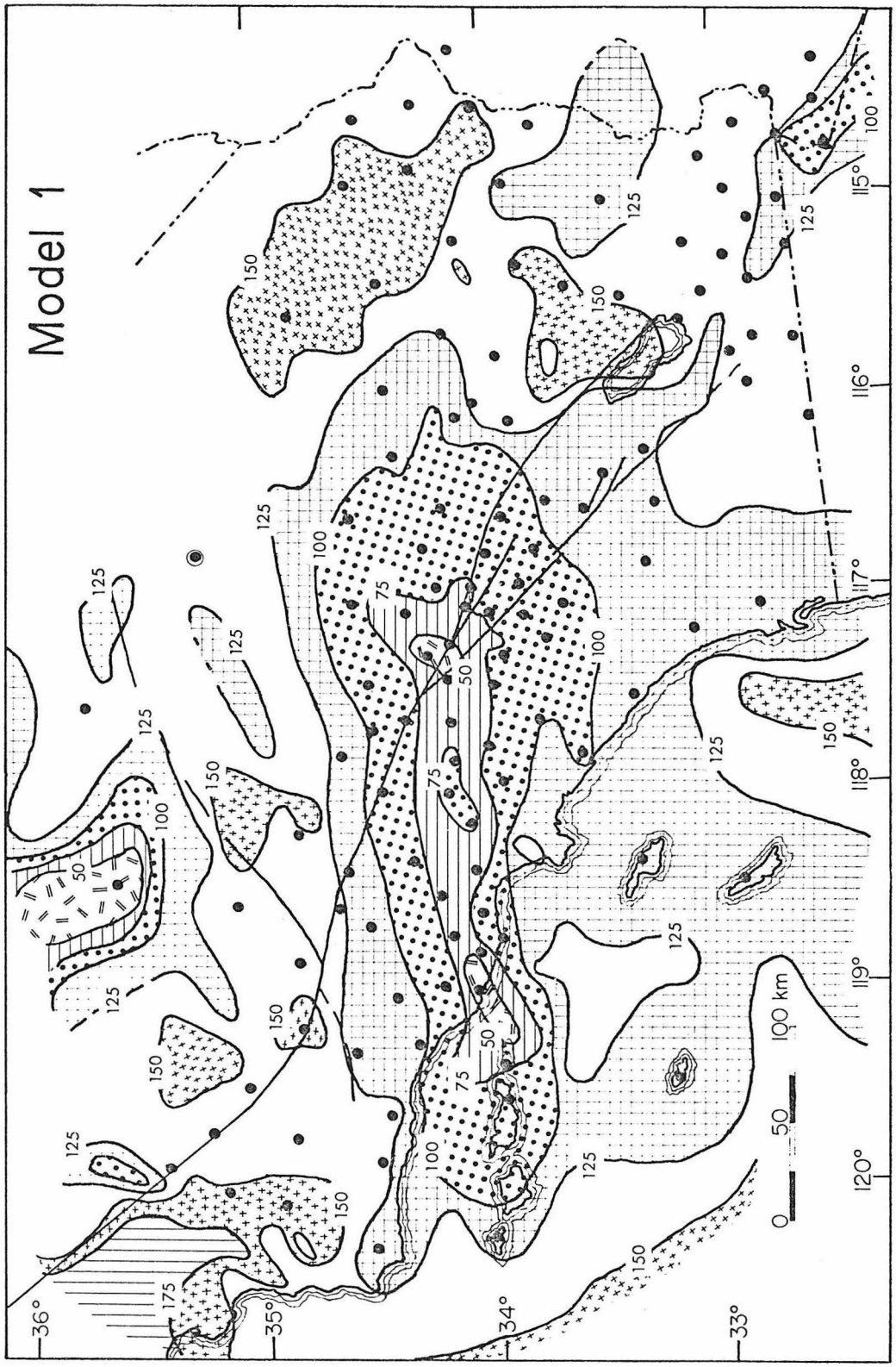

Figure 5-1. Model 1: Contours of depth to the top of the 8.3 km/s region; contour interval is 25 km.

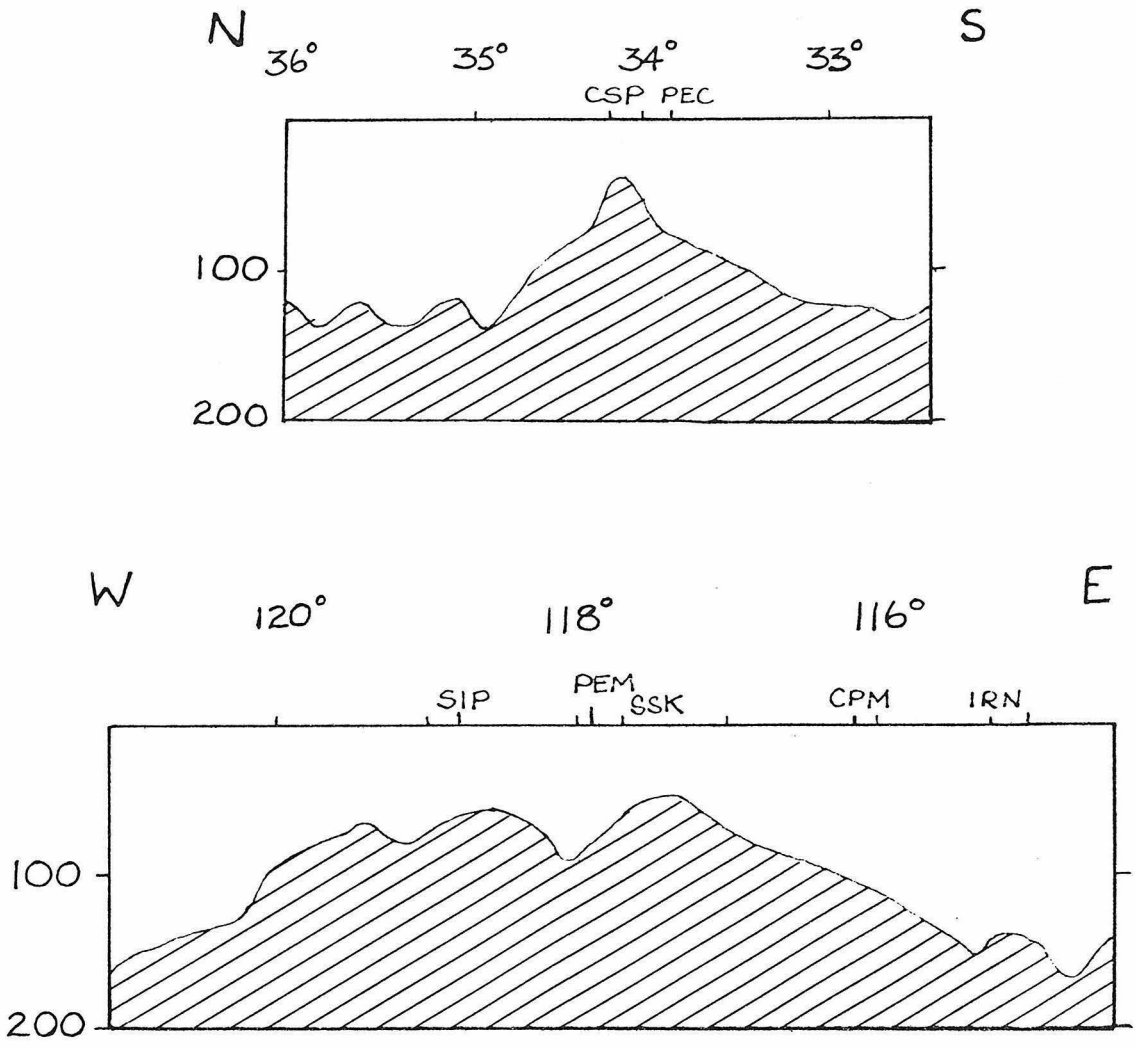

Figure 5-2. Vertical cross section through Model 1 showing the variation in depth to the 8.3 km/s layer (shaded). There is no vertical exaggeration, and the depths are labelled in km.

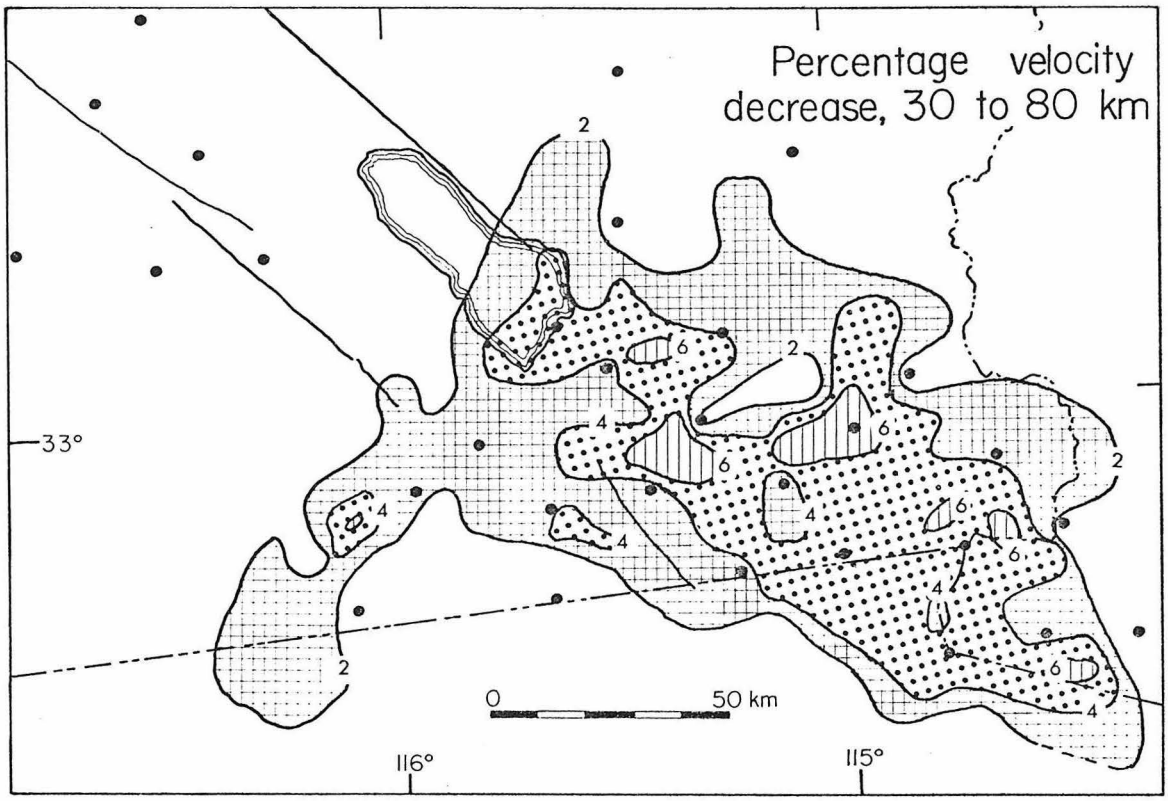

Figure 5-3. Velocity structure beneath the Imperial Valley. The contours are of percentage velocity decrease over a region extending from 30 to 80 km depth, and the contour interval is 2%.

decrease is ∿6.5%, implying a velocity of about 7.3 km/s (if the region is allowed a greater depth extent the contrast will be decreased), which can be compared to a P_n velocity of 7.5 km/s observed in the zone of crustal thinning and high heat flow that marks the transition from the Great Basin to the Colorado Plateau (Keller et al., 1975). "Upper mantle" velocities of this order have also been reported at shallow depths beneath oceanic ridges (e.g., beneath the East Pacific Rise (Rosendahl et al., 1976), the Reykjanes Ridge (Talwani et al., 1971), and the Mid-Atlantic Ridge (Fowler, 1976)). However, beneath the Rio Grande rift, where the crust is somewhat thicker (30 to 35 rather than 20 km in the Imperial Valley) P_n is as high as 8.1 km/s (Sanford et al., 1973).

The contour map of percentage velocity increase derived in Model II is shown in Figure 5-4. The apparent complexity of this model is in part due to the choice of contour interval, but many of the features are similar to those of Model 1. There are regions of low velocity in the Carrizo Plains area, the eastern Mojave Desert, the continental margin, the southern offshore borderland, and the general area of the Salton Trough, where the lowest velocities (∿7.5 km/s) occur in the Imperial Valley. A narrow high velocity (greater than 4% increase) region extends from the eastern Santa Barbara Channel to the eastern San Bernardino mountains, with the highest velocities in the vicinity of SBLG and CSP, and a slower area between SIP and PEM. Again, much of the northern Peninsular Ranges are relatively fast, and there is a region of extremely high velocity to the NNW of ISA (an 8% increase represents a velocity of 8.4 km/s). In both models, the so-called

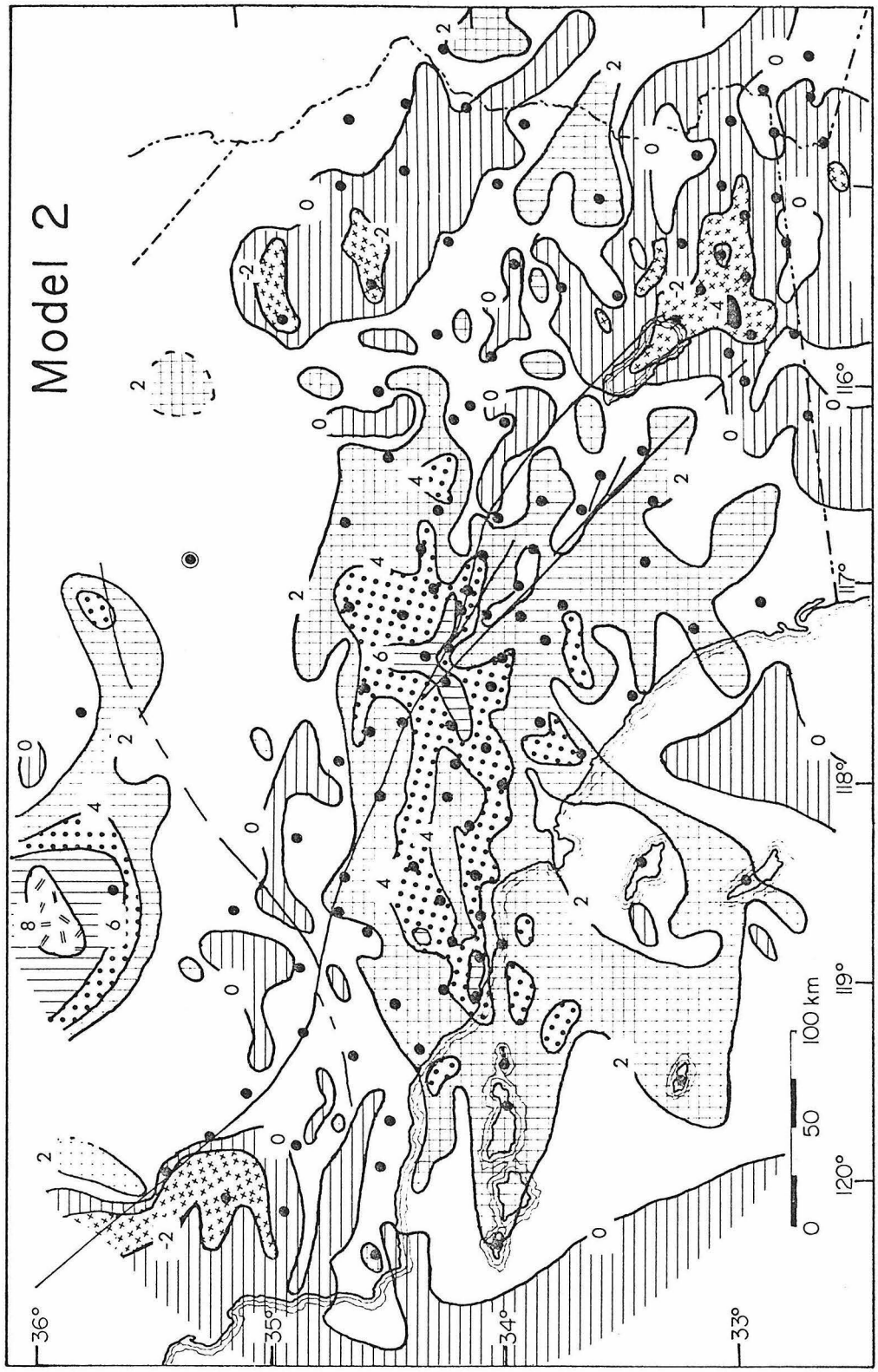

Figure 5-4. Model 2: contours of the percentage velocity increase over the depth range 50 t0 150 km. The contour interval is 2%.

Sierran anomaly lies largely beneath the western Sierra Nevada, and there are somewhat lower velocities under the eastern margin of the Sierra and the Owen's Valley, which has been the site of Quaternary volcanic activity.

The residuals predicted by these models are compared with the observed delays in Table 5-3.

A more easily digested comparison is provided by Tables 5-4 and 5-5, which list the mean misfits by source region and station. The mean misfits for a given source region are in general less than the mean standard deviation at a single station. Notable areas of misfit include the negative residuals observed for many of the Santa Barbara stations for the Leeward Islands, and the negative delays observed at the southern Imperial Valley stations for the events in the Leeward Islands and South America (which may in part be due to source structure, but suggests the existence of a high velocity region at greater depths to the south-east). Many of the north-western Los Angeles Basin stations are anomalously slow for events in the Marianas-Bonin Region, and a number of the Mojave stations very early for events in Alaska and the Aleutians. The station misfits are somewhat higher, although in only 20 cases for Model 1 and 13 cases for Model 2 do they exceed the observed standard deviation by more than 0.03 sec. (The difference between Models 1 and 2 is largely because the latter is better adapted to model positive residuals.) As a result of the analysis of station misfits, it appears that additional crustal or sediment corrections are required for PAS, IRC, MWC, MLL, VGR, HOT, LRR, RDM, SBCD and CRG (0.1 sec), DVL, BTL, SIL and BLU (0.15 sec), CFT (0.2 sec), PTD (0.25

Table 5-3

OBSERVED AND PREDICTED RESIDUALS
(normalised with respect to GSC)

* indicates stations with crustal corrections applied

1. Java Trench GSC ≡ 0.0

Station	Obs.	Model 1	Model 2	Station	Obs.	Model 1	Model 2
SYP	-.05	-.15	-.05	CKC	-.33	-.50	-.35
ISA*	-.77	-.80	-.75	MDA	-.23	-.45	-.20
CLC	-.11	-.10	-.10	RAY	-.34	-.45	-.45
SBB	-.15	-.20	-.15	WWR	-.26	-.40	-.25
CSP	-.81	-.80	-.80	VGR	-.21	-.40	-.30
RVR	-.58	-.55	-.60	DB2	-.43	-.45	-.40
PEC	-.33	-.45	-.35	PSP	-.38	-.35	-.35
TPC	-.17	-.15	-.15	KEE	-.29	-.30	-.25
PLM	-.37	-.35	-.35	THR	-.44	-.45	-.45
VST	-.29	-.30	-.30	BLU	-.33	-.45	-.35
CPE	-.22	-.25	-.20	ADL*	-.66	-.60	-.60
SCI*	-.25	-.25	-.25	SDW	-.64	-.60	-.60
IKP	-.05	.05	.05	SIL	-.45	-.45	-.50
GLA*	-.01	-.05	-.05	SSK	-.70	-.70	-.70
SNS*	-.23	-.25	-.20	SSV	-.73	-.75	-.75
SJQ*	-.52	-.50	-.50	CHM	-.04	-.05	-.05
CIS*	-.22	-.25	-.20	TTM	.20	.10	.15
VPD*	-.45	-.45	-.45	WH2	-.15	-.15	-.10
TCC*	-.56	-.55	-.55	BPK	-.10	-.10	-.15
MWC	-.45	-.50	-.45	RVS	.01	.05	0.0
PAS	-.35	-.45	-.40	LTM	-.20	-.20	-.20
SCY	-.63	-.65	-.60	BMM	-.13	-.15	-.10
TWL*	-.59	-.60	-.60	LGA*	-.13	-.10	-.10
IRC	-.58	-.55	-.55	FTM*	-.07	-.10	-.10
PYR	-.03	-.20	-.15	YMD*	.03	.05	.05
RMR	-.35	-.45	-.35	SBLP	-.30	-.30	-.30
HDG	-.37	-.35	-.30	SBSM	-.25	-.25	-.25
CPM	-.16	-.25	-.20	SBLC	-.15	-.15	-.15
INS	-.13	-.15	-.10	SBSC	-.45	-.45	-.40
PNM	-.08	-.10	-.10	SBSN	-.30	-.30	-.30
LED	-.23	-.25	-.20	SBCD*	-.29	-.30	-.25
SHH	-.15	-.15	-.15	SBLG	-.78	-.80	-.75
GRP	.28	.20	.25	CCM	-.05	-.05	-.05
SPM	.27	.20	.25	OBB*	.26	.25	.25
IRN	-.02	0.0	-.05	SUP*	.21	.15	.20
CO2	.06	.10	.05	SGL*	-.08	-.05	-.05
BC2	.01	.05	0.0	ING*	-.13	-.10	0.0
LTC	-.30	-.30	-.30	SNR*	.07	.05	.10
				COA*	0.0	.05	.15

Note: Obs. = observed residual, sec.
Theoretical residuals are calculated to the nearest .05 sec.

Table 5-3 (continued)

2. Novaya Zemlya GSC ≡ 0.0

Station	N	Obs.	S.D.	Model 1	Model 2
SYP	5	-.16	.07	-.15	-.15
ISA*	7	-1.26	.05	-1.00	-1.20
CLC	5	-.22	.06	-.20	-.20
SBB	7	-.33	.04	-.35	-.35
CSP	4	-.16	.04	-.40	-.30
RVR	7	-.92	.04	-.90	-.90
PEC	7	-.82	.04	-.80	-.80
TPC	7	.20	.04	-.20	.15
PLM	7	-.07	.05	-.40	-.30
VST	5	-.19	.05	-.30	-.25
CPE	6	-.22	.04	-.25	-.25
SCI*	5	-.02	.03	-.05	-.05
IKP	7	.52	.05	.45	.30
GLA*	7	.22	.03	.10	.10
SNS*	3	-.37	.04	-.45	-.40
SJQ*	3	-.70	.07	-.65	-.65
CIS*	4	-.10	.07	-.10	-.10
VPD*	6	-.98	.07	-.80	-.85
TCC*	2	-1.08	.10	-.90	-.80
MWC	7	-.31	.05	-.40	-.35
PAS	4	-.54	.06	-.55	-.55
SCY	5	-.69	.06	-.70	-.60
TWL*	5	-.43	.05	-.40	-.40
IRC	7	-.19	.06	-.20	-.20
SWM	2	-.08	.01	-.10	-.10
PYR	4	-.08	.03	-.10	-.10
CKC	3	-.20	.05	-.70	-.45
MLL	4	-.38	.03	-.60	-.50
CFT	3	-.63	.06	-.70	-.55
MDA	2	-.52	.01	-.65	-.45
RAY	2	-.51	.01	-.55	-.45
WWR	3	-.45	.06	-.55	-.45
DB2	3	-.87	.03	-.70	-.80
PSP	3	-.62	.11	-.60	-.55
DVL	3	-.19	.03	-.85	-.60
COY	1	.07		-.20	-.10
HOT	1	-.02		-.20	-.10
LRR	1	-.18		-.15	-.15
TPO	2	-.22	.02	-.20	-.20

Note: N = No. of events recorded
Obs. = mean observed residual, sec.
S.D. = standard deviation, sec.

Table 5-3 (continued)

2. Novaya Zemlya (continued)

Station	N	Obs.	S.D.	Model 1	Model 2
SDW	3	.01	.02	-.05	0.0
BLU	2	-.02	.01	-.10	-.05
ADL*	1	-.14		-.15	-.15
PEM	1	-.52		-.55	-.45
BTL	2	.02	.02	-.40	-.40
SIL	2	.04	.01	-.35	-.25
SSK	1	-.36		-.50	-.45
SSV	1	-.39		-.50	-.50
SME	4	-1.02	.04	-.80	-.80
STP	3	-.10	.09	-.10	-.10
CHM	2	-.29	.04	-.25	-.25
TTM	6	-.11	.02	-.10	-.10
WH2	4	-.29	.06	-.25	-.25
BPK	4	-.13	.08	-.15	-.15
RVS	4	-.10	.06	-.10	-.10
LTM	2	-.10	.01	0.0	0.0
BMM	4	-.06	.03	-.10	0.0
PIC	5	.12	.06	.10	.10
LGA*	4	.14	.05	.10	.15
FTM*	3	.12	.01	.10	.10
YMD*	5	.20	.03	.20	.20
RMR	6	-.22	.04	-.25	-.30
HDG	7	.16	.05	0.0	.10
CPM	7	.20	.05	-.20	.20
INS	7	-.08	.05	-.25	-.10
PNM	4	.19	.05	-.10	.10
LED	4	.04	.07	.05	.05
SHH	5	.16	.05	.15	.15
GRP	5	-.13	.07	-.10	-.10
SPM	4	-.25	.06	.05	.05
IRN	5	-.23	.07	.05	.05
CO2	5	.12	.03	.10	.10
BC2	5	-.01	.07	-.05	-.05
LTC	4	-.29	.02	-.30	-.30
ROD	2	-.06	.01	-.05	-.05
SBCC	1	-.18		-.15	-.15
SBLP	4	-.22	.03	-.15	-.15
SBSM	5	-.42	.06	-.40	-.30
SBLC	7	-.21	.05	-.20	-.20
SBSC	4	-.49	.05	-.50	-.45
SBAI	1	-.70		-.70	-.70
SBSN	3	-.09	.03	-.10	-.10
ECF*	5	-.16	.02	-.15	-.15
SBCD*	5	-.18	.03	-.20	-.20

Table 5-3 (continued)

2. Novaya Zemlya (continued)

Station	N	Obs.	S.D.	Model 1	Model 2
CAM *	4	-.36	.01	-.35	-.30
SBLG	6	-.59	.02	-.55	-.50
SIP	4	-.37	.02	-.35	-.35
KYP	4	-.86	.02	-.80	-.80
SAD	5	-.76	.03	-.75	-.75
PTD	4	-.19	.06	-.70	-.55
CJP	3	-.42	.05	-.50	-.40
CLP	4	-.84	.04	-.80	-.80
CCM	2	-.01	0	-.05	-.05
OBB*	3	.47	.09	.40	.40
AMS*	3	.18	.02	.15	.15
WLK*	2	.44	.06	.40	.40
SUP*	4	.39	.04	.40	.40
CRR*	4	.45	.04	.35	.30
COK*	3	.35	.05	.35	.35
SGL*	4	.40	.03	.40	.40
ING*	5	.44	.03	.40	.45
SNR*	3	.25	.05	.25	.25
COA*	5	.18	.08	.15	.15
RUN*	3	.23	.06	.15	.20
BCK*	1	.16		.20	.15
PLT*	5	.26	.07	.25	.20
SLU*	4	.24	.05	.20	.20
LHU	2	-.12	.02	-.15	-.10
BCH	1	-.42		-.40	-.40
YEG	2	-.45	.02	-.40	-.40
RYS	2	-.03	.04	-.05	-.05
PKM	2	-.11	.04	-.10	-.10

3. Leeward Islands

					Model 1	
Station	N	Obs.	S.D.	GSC = 0	-.10	0
SYP	3	-.92	.10	-.55	-.45	-.30
ISA*	1	-.51		-.60	-.50	-.45
CLC	1	-.81		-.85	-.75	-.85
SBB	3	-.33	.04	-.45	-.35	-.35
CSP	3	-.09	.05	-.45	-.35	-.50
RVR	2	-.40	.10	-.50	-.40	-.45
PEC	3	-.19	.07	-.30	-.20	-.25
TPC	3	-.07	.04	-.15	-.05	-.10
PLM	3	.03	.08	-.20	-.10	-.25
VST	1	-.28		-.30	-.20	-.25
CPE	2	-.46	.08	-.30	-.20	-.45
SCI*	2	.16	.05	.05	.15	.15
IKP	1	-.06		-.15	-.05	.05

Table 5-3 (continued)

3. Leeward Islands (continued)

Station	N	Obs.	S.D.	GSC =	Model 1 0	Model 1 -.10	Model 2 0
GLA*	3	-.04	.08		-.15	-.05	-.05
SNS*	1	-.29			-.40	-.30	-.40
SJQ*	1	-.59			-.50	-.40	-.60
CIS*	2	.04	.02		-.25	-.15	.05
VPD*	3	-.32	.06		-.50	-.40	-.40
MWC	1	-.66			-.70	-.60	-.70
PAS	1	-.59			-.70	-.60	-.70
SCY	2	-.63	.03		-.75	-.65	-.60
TWL*	3	-.95	.04		-.95	-.85	-.55
IRC	3	-.85	.04		-.85	-.75	-.80
SWM	1	-.43			-.45	-.35	-.35
PYP	3	-1.03	.04		-.90	-.80	-.60
CFT	1	.09			-.60	-.50	0.0
RAY	1	-.01			-.20	-.10	-.10
WWR	1	.18			-.10	0.0	.10
VGR	1	.04			-0.05	.05	.05
DB2	1	-.34			-.40	-.30	-.30
PSP	1	-.18			-.15	-.05	-.15
KEE	1	-.18			-.30	-.20	-.30
SDW	1	-.14			-.45	-.35	-.30
BLU	1	-.23			-.65	-.55	-.45
PEM	1	-.44			-.70	-.60	-.55
BTL	1	.21			-.50	-.40	-.45
SIL	1	.14			-.40	-.30	-.30
SSK	1	-.48			-.80	-.70	-.65
SSV	1	-.61			-.80	-.70	-.60
GAV	1	-.55			-.65	-.55	-.55
SME	1	-.53			-.60	-.50	-.50
CHM	1	-.13			-.20	-.10	-.20
TTM	2	.20	.09		-.15	-.05	-.05
WH2	1	-.06			-.15	-.05	-.15
BPK	3	-.17	.09		-.25	-.15	-.20
RVS	1	-.06			-.15	-.05	-.10
LTM	1	.14			-.05	.05	.05
BMM	1	-.14			-.20	-.10	-.15
PIC	1	-.02			-.15	-.05	-.05
LGA*	1	-.03			-.15	-.05	-.05
FTM	1	.13			-.05	.05	-.10
RMR	1	.07			-.45	-.35	-.35
HDG	3	.17	.04		0.0	.10	.05
CPM	2	.24	.02		-.05	.05	-.05
INS	3	-.14	.07		-.25	-.15	-.10
PNM	1	-.22			-.30	-.20	-.25

Table 5-3 (continued)

3. Leeward Islands (continued)

Station	N	Obs.	S.D.	GSC =	Model 1 0	Model 1 -.10	Model 2 0
LED	1	.11			.05	.15	.15
SHH	2	-.06	.01		0.0	.10	0.0
GRP	1	-.36			-.30	-.20	-.20
SPM	3	-.21	.01		-.25	-.15	.05
IRN	3	.11	.02		0.0	.10	.10
CO2	1	-.05			-.15	-.05	-.05
BC2	1	-.30			-.40	-.30	-.25
LTC	1	-.33			-.40	-.30	-.35
SBLP	1	-.93			-.30	-.20	-.25
SBLC	3	-.94	.04		-.55	-.45	-.50
SBSC	3	-1.13	.16		-1.00	-.90	-.85
SBAI	1	-1.03			-1.05	-.95	-.85
SBSN	1	-.46			-.50	-.40	-.45
ECF*	2	-.47	.05		-.60	-.50	-.50
SBCD*	2	-.92	.04		-.70	-.60	-.85
SBLG	2	-.92	.06		-.95	-.85	-.80
SIP	2	-1.08	.08		-.90	-.80	-.75
SAD	2	-.72	.06		-.85	-.75	-.70
PTD	2	.05	.02		-.50	-.40	-.35
CCM	1	-.17			-.30	-.20	-.15
AMS*	1	-.33			-.20	-.10	-.20
SUP*	1	-.15			-.05	.05	.05
CRR*	1	-.16			-.25	-.15	.05
SGL*	2	-.06	.08		-.20	-.10	-.10
SNR*	1	-.52			-.20	-.10	.05
COA*	1	-.51			0.0	.10	-.20
RUN*	2	-.36	.04		-.20	-.10	0.0
PLT*	2	-.07	.05		-.20	-.10	0.0

4. South America I, Azimuth $\lesssim$ 130°

Station	N	Obs.	S.D.	GSC ≡ 0.0	Model 1	Model 2
SYP	10	-.65	.04		-.55	-.35
ISA*	14	-.36	.06		-.35	-.40
CLC	5	-.55	.08		-.55	-.55
SBB	13	-.54	.06		-.55	-.60
CSP	8	.05	.04		-.65	-.30
RVR	13	-.31	.07		-.40	-.35
PEC	12	-.15	.04		-.30	-.20
TPC	12	-.23	.03		-.10	-.10
PLM	15	-.03	.10		-.10	-.10
VST	7	-.38	.05		-.35	-.35
CPE	8	-.23	.04		-.20	-.20
SCI*	8	.14	.07		.15	-.15

Table 5-3 (continued)

4. South America I (continued)

Station	N	Obs.	S.D.	Model 1	Model 2
IKP	8	.07	.09	.05	.10
GLA*	10	.21	.05	.20	.20
SNS*	8	-.39	.04	-.40	-.35
SJQ*	4	-.08	.05	-.40	-.10
CIS*	6	.05	.03	-.20	0.05
VPD*	10	-.26	.16	-.30	-.35
TCC*	3	-.24	.06	-.40	-.35
MWC	10	-.44	.06	-.60	-.50
PAS	9	-.31	.08	-.55	-.40
SCY	6	-.10	.14	-.35	-.25
TWL	9	-.15	.08	-.35	-.50
IRC	10	-.24	.03	-.50	-.40
SWM	3	-.62	.04	-.65	-.55
PYR	7	-.67	.07	-.70	-.65
CKC	2	-.03	.08	-.60	-.25
MLL	10	-.11	.10	-.40	-.20
CFT	4	-.12	.02	-.40	-.30
MDA	4	-.34	.14	-.35	-.35
RAY	5	-.14	.06	-.40	-.15
WWR	6	.19	.06	.15	-.20
VGR	3	-.18	.08	-.25	-.20
DB2	8	-.35	.08	-.35	-.35
PSP	2	-.31	.06	-.30	-.30
KEE	8	-.22	.07	-.25	-.20
DVL	2	-.28	.04	-.50	-.40
COY	4	-.27	.05	-.25	-.05
SMO	2	-.22	.05	-.20	-.15
HOT	4	-.30	.03	-.30	-.30
LRR	5	-.35	.03	-.50	-.45
TPO	3	-.74	.07	-.40	-.40
THR	2	-.50	.02	-.65	-.60
SDW	6	-.39	.06	-.45	-.40
BLU	8	-.29	.05	-.70	-.80
ADL*	3	-.34	.05	-.70	-.60
PEM	3	-.40	.03	-.70	-.55
RDM	2	-.19	.03	-.55	-.30
PCF	2	-.38	.01	-.50	-.40
BTL	5	.11	.05	-.50	.05
SIL	5	-.01	.06	-.35	-.30
SSK	6	-.54	.05	-.60	-.50
SSV	3	-.57	.01	-.60	-.50
GAV	4	-.50	.07	-.55	-.45
SME	6	-.39	.05	-.40	-.40
CHM	5	-.11	.07	-.10	-.10
TTM	8	.08	.05	0.0	-.05
WH2	10	-.20	.09	-.20	-.20

Table 5-3 (continued)

4. South America I (continued)

Station	N	Obs.	S.D.	Model 1	Model 2
BPK	5	-.25	.13	-.20	-.25
RVS	6	-.16	.12	-.15	-.15
LTM	5	-.15	.07	-.15	-.15
BMM	5	.10	.02	-.05	.10
PIC	6	.02	.10	0.0	.05
LGA*	4	-.02	.05	-.05	-.05
FTM*	4	.09	.02	-.05	-.05
YMD*	3	-.26	.01	-.10	-.25
RMR	12	.15	.07	-.10	-.05
HDG	12	.04	.13	-.20	-.05
CPM	10	.11	.05	.05	.10
INS	12	-.14	.10	-.10	-.15
PNM	10	-.22	.09	-.20	-.15
LED	8	-.12	.08	0.05	-.10
SHH	12	-.19	.08	-.20	-.20
GRP	8	-.26	.09	-.20	0.0
SPM	8	-.16	.13	-.10	.05
IRN	10	-.14	.05	-.15	-.05
CO2	20	-.37	.06	-.35	-.35
BC2	10	-.29	.11	-.35	-.30
LTC	8	-.20	.09	-.30	-.20
ROD	5	0.0	.08	-.20	-.20
SBCC	4	-.47	.05	-.30	-.30
SBLP	7	-.55	.04	-.50	-.50
SBSM	5	-.45	.03	-.50	-.45
SBLC	8	-.66	.05	-.60	-.55
SBSC	8	-.74	.07	-.70	-.75
SBAI	3	-.56	.07	-.55	-.55
SBSN	6	-.37	.05	-.35	-.35
ECF*	4	-.48	.07	-.60	-.60
SBCD*	3	-.37	.05	-.60	-.50
CAM*	5	-.50	.11	-.55	-.50
SBLG	7	-.48	.05	-.50	-.45
SIP	6	-.51	.05	-.55	-.50
KYP	6	-.27	.05	-.30	-.35
SAD	5	-.22	.03	-.30	-.25
PTD	4	-.10	.04	-.30	-.25
CJP	3	-.51	.03	-.50	-.50
CLP	2	-.40	.16	-.35	-.40
CCM	6	-.20	.08	-.15	-.20
AMS*	2	-.05	.03	.15	.05
WLK*	1	.36		-.40	-.35
SUP*	9	.01	.03	-.05	0.0
CRR*	6	.11	.02	-.10	.10
COK*	1	-.17		-.10	-.15
SGL*	8	0.0	.07	0.0	.05

Table 5-3 (continued)

4. South America I (continued)

Station	N	Obs.	S.D.	Model 1	Model 2
ING*	1	.29		.30	.20
COA*	8	-.38	.09	-.10	-.05
RUN*	3	-.50	.03	.10	-.25
BON*	1	.08		.05	.05
BCK*	2	-.67	.02	-.40	-.10
PLT*	8	-.24	.13	-.10	-.25
LHU	6	-.52	.05	-.60	-.45
CRG	7	.04	.03	-.05	.05
BCH	7	-.05	.05	-.05	-.05
ABL	6	-.49	.05	-.35	-.25
TMB	4	-.06	.02	-.05	-.05
YEG	7	-.07	.03	-.10	-.05
RYS	7	-.36	.05	-.40	-.35
BMT	6	-.28	.04	-.25	-.10
FTC	6	-.31	.03	-.30	-.35
PKM	7	-.24	.07	-.30	-.20

5. South America II, Azimuths $\gtrless$ 130°

Station	N	Obs.	S.D. GSC ≡ 0.0	Model 1	Model 2
SYP	20	-.40	.09	-.40	-.30
ISA*	26	-.15	.09	-.20	-.15
CLC	18	-.47	.03	-.30	-.45
SBB	23	-.54	.07	-.55	-.55
CSP	18	-.22	.12	-.40	-.65
RVR	18	-.24	.07	-.45	-.30
PEC	18	-.32	.07	-.35	-.30
TPC	23	-.11	.06	-.15	-.10
PLM	23	-.20	.10	-.20	-.20
VST	17	-.35	.09	-.30	-.30
CPE	13	-.25	.06	-.25	-.20
SCI*	15	-.23	.06	-.20	-.20
IKP	21	-.11	.06	-.10	-.10
GLA*	26	-.26	.09	-.05	-.20
SNS*	15	-.15	.06	-.25	-.15
SJQ*	8	-.19	.10	-.25	-.20
CIS*	16	-.09	.10	-.25	-.10
VPD*	23	-.12	.10	-.25	-.30
TCC*	4	-.31	.36	-.35	-.40
MWC	23	-.23	.07	-.50	-.50
PAS	19	-.09	.09	-.35	-.30
SCY	12	-.26	.08	-.30	-.30
TWL*	15	-.35	.06	-.65	-.50
IRC	23	-.39	.07	-.55	-.40
SWM	10	-.52	.06	-.50	-.45

Table 5-3 (continued)

5. South America II (continued)

Station	N	Obs.	S.D.	Model 1	Model 2
PYR	16	-.45	.04	-.50	-.55
CKC	4	.16	.04	-.50	-.25
MLL	4	.15	.04	-.50	-.25
CFT	9	.05	.05	-.50	-.10
MDA	7	-.20	.07	-.25	-.20
RAY	14	-.22	.07	-.25	-.20
WWR	8	-.18	.07	-.25	-.25
VGR	6	-.18	.08	-.25	-.20
DB2	18	-.45	.06	-.40	-.45
PSP	10	-.37	.09	-.35	-.35
KEE	13	-.18	.07	-.25	-.20
COY	7	-.17	.06	-.20	-.20
SMO	3	-.29	.04	-.30	-.30
HOT	3	-.18	.05	-.20	-.20
LRR	7	-.45	.04	-.60	-.55
TPO	6	-.64	.05	-.45	-.30
THR	5	-.45	.07	-.50	-.55
SDW	12	-.42	.08	-.50	-.40
BLU	19	-.32	.06	-.70	-.55
ADL*	8	-.46	.04	-.60	-.55
PEM	10	-.29	.04	-.50	-.45
RDM	4	-.23	.09	-.45	-.35
PCF	3	-.31	.02	-.50	-.35
BTL	9	.04	.06	-.45	-.25
SIL	12	.06	.08	-.45	-.25
SSK	15	-.43	.06	-.45	-.55
SSV	7	-.42	.09	-.60	-.40
GAV	12	-.40	.07	-.45	-.40
SME	13	-.35	.07	-.35	-.35
STP	4	-.12	.07	-.10	-.10
CHM	15	-.16	.05	-.15	-.15
TTM	18	-.20	.05	-.20	-.05
WH2	20	-.30	.05	-.25	-.30
BPK	13	-.40	.09	-.25	-.40
RVS	16	-.30	.07	-.25	-.30
LTM	16	-.26	.07	-.25	-.25
BMM	10	-.24	.06	-.25	-.15
PIC	16	-.18	.06	-.10	-.20
LGA	10	-.40	.09	-.25	-.25
FTM	10	-.21	.15	-.20	-.20
YMD	8	-.42	.05	-.30	-.25
RMR	20	.11	.07	-.40	-.15
HDG	24	-.04	.08	-.35	-.30
CPM	26	-.06	.06	-.05	-.05

Table 5-3 (continued)

5. South America II (continued)

Station	N	Obs.	S.D.	Model 1	Model 2
INS	24	-.31	.05	-.20	-.30
PNM	20	-.38	.06	-.20	-.35
LED	16	-.25	.08	-.25	-.25
SHH	25	-.35	.05	-.25	-.25
GRP	22	-.15	.08	.05	.05
SPM	19	-.25	.07	0.0	.05
IRN	22	-.30	.09	-.30	-.25
CO2	10	-.66	.05	-.45	-.30
BC2	24	-.34	.04	-.35	-.35
LTC	21	-.28	.05	-.25	-.20
ROD	5	-.08	.05	-.25	-.30
SBCC	9	-.15	.07	-.15	-.15
SBLP	13	-.52	.07	-.40	-.35
SBSM	10	-.45	.06	-.40	-.40
SBLC	15	-.66	.08	-.60	-.55
SBSC	13	-.68	.06	-.55	-.60
SBAI	2	-.61	.05	-.60	-.60
SBSN	5	-.35	.08	-.35	-.35
ECF*	8	-.22	.08	-.55	-.55
SBCD*	2	-.28	0	-.55	-.55
CAM*	4	-.47	.02	-.55	-.45
SBLG	13	-.72	.04	-.60	-.60
SIP	12	-.54	.05	-.55	-.55
KYP	7	-.43	.11	-.40	-.40
SAD	3	-.29	.12	-.35	-.35
PTD	4	-.19	.07	-.30	-.30
CJP	3	-.49	.03	-.45	-.50
CLP	3	-.49	.09	-.40	-.50
CCM	16	-.39	.06	-.15	-.20
OBB*	4	-.08	.07	.10	.10
AMS*	6	-.05	.04	-.05	.10
WLK*	2	.36	.04	.30	.35
SUP*	18	-.18	.08	0.0	-.05
CRR*	18	-.19	.05	-.05	-.10
COK*	4	-.20	.15	-.05	-.10
SGL*	20	-.21	.04	-.20	0.0
ING*	6	-.30	.08	-.15	.05
SNR*	2	-.21	.06	-.10	-.15
COA*	17	-.56	.07	-.15	.05
RUN*	8	-.50	.04	.05	-.25
BON*	4	-.18	.07	-.10	0.0
BCK*	1	-.60		-.40	.05
PLT*	17	-.52	.08	-.10	-.15
SLU*	4	-.78	.03	-.35	-.20
LHU	2	-.46	.04	-.50	-.45
CRG	3	-.04	.04	-.05	-.05

Table 5-3 (continued)

5. South America II (continued)

Station	N	Obs.	S.D.	Model 1	Model 2
BCH	3	.09	.02	-.05	.05
ABL	2	-.56	.03	-.30	-.25
TMB	2	-.04	.03	-.05	-.05
YEG	2	.06	.02	.05	.05
RYS	2	-.42	.02	-.35	-.35
BMT	2	-.34	.04	-.20	-.20
FTC	2	-.21	.03	-.25	-.30
PKM	3	-.26	.04	-.25	-.25

6. South Pacific I, Azimuths $\leq 235°$

Station	N	Obs.	S.D. GSC = 0.15	Model 1	Model 2
SYP	7	-.16	.03	-.10	-.10
ISA*	15	-.14	.04	-.15	-.05
CLC	6	-.11	.02	-.15	-.10
SBB	11	-.40	.05	-.40	-.40
CSP	6	-.22	.04	-.45	-.45
RVR	8	-.36	.06	-.35	-.35
PEC	7	-.33	.06	-.35	-.35
TPC	11	.07	.02	-.10	.15
PLM	10	-.26	.09	-.20	-.25
VST	7	-.16	.06	.05	-.15
CPE	6	-.09	.05	-.05	-.05
SCI*	7	-.16	.05	-.15	-.15
IKP	8	.21	.07	.20	.20
GLA*	8	.57	.04	.50	.45
SNS*	5	-.09	.04	-.10	.05
SJQ*	3	0.0	.03	-.10	-.05
CIS*	7	-.28	.06	-.20	-.25
VPD*	8	-.28	.07	-.30	-.30
TCC*	2	-.36	.02	-.15	-.30
MWC	10	-.34	.09	-.40	-.35
PAS	9	-.28	.04	-.20	-.30
SCY	5	-.37	.03	-.20	-.35
TWL*	4	-.68	.16	-.60	-.60
IRC	6	-.53	.04	-.55	-.50
SWM	3	-.52	.11	-.25	-.30
PYR	6	-.24	.07	-.30	-.25
CKC	4	.16	.03	-.30	-.25
MLL	3	.07	.04	-.30	-.20
CFT	4	.06	.10	-.30	-.20
MDA	4	.03	.04	-.30	-.30
RAY	4	-.31	.08	-.30	-.30
WWR	4	-.01	.04	-.25	-.15
VGR	2	-.10	.05	-.25	-.20

Table 5-3 (continued)

6. South Pacific I (continued)

Station	N	Obs.	S.D.	Model 1	Model 2
DB2	12	-.38	.06	-.20	-.35
PSP	2	-.36	.09	-.30	-.30
KEE	2	-.23	.01	-.20	-.25
DVL	1	-.29		-.40	-.30
COY	1	-.06		-.20	-.05
SMO	1	-.09		-.20	-.10
HOT	1	-.03		-.20	-.10
TPO	2	-.16	.14	-.15	-.20
THR	2	-.42	.05	-.45	-.45
SDW	6	-.75	.04	-.60	-.70
BLU	5	-.35	.01	-.35	-.35
ADL*	2	-.36	.09	-.40	-.35
PEM	1	-.49		-.45	-.40
RDM	1	-.28		-.70	-.30
PCF	1	-.35		-.25	-.20
BTL	1	-.18		-.30	-.20
SIL	4	-.30	.04	-.30	-.35
SSK	5	-.61	.05	-.50	-.50
SSV	2	-.60	.04	-.50	-.50
GAV	3	-.49	.03	-.40	-.50
SME	7	-.42	.06	-.40	-.40
STP	2	.19	.01	.15	.20
CHM	3	.19	.06	.20	.20
TTM	7	.52	.05	.15	.30
WH2	4	.28	.05	.15	.30
BPK	3	.29	.04	.10	.30
RVS	5	.29	.06	.10	.20
LTM	5	0.0	.06	.05	0.0
BMM	2	.13	.03	-.05	-.05
PIC	8	.45	.08	.45	.35
LGA*	5	.43	.05	.35	.35
FTM*	7	.40	.05	.30	.35
YMD*	5	.29	.06	.30	.30
RMR	6	-.27	.07	-.30	-.25
HDG	7	-.34	.05	-.35	-.35
CPM	7	.10	.10	-.20	.10
INS	6	-.25	.08	-.20	-.20
PNM	6	.18	.05	-.10	.20
LED	3	-.32	.07	-.20	-.30
SHH	6	-.09	.08	-.05	-.10
GRP	6	-.23	.05	-.10	-.20
SPM	5	.13	.04	-.05	.15
IRN	5	.08	.10	.20	.10
CO2	6	.23	.06	.30	.25
BC2	8	.19	.03	.25	.20
LTC	8	.18	.04	.20	.20

Table 5-3 (continued)

6. South Pacific I (continued)

Station	N	Obs.	S.D.	Model 1	Model 2
ROD	1	-.41		-.45	-.40
SBCC	3	.01	.10	-.05	0.0
SBLP	8	.11	.05	.10	.10
SBSM	3	.20	.04	.20	.20
SBLC	10	.01	.07	-.15	0.0
SBSC	7	.01	.04	-.05	0.0
SBAI	5	.07	.03	-.05	-.05
SBSN	4	-.09	.12	-.10	-.10
ECF*	5	-.18	.10	-.30	-.25
SBCD*	7	.01	.07	-.30	-.10
CAM*	1	-.05		-.45	-.15
SBLG	4	-.28	.07	-.45	-.35
SIP	11	-.21	.07	-.45	-.25
KYP	3	-.23	.09	-.15	-.25
SAD	2	-.22	.06	-.10	-.25
PTD	1	0.0		0.0	-.20
CJP	4	-.44	.10	-.40	-.45
CLP	3	-.34	.05	-.30	-.35
CCM	6	-.09	.06	.20	.20
AMS*	2	.39	.01	.40	.45
WLK*	1	.31		.35	.30
SUP*	7	.05	.10	.20	.20
CRR*	5	-.19	.08	.10	-.05
COK*	3	.20	.02	.20	.20
SGL*	7	-.17	.09	-.10	-.10
ING*	2	.54	.09	.50	.50
SNR*	2	.55	.07	.45	.40
COA*	8	.43	.07	.45	.40
RUN*	6	.36	.04	.35	.35
BON*	2	.22	.08	.25	.25
BCK*	2	.26	.04	.25	.25
PLT*	4	.06	.12	.25	.20
SLU*	2	.30	.08	.30	.30
LHU	1	-.19		-.30	-.30
CRG	2	.55	.01	.45	.45
BCH	2	.40	.03	.40	.40
ABL	2	-.02	.01	-.10	0.0
TMB	2	.44	.04	.35	.35
YEG	2	.46	0	.50	.45
RYS	2	.39	.03	-.10	.10
BMT	2	.13	.03	.10	.10
FTC	1	-.04		-.05	-.05
PKM	1	.15		.10	.20

Table 5-3 (continued)

7. South Pacific II, Azimuths $\gtrsim$ 235°

Station	N	Obs.	S.D.	GSC = -.20	Model 1	Model 2
SYP	21	.22	.08		.15	.20
ISA*	16	-.05	.04		-.05	-.05
CLC	12	.15	.04		-.05	.10
SBB	19	-.30	.03		-.30	-.25
CSP	15	-.22	.04		-.50	-.45
RVR	16	-.25	.04		-.25	-.25
PEC	20	-.20	.04		-.25	-.15
TPC	17	.10	.06		-.10	.15
PLM	21	.11	.04		.05	.10
VST	14	-.11	.04		0.0	-.05
CPE	17	.02	.03		.10	.05
SCI*	18	.10	.07		.10	.10
IKP	18	.24	.07		.25	.25
GLA*	22	.72	.06		.70	.65
SNS*	13	.04	.03		-.05	.10
SJQ*	8	-.06	.08		-.05	0.0
CIS*	17	-.10	.04		-.10	-.10
VPD*	19	-.20	.06		-.15	-.20
TCC*	1	-.35			-.20	-.30
MWC	18	-.16	.03		-.30	-.30
PAS	17	-.14	.03		-.15	-.15
SCY	13	-.21	.06		-.20	-.20
TWL*	10	-.58	.06		-.55	-.60
IRC	10	-.47	.06		-.45	-.45
SWM	9	.01	.08		-.10	-.05
PYR	17	.17	.06		-.10	0.0
CKC	10	.16	.08		-.30	-.30
MLL	11	-.03	.06		-.30	-.25
CFT	13	.13	.06		-.30	-.10
MDA	9	.02	.05		-.25	-.10
RAY	14	.13	.07		-.30	-.10
WWR	5	.01	.02		-.25	.05
VGR	3	-.03	.03		-.20	-.10
DB2	11	-.31	.04		-.30	-.30
PSP	7	-.25	.09		-.20	-.25
KEE	14	-.13	.04		-.15	-.15
DVL	2	-.23	.03		-.50	-.30
COY	8	.14	.07		.05	.10
SMO	1	-.10			-.10	-.10
HOT	5	.15	.09		-.05	.10
LRR	5	-.21	.06		-.25	-.30
TPO	7	-.11	.04		-.05	-.10
THR	2	-.15	.06		-.25	-.20
SDW	6	-.64	.03		-.50	-.60

Table 5-3 (continued)

7. South Pacific II (continued)

Station	N	Obs.	S.D.	Model 1	Model 2
BLU	14	-.34	.07	-.40	-.35
ADL*	1	-.26		-.40	-.25
PEM	8	-.42	.06	-.40	-.40
RDM	6	-.29	.07	-.60	-.35
PCF	1	-.20		-.20	-.20
BTL	7	-.19	.01	-.40	-.20
SIL	7	-.15	.07	-.35	-.30
SSK	10	-.33	.04	-.35	-.30
SSV	8	-.42	.02	-.40	-.40
GAV	3	-.42	.05	-.40	-.45
SME	14	-.30	.04	-.25	-.25
STP	2	.50	.08	.40	.50
CHM	11	.33	.07	.40	.35
TTM	14	.43	.05	.30	.30
WH2	15	.33	.05	.35	.35
BPK	8	.29	.08	.30	.30
RVS	19	.28	.05	0.0	.20
LTM	12	.39	.09	.40	.30
BMM	6	.25	.05	0.05	.15
PIC	9	.77	.06	.60	.45
LGA*	6	.62	.04	.50	.45
FTM*	9	.66	.08	.60	.40
YMD*	15	.40	.05	.45	.45
RMR	19	-.21	.07	-.30	-.30
HDG	19	-.44	.06	-.35	-.40
CPM	18	.11	.06	-.20	.20
INS	16	-.34	.08	-.20	-.20
PNM	18	.28	.07	-.05	.30
LED	11	-.24	.04	-.20	-.25
SHH	15	.17	.07	.10	.15
GRP	16	-.09	.04	.05	-.10
SPM	13	.01	.07	-.05	.05
IRN	15	.22	.07	.15	.15
CO2	18	.29	.05	.30	.20
BC2	19	.27	.04	.30	.30
LTC	14	.37	.04	.30	.35
ROD	9	-.40	.05	-.30	-.35
SBCC	9	.36	.06	.15	.30
SBLP	10	.28	.08	.30	.30
SBSM	9	.24	.04	.30	.25
SBLC	15	.14	.04	0.0	.05
SBSC	14	.05	.03	.10	.05
SBAI	5	-.27	.04	-.20	-.20
SBSN	4	.27	.04	.30	.15
ECF*	9	.04	.07	-.10	-.10
SBCD*	7	.06	.09	-.20	-.05
CAM*	3	-.21	.02	-.30	-.20
SBLG	6	-.33	.04	-.40	-.30

Table 5-3 (continued)

7. South Pacific II, (continued)

Station	N	Obs.	S.D.	Model 1	Model 2
SIP	9	-.23	.06	-.30	-.25
KYP	5	-.36	.03	-.30	-.35
SAD	11	-.13	.06	-.05	-.30
PTD	7	-.10	.05	-.05	-.15
CJP	6	-.15	.05	-.20	-.15
CLP	6	-.22	.05	-.20	-.20
CCM	8	.30	.02	.35	.30
OBB*	4	.50	.08	.40	.20
AMS*	8	.54	.09	.50	.50
WLK*	2	.28	.01	.30	.30
SUP*	13	.30	.05	.30	.30
CRR*	12	.37	.08	.45	.15
COK*	3	.29	.04	.30	.30
SGL*	15	.14	.05	.20	.30
ING*	4	.66	.09	.70	.60
SNR*	3	.31	.07	.40	.20
COA*	13	.64	.04	.55	.40
RUN*	10	.45	.02	.45	.45
BON*	2	.35	.01	.35	.35
BCK*	3	.41	.04	.40	.35
PLT*	13	.48	.07	.50	.40
SLU*	2	.35	.01	.35	.35
LHU	7	-.05	.03	-.05	-.05
CRG	5	.63	.02	.50	.60
BCH	6	.48	.04	.50	.50
ABL	7	-.02	.03	.05	.05
TMB	5	.50	.03	.50	.40
YEG	8	.42	.05	.50	.45
RYS	8	.42	.03	.15	.20
BMT	7	.22	.04	.20	.25
FTC	1	.06		.05	.05
PKM	9	.25	.04	.20	.25

8. Central Pacific

Station	N	Obs.	S.D.	GSC =	Model 1 -.25	Model 2 -.20
SYP	14	.23	.06		0.05	.20
ISA*	14	-.46	.08		-.40	-.45
CLC	10	-.11	.04		-.10	-.10
SBB	16	0.0	.04		-.05	0.0
CSP	10	-.10	.04		-.40	-.35
RVR	15	-.08	.05		-.20	-.15
PEC	10	-.13	.04		-.25	-.10
TPC	13	-.07	.06		-.20	.10
PLM	14	.11	.04		-.05	.10

Table 5-3 (continued)

8. Central Pacific (continued)

Station	N	Obs.	S.D.	GSC =	Model 1 -.25	Model 2 -.20
VST	14	.10	.06		.15	.10
CPE	10	.25	.07		.30	.25
SCI*	9	.37	.05		.20	.35
IKP	7	.52	.07		.45	.40
GLA*	13	.69	.05		.70	.60
SNS*	8	.22	.07		.10	.20
SJQ*	2	.16	.04		.10	.10
CIS*	10	.26	.07		.20	.25
VPD*	13	-.27	.05		-.10	-.25
MWC	14	-.12	.06		-.40	-.20
PAS	13	.01	.05		-.10	-.20
SCY	6	-.02	.10		-.10	-.10
TWL*	6	-.16	.04		-.40	-.25
IRC	10	-.04	.11		-.20	-.25
SWM	5	.27	.04		.05	.15
PYR	7	.18	.05		0.0	.10
CKC	3	.18	.04		-.30	-.30
MLL	4	-.27	.06		-.30	-.25
CFT	6	.02	.05		-.30	-.20
MDA	6	0.0	.08		-.25	-.15
RAY	11	-.13	.05		-.25	-.15
WWR	9	.09	.04		-.25	.10
VGR	5	-.31	.08		-.30	-.30
DB2	14	-.39	.05		-.35	-.40
PSP	13	-.23	.06		-.15	-.25
KEE	7	-.32	.06		-.15	-.25
DVL	1	-.30			-.35	-.35
COY	4	-.02	.08		0.0	0.0
HOT	1	-.05			-.05	-.05
LRR	5	.08	.06		-.25	-.20
TPO	4	.14	.09		.15	.10
SDW	7	-.29	.07		-.30	-.35
BLU	10	-.31	.06		-.35	-.35
ADL*	3	-.22	.07		-.25	-.25
PEM	6	-.35	.06		-.35	-.35
RDM	1	-.38			-.55	-.45
BTL	7	-.41	.05		-.45	-.35
SIL	8	-.42	.06		-.40	-.40
SSK	8	-.34	.01		-.35	-.35
SSV	5	-.47	.07		-.45	-.45
GAV	6	-.25	.05		-.25	-.25
SME	5	-.25	.05		-.25	-.15
STP	3	.55	.06		.45	.55
CHM	5	.29	.08		.35	.30
TTM	9	.44	.11		.30	.40

Table 5-3 (continued)

8. Central Pacific (continued)

Station	N	Obs.	S.D.	Model 1	Model 2
WH2	13	.30	.06	.35	.30
BPK	11	.26	.06	.30	.25
RVS	8	.29	.08	.20	.25
LTM	11	.16	.05	.20	.15
BMM	9	.20	.06	.05	-.05
PIC	11	.67	.05	.60	.60
LGA*	6	.76	.06	.75	.40
FTM*	7	.70	.06	.70	.40
YMD*	8	.70	.06	.50	.60
RMR	12	-.40	.06	-.40	-.40
HDG	12	-.50	.06	-.40	-.35
CPM	14	-.16	.06	-.20	-.10
INS	12	-.22	.06	-.25	-.10
PNM	14	.14	.04	.10	.15
LED	8	-.30	.05	-.20	-.25
SHH	9	-.11	.08	-.10	-.05
GRP	8	-.10	.04	0.5	-.10
SPM	10	-.23	.07	-.10	.05
IRN	13	-.05	.06	.05	0.0
CO2	13	.27	.05	.30	.25
BC2	14	.27	.08	.30	.25
LTC	11	.26	.08	.20	.25
ROD	2	-.42	.01	-.30	-.35
SBCC	7	.17	.08	.15	.20
SBLP	8	.16	.04	.15	.15
SBLC	9	.02	.05	0.0	.10
SBSC	4	.01	.09	-.05	-.05
SBAI	1	-.24		-.25	-.20
SBSN	8	.04	.05	.05	.10
ECF*	8	-.04	.06	-.15	-.05
SBCD*	6	-.09	.11	-.20	-.10
CAM*	4	-.07	.10	-.25	-.10
SBLG	3	-.13	.01	-.55	-.15
SIP	5	-.15	.16	-.40	-.25
KYP	3	-.26	.08	-.40	-.25
SAD	4	-.27	.06	-.30	-.25
PTD	2	.14	.01	-.15	-.20
CJP	1	-.12		-.20	-.20
CCM	8	.30	.04	.40	.35
OBB*	1	.41		.40	.30
AMS*	1	.50		.50	.45
SUP*	14	.38	.06	.35	.35
CRR*	12	.17	.05	.35	.15
COK*	1	.36		.35	.35
SGL*	14	.20	.06	.20	.20
ING*	1	.81		.75	.75
COA*	7	.61	.07	.50	.45

Table 5-3 (continued)

8. Central Pacific (continued)

Station	N	Obs.	S.D.	Model 1	Model 2
RUN*	6	.60	.09	.60	.60
BON*	2	.06	.05	.25	.25
BCK*	1	.45		.45	.35
PLT*	12	.40	.07	.40	.40
SLU*	3	.42	.07	.40	.40
LHU	2	.14	.06	-.05	.15
CRG	4	.67	.05	.60	.60
BCH	3	.32	.05	.30	.35
ABL	3	.12	.12	.15	.15
TMB	2	.50	.04	.45	.40
YEG	3	.46	.03	.50	.50
RYS	3	.31	.03	.15	.30
BMT	3	.34	.04	.20	.35
PKM	4	.19	.06	.20	.20

9. North Pacific I, Azimuths $\lesssim$ 305°

Station	N	Obs.	S.D. GSC ≡ 0.0	Model 1	Model 2
SYP	10	.16	.06	.15	.15
ISA*	17	-1.13	.05	-1.00	-1.05
CLC	8	-.06	.10	-.10	-.05
SBB	12	-.08	.05	-.10	-.10
CSP	10	-.36	.04	-.50	-.40
RVR	10	-.65	.05	-.65	-.70
PEC	13	-.52	.04	-.50	-.55
TPC	10	-.56	.08	-.50	-.55
PLM	12	-.50	.07	-.45	-.45
VST	10	-.27	.06	-.30	-.25
CPE	9	-.21	.04	-.20	-.25
SCI*	3	-.07	.12	-.15	-.10
IKP	10	.03	.03	0.0	-.05
GLA*	13	.33	.05	.25	.10
SNS*	8	-.14	.04	-.30	-.15
SJQ*	2	.08	.04	-.25	-.10
CIS*	8	-.27	.08	-.30	-.20
VPD*	10	-.50	.04	-.50	-.50
TCC*	3	-.72	.04	-.70	-.65
MWC	13	-.40	.07	-.60	-.45
PAS	8	-.23	.06	-.65	-.50
SCY	3	-.21	.12	-.55	-.50
TWL*	12	-.10	.10	-.25	-.30
IRC	13	-.08	.17	-.25	-.25
SWM	4	.02	.03	-.05	-.05

Table 5-3 (continued)

9. North Pacific I (continued)

Station	N	Obs.	S.D.	Model 1	Model 2
PYR	13	.07	.13	.05	.05
CKC	1	-.08		-.65	-.70
MLL	3	-.65	.09	-.65	-.70
CFT	4	-.31	.10	-.65	-.50
MDA	7	-.37	.08	-.55	-.40
RAY	6	-.83	.06	-.70	-.80
WWR	2	-.66	.05	-.60	-.65
VGR	2	-.47	.07	-.55	-.55
DB2	6	-.59	.05	-.55	-.50
PSP	4	-.59	.04	-.50	-.45
KEE	7	-.39	.04	-.50	-.40
COY	3	-.44	.05	-.35	-.40
SMO	3	-.33	.10	-.35	-.25
HOT	3	-.38	.06	-.35	-.40
LRR	4	-.10	.05	-.20	-.15
TPO	6	.14	.09	-.05	.15
THR	2	-.02	.03	-.10	.05
SDW	5	-.51	.10	-.50	-.45
BLU	6	-.18	.07	-.50	-.25
ADL*	3	-.15	.08	-.15	-.15
PEM	3	-.66	.09	-.65	-.65
RDM	3	-.34	.07	-.50	-.50
BTL	4	-.43	.08	-.65	-.45
SIL	6	-.51	.07	-.60	-.50
SSK	6	-.68	.09	-.70	-.65
SSV	1	-.61		-.65	-.60
GAV	5	-.82	.06	-.75	-.75
SME	5	-.61	.03	-.55	-.60
STP	3	.27	.13	.20	.20
CHM	3	.20	.07	.15	.15
TTM	8	.18	.06	.20	.25
WH2	7	-.18	.09	.05	-.15
BPK	4	.19	.05	-.05	.15
RVS	7	.14	.08	.15	.15
LTM	12	0.0	.06	0.0	0.0
BMM	4	.14	.11	-.05	.15
PIC	9	.24	.04	.25	.15
LGA*	5	.24	.05	.25	.20
FTM*	6	.05	.01	.05	.05
YMD*	5	.05	.04	.05	.05
RMR	9	-.59	.06	-.55	-.55
HDG	9	-.52	.08	-.50	-.45
CPM	10	-.53	.06	-.50	-.55
INS	12	-.54	.06	-.50	-.40
PNM	10	-.46	.08	-.35	-.40
LED	7	-.37	.06	-.35	-.35

Table 5-3 (continued)

9. North Pacific I (continued)

Station	N	Obs.	S.D.	Model 1	Model 2
SHH	16	-.44	.05	-.35	-.30
GRP	8	-.17	.08	-.15	-.15
SPM	6	-.10	.03	-.10	-.10
IRN	10	-.12	.08	-.15	-.10
CO2	11	-.15	.09	-.15	-.15
BC2	11	-.12	.05	-.10	-.10
LTC	9	-.15	.03	-.05	-.10
ROD	4	-.27	.08	-.35	-.25
SBCC	8	.20	.06	.20	.20
SBLP	6	-.12	.07	-.15	-.15
SBSM	6	-.11	.02	-.10	-.10
SBLC	8	.02	.07	.05	.05
SBSC	4	-.23	.13	-.25	-.25
SBSN	5	-.03	.09	-.20	-.05
ECF*	5	-.05	.05	-.25	-.05
SBCD*	3	-.01	.05	-.05	0.0
CAM*	3	-.21	.03	-.25	-.25
SBLG	6	-.26	.06	-.50	-.30
SIP	8	-.03	.04	-.35	-.30
KYP	5	-.41	.09	-.50	-.40
SAD	3	-.56	.04	-.65	-.60
PTD	1	-.05		-.70	-.60
CJP	1	-.04		-.45	-.30
CLP	1	-.27		-.40	-.30
CCM	5	.15	.06	.20	.15
OBB*	3	.05	.03	.10	.05
AMS*	7	.22	.10	.25	.20
WLK*	1	.23		.25	.25
SUP*	9	-.10	.07	-.10	-.10
CRR*	7	-.02	.03	-.05	-.05
COK*	2	.05	.03	.05	.05
SGL*	11	-.13	.05	-.15	-.15
ING*	4	.46	.04	.45	.45
SNR*	2	.22	.01	.25	.20
COA*	6	.27	.06	.35	.25
RUN*	5	.18	.06	.20	.20
BON*	3	.13	.01	.20	.20
BCK*	1	.08		.10	.30
PLT*	8	.42	.09	.35	.35
SLU*	3	.36	.07	.20	.20
LHU	3	.03	.05	-.05	.05
CRG	3	.29	.05	.30	.30
BCH	4	.21	.09	.25	.20
ABL	3	-.14	.07	-.15	-.15
TMB	3	.39	.07	.20	.35
YEG	4	.28	.08	.35	.25

Table 5-3 (continued)

9. North Pacific I (continued)

Station	N	Obs.	S.D.	Model 1	Model 2
RYS	5	.24	.05	-.05	.10
BMT	3	.01	.08	-.05	0.0
FTC	4	-.12	.02	-.10	-.10
PKM	4	.22	.07	-.25	.25

10. North Pacific II, Azimuths $\gtrless$ 305°

Station	N	Obs.	S.D. GSC ≡0.0	Model 1	Model 2
SYP	14	.03	.05	.05	.05
ISA*	18	-1.20	.05	-1.10	-1.15
CLC	14	.03	.05	-.05	.05
SBB	22	.02	.04	.05	.05
CSP	14	-.08	.07	-.55	-.30
RVR	15	-.70	.05	-.70	-.70
PEC	17	-.65	.05	-.65	-.65
TPC	17	-.50	.05	-.50	-.50
PLM	19	.33	.06	-.35	-.35
VST	14	-.37	.06	-.30	-.30
CPE	17	-.30	.03	-.25	-.30
SCI*	12	-.02	.08	-.10	-.10
IKP	12	-.15	.04	-.10	-.15
GLA*	19	-.33	.05	.30	.20
SNS*	12	-.16	.04	-.35	-.35
SJQ*	2	-.50	.03	-.40	-.45
CIS*	13	-.19	.06	-.20	-.20
VPD*	19	-.47	.10	-.50	-.50
TCC*	3	-.79	.03	-.70	-.65
MWC	16	-.27	.05	-.60	-.35
PAS	15	-.33	.05	-.60	-.50
SCY	14	-.57	.07	-.60	-.60
TWL*	16	-.11	.05	-.30	-.30
IRC	17	-.07	.03	-.15	-.15
SWM	13	.18	.06	.10	.10
PYR	12	.23	.05	.15	.15
CKC	4	-.41	.05	-.75	-.85
MLL	3	-.59	.04	-.65	-.65
CFT	3	-.47	.02	-.70	-.80
MDA	6	-.57	.06	-.60	-.60
RAY	8	-.71	.05	-.65	-.70
WWR	3	-.64	.08	-.55	-.60
VGR	4	-.54	.07	-.55	-.55
DB2	10	-.64	.07	-.55	-.60
PSP	7	-.68	.02	-.55	-.60
KEE	6	-.53	.06	-.50	-.45
COY	8	-.29	.05	-.30	-.25

Table 5-3 (continued)

10. North Pacific II (continued)

Station	N	Obs.	S.D.	Model 1	Model 2
SMO	3	-.36	.04	-.35	-.35
HOT	8	-.26	.05	-.35	-.35
LRR	9	-.01	.05	-.15	-.05
TPO	8	-.03	.06	-.05	-.05
THR	2	.06	.01	.05	.05
SDW	10	-.17	.04	-.15	-.20
BLU	11	.04	.03	-.40	-.20
ADL*	6	.10	.12	.10	.10
PEM	2	-.56	0	-.65	-.55
RDM	4	-.42	.07	-.50	-.40
PCF	1	-.65		-.55	-.65
BTL	7	-.46	.02	-.65	-.45
SIL	7	-.32	.04	-.55	-.40
SSK	8	-.53	.09	-.60	-.45
SSV	4	-.55	.03	-.60	-.45
GAV	6	-.71	.04	-.65	-.65
SME	11	-.62	.08	-.55	-.60
STP	2	.34	.05	.30	.35
CHM	9	-.03	.05	0.0	-.05
TTM	12	.35	.07	.30	.30
WH2	11	-.06	.06	.10	-.05
BPK	7	.09	.04	-.05	-.05
RVS	13	.35	.06	.30	.30
LTM	6	.08	.10	.05	.05
BMM	2	.16	.02	-.05	.15
PIC	11	.12	.07	.20	-.05
LGA*	4	-.09	.05	.10	-.05
FTM*	11	-.11	.06	0.0	-.10
YMD*	10	-.05	.05	.05	-.05
RMR	18	-.51	.07	-.50	-.50
HDG	14	-.27	.05	-.40	-.20
CPM	16	-.43	.05	-.40	-.40
INS	12	-.67	.06	-.60	-.65
PNM	16	-.58	.06	-.40	-.45
LED	9	-.09	.03	-.10	-.10
SHH	15	-.33	.04	-.30	-.25
GRP	14	-.07	.06	-.05	-.10
SPM	12	.14	.07	.15	.10
IRN	13	.05	.06	.05	.05
CO2	16	-.33	.04	-.20	-.30
BC2	13	-.37	.05	-.20	.05
LTC	10	-.32	.04	-.15	-.15
ROD	9	-.16	.04	-.25	-.15
SBCC	8	-.13	.03	.15	.15
SBLP	2	-.19	.08	-.10	-.15
SBSM	5	-.08	.04	-.05	-.10

Table 5-3 (continued)

10. North Pacific II (continued)

Station	N	Obs.	S.D.	Model 1	Model 2
SBLC	9	-.01	.05	.05	0.0
SBSC	5	-.45	.06	-.45	-.35
SBAI	2	-.49	.01	-.50	-.40
SBSN	7	-.26	.04	-.20	-.25
ECF*	8	-.22	.03	-.20	-.20
SBCD*	8	-.10	.04	-.10	-.10
CAM*	3	-.18	.06	-.30	-.20
SBLG	7	-.31	.05	-.40	-.30
SIP	12	-.31	.05	-.30	-.30
KYP	7	-.50	.05	-.45	-.40
SAD	4	-.52	.02	-.50	-.45
PTD	5	-.43	.04	-.70	-.45
CJP	1	-.31		-.35	-.35
CLP	2	-.54	.01	-.50	-.50
CCM	7	.03	.04	.15	.05
OBB	2	.05	.02	.10	.05
AMS*	9	.22	.04	.30	.20
WLK*	3	.18	.06	.40	.20
SUP*	14	-.41	.04	-.20	-.35
CRR*	13	-.18	.06	-.10	-.20
COK*	4	.01	.05	.05	-.05
SGL*	13	-.21	.05	-.10	.05
ING*	8	.37	.03	.45	.35
SNR*	3	.23	.08	.25	.25
COA*	6	.22	.02	.20	.20
RUN*	5	.24	.06	.20	.25
BON*	3	.31	.04	.30	.30
BCK*	2	.39	.04	.45	.35
PLT*	13	.10	.05	.20	.10
SLU*	6	-.07	.08	.10	.05
LHU	6	-.05	.03	-.05	-.05
CRG	5	.36	.05	.35	.35
BCH	5	.21	.05	.30	.20
ABL	4	-.14	.03	-.10	-.15
TMB	5	.33	.06	.25	.30
YEG	6	.30	.06	.35	.30
RYS	7	-.08	.03	-.05	-.05
BMT	7	-.37	.04	-.30	-.35
FTC	6	-.25	.04	-.15	-.20
PKM	8	.24	.04	.30	.30

Table 5-3 (continued)

11. Aleutians - Alaska

Station	N.	Obs.	S.D.	GSC ≡ 0.0	Model 1	Model 2
SYP	3	-.08	.05		-.05	-.10
ISA*	6	-.89	.10		-.90	-.90
SBB	7	-.18	.12		-.20	-.15
CSP	4	.18	.06		-.15	-.20
RVR	2	-.62	.05		-.75	-.65
PEC	7	-.55	.05		-.75	-.65
TPC	6	-.33	.05		-.35	-.35
PLM	7	-.26	.06		-.40	-.35
VST	3	-.25	.03		-.40	-.25
CPE	6	-.28	.04		-.30	-.30
SCI*	3	.04	.03		-.10	0.0
IKP	7	-.41	.09		-.35	-.25
GLA*	6	-.39	.04		-.25	-.35
SNS*	1	-.28			-.30	-.30
SJQ*	3	-.73	.02		-.75	-.65
CIS*	4	-.19	.07		-.25	-.30
VPD*	5	-.72	.05		-.75	-.70
MWC	6	-.29	.04		-.25	-.30
PAS	4	-.26	.05		-.35	-.35
SCY	1	-.56			-.55	-.45
TWL*	5	-.08	.07		-.15	-.05
IRC	4	-.02	.03		-.05	-.05
PYR	6	.28	.05		.20	.20
CKC	2	-.26	.11		-.60	-.60
MLL	2	-.34	.10		-.80	-.60
WWR	1	-.20			-.60	-.50
DB2	3	-.63	.02		-.75	-.70
PSP	1	-.52			-.70	-.60
KEE	1	-.74			-.75	-.70
DVL	2	-.40	.01		-.40	-.35
BLU	1	.07			-.10	-.05
ADL	1	.31			.20	.20
SME	2	-.68	.03		-.75	-.75
STP	1	.27			0.0	.30
TTM	4	-.29	.07		.10	-.10
WH2	2	-.08	.05		-.10	.10
RVS	5	-.47	.04		.10	0.0
LTM	3	-.34	.05		-.25	-.05
BMM	4	-.59	.06		0.05	0.0
PIC	1	.08			.10	0.0
LGA*	1	.16			.10	.15
FTM*	1	.23			.20	0.05
RMR	4	-.42	.06		-.60	-.45
HDG	5	-.46	.07		-.40	-.30
CPM	5	-.66	.07		-.65	-.50
INS	5	-1.04	.04		-.80	-.60

Table 5-3 (concluded)

11. Aleutians - Alaska (continued)

Station	N	Obs.	S.D.	Model 1	Model 2
PNM	4	-.56	.04	-.60	-.45
LED	4	-.35	.04	-.40	-.25
SHH	4	-.86	.07	-.45	-.45
GRP	5	-.51	.05	-.35	-.45
IRN	7	-.69	.06	-.30	-.25
CO2	3	-.43	.04	-.45	-.25
BC2	2	-.66	.02	-.50	-.45
LTC	1	-.59		-.35	-.25
SBLP	1	.12		.10	.10
SBSM	1	-.09		-.10	-.10
SBLC	2	-.02	.04	-.05	-.05
SBSC	1	-.20		-.20	-.20
SBAI	2	-.32	.02	-.35	-.30
ECF*	1	-.03		-.05	-.05
SBCD*	2	0.0	.12	0.0	0.0
SBLG	2	-.36	.01	-.40	-.25
SIP	1	-.26		-.35	-.25
CJP	2	-.29	.02	-.35	-.30
CLP	1	-.54		-.50	-.50
AMS*	1	-.01		0.0	0.0
SUP*	3	-.23	.04	-.30	-.25
CRR*	2	-.13	.10	-.25	-.25
SGL*	3	-.08	.06	-.05	-.10
ING*	1	.29		.30	.30
COA*	1	-.08		.30	.10
RUN*	1	-.09		.15	-.10
PLT*	3	.11	.02	.15	.10
SLU*	2	-.41	0	.15	.15

Table 5-4

MEAN MISFITS FOR A GIVEN SOURCE REGION

Region	Mean S.D. at one station, sec.	Mean misfit, sec Model 1	Model 2	Comments
Java Trench	--	-.02	0.0	BLU, PYR, PAS slow
Novaya Zemlya	.04	-.04	-.02	TPC, CPM area slow ISA, DB2, SME fast
Leeward Is.	.06	-.09/.01	-.01	Model 1 fits better with GSC .1 sec early I.V. + S. Barb fast.
South America I	.06	-.05	-.01	Model 1 fits slightly better if GSC early. IV fast.
South America II	.07	-.02	.02	I.V., TPO, BMT, SBLP fast, W. L.A.B slow
South Pacific I	.06	-.04	-.02	I.V., S. Barb slow
South Pacific II	.05	-.06	-.03	Main misfit for model 1 is area between S.A. & S.J. faults. (Other stations, -.03)
Central Pacific	.06	-.05	-.03	S. Barb, area between faults slow.
North Pacific I	.06	-.06	-.02	L.A.B. slow, C. Mojave fast.
North Pacific II	.05	.04	0.0	
Aleutians-Alaska	.05	.01	.04	Much of Mojave fast.

Note: I.V. = Imperial Valley; S. Barb = Santa Barbara net,
L.A.B. = Los Angeles Basin

Table 5-5

MEAN MISFIT FOR A GIVEN STATION

Station	Mean S.D.	Mean misfit, sec. Model 1	Model 2	Comments
SYP	.06	.03	.09	Leeward Is fast
ISA*	.06	.04	.03	Fast to north
CLC	.05	-.01	0.0	
SBB	.05	-.02	0.0	
CSP	.05	-.31	-.24	All but Java Trench slow; effects of refraction
RVR	.06	-.02	-.03	
PEC	.05	-.06	-.01	Slower structure near San Jacinto fault?
TPC	.05	-.07	.03	Slow, Novaya Zemlya and South and Central Pacific
PLM	.07	-.06	-.06	Slow, Novaya Zemlya and Alaska
VST	.05	.03	.02	Fast, South Pacific
CPE	.06	.04	.01	
SCI*	.06	-.04	-.01	Slow, N. Pacific, C. Pacific
IKP	.06	-.01	-.01	
GLA*	.05	0.0	-.07	Model 2 needs extra shallow delay

(CIT Tele Network)

Table 5-5 (continued)

Station	Mean S.D.	Mean Misfit, sec. Model 1	Model 2	Comments
SNS*	.05	-.07	-.01	Model 1 needs added shallow delay
SJQ*	.05	-.04	-.01	Slow, Mariana-Bonin
CIS*	.06	-.06	0.0	Slow, Leeward, S. America (Model 1)
VPD*	.08	.01	-.02	
TCC*	.10	.05	.05	Fast, Novaya Zemlya, South Pacific, Japan-Kuril.
MWC	.06	-.14	-.07	Slow; crustal correction of .1-.15 needed
PAS	.06	-.13	-.11	Slow, especially N. Pacific. Crustal correction of .1-.15 sec.
SCY	.08	-.05	-.03	Slow, Marianas-Bonin and N. South America
TWL*	.07	-.08	-.05	Slow, S. America, N. Pacific. Larger sediment correction?
IRC	.06	-.07	-.05	Slow, S. America, N. Pacific. .1 sec crustal correction?
SWM	.05	-.07	-.04	Slow, S. and C. Pacific.
PYR	.06	-.07	-.02	Fast, Leeward Is.; slow S. Pacific. .05-.1 sec crustal correction

(CIT Los Angeles Basin Network)

Table 5-5 (continued)

Station	Mean S.D.	Mean misfit, sec. Model 1	Model 2	Comments
CKC	.06	-.46	-.36	Sediment/crustal correction of .30 sec required.
MLL	.06	-.26	-.16	Largely slow to S. Possibly .1 sec sediment/crustal correction
CFT	.06	-.35	-.15	Probable correction of .2 sec.
MDA	.07	-.16	-.06	Slow to west; effect of fault?
RAY	.06	-.09	-.03	Slow, Tonga-Fiji
WWR	.05	-.15	-.04	Slow, South and Central Pacific
VGR	.07	-.08	-.04	Crustal correction of .1 sec.
DB2	.05	.04	.02	
PSP	.07	.04	.03	Fast to west.
KEE	.05	0.0	.01	
DVL	.03	-.22	-.10	Slow, Novaya Zemlya and south. Probable .15 sec crustal correction
COY	.06	-.07	.01	
SMO	.06	-.02	.02	
HOT	.06	-.08	-.04	Possible .1 sec crustal correction

(San Bernardino SE Network)

Table 5-5 (continued)

Station	Mean S.D.	Mean misfit, sec. Model 1	Model 2	Comments
LRR	.05	-.13	-.09	.1 sec crustal correction
TPO	.07	.05	.09	Fast, S. America; slow, Japan (Model 1)
THR	.04	-.06	-.04	
SDW	.06	-.01	-.01	Slow, Leeward; fast, S. Pacific
BLU	.05	-.21	-.14	.15 sec crustal correction; slow, S. America, N. Pacific
ADL*	.08	-.08	-.04	Slow, S. America, Alaska
PEM	.05	-.08	-.02	Slow, S. America
RDM	.07	-.25	-.07	.1 sec crustal correction. Model 1 needs slow, shallow structure.
BTL	.05	-.36	-.16	Slow, except N. and Central Pacific. .15 sec correction -- ? elevation
SIL	.06	-.22	-.16	? .15 sec correction.
SSK	.06	-.03	-.01	Slow, Leeward
SSV	.05	-.03	.02	
GAV	.05	.02	.02	
SME	.05	.04	.04	Fast, Novaya Zemlya

(San Bernardino NW Network)

Table 5-5 (continued)

Station	Mean S.D.	Mean misfit, sec. Model 1	Model 2	Comments
STP	.07	-.08	0.0	Model 1, slow Aleutians
CHM	.06	.02	-.01	
TTM	.06	-.06	-.04	Aleutians fast; Leeward, S. Pacific slow
WH2	.06	.01	.01	
BPK	.09	-.03	-.03	Slow, N. Pacific
RVS	.07	.01	.02	Fast, Aleutians; slow, S. Pacific
LTM	.06	.02	.02	
BMM	.05	-.04	.02	Fast, Aleutians; slow, South and Central Pacific
PIC	.07	-.01	-.09	Model 2 needs extra shallow slow structure.
LGA*	.06	0.0	-.04	Model 2 slow South and Central Pacific
FTM*	.05	-.03	-.10	Model 2, slow South, Central Pacific and Aleutians
YMD*	.05	-.10	.02	Slow, Central Pacific

(Mojave-East Network)

Table 5-5 (continued)

Station	Mean S.D.	Mean misfit, sec. Model 1	Model 2	Comments
RMR	.06	-.14	-.09	Slow to south
HDG	.07	-.06	.01	Slow, South America
CPM	.06	-.12	0.0 S1	Slow, Leeward; Model 1, slow South Pacific
INS	.07	.04	.09	Fast, Aleutians
PNM	.06	-.04	.03	Model 1: slow Novaya Zemlya, South and Central Pacific; fast, N. Pacific (also Model 2)
LED	.06	.04	.03	
SHH	.06	.07	.07	Fast, Aleutians
GRP	.06	.09	.06	Model 1, fast to south. Model 2, fast South America
SPM	.06	.05	.14	Fast, South America, Central Pacific, Novaya Zemlya
IRN	.07	.07	.08	Fast, Novaya Zemlya, Aleutians
CO2	.05	.04	.04	Fast, southern S. America
BC2	.06	.04	.06	Fast, Japan, Aleutians
LTC	.05	.03	.05	Fast, Japan, Aleutians
ROD	.05	-.04	-.03	

(Mojave-West Network)

Table 5-5 (continued)

Station	Mean S.D.	Mean misfit, sec. Model 1	Model 2	Comments
SBCC	.06	-.01	.02	Fast, S. America; slow, Tonga-Fiji
SBLP	.06	.09	.09	Fast, Leeward, S. America
SBSM	.04	.01	.02	
SBLC	.05	.03	.06	Fast, Leeward; slow, S. Pacific (Model 1)
SBSC	.08	.03	.04	Fast, Leeward
SBAI	.04	0.0	.03	Fast, Leeward
SBSN	.06	0.0	-.01	
ECF*	.06	-.08	-.04	Slow, southern S. America, South Pacific
SBCD*	.07	-.08	-.05	Fast, Leeward. Additional .1 sec sediment correction
CAM*	.05	-.12	-.01	Slow, Kermadec
SBLG	.04	-.07	.04	Model 1, slow C. Pacific, Marianas
SIP	.06	-.07	-.01	Fast, Leeward. Model 1, slow Kermadec, C. Pacific, Marianas
KYP	.07	0.0	.02	
SAD	.05	-.01	-.02	
PTD	.05	-.28	-.24	Slow to north. Probable .25 sec sediment correction
CLP	.07	.01	.01	
CJP	.05	-.06	-.04	Slow, Marianas

(Santa Barbara Network)

Table 5-5 (continued)

Station	Mean S.D.	Mean misfit, sec. Model 1	Model 2	Comments
CCM	.05	.08	.05	Fast, south S. America, Kermadec
OBB*	.06	.01	-.04	Fast, south S. America. Model 2 slow, Central and South Pacific
AMS*	.05	.05	.03	Fast, Leeward, South America
WLK*	(.05)	.03	0.0	Model 1, fast, Japan
SUP*	.06	.05	.04	Fast, Leeward, south S. America, Kermadec
CRR*	.06	.05	-.01	Fast, southern S. America, Kermadec
COK*	.06	.03	.01	Fast, S. America
SGL*	.06	.02	.06	Fast, Japan
ING*	.06	.02	.02	Fast, S. America
SNR*	(.05)	.07	.05	Fast, Leeward, southern S. America
COA*	.06	.14	.10	Fast, Leeward, S. America, Aleutians
RUN*	.05	.15	.09	Fast, Leeward, S. America. Model 1 fast Aleutians.
BON*	(.05)	.05	.05	Fast, C. Pacific
BCK*	(.04)	.07	.10	Fast, S. America
PLT*	.08	.08	.04	Fast, S. America, Kermadec
SLU*	.06	.12	.13	Fast, S. America, Japan, Aleutians

(Imperial Valley Network)

Table 5-5 (concluded)

Station	Mean S.D.	Mean misfit, sec. Model 1	Model 2	Comments
LHU	.05	-.07	0.0	
CRG	.04	-.06	-.03	Possible .1 sec "sediment" correction
BCH	.05	0.0	.01	
ABL	.06	.05	.07	Fast, S. America
TMB	.04	-.06	-.05	Model 1, slow N. Pacific
YEG	.04	.01	.04	
RYS	.04	-.15	-.07	Slow, S. Pacific, Marianas. Also C. Pacific (Model 1)
BMT	.05	0.0	.05	
FTC	(.04)	.01	-.01	
PKM	.06	-.01	.03	

(Carrizo Plains Network)

sec) and CKC (0.3 sec). The last three are not unexpected, but no corrections were introduced initially because no good estimates of sediment thicknesses were available. Of the 1,232 data used, Model 1 fits 70% to 0.1 sec and 86% to 0.2 sec; Model 2 fits 77% to 0.1 sec and 87% to 0.2 sec. After the additional crustal corrections have been applied Model 1 fits 73% to 0.1 sec and 89% to 0.2 sec, and Model 2 78% to 0.1 sec and 88% to 0.2 sec. Model 1 may be further improved by the introduction of a shallow ($\sim$20-50 km) region of low velocity in the area indicated by Figure 5-5, which would add delays of up to 0.3 sec at the surrounding stations. The observation of low velocities in this region is consistent with the travel times for local earthquakes, which indicate a lower value of P_n in this region (Hadley, 1978, personal communication).

In all these models it was assumed that the change in ray path caused by the velocity variations was second order. The actual changes are hard to calculate precisely because of the complexity of the structure -- for horizontal layers, the changes will certainly be small, as was illustrated by Table 5-1(b). Calculations for a ray inclined at 20° to the vertical (a fairly typical angle for the depth and distance range under consideration) incident on an interface between materials of velocity 7.8 and 8.3 km/s dipping at 30 and 45° indicate that even when the ray is subparallel to the interface the change in path is such that the depth to the 8.3 km/s layer will be in error by less than 5 or 15 km, respectively, representing an error of about 0.1 sec at most. For dips approaching 70°, the change in depth is still $\sim$15 km if the ray approaches in the opposite direction to the dip, but when the ray approaches in the

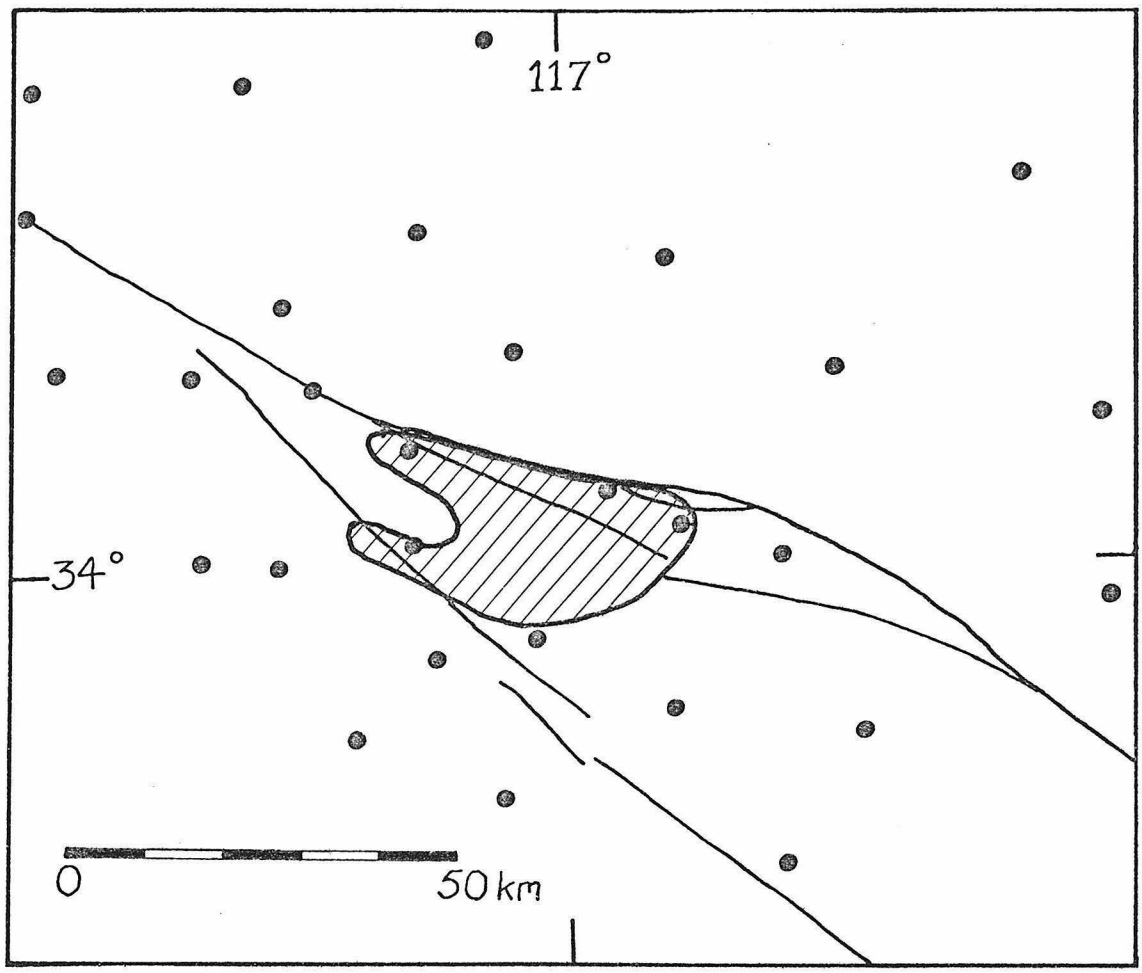

Figure 5-5. Location of the proposed region of low velocity between the San Andreas and San Jacinto faults (shaded area). The estimated depth of this anomaly is ∿20-50 km.

reverse direction, it is parallel to the interface, and large distortions may result, especially if the dip changes direction. The effects of refraction are thus expected to be most severe where the boundary is steeply dipping, and especially near local maxima or minima in the depth to the high velocity region, such as near SBLG and CSP.

5.3. Models Obtained by Inversion

The inversion technique used in this study was the damped least squares or stochastic inverse whose application to this type of problem was developed by Aki and others. The method is described in detail by Aki et al. (1977), Aki et al.,(1976) and Husebye et al. (1976) who applied it to the determination of lithospheric structure beneath NORSAR, LASA Montana, and Central California; their computer programme was used, and the technique will only be discussed briefly here.

The velocity perturbations $\underline{m}$ to the initial model are given by the solution of

$$\underline{r} = \underline{\underline{A}}\,\underline{m} + \underline{e} \qquad (1)$$

where $\underline{r}$ is a vector containing the residual data, $\underline{\underline{A}}$ is a matrix containing the partial derivatives of travel time along each ray with respect to the velocity perturbations, and $\underline{e}$ contains higher order and error terms. Let

$$\underline{\underline{A}}^T\ \underline{\underline{A}} = \underline{\underline{G}} \qquad (2)$$

then (1) becomes, to first order,

$$\underline{\underline{G}}\,\underline{m} = \underline{\underline{A}}^T\ \underline{r} \qquad (3)$$

A least squares solution to (3) fails because $\underline{\underline{G}}$ contains one zero eigenvalue for each layer in the initial model (Aki et al., 1977).

A generalised inverse solution would be possible, but requires the decomposition of $\underline{\underline{G}}$ into its eigenvalues and eigenvectors, which is rather costly for the rank (typically $\sim$200) of matrix involved. The damped least squares method (Levenberg, 1944) is an alternative which may be used to approximate the general inverse, and only requires an elimination algorithm for its solution. The damped least squares solution to (3) is given by

$$\underline{\hat{m}} = (\underline{\underline{G}} + \theta^2 \underline{\underline{I}})^{-1} \underline{\underline{A}}^T \quad r \qquad (4)$$

where $\underline{\hat{m}}$ is an approximate solution of (1), θ^2 is a (positive) damping constant and $\underline{\underline{I}}$ the identity matrix. The resolution matrix corresponding to this solution is

$$\underline{\underline{R}} = (\underline{\underline{G}} + \theta^2 \underline{\underline{I}})^{-1} \underline{\underline{G}} \qquad (5)$$

The initial model consists of a number of plane parallel layers each having a constant velocity, and each of which is divided into an array of right rectangular prisms, for which the velocity perturbations $\underline{\hat{m}}$ are sought. It is assumed that residual variations arise solely from differences within the upper mantle beneath the array; outside this finite region the velocity structure is assumed to be known. The residuals are first calculated with respect to the theoretical J-B arrival time, as described in Chapter 2, and then they are normalised by subtracting the mean residual to minimise effects such as source mislocation. Ray paths through the layered structure are computed for each station-event pair, and the procedure is simplified by assigning the entire ray path in each layer to the block in which the ray spends the most time. This also has the effect of smoothing artificial boundaries in the model introduced by the vertical sides of the blocks.

In order to determine successfully the laterally varying upper mantle structure, good distribution of rays through the blocks is needed. This is helped by having uniform azimuthal coverage, which is unfortunately not entirely true for the Caltech array, which has poor coverage between 5 and 90° and 150 and 225°. The optimal mixing of ray paths and blocks occurs if the block size is chosen such that the vertical and horizontal travel times through any element are equal. An appropriate selection for teleseisms is a ratio of vertical to horizontal length of 2:1 (Ellsworth and Koyanagi, 1977); a ratio of less than this will increase vertical linkage between blocks thus degrading the resolution. The average velocity in each layer is indeterminate when relative residuals are used because changes in the mean travel time through the model cannot be separated from changes in origin time; the mean velocity in each layer is consequently held constant.

As discussed in Section 5.1, the application of this inversion technique to the Southern California set meets with some problems owing to the size and changeability of the array. The eighty-eight stations that were selected for use in this study are given in Table 5-6, and also on the map of Figure 5-6; note in particular that most of the Carrizo Plains and Imperial Valley stations had too few arrivals to be included, and that stations such as CKC and CFT, which defined the anomalously slow area between the San Andreas and San Jacinto faults for the models of the last section, are also omitted. A total of seventy-four events, listed in Table 5-7, was chosen for use in the inversion; they are fairly well distributed among the available azimuths, but no event with azimuth greater than 318° had sufficient first arrivals to be included.

Table 5-6

LIST OF STATIONS USED IN THE INVERSION STUDY

SYP	MLL	CPM	SGL
ISA*	MDA	INS	COA
CLC*	RAY*	PNM	RUN
GSC*	DB2	LED	PLT
SBB	PSP	SHH	YEG*
CSP*	KEE	GRP*	BCH
RVR	COY	SPM	PKM
PEC	LRR	IRN	ABL*
TPC*	TPO	CO2	RYS
PLM*	BLU	BC2	BMT
VST*	SDW	LTC*	
CPE*	BTL	ROD	
SCI*	SIL	SBCC	
IKP*	SSK	SBLP*	
GLA*	SME	SBSM	
SNS	TTM	SBLC	
SJQ*	CHM*	SBSC	
CIS	WH2	SBSN*	
VPD	BPK*	EDF	
MWC	RVS	SBLG	
PAS	LTM	SIP	
SCY	PIC	KYP	
TWL	FTM	AMS	
IRC*	YMD*	CCM	
PYR	RMR	CRR	
SWM	HDG	SUP	

Stations indicated by asterisks are plotted on the figures giving the results of the inversion.

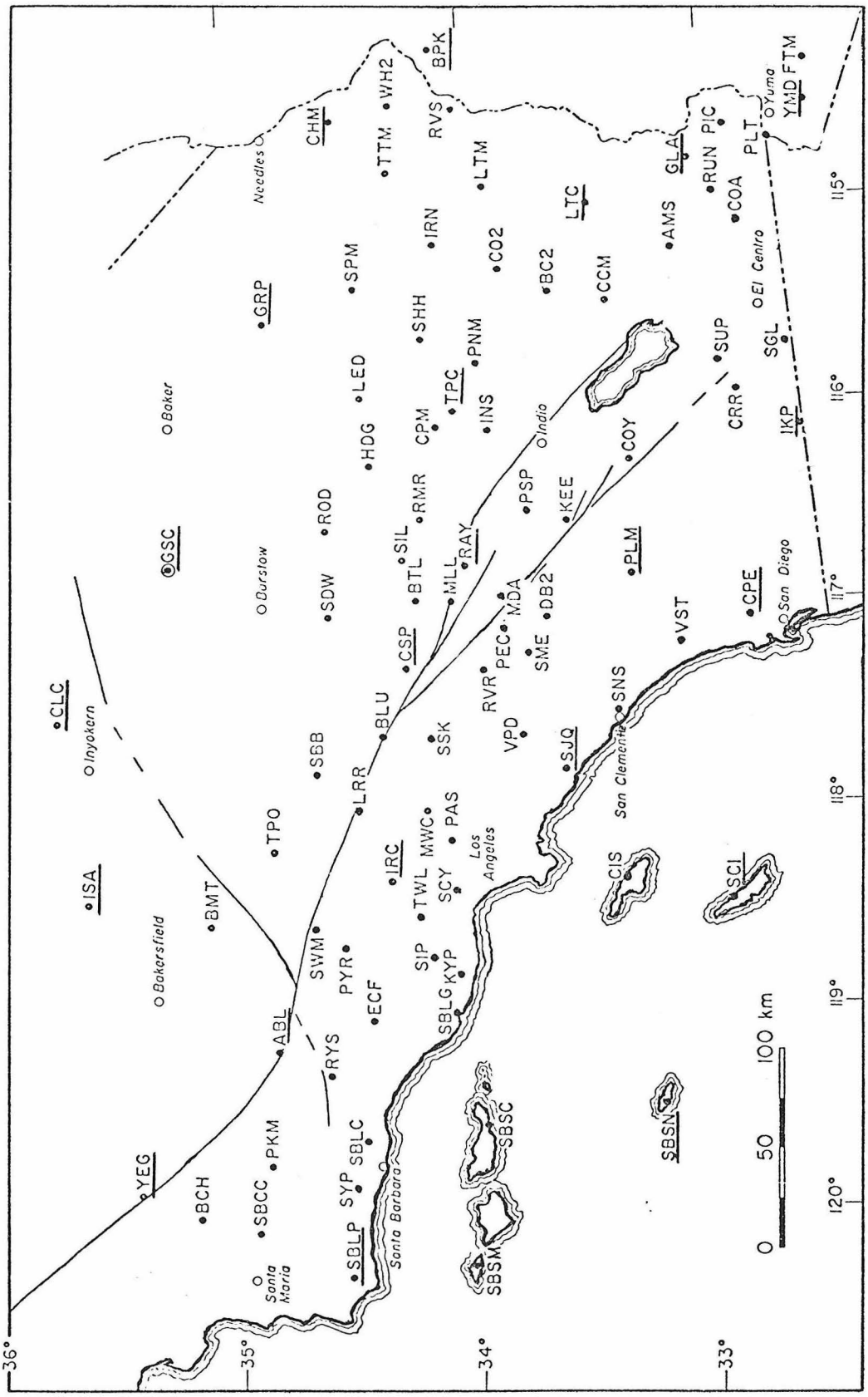

Figure 5-6. Stations used in the inversion study. The stations underlined will be plotted on the diagrams of the velocity models obtained to aid in orientation.

Table 5-7.

LIST OF EVENTS USED IN THE INVERSION STUDY.

N = Total number of arrivals, Az = Azimuth to event, deg., P = dT/dΔ, sec/deg.

LOCATION	DATE	N	AZ	P	LOCATION	DATE	N	AZ	P
JAVA TRENCH	JAN23 76	72	283.00	1.92	NOVAYA ZEMLYA	OCT21 75	98	1.75	5.90
NOVAYA ZEMLYA	AUG23 75	82	2.00	5.90	NOVAYA ZEMLYA	OCT18 75	77	2.55	5.72
NOVAYA ZEMLYA	SEP01 77	77	2.00	5.91	JAN MAYEN	APR16 75	50	20.15	6.62
N ATLANTIC	MAY14 76	59	89.75	6.10	LEEWARD	MAR10 76	82	94.35	7.40
COLOMBIA	MAR23 77	101	113.60	7.57	N COLOMBIA	MAR13 76	56	113.66	7.66
COLOMBIA	MAY19 76	72	118.45	7.70	PERU-BRAZIL	APR09 77	103	127.00	6.48
PERU	OCT08 77	87	129.10	6.78	PERU-BOLIVIA	JUN05 75	73	130.40	6.21
PERU	DEC11 75	73	130.88	6.83	ARGENTINA	FEB04 77	91	131.50	5.33
PERU	JAN05 76	86	132.33	6.72	CHILE-BOLIVIA	DEC17 76	83	132.70	5.97
CHILE-BOLIVIA	DEC04 76	66	132.40	6.00	CHILE-BOLIVIA	DEC03 76	63	132.60	6.00
CHILE-BOLIVIA	DEC28 76	85	132.60	6.00	CHILE-BOLIVIA	FEB05 76	82	133.20	5.93
N CHILE COAST	AUG20 76	85	133.37	6.08	CHILE-ARG	APR18 76	68	136.70	5.73
NORTH CHILE	FEB27 76	80	132.20	6.09	CHILE-BOLIVIA	NOV30 76	101	132.60	6.00
ARGENTINA	OCT22 77	106	134.00	5.16	CHILE-ARG	OCT10 75	60	135.40	5.75
KERMADEC	MAR27 76	67	229.75	4.92	KERMADEC	JAN24 76	63	231.00	5.03
SOUTH FIJI	JUL24 75	76	235.25	5.02	TONGA	DEC15 76	72	236.13	5.78
TONGA	FEB03 76	77	236.50	5.62	SOUTH FIJI	FEB03 76	81	234.90	4.96
FIJI	NOV25 76	94	237.05	5.36	FIJI	MAY15 77	81	237.20	5.36
FIJI	APR14 77	93	239.10	5.36	FIJI	NOV27 76	76	239.10	5.33
FIJI	NOV01 75	71	238.45	5.43	FIJI REGION	OCT18 77	79	239.14	5.30
FIJI	JUN03 77	77	237.55	5.33	FIJI	JUN06 75	90	237.70	5.15
TONGA	MAY20 76	75	238.10	5.76	FIJI	APR10 76	71	239.40	5.34
TONGA	JUN22 77	101	232.90	5.43	FIJI	JAN21 77	92	238.60	5.32
TONGA	JUN04 74	58	238.50	5.75	FIJI	FEB27 75	57	238.00	5.31
SOLOMON IS	MAR02 76	59	263.70	4.59	NEW HEBRIDES	AUG02 76	79	244.65	4.74
NEW HEBRIDES	MAY18 77	71	245.70	4.72	SANTA CRUZ	DEC19 75	89	255.00	4.85
SOLOMON IS	SEP04 76	72	256.50	4.73	SOLOMON IS	OCT12 76	91	256.70	4.72
SOLOMON IS	JUN05 76	88	258.30	4.73	MARIANAS	JUN06 77	79	284.90	4.69
VOLCANO IS	DEC22 76	98	294.15	5.00	BONIN IS	FEB14 76	69	298.30	4.82
BONIN IS	DEC12 76	105	299.30	4.82	SOUTH JAPAN	JUN25 76	83	302.48	4.91
SOUTH HONSHU	FEB18 77	87	303.30	5.24	KURILE IS	APR10 77	85	310.37	6.01
KAMCHATKA	NOV17 76	84	314.20	6.50	NORTH KOREA	MAR09 77	104	314.70	5.02
KURILE IS	MAR29 76	73	311.20	5.61	SEA OF OKHOTSK	DEC21 75	82	316.55	6.24
SEA OF OKHOTSK	JUL10 76	75	314.50	5.97	JAPAN SEA	JUN29 75	61	313.30	4.86
KURIL IS	SEP22 76	78	310.00	5.90	KURILE IS	NOV24 76	65	314.40	6.87
EAST RUSSIA	SEP09 77	66	315.50	5.17	KAMCHATKA	FEB13 77	63	317.05	6.78
ANDREANOF IS	FEB22 75	60	311.35	7.78	SOUTH ALASKA	AUG03 75	59	315.60	8.38

In order to include the stations of the Carrizo Plains network, which are important for controlling the structure in the north-west of the array, and also COY, events were chosen largely in 1976-1977. Some critical stations, such as SJQ, were not operational during the latter half of this period, so the data set was augmented, where possible, by adding residuals from nearby events that occurred earlier. (These were constructed using the residual normalised with respect to GSC for the earlier event, and adding the residual at GSC for the later one.) All the residuals used were unnormalised and uncorrected for sediments or crustal thickness.

The large size of the Caltech array limits the minimum horizontal block size: most models, which contained 12 x 12 blocks per layer, had 50 or 60 km square blocks in the first layer, 60 km blocks in the second and 70 km blocks in the third layer. Using blocks this large unfortunately has the effect of impairing both horizontal and vertical resolution, especially since the ratio of horizontal to vertical size is only of the order of 1:1. Smaller blocks increase the size of the matrix too much, and the problem is somewhat circular: increasing the vertical dimension to improve the resolution then requires that the horizontal size be increased to include all rays.

The initial run of this technique was made for a two layer model which approximated the ray tracing situation for model 2. The details of this model, and the results using $\theta^2=200$, are given in Figure 5-7(a); the contours are of slowness perturbations in per cent, which are approximately equal to minus the velocity variations. The first layer has areas of low velocity in the Imperial Valley, near SJQ, SNS

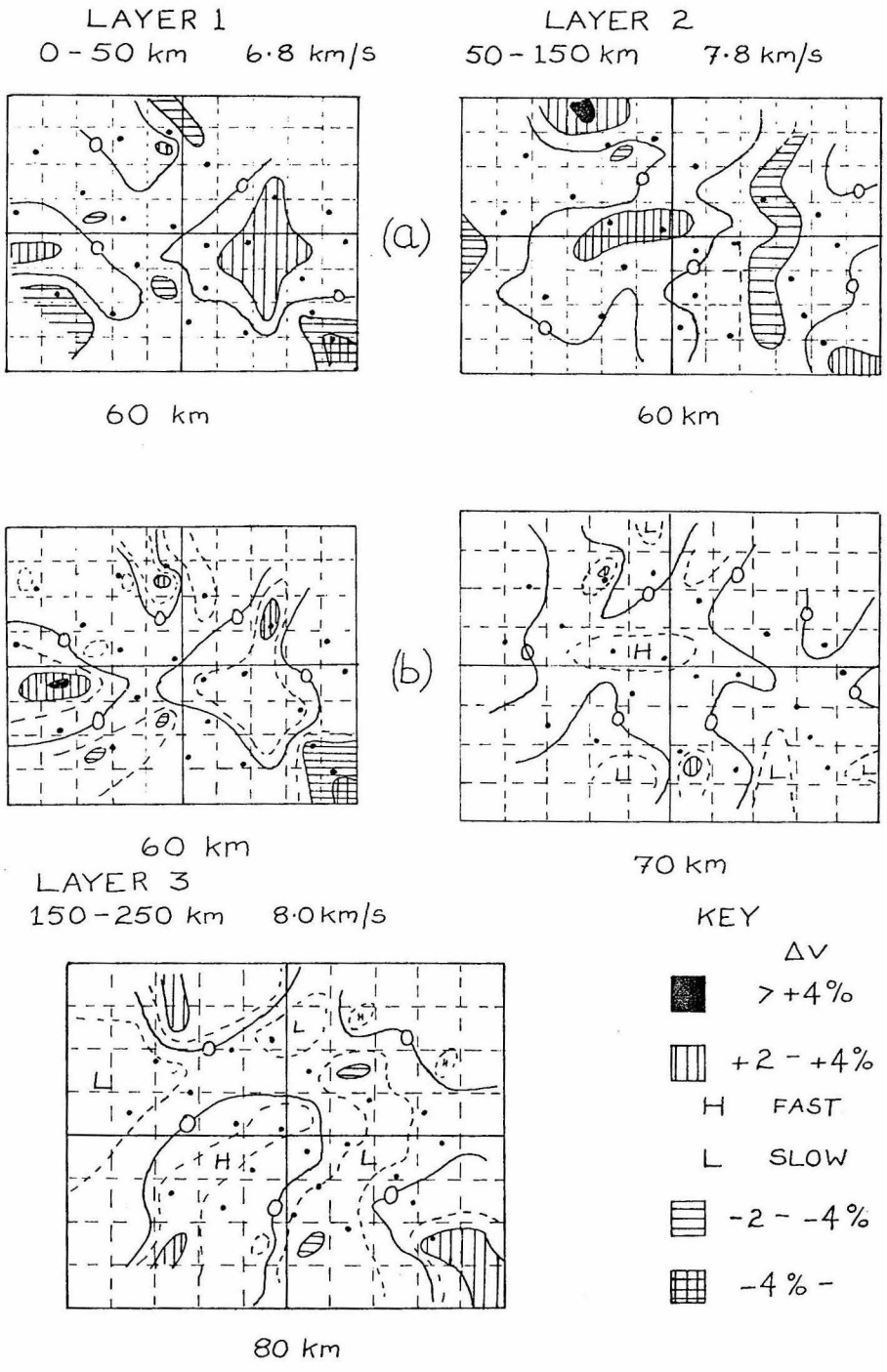

Figure 5-7. Slowness perturbations in per cent for two initial models. The two-layer model (A) approximates the ray tracing case of Model 2 (Figure 5-4). Stations are shown as solid circles, and the contour interval is 2%.

and TWL as expected from the sediment corrections and previous models. There is also an area of low velocity north east of CLC. The main regions of high velocity are between ISA and CLC, in the western Santa Barbara Channel, and in the central Mojave-northern Salton Trough. In Layer 2, high velocities appear north of ISA, under much of the Transverse Ranges and south-east of the Imperial Valley, as expected. Low velocities are found under the continental margin, and in the central Mojave-Salton Trough. The overall pattern is very similar to that of model 2, although the magnitude of the changes are somewhat smaller in the regions of high velocity. This is in part due to the smoothing introduced by this technique, but may also occur because many of the stations used are fast with respect to GSC, and so normalisation with respect to the average residual will tend to cause a shift towards a slightly faster average structure. The data variance for this case was .094 sec^2 and the variance improvement was 46.6%

Figure 5-7 (b) shows the effect of adding an extra layer to this model and extending the structure to 250 km. The improvement in variance rises to 54.4% in this case, suggesting that some deeper structure may be present. The velocities for Layer 1 are similar to those in Figure 5-7(a), although the magnitude of the perturbations is somewhat smaller; this effect is more marked in Layer 2, which has larger blocks in the three layer case. The main features of Layer 3 are the high velocities north-west of ISA and south-east of the Imperial Valley. It was suggested in the previous section that these might well persist to depths greater than 150 km, and this does seem to be the case.

The next models run are illustrated in Figure 5-8 (a, b and c). These had a slightly more natural division into three layers, with a first crustal layer from 0 to 30 km, with a velocity of 6.3 km/s, and a block size of 60 or 50 km, a second layer from 30 to 80 km, with a block size of 60 km and a velocity of 7.8 km/s, and the third layer from 80 to 170 km with a velocity of 8.0 km/s and a block size of 70 km. All models had a data variance of .094 sec^2. This figure was drawn primarily to illustrate the effect of varying the damping parameter. The model with θ^2=20 had a 53.2% variance improvement, but the slowness perturbations show rather oscillatory and undamped behaviour, and are sometimes rather unreasonable -- for example an 11.2% increase in one crustal block. The opposite effect is visible for θ^2=200 which is rather overdamped, and has much smaller changes; the variance improvement is only 50.7%. The third model has a damping factor of 100, and the crustal resolution has been increased by making the block size 50 km. The variance improvement is now 53.6%. Apart from the obvious differences in the magnitude of the perturbations, the three models are rather similar. All have high crustal velocities near ISA and CLC (the former is perhaps surprising in view of the crustal thickening), the Santa Barbara Channel region and the Central Mojave-northern Salton Trough. There are low velocities in the Carrizo Plains, near TWL and SJQ, and in the eastern Imperial Valley and eastern Mojave. The high velocities between SGL and YMD are possibly due to the crustal thinning here. Layer 2 shows a similar pattern of high velocities to the north, and low velocities to the south, of ISA, and low velocities in the Imperial Valley. There is no particularly marked velocity increase in the CSP region that could

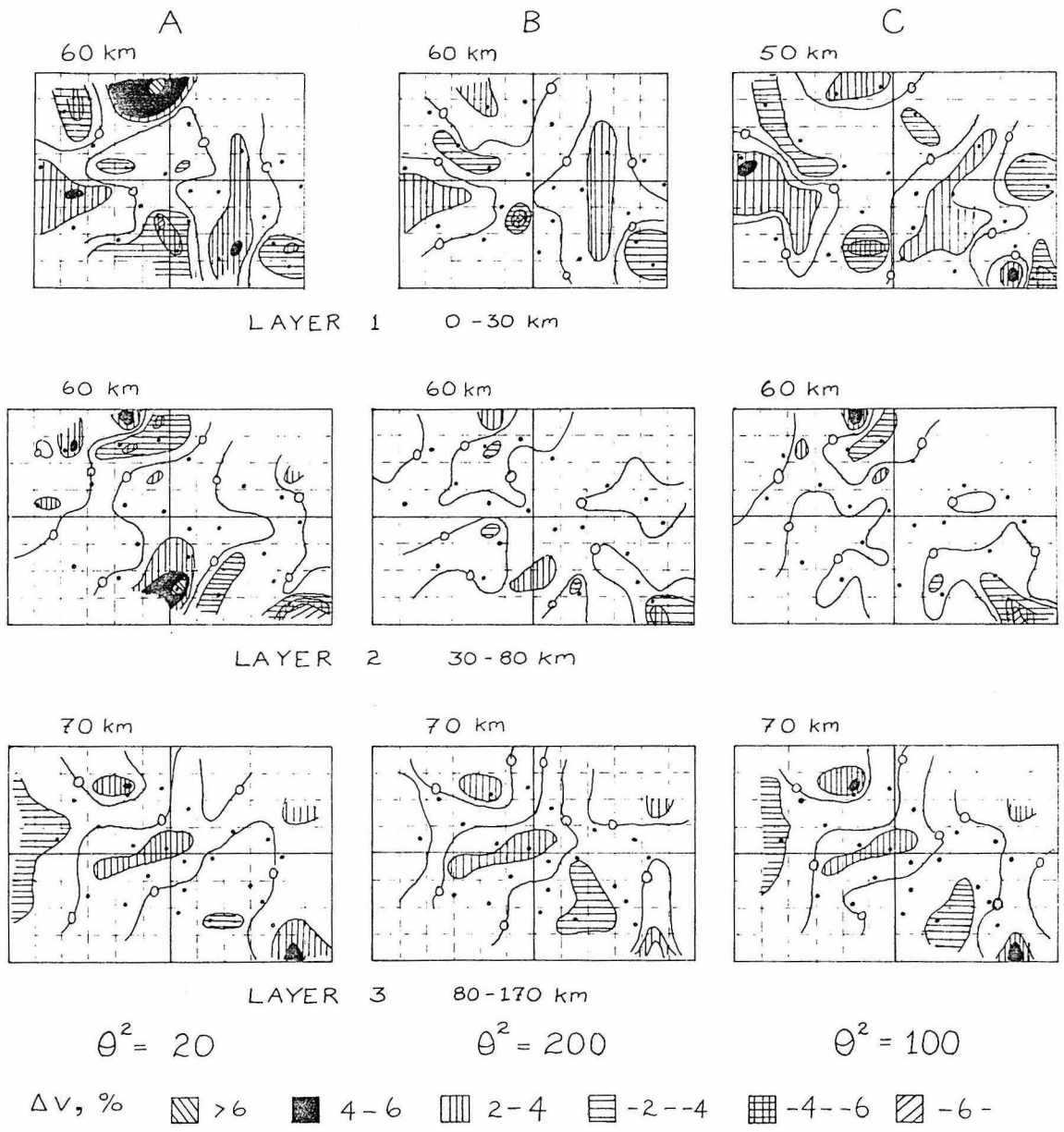

Figure 5-8. The effect of varying the damping parameter θ^2 for 3-layer models.

be associated with the local thinning of the 7.8 km/s layer observed by Hadley and Kanamori (1977), and in Model 1 of the previous section. However, there is a marked high velocity in Layer 3 in this region, which extends slightly south of west. This layer (3) also has high velocities in the north-east Mojave, to the north-west of ISA, and south-east of the Imperial Valley, as expected. There are low velocities under the western Imperial Valley and the continental margin.

The choice of a damping factor of 100 seemed most reasonable, but it was thought that the vertical smoothing could be lessened by altering the layering. The final models were run with the first crustal layer from 0 to 40 km, the second layer from 40 to 100 km, and the third from 100 to 180 km; the velocities are the same as in the previous models. One run was made with the coordinate axes north-south and east-west; the second had the axes rotated 40° anticlockwise, with the origin shifted 20 km S.40° E.

This latter choice of axes is perhaps somewhat more natural for California since the trend N 40° W is approximately that of the plate boundary; it was chosen to investigate the possibility of velocity contrasts across the San Andreas fault. The variance improvement was 56.8% for the second (rotated) case as opposed to 56.6% for the first. The results are shown in Figures 5-9 and 5-10, with sections across the models presented in Figure 5-11.

The crustal layers for both orientations have high velocities in the western Santa Barbara Channel region: these are consistent with the refraction data (Hadley and Kanamori, 1977) which indicate a westward thickening of the 6.7 km/s lowermost crustal layer. The maximum

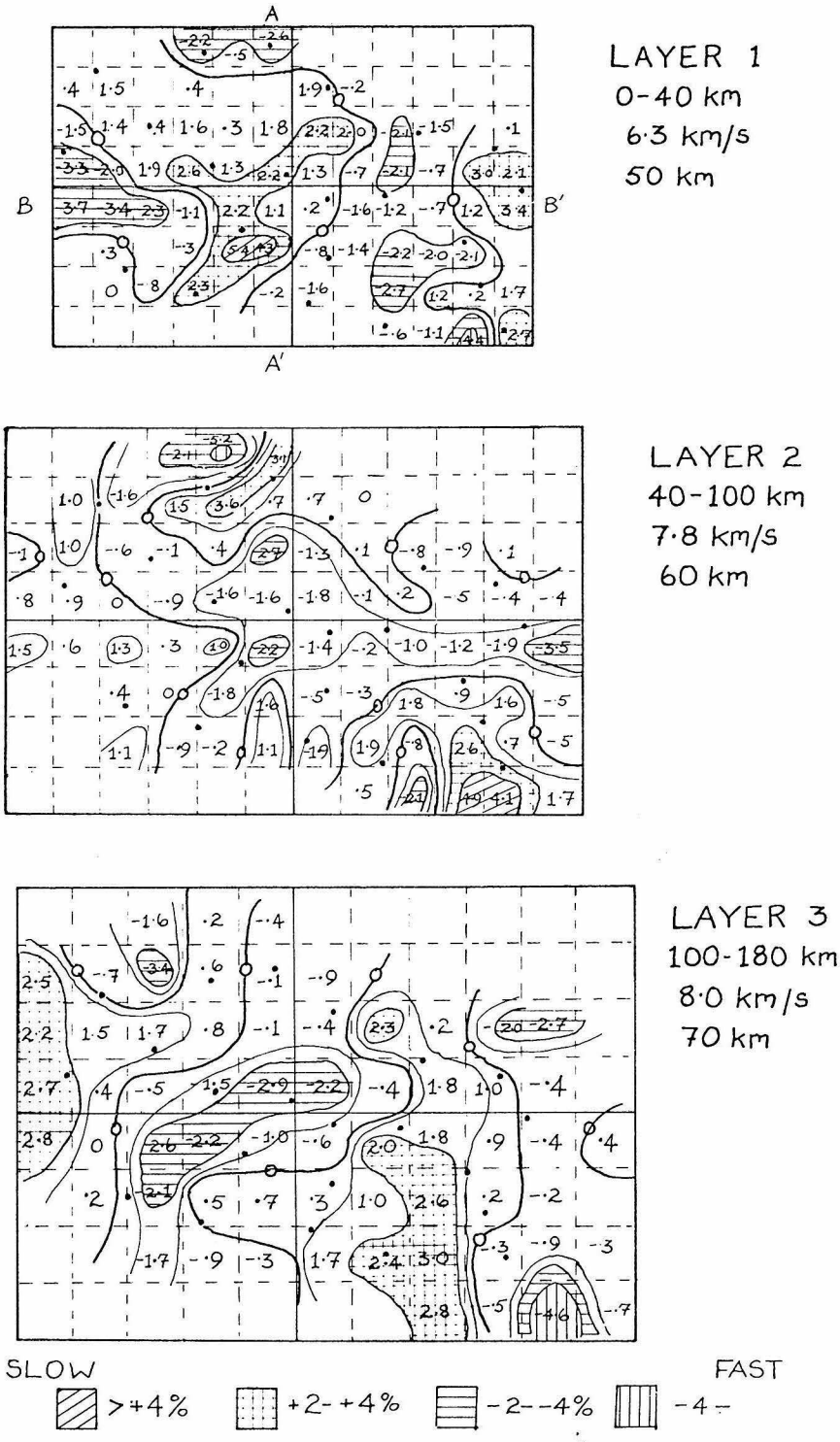

Figure 5-9. Details of the slowness perturbation in per cent for the preferred 3-layer model, with $\theta^2 = 100$. The contour interval is 2%, but in layers 2 and 3 the ±1% contours have been added. AA' and BB' are the section lines used in Figure 5-11.

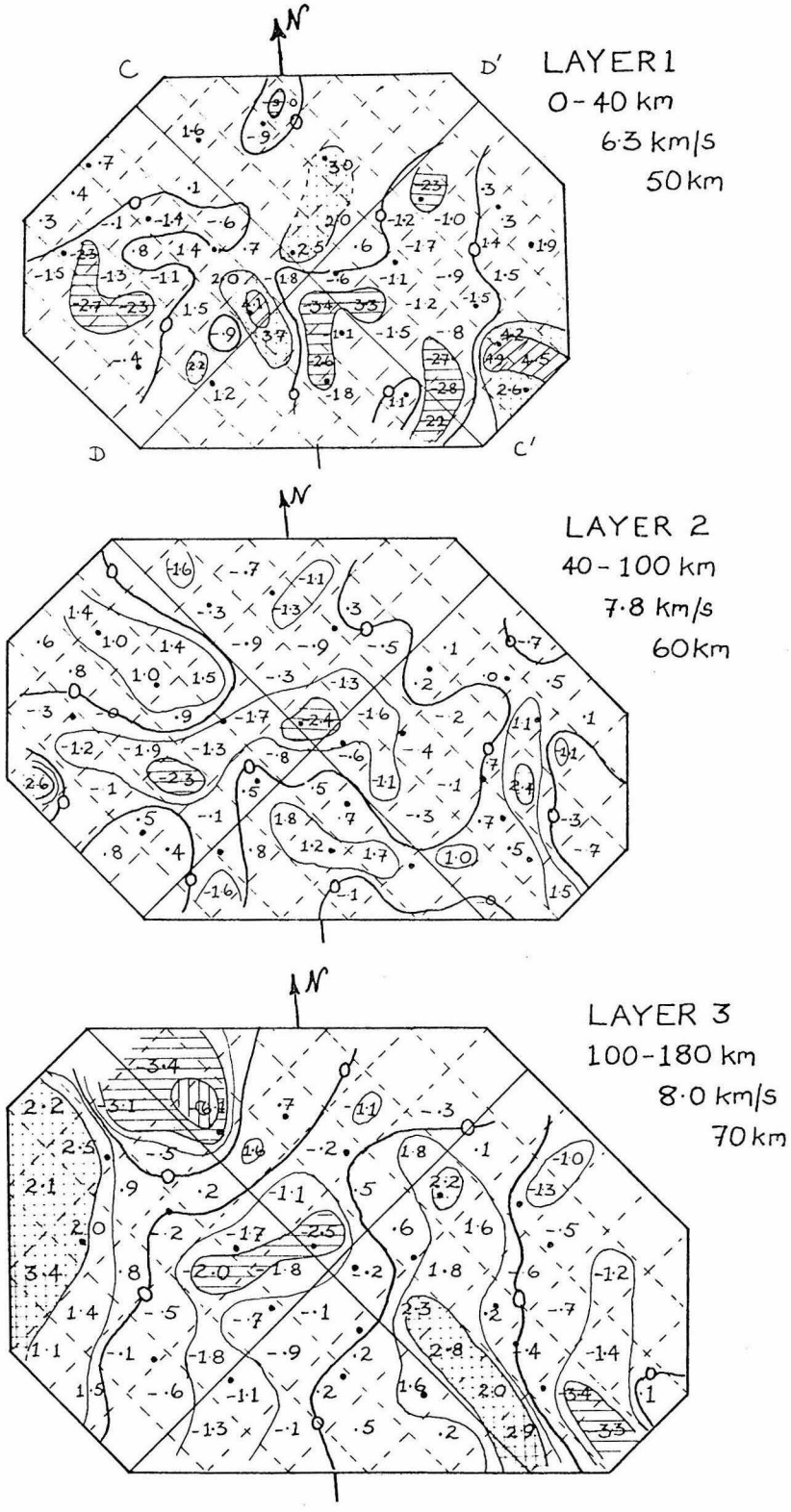

Figure 5-10. Slowness perturbations for the model of Figure 5-9, but with the coordinate axes rotated N 40° W. Notations as in Figure 5-9; CC' and DD' are the section lines.

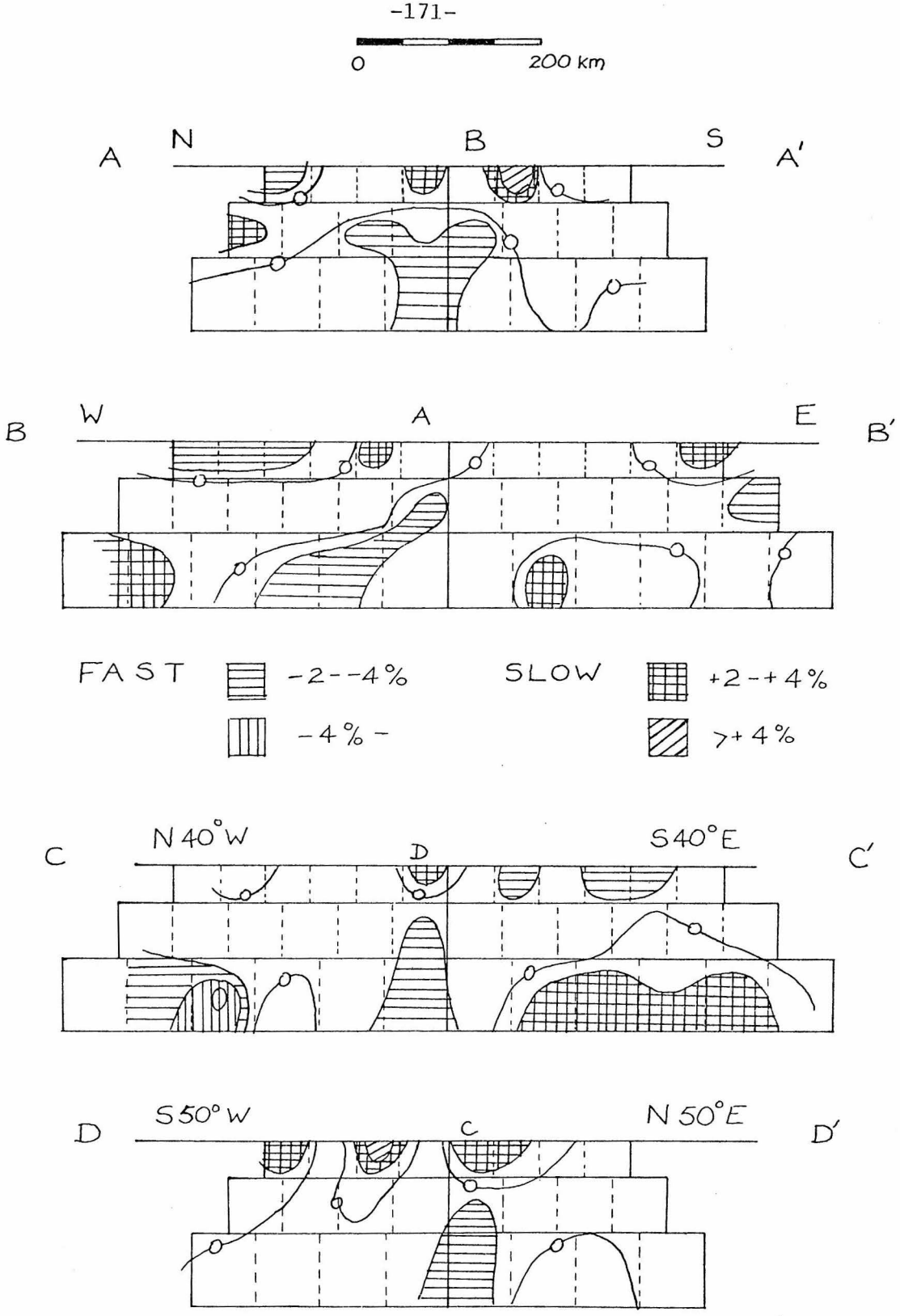

Figure 5-11. Vertical cross sections through the final models of Figure 5-9 (AA', BB') and Figure 5-10 (CC', DD'). There is no vertical exaggeration.

percentage decreases in slowness represent a mean crustal velocity of ∿6.5 km/s, in good agreement with the refraction data. Both models have low velocities in the vicinity of SJQ and SNS, and the Los Angeles and Ventura Basins as expected from the sediment corrections; the magnitude of the perturbations is higher in Figure 5-9. The Imperial Valley stations, especially those in the centre of the Valley, were omitted, so the control over this region is not as good as in the ray tracing models. The high velocities observed in an approximately north-south trending belt through the central Mojave Desert and northern Salton Trough in many of the inversion models, including Figures 5-9 and 5-10, may be a reflection of the high P_n velocity (8.0 km/s) that has been observed on long refraction profiles for this region from blasts in the Nevada Test Site (Hadley, 1978, personal communication). Those in the northern Salton Trough are probably also related to the crustal thinning in this area. Both models have high velocities under CLC, which are also seen in a number of other models, but the model of Figure 5-9 also has high velocities under ISA, which is surprising in view of the crustal thickening; the lower velocities of the rotated model are probably more acceptable. Refraction data indicate high crustal velocities in the northern Peninsular Ranges; these show up more strongly in Figure 5-10.

Layer 2, from 40 to 100 km, has larger perturbations for the non-rotated model, although the general pattern is similar for the two models. Both have an east-west trending zone of high velocities under much of the Transverse Ranges, as expected from the refraction data but the positions of the maxima for the rotated model (i.e., under CSP and SBLG) are closer to those determined by the ray tracing models. The

percentage increase is also rather small compared with refraction measurements. The velocities under the Imperial Valley are low for both models, although Figure 5-9 shows both lower velocities and a region of increased velocity south-east of IKP. High velocities occur to the north of ISA as expected, but Figure 5-9 also has marked low velocities to the south-east.

The third layer of both models is marked by high velocities under much of the Transverse Ranges, trending approximately east-west under the land, but extending south towards SCI offshore, high velocities under the eastern Mojave Desert, south-east of the Imperial Valley, and north-west of ISA. Low velocities mark the western margin of the array: these are probably associated with the transition to oceanic structure with a more marked low velocity zone. There is also a low velocity region extending roughly north-south through the central Mojave, across the Salton Trough and into the southern Peninsular Ranges which shows a closer alignment with the axis of the Imperial Valley for the rotated model.

Overall, the inversion models are quite similar, with the greatest resemblance occurring in the third layer. They are also quite consistent with the seismic refraction data and the models derived in the previous section, although the magnitude of the variations is somewhat smaller, largely due to the choice of block size and smoothing in the inversion. The similarity of the ray tracing and inversion models is enhanced by the sections of Figure 8-11, which show the high velocity "ridge" beneath the Transverse Ranges, although the model with the north-south axis has this feature dipping to the west.

In a study of the three-dimensional lithospheric structure beneath Central California, Aki et al. (1976) found a remarkable correlation between the observed velocity anomalies and the San Andreas fault zone down to a depth of 75 km. This is not the case for southern California, where there appears to be little or no evidence for velocity discontinuities across the fault even in the crustal layer, and even when the coordinate system was rotated so one axis paralleled the plate boundary. A further rotation so one axis paralleled the "Big Bend" of the San Andreas produced no significant changes in the structure. Although there are no contrasts visible across the fault, there may be some structure associated with the fault zone itself, which is not well resolved because of the block size. In particular, layers 2 and 3 generally have low velocities in the Carrizo Plains region and in the approximate vicinity of the southern end of the fault in the Salton Sea. The extension of the latter slow zone northwards into the Mojave is of interest in view of the suggestion by Hadley and Kanamori (1977) that the plate boundary at depth may lie to the east of its surface expression in the neighbourhood of the Transverse Ranges.

As discussed earlier, the choice of block size used in the inversion leads to substantial smoothing of the resultant velocity model, accounting for most of the differences in the magnitude of the velocity changes obtained by ray tracing and inversion. Following Ellsworth and Koyanagi (1977), one may estimate the maximum error Δm in the model perturbations:

$$\Delta m \leq \frac{\sigma_d}{2\Theta} \qquad (6)$$

where σ_d is the average error in the data and θ^2 is the damping constant. For the preferred models, θ^2 was 100, and the estimated error in the data 0.1 sec, leading to a maximum error of 0.5%. (Note that the data variance quoted in this chapter is representative of the scatter due to both velocity variations and errors in the data; using this value of 0.09 sec^2 would give an overestimate for the maximum error of 1.5%.) In view of this estimate, velocity or slowness perturbations in excess of 1% may be considered significant. The smoothing of the results is illustrated by the resolution matrix: Figure 5-13 shows selected elements of the matrix for eight blocks whose locations are shown in Figure 5-12. The portions of the matrix are shown in the layer block format used to display the velocity models (Figure 5-7 to 5-10), and the diagonal elements are encircled. In general, the diagonal element is a well-defined maximum, but the resolution is better horizontally than vertically, as would be expected from the smoothing introduced by the choice of block size. This smoothing causes broad maxima in the layers above or below the selected block; the width of the peak increases with vertical distance from the chosen block, and its amplitude decreases. Thus the resolution matrix for block A has a well defined maximum of 91.2 confined to a 50 x 50 km^2 block in Layer 1, in Layer 2 the positive values extend over some 300 by 250 km^2, but they do not exceed 4.1, and in Layer 3 positive values are found over about 400 x 400 km^2 (7 x 7 blocks), although they are no larger than 0.6. As expected, the smoothing is most apparent between the first and second layers where the choice of block size causes greatest coupling, and the resolution is highest for the third layer. Of the blocks investigated, the least well resolved

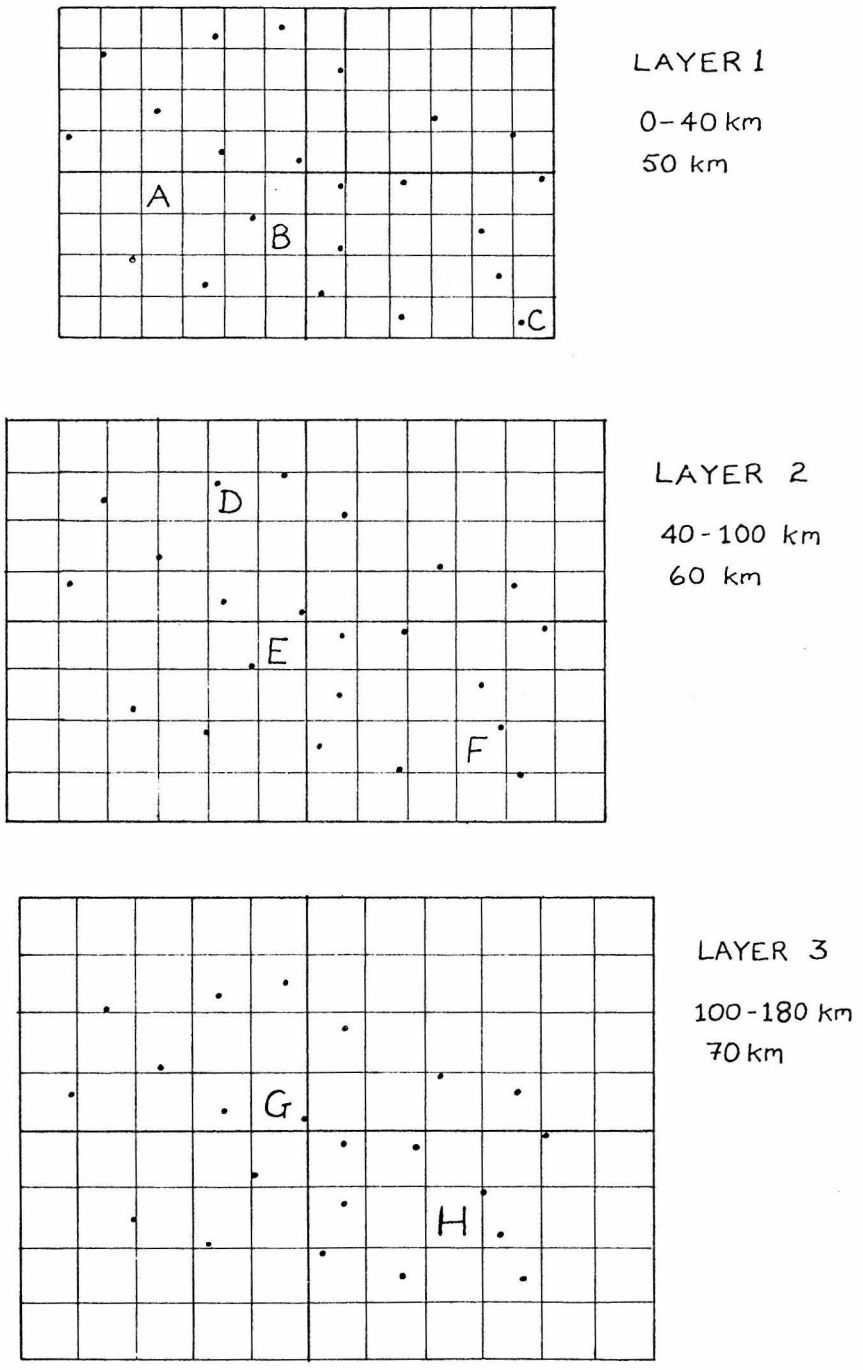

Figure 5-12. Index grid showing locations of blocks (lettered) for which the resolution matrix was calculated. Key stations are indicated by solid circles.

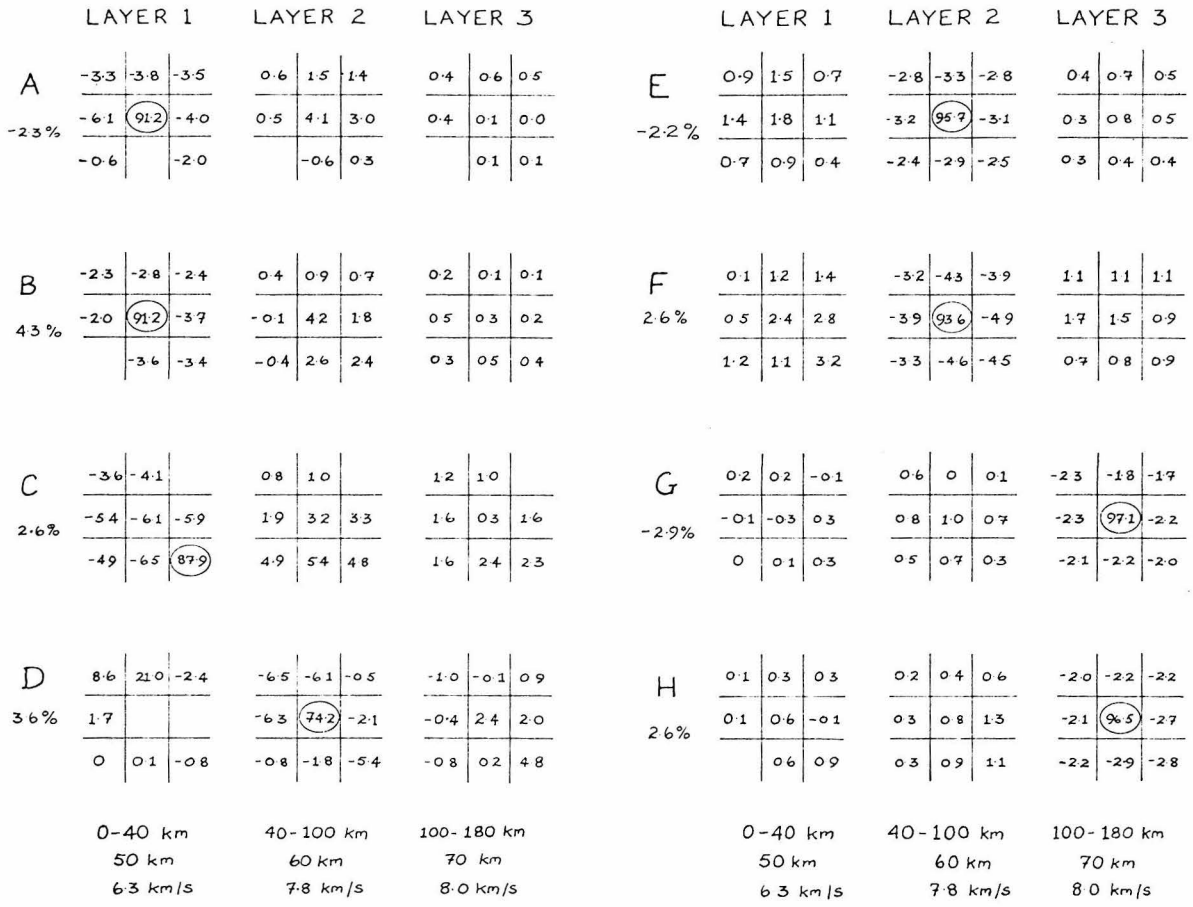

Figure 5-13. Selected elements of the resolution matrix for the blocks indicated by letters in Figure 5-12, and for the initial velocity model shown; these correspond to the velocity (slowness) perturbations of Figure 5-10. The diagonal elements of the matrix are encircled.

is D, which has a diagonal element of only 74.2 and a large coupling to the north from Layer 2 to Layer 1 which has a clear maximum of 21.0. This is in part explained by the absence of data in the first layer above D, but may also represent the effect of the deepening Moho beneath the Sierra Nevada which serves as a link between the first and second layers. For the rotated block configuration (Figure 5-10), which allows greater separation of the ray paths to CLC and ISA, the low velocity was in fact located in the crust beneath ISA.

Chapter 6

DISCUSSION

In this study the upper mantle compressional velocity structure beneath the Caltech-U.S.G.S. Southern California Seismograph Network has been investigated by analysing the azimuthal variation of teleseismic residuals at individual stations of the network. The variations at a single station may be in excess of 1 sec, and the size of the residuals requires that they be caused mainly by lateral variations of velocity within the upper mantle.

Velocity models were derived to account for the observed variation of residuals using both simplified ray tracing and inversion techniques. The structures obtained by these methods were similar, and did indeed exhibit marked lateral heterogeneity within the upper mantle to depths of 150 to 200 km, although the magnitude of the changes predicted by the inversion technique was somewhat smaller than that of the ray tracing models, largely because of the smoothing that the inversion entailed. The possible origins of the main features present in these models, and their relation to other geophysical observations and regional tectonics will now be discussed.

In the derivation of models by ray tracing, sediment and crustal thickness corrections were applied to those stations where these could be adequately determined; several stations appeared, from the analysis of model misfits, to require additional corrections. Apart from these few stations, it was assumed throughout this modelling procedure that the velocity variations were limited to the upper mantle, and no allowance was made for regional variations in crustal velocities such as have

been observed in seismic refraction studies (e.g., Hadley and Kanamori, 1977). The latter changes will, in general, cause residual variations of at most 0.15 sec, nevertheless, variations in crustal structure were observed in the inversion models. These were discussed in the previous chapter; they consist primarily of low velocities in the Carrizo Plains, and in the Los Angeles Basin and Imperial Valley areas as expected from a knowledge of sediment thicknesses, and high velocities in the Santa Barbara Channel, northern Peninsular Ranges and central Mojave Desert, which can be related to seismic refraction observations.

The variations within the upper mantle may be divided into a number of distinct areas, of which the Sierra Nevada, Imperial Valley, the western margin of the array and the Transverse Ranges are the foremost. (There are also lateral variations beneath the Mojave Desert.) These regions will be considered in turn.

The anomaly associated with the Sierra Nevada consists of a high velocity region to the north and west of Isabella (ISA); the eastern margin of the Sierra and the Owen's Valley (which has been an area of recent vulcanism) are characterised by lower velocities. For Model 1 (Figure 5-1) there was a conflict between the depth to the high velocity region ($\sim$25 km) and the Moho depth ($\sim$45 km), and the percentage increase required by Model 2 (Figure 5-4) to exist from 50 to 150 km was perhaps rather high; these observations suggest that the velocity contrast between this region and the surrounding upper mantle persists to depths greater than 150 km, and this is supported by evidence from the inversion study. The Sierra Nevada is a region of low heat flow, and it has been suggested (Roy et al., 1972) that this is caused by lower temperatures

and an absence of partial melt in the upper mantle beneath the Range to depths of 200 km. The velocity increase is consistent with this interpretation of the data, which also agrees with the suggestion by Solomon and Butler (1974) that a "dead slab" exists beneath the northern Sierra and southern Cascades. However, as pointed out by Crough and Thompson (1977), it would take over 10 m.y. before heating at the base of the crust would show up in increased surface heat flow. They suggest that heating of the base of the lithosphere, and its resultant thinning, in the past 10 m.y. as the active subducting slab has moved northward, has caused the uplift of the Sierra Nevada, and cite the low P_n velocity (7.9 km/s) and Rayleigh wave phase velocities as supporting this model. The teleseismic data at ISA are not consistent with low velocities caused by heating at depths greater than 50 km beneath the southern Sierra Nevada, which suggests that this model for the uplift is incorrect. Ultramafic rocks outcrop in the southern and western Sierra Nevada, and provide accessible samples of upper mantle material. Lherzolite xenoliths found in Fresno County have been investigated by Peselnick and others (1977), who found that the elastic velocities of these xenoliths, which were derived from the upper mantle beneath the Sierra Nevada, exhibit considerable anisotropy. They estimated the maximum and minimum compressional velocities at 50 km and 500°C to be 8.4 and 7.85 km/s. This observation, coupled with a P_n velocity parallel to the long axis of the batholith of 7.9 km/s, led them to propose that large scale anisotropy exists beneath the Sierra Nevada, possibly as a consequence of the subduction of oceanic lithosphere. It is difficult to relate this conclusion to the observed velocities of the present

study, since the highest velocities would then be required to exist perpendicular to the long axis of the batholith, and possibly dipping to the east parallel to the subducted slab, which does not appear to be the case. (This is the orientation of velocities required by conventional models of the anisotropy of the oceanic lithosphere such as that proposed by Hess (1964).) However, the maximum velocity of 8.4 km/s is consistent with the velocity increase predicted by the models of Chapter 5.

Upper mantle velocities beneath the Imperial Valley were found to be low, as might be expected for an area of high heat flow that is regarded as an extension of the active spreading centre from the Gulf of California on to the continent. The velocity low is largely associated with the middle of the valley, and for Model 2 (Figure 5-4) a 2 to 4% decrease from 50 to 150 km was calculated over most of this region; this is equivalent to mean velocities of 7.64 to 7.49 km/s, which are akin to the values that have been observed in other areas of high heat flow such as the transition zone from the Basin and Range to the Colorado Plateau (Keller et al., 1975) and near oceanic ridge crests (e.g., Talwani et al., 1971). The changes observed for the inversion models are also of this magnitude. In addition to the low velocities, which are presumably associated with high temperatures and possibly partial melting in the upper mantle, there is also a zone of high velocity trending south-east from the eastern boundary of the valley. This zone is partially responsible for the early arrivals for South American events, which are probably enhanced by the effect of near source structure which is thought to cause the decrease in apparent velocity, as measured by the array, for events in South America. The velocity increase probably

extends to depths in excess of 200 km. As was explained in the last chapter, the assumption of a constant velocity contrast (Model 1) does not provide an adequate description of the variations within the Imperial Valley, and so an additional low velocity region from 30 to 80 km was added to explain the residuals in this case. This model, shown in Figure 5-3, provides a better fit to the data than does Model 2, and is more detailed than those resulting from the inversion where a large block size and fewer stations were used. Although surface heat flow is controlled largely by the properties of the upper crustal layers, and heat from the base of the base of the 20 km crust will take about 2 m.y. to reach the surface, it is interesting to compare the model of Figure 5-3 with the contours of near surface temperature gradient (from Rex, 1970) which are plotted in Figure 6-1. The region of high heat flow corresponds quite well to that of low velocity, although there are no data suggesting that the high heat flow extends west towards IKP as the low velocity does. Most of the regions of highest temperature gradient lie within the 4% velocity decrease contour, with the possible exception of the Heber maximum; however, the maximum temperature gradients appear to lie to the north and west of the velocity minima although the general pattern is somewhat similar. The heat flow highs are at Buttes (1), an east-west trending high south of that through the Brawley fields (2, 3) and Glamis (4) and one further south at Mesa. This pattern, stepped south-east, is approximately repeated by the areas of 6% velocity decrease. It is tempting to speculate that the crust in this region has moved some 15 km north-west over the mantle since the velocity anomalies, which are presumably associated with high temperatures, originated and

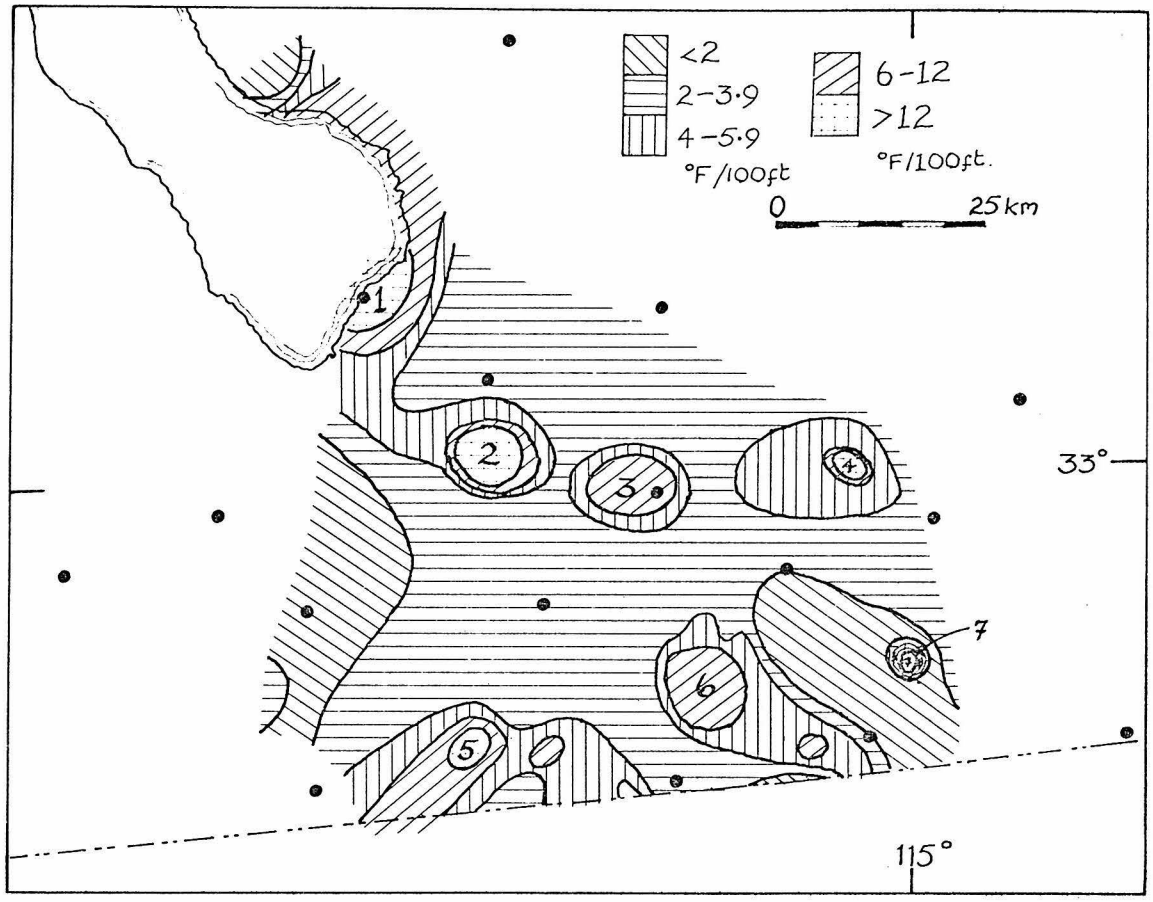

Figure 6-1. Contours of near surface temperature gradients in the Imperial Valley (after Rex, 1970). The numbered maxima correspond to the following geothermal fields: 1 Buttes, 2 N. Brawley, 3 E. Brawley, 4 Glamis, 5 Heber, 6 Mesa, 7 Dunes. Stations are shown as solid circles.

this is in the general sense of motion of the Pacific plate. However, the details of the plate boundary in this area are extremely complex, and such an assumption may be rather facile.

The western margin of the array is marked by low velocities at depths of about 100 to 200 km, as is evident from both the ray tracing and inversion studies. These velocities are largely controlled by positive residuals observed at the westernmost stations for events in the South and Central Pacific. This anomaly may well represent the ocean to continent transition, with the oceanic structure having lower velocities at depths down to 200 or 250 km. Velocities in the southern offshore borderland between SCI and CPE are also low for models 1 and 2 and some of the inversion models. It is interesting to note that this is an area of relatively high heat flow (Roy et al., 1972) which may be related to the ridge which existed off Baja California until spreading began in the Gulf some 5 m.y. ago (Atwater, 1970).

Hadley and Kanamori (1977) discovered the existence of a high velocity "ridge" extending roughly east-west in the upper mantle beneath much of the Transverse Ranges. The models of the present study support this observation, as is indicated most clearly by the sections of Figures 5-2 and 5-11, although the maximum changes seem to be more localised in the vicinity of CSP and SBLG than would be expected from the distance range over which the arrival from the 8.3 km/s layer is observed in the refraction study. The ray tracing models could easily be modified by varying the velocity contrast with depth, or by allowing the bottom of the high velocity region to undulate. The differences observed in the inversion models were somewhat smaller in magnitude than expected, an

effect that is largely caused by the smoothing due to the choice of block size, and were most apparent in Layer 3 at depths of about 100 to 180 km. The model in which the co-ordinates were rotated to lie about the San Andreas fault did show maxima in Layer 2 (40 to 100 km) close to CSP and SBLG. The residuals in this study confirm that the anomaly is bounded to the north (this was somewhat poorly defined by the Java Trench data alone) and also indicate that it does not extend much further west than San Miguel Island, where the apparent effect of the ocean to continent transition begins to dominate the structure. The southern boundary of the region is less well defined: there appear to be high velocities extending southward between San Nicholas and San Clemente Islands, and into the northern Peninsular Ranges, although these are slower than the central Transverse Ranges, and may be associated with the choice of initial velocity model.

As in the model proposed by Hadley and Kanamori, an important characteristic of the high velocity region beneath the Transverse Ranges is its continuity across the San Andreas Fault at depths of 50 to 100 km in an area where the surface geology has been offset by some 275 km since the Miocene. The maximum amount of displacement that could exist without being detected is estimated at 30 km; with an average slip rate of 3 to 6 cm/year on the San Andreas, this would place the maximum age of the anomaly at 1 to 0.5 m.y. It is hard to find a convincing argument whereby the anomaly could have been formed at that time, and so some other explanation must be sought for its existence. The alignment could, of course, be purely coincidental, but without knowing the distribution of high velocity regions on both sides of the

fault it is hard to assess how likely this would be; based on currently available data, it seems somewhat improbable. Hadley and Kanamori discussed the possibility that the anomaly was maintained by a phase change which continually adjusts to yield no apparent displacement across the fault, but rejected this hypothesis on the grounds that the temperature or pressure conditions required to drive such a change were unlikely to exist. A phase change maintained by the relatively long-lived lithostatic load was also proposed, but whilst it is true that much of the anomaly lies beneath a region of substantial relief (see Figure 2-4), there is no large anomaly associated with Mount San Jacinto, the second highest peak in Southern California, and velocities appear just as high under the low-lying Los Angeles Basin and near SBLG. This implies the lithospheric load is not the controlling factor. A more reasonable explanation is that the fault simply does not pass through the anomaly. This could arise in two ways: firstly, the lithosphere could be confined to the crust in this region, with the regionally observed 7.8 km/s layer being the asthenosphere; secondly, the plate boundary at depth could be located somewhere other than beneath its surface expression. The former explanation is hard to reconcile with the concentration of the plate motion on the San Andreas fault: with a lithosphere only about 30 km thick, one might reasonably expect the movement to be distributed across a number of faults. The latter explanation is probably the most attractive, and, as pointed out by Hadley and Kanamori, the regionally observed 7.8 km/s layer would then act as a decoupling zone necessary to accommodate the horizontal shear resulting from the divergence of crust and mantle plate

boundaries. Enhanced coupling between crust and mantle motions where this layer thins would then result in crustal buckling within the Transverse Ranges.

Having suggested that the plate boundary at depth does not lie under its surface trace, one must now address the question of where it does lie. In Central California, the plate boundary is a well defined feature to depths of 75 km (Husebye et al., 1976), and the crustal and mantle boundaries presumably coincide beneath the Imperial Valley, so there is an additional problem of how the two boundaries can be recombined. It is unlikely that the mantle boundary lies to the west of the anomaly, since if it did it would have to cut completely across the regional structural grain. A more probable location would be off the east end of the anomaly, in the general region of the active Helendale-Lenwood-Camp Rock faults and the western limit of quaternary vulcanism in the Mojave Desert; the latter certainly suggests that there are changes occurring at depth in this area. The velocity models presented in Chapter 5 are not very helpful in resolving this problem, although they do have low velocity regions in the eastern Mojave whose trend is approximately that of the plate boundary, and low velocities similar to those seen close to the fault in the Carrizo Plains do extend northwards from the Salton Trough into the Mojave Desert at depths of about 40 to 180 km. It is attractive to speculate that these trends are manifestations of the presence of a plate boundary at depth, but the evidence is certainly far from conclusive.

In view of the apparent association between heat flow and upper mantle velocities beneath the Sierra Nevada, the Imperial Valley and

the southern offshore borderland, it is perhaps reasonable to suggest that most of the lateral velocity variations under southern California originate because of temperature differences that may well be related to the plate tectonic history of the region. The connections between plate tectonics and the Sierran and Imperial Valley anomalies are fairly obvious, and have already been discussed, but the possible link with the Transverse Ranges is more subtle. However, as was noted by Hadley and Kanamori (1977) this last anomaly is roughly on strike with the Murray Fracture Zone, although the evidence presented in this study indicates that the high velocities do not extend that far west, and there may be structures between the end of the anomaly and the fracture zone along which significant right lateral offset has occurred so that alignment is fortuitous. The material near the fracture zone probably had different temperature characteristics, and maybe different chemical ones, from that on the ridge itself. Consequently, subduction of the fracture zone and ridge system some 15 to 20 m.y. ago could have introduced temperature (or compositional) variations into the upper mantle; such a temperature field would be stable over millions of years, and could still affect the velocities observed today. The temperature field can cause large velocity variations in two ways: it may drive a phase change or possibly cause partial melting. The most likely phase change to occur at shallow depths within the upper mantle is from garnet granulite to eclogite, and the position of this boundary can be significantly affected by small variations in chemistry (Ringwood, 1975). The possibility of partial melting within the upper mantle is a matter of some discussion among petrologists, some of whom argue that

it is impossible; it is probably highly dependent on various factors including the presence of carbon dioxide or water. Gravity data might distinguish between the two possibilities: less than 1% partial melt is required to lower the velocity from 8.3 to 7.8 km/s (Anderson and Spetzler, 1970), which causes a density change not exceeding 0.03 g/cm^3, whereas if the eclogite-garnet granulite phase change is responsible for the reduction in velocity, the minimum density change is 0.15 g/cm^3. On the basis of the gravity changes produced by such density variations -- 30 and 150 mgal respectively, assuming a suitable model -- and the available Bouguer anomaly data, Hadley and Kanamori (1977) concluded that the partial melt model was preferable. Further evidence for partial melting might be found by using deep electrical conductivity measurements (see, e.g., Shankland and Waff, 1977), or by analysis of S-wave velocities which should be more severely affected by the presence of partial melt.

Many recent studies (e.g., Fuchs, 1977) have emphasised the possibility of anisotropy in the subcrustal lithosphere, and its relationship to dynamical processes in the upper mantle. Anisotropy within the Pacific Ocean basin, and its explanation in terms of the orientation of olivine crystals, was discussed by Hess (1964), and similar azimuthal variations of P_n velocities were reported by Bamford (1973) for southern Germany. Seismic anisotropy has also been investigated by a number of Russian authors, including Chesnokov and Nevskiy (1977). Since the velocity structures beneath Southern California appear to be related to the plate tectonic history of the region, and the interactions between the American, Pacific and Farallon plates, it might be supposed

that anisotropy should be observed. This was proposed by Peselnick and others (1977) to account for the low P_n velocity observed parallel to the long axis of the Sierra Nevada, but this explanation is not entirely consistent with the observations of this study. There is little evidence for seismic anisotropy beneath Southern California from the teleseismic travel times, although the effects would probably be masked by the lateral heterogeneity, and would be less distinct for the steeply incident teleseismic waves. The area most likely to exhibit seismic anisotropy is the Imperial Valley, which is an extension of the ridge system of the Gulf of California on land. There is a slight indication that velocities may be faster in the north-west-south-east direction than perpendicular to it, and this is in fact the sense observed in the Pacific Ocean.

This study has provided evidence for, and models of, large lateral variations in upper mantle compressional velocities beneath southern California. More precise mapping of the variations may be possible as detailed crustal models, which can be used to remove the contribution of the crust to the residuals, become available. Studies of S wave travel times, and a search for possible P to S conversions at the top of the high velocity layer, together with detailed analysis of phases appearing on local earthquake records, may also provide further constraints and solve such problems as the real behaviour and location of the plate boundary at depth. These studies should now be feasible with the availability of high quality digital data from the CEDAR system.

BIBLIOGRAPHY

Aggarwal, Y. P., L. R. Sykes, J. Armbruster and M. L. Sbar, Premonitory changes in seismic velocities and prediction of earthquakes, Nature, 241, 101-104, 1973.

Aki, K., A. Christofferson and E. S. Husebye, Three-dimensional seismic structure of the lithosphere under Montana LASA, Bull. Seismol. Soc. Am., 66, 501-524, 1976.

Aki, K., A. Christofferson and E. S. Husebye, Determination of the three-dimensional seismic structure of the lithosphere, J. Geophys. Res., 82, 277-296, 1977.

Allen, C. R., San Andreas fault zone in San Gorgonio Pass, Southern California, Geol. Soc. Amer. Bull., 68, 315-350, 1957.

Anderson, D. L., Chemical plumes in the mantle, Geol. Soc. Am. Bull., 86, 1593-1600, 1975.

Anderson, D. L. and H. Spetzler, Partial melting and the low-velocity zone, Phys. Earth Planet. Int., 4, 62-64, 1970.

Anderson, D. L. and J. H. Whitcomb, Time-dependent seismology, J. Geophys. Res., 80, 1497-1503, 1975.

Archambeau, C. B., E. A. Flinn and D. G. Lambert, Fine structure of the upper mantle, J. Geophys. Res., 74, 5825-5865, 1969.

Atwater, T., Implications of plate tectonics for the Cenozoic tectonic evolution of western North America, Bull. Geol. Soc. Am., 81, 3513-3536, 1970.

Bamford, D., Refraction data in West Germany: a time term interpretation, Z. Geophys., 39, 907-927, 1973.

Bateman, P. C. and C. Wahrhaftig, Geology of the Sierra Nevada, Calif. Div. Mines Bull., 190, 107-172, 1966.

Biehler, S., R. L. Kovach and C. R. Allen, Geophysical framework of northern end of Gulf of California structural province, Am. Assoc. Petroleum Geologists Mem. 3, 126-143, 1964.

Biswas, N. N. and L. Knopoff, The structure of the upper mantle under the United States from the dispersion of Rayleigh waves, Geophys. J. R. astr. Soc., 36, 515-539, 1974.

Bolt, B. A., Constancy of P travel-times from Nevada explosions to Oroville Dam station 1970-1976, Bull. Seism. Soc. Am., 67, 27-32, 1977.

Bolt, B. A. and O. W. Nuttli, P wave residuals as a function of azimuth, 1. Observations, J. Geophys. Res., 71, 5977-5985, 1966.

Butler, R. and D. L. Anderson, Equation of state fits to the lower mantle and outer core, preprint, 1977.

Campbell, R. H. and R. F. Yerkes, Cenozoic evolution of the Los Angeles basin area: relation to plate tectonics, in Howell, D. G., ed., Aspects of the geologic history of the California continental borderland, Am. Assoc. Pet. Geol. Misc. Pub., 24, 541-558, 1976.

Carder, D. S., D. W. Gordon and J. N. Jordan, Analysis of surface-foci travel times, Bull. Seism. Soc. Am., 56, 815-840, 1966.

Castle, R. O., J. P. Church and M. R. Elliott, Aseismic uplift in Southern California, Science, 192, 251-253, 1976.

Castle, R. O., M. R. Elliott and S. H. Wood, The Southern California uplift, EOS Trans. Am. Geophys. U., 58, 495, 1977.

Chesnokov, Y. M. and M. V. Nevskiy, Seismic anisotropy investigations in the U.S.S.R., Geophys. J. R. astr. Soc., 49, 115-121, 1977.

Cramer, C. H., Teleseismic residuals prior to the November 28, 1974, Thanksgiving Day earthquake near Hollister, California, Bull. Seism. Soc. Am., 66, 1233-1248, 1976.

Cramer, C. H., C. G. Bufe and P. W. Morrison, P-wave travel-time variations before the August 1, 1975 Oroville earthquake, Bull. Seism. Soc. Am., 67, 9-26, 1977.

Crough, S. T. and G. A. Thompson, Upper mantle origin of the Sierra Nevada uplift, Geology, 5, 396-399, 1977.

Crowell, J. C., Movement histories of faults in the Transverse Ranges and speculations of the tectonic history of California, in Dickenson, W. R. and A. Grantz eds., Proc. Conf. on geol. problems of San Andreas fault system: Stanford Univ. Pubs. Geol. Sci., 11, 323-341, 1968.

Dibblee, T. W., Geologic map of the Lucerne Valley quadrangle, San Bernardino County, California, U. S. Geol. Survey Misc. Geol. Inv. Map 1-426, 1964.

Doyle, L. J. and O. L. Bandy, Southern continental borderland, Baja California: its tectonic and environmental development, Bull. Geol. Soc. Am., 83, 3285-3794, 1972.

Dziewonski, A. M., B. H. Hager and R. J. O'Connell, Large scale heterogeneities in the lower mantle, J. Geophys. Res., 82, 239-255, 1977.

Ellsworth, W. L. and R. Y. Koyanagi, Three-dimensional crust and mantle structure of Kilauea Volcano, Hawaii, J. Geophys. Res., 82, 5379-5394, 1977.

Engdahl, E. R., Effects of plate structure and dilatancy on relative teleseismic P-wave residuals, Geophys. Res. Lett., 2, 420-422, 1975.

Engdahl, E. R., J. G. Sinndorf, and R. A. Eppley, Interpretation of relative teleseismic P-wave residuals, J. Geophys. Res., 82, 5671-5682, 1977.

Fowler, C. M. R., Crustal structure of the mid-Atlantic ridge crest at 37°N, Geophys. J. R. astr. Soc., 47, 459-491, 1976.

Fuchs, K., Seismic anisotropy of the subcrustal lithosphere as evidence for dynamical processes in the upper mantle, Geophys. J. R. astr. Soc., 49, 167-179, 1977.

Gupta, I. N., Dilatancy and premonitory variations of P, S travel times, Bull. Seism. Soc. Am., 63, 1157-1161, 1973a.

Gupta, I. N., Seismic velocities in rock subjected to axial loading up to shear fracture, J. Geophys. Res., 78, 6936-6942, 1973b.

Gutenberg, B., Travel times of principal P and S waves over small distances in southern California, Bull. Seism. Soc. Am., 34, 13-32, 1944.

Gutenberg, B., Revised travel times in southern California, Bull. Seism. Soc. Am., 62, 427-439, 1951.

Gutenberg, B., Waves from blasts recorded in Southern California, Trans. Am. Geophys. Union, 33, 427-431, 1952.

Hadley, D. and J. Combs, Micro-earthquake distribution and mechanisms of faulting in the Fontana-San Bernardino area of Southern California, Bull. Seism. Soc. Am., 64, 1477-1499, 1974.

Hadley, D. and H. Kanamori, Seismic structure of the Transverse Ranges, Bull. Geol. Soc. Am., 88, 1469-1478, 1977.

Hadley, D. M., G. S. Stewart and J. E. Ebel, Yellowstone: Seismic evidence for a chemical mantle plume, Science, 193, 1237-1239, 1976.

Hart, R. S., The distribution of seismic velocities and attenuation in the earth, Ph.D. Thesis, California Institute of Technology, 1977.

Healy, J. H., Crustal structure along the coast of California from seismic refraction measurements, J. Geophys. Res., 68, 5777-5787, 1963.

Helmberger, D. V., On the structure of the low velocity zone, Geophys. J. R. astr. Soc., 34, 251-263, 1973.

Herrin, E., 1968 Seismological tables for P phases, Bull. Seism. Soc. Am., 58, 1193-1241, 1968.

Hess, H. H., Seismic anisotropy of the upper mantle under oceans, Nature, 203, 629-631, 1964.

Higgins, J. W., ed., A Guide to the Geology and Oilfields of the Los Angeles and Ventura Regions, Pacific Section, Am. Assoc. Petrol. Geol., 1958.

Huffman, O. F., Miocene and post-Miocene offset on the San Andreas fault in central California, Geol. Soc. Amer. Cord. Sect. 66th Ann. Mtg., 2, 104-105 (Abstract), 1970.

Husebye, E. S., A. Christofferson, K. Aki and C. Powell, Preliminary results on the three-dimensional seismic structure of the lithosphere under the U.S.G.S. central California seismic array, Geophys. J. R. astr. Soc., 46, 319-340, 1976.

Iyer, H. M., Anomalous delays of teleseismic P-waves in Yellowstone National Park, Nature, 253, 425-427, 1975.

Iyer, H. M., J. R. Evans, and J. Coakley, Teleseismic evidence for the existence of low-velocity material deep into the upper mantle under the Yellowstone Caldera, EOS Trans. Amer. Geophys. Union, 55, 1191, (Abstract), 1974.

Jeffreys, H. and K. E. Bullen, Seismological Tables, Brit. Assoc. Adv. of Sci., Gray-Milne Trust, London, 55 pp., 1940.

Johnson, L. R., Array measurements of P-velocities in the lower mantle, Bull. Seism. Soc. Am., 59, 973-1008, 1969.

Johnston, A. C., Localized compressional velocity decrease precursory to the Kalapana, Hawaii, earthquake, Science, 199, 882-885, 1978.

Kanamori, H. and W. Y. Chung, Temporal changes in P-wave velocity in Southern California, Tectonophys., 23, 67-78, 1974.

Kanamori, H. and G. Fuis, Variation of P-wave velocity before and after the Galway Lake earthquake (M_L = 5.2) and the Goat Mountain earthquakes (M_L = 4.7, 4.7), 1975 in the Mojave Desert, California, Bull. Seism. Soc. Am., 66, 2017-2037, 1976.

Kanamori, H. and D. Hadley, Crustal structure and temporal velocity change in Southern California, Pageoph., 113, 257-280, 1975.

Keller, G. R., R. B. Smith and L. W. Braile, Crustal structure along the Great Basin-Colorado Plateau transition from seismic refraction studies, J. Geophys. Res., 80, 1093-1098, 1975.

Koizumi, C. J., A. Ryall and K. F. Priestley, Evidence for a high velocity lithospheric plate under northern Nevada, Bull. Seism. Soc. Am., 63, 2135-2144, 1973.

Kovach, R. L., C. R. Allen and F. Press, Geophysical investigations in the Colorado Delta region, J. Geophys. Res., 67, 2845-2871, 1962.

Kraus, D. C., Tectonics, bathymetry and geomagnetism of the southern continental borderland west of Baja California, Mexico, Bull. Geol. Soc. Am., 76, 617-650, 1965.

Lang, H. R., San Clemente Oilfield, Calif. Div. Oil and Gas,,Summary of Operations, Oilfields, 58, 51-56, 1972.

Larsen, E. S., Jr., Crystalline rocks of the Corona, Elsinore and San Luis Rey quadrangles, Southern California, Geol. Soc. Am. Mem., 29, 1948.

Levenberg, K., A method for the solution of certain non-linear problems in least squares, Quart. Appl. Math., 2, 164-168, 1944.

McCulloh, Thane H., Gravity variations and the geology of the Los Angeles Basin of California, U.S. Geol. Surv. Prof. Paper 400-5, 320-325, 1960.

Menke, W. H., Lateral inhomogeneities in P-velocity under the Tarbela array of the Lesser Himalayas of Pakistan, Bull. Seism. Soc. Am., 67, 725-734, 1977.

Morton, P. K., Geology of the southern half of the Cañada Gobernadora quadrangle, Calif. Div. Mines and Geol. Spec. Report, 111, 1974.

Nuttli, O. W. and B. A. Bolt, P-wave residuals as a function of azimuth 2. Undulations of the mantle low-velocity layer as an explanation, J. Geophys. Res., 74, 6594-6602, 1969.

Ohtake, M., Changes in the v_p/v_s ratio related with the occurrence of some shallow earthquakes in Japan, J. Phys. Earth, 21, 173-184, 1973.

Peake, L. G. and J. H. Healy, A method for determination of the lower crustal structure along the San Andreas fault system in central California, Bull. Seism. Soc. Am., 67, 793-807, 1977.

Peselnick, L., J. P. Lockwood and R. Stewart, Anisotropic elastic velocities of some upper mantle xenoliths underlying the Sierra Nevada batholith, J. Geophys. Res., 82, 2005-2010, 1977.

Powell, C. A., Mantle heterogeneity: evidence from large seismic arrays, Ph.D. Thesis, Princeton University, 1976.

Powell, C. A. and S. A. Raikes, The Caltech array diagram, manuscript in preparation, 1978.

Powell, C. J. and J. H. Whitcomb, The variations of local P-wave residuals with time at Caltech-U.S.G.S. Southern California seismic stations, Bull. Seism. Soc. Am., submitted, 1978.

Press, F., Determination of crustal structure from phase velocity of Rayleigh waves, Part 1: Southern California, Bull. Geol. Soc. Am., 67, 1647-1658, 1956.

Press, F., Crustal structure in the California-Nevada region, J. Geophys. Res., 65, 1039-1051, 1960.

Raikes, S. A., The azimuthal variation of teleseismic P-wave residuals in Southern California, Earth Planet. Sci. Lett., 29, 367-372, 1976.

Rex, R. W., Investigations of geothermal resources in the Imperial Valley and their potential value for desalination of water and electricity production, University of California at Riverside Education Research Service, June, 1970, 14 pp.

Richter, C. F., Velocities of P at short distances, Bull. Seism. Soc. Am., 40, 281-289, 1950.

Rikitake, T., Earthquake precursors, Bull. Seism. Soc. Am., 65, 1133-1162, 1975.

Ringwood, A. E., Composition and Petrology of the Earth's Mantle, McGraw-Hill, New York, 1975, 618 pp.

Roller, J. C. and J. H. Healy, Seismic-refraction measurements between Santa Monica Bay and Lake Mead, J. Geophys. Res., 68, 5837-5849, 1963.

Rosendahl, B. R., R. W. Raitt, L. M. Dorman, L. D. Bibee, D. M. Hussong, and G. H. Sutton, Evolution of oceanic crust. 1. A physical model of the East Pacific Rise crest derived from seismic refraction data, J. Geophys. Res., 81, 5294-5314, 1976.

Roy, R. F., D. D. Blackwell and E. R. Decker, Continental heat flow, in The Nature of the Solid Earth, E. C. Robertson ed., McGraw-Hill, New York, 506-543, 1972.

Sanford, A. R., O. Alpetkin, and T. R. Toppozada, Use of reflection phases on microearthquake seismograms to map an unusual discontinuity beneath the Rio Grande rift, Bull. Seism. Soc. Am., 63, 2021-2034, 1973.

Savarensky, E. F., On the prediction of earthquakes, Tectonophys., 6, 17-27, 1968.

Semenov, A. M., Variations in the travel-time of transverse and longitudinal waves before violent earthquakes, Izv. Earth Phys., 4, 245-248 (English Trans.), 1969.

Sengupta, M. K. and B. R. Julian, P-wave travel times from deep earthquakes, Bull. Seism. Soc. Am., 66, 1555-1579, 1976.

Shankland, T. J. and H. S. Waff, Partial melting and electrical conductivity anomalies in the upper mantle, J. Geophys. Res., 82, 5409-5417, 1977.

Shor, G. G. and R. W. Raitt, Seismic studies in the Southern California borderland, International Geological Congress, 20th, Mexico, 1956, Geofisica aplicada (Secc. 9) t2, 243-259.

Solomon, S. C. and R. G. Butler, Prospecting for dead slabs, Earth Planet. Sci. Lett., 21, 421-430, 1974.

Spence, W., P-wave residual differences and inferences on an upper mantle source for the Silent Canyon volcanic centre, southern Great Basin, Nevada, Geophys. J. R. astr. Soc., 38, 505-523, 1974.

Steeples, D. W. and H. M. Iyer, Low velocity zone under Long Valley as determined from teleseismic events, J. Geophys. Res., 81, 849-860, 1976.

Stewart, G. S., Prediction of the Pt. Mugu earthquake by two methods, in, Proceedings of the Conference on Tectonic Problems of the San Andreas Fault System, Robert L. Kovach and Amos Nur eds., Geological Sciences 13, School of Earth Sciences, Stanford Univ., 473-478, 1973.

Talwani, M., C. C. Windisch and M. G. Langseth, Jr., Reykjanes Ridge crest: a detailed geophysical study, J. Geophys. Res., 76, 473-517, 1971.

Thompson, G. A. and M. Talwani, Crustal structure from Pacific Basin to Central Nevada, J. Geophys. Res., 69, 4813-4837, 1964.

United States Geological Survey, Preliminary Report on the Geology of the Continental Borderland, Southern California, Map MF-624, 1974.

Vedder, J. G., H. Wagner and J. E. Schoellhamer, Geologic Framework of the Santa Barbara Channel region, U. S. Geol. Surv. Prof. Paper 679, 1-12, 1969.

Whitcomb, J. H., Earthquake prediction: a hypothesis test. Seismic velocity variations in a region of Southern California predict a magnitude 5.5-6.5 earthquake, in, "Some Aspects of the Developing Science of Earthquake Prediction", J. H. Whitcomb, ed., Final report of the Seismological Laboratory for its portion of the California Institute of Technology study "Earthquake Predictions: A social

and Economic Assessment of Emerging Technical Possibilities", July, 1976.

Whitcomb, J. H. and D. L. Anderson, Reflection of P'P' seismic waves from discontinuities in the mantle, J. Geophys. Res., 75, 5713-5728, 1970.

Whitcomb, J. H., J. D. Garmany and D. L. Anderson, Earthquake prediction: variation of seismic velocities before the San Fernando earthquake, Science, 180, 632-635, 1973.

Whitcomb, J. H., H. Kanamori and D. M. Hadley, Earthquake prediction: variation of seismic velocities in Southern California, EOS Trans. Am. Geophys. U., 55, 355, 1974.

Wyss, M. and A. J. Johnston, A search for teleseismic P residual changes before large earthquakes in New Zealand, J. Geophys. Res., 79, 3283-3290, 1974.

Yeats, R. S., Neogene tectonics of the central Ventura Basin, California, in, The Neogene Symposium, E. Fritsche et al., eds., S.E.P.M. Spec. Pub., 19-32, 1976.

Yerkes, R. F., T. H. McCulloh, J. E. Schoellhamer and J. G. Vedder, Geology of the Los Angeles Basin, California -- an introduction U. S. Geol. Surv. Prof. Paper 420-A, 1965.

PART II

POST-SHOCK TEMPERATURES: THEIR EXPERIMENTAL DETERMINATION, CALCULATION, AND IMPLICATIONS

Chapter 7

INTRODUCTION

Shock wave equation of state data have long been used in the interpretation of impact metamorphism (e.g., Stoffler, 1971, 1972) and of density-depth profiles of the earth obtained from seismic data (e.g., Al'tschuler, 1965). However, one of the limitations to these uses of Hugoniot data is the uncertainty in the temperatures reached both during the passage of the shock wave through the material and after unloading. For comparison with earth structure, Hugoniot data must first be reduced to isothermal or adiabatic form. This is generally done by introducing a Mie-Grüneisen equation of state, which has the form

$$P_H - P_O = \frac{\gamma}{v} (E_H - E_O) \tag{1}$$

where P_H = Hugoniot pressure, v = corresponding specific volume, E_H = Hugoniot energy, γ = Grüneisen parameter, E_O = internal energy of isothermal compression at 0°K to specific volume v, P_O = pressure required for isothermal compression = $-(\partial E_O/\partial v)_T$. An alternative way of expressing this, due to Shapiro and Knopoff (1969), is that the Hugoniot pressure is the sum of an "elastic" pressure P_e and a term proportional to the thermal energy, P_T:

$$P_H = P_e + P_T \tag{2}$$

Introducing the Debye formulation for the thermal energy this becomes

$$P_H = P_e(v) + \frac{\gamma(v)}{v} \cdot \frac{3RT}{M} D\left[\frac{\Theta(v)}{T}\right] \tag{3}$$

where T = temperature, M = molecular weight, R = gas constant, $D\left[\frac{\Theta(v)}{T}\right]$ = the Debye function.

But, for materials which undergo phase changes, such as silicates, the Mie-Grüneisen equation of state is not really adequate, and the reduction involves the use of Grüneisen's parameter, the behaviour of which is poorly known. Possible constraints on these problems could be derived if the nature of the thermal processes taking place under shock conditions, as indicated by the shock or post-shock temperatures, were better understood.

Shock temperatures are generally calculated using the Hugoniot data and the Mie-Grüneisen theory (e.g., Walsh and Christian, 1955; Wackerle, 1962; Ahrens et al., 1969; McQueen et al., 1970) which should yield fairly reliable results for metals. However, the Mie-Grüneisen theory is inadequate for silicates since these all undergo major phase changes which may involve substantial changes in thermodynamic properties. These Hugoniot temperatures are then used to calculate post-shock temperatures assuming adiabatic release, but the latter are highly dependent on the release path, which must be estimated. In the absence of release adiabat data, the path is generally implicitly assumed to lie above the Hugoniot in (P, V) space (Figure 7-1). The decompression is usually taken to be isentropic, in which case the release temperature is calculated from the Hugoniot temperature using the relation

$$T_R = T_H \exp\left[-\int_{V_H}^{V_R} \frac{\gamma}{v}\, dv \right] \qquad (4)$$

where T = temperature, v = specific volume, γ = Grüneisen parameter, and the subscripts R and H refer to the release and Hugoniot states,

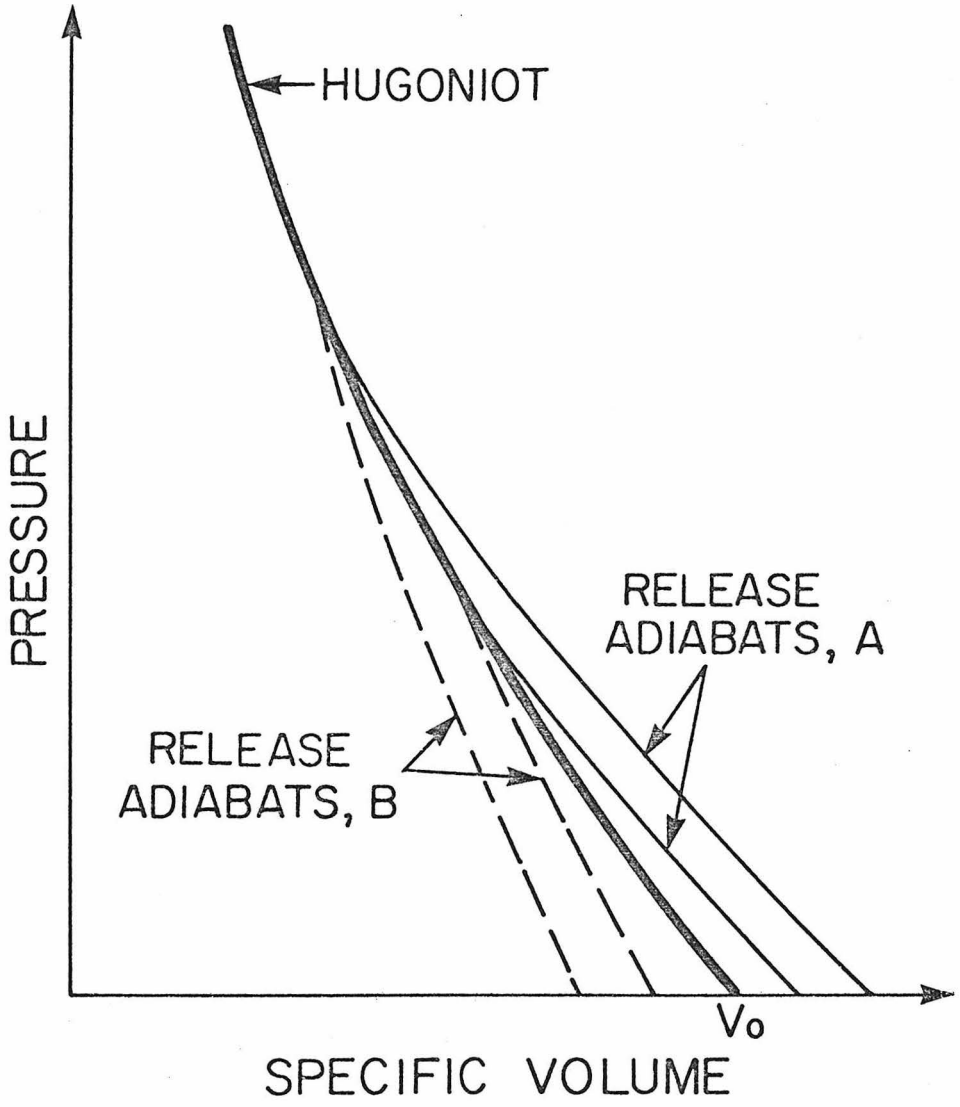

Figure 7-1. Schematic diagram of Hugoniot and possible release adiabats. The solid release curves lie above the Hugoniot, and the dashed ones below it.

respectively. It has been suggested, however, that the release might be isenthalpic rather than isentropic (Waldbaum, 1971); in this case, the change in temperature is given by the Joule-Thompson coefficient

$$\left(\frac{\partial T}{\partial P}\right) = \frac{V(T\alpha_p - 1)}{C_p} \qquad (5)$$

where T = temperature, P = pressure, V = volume at P, T, α_p = isobaric thermal expansion, C_p = isobaric heat capacity. The value of this coefficient is negative for a number of materials including spinel, forsterite, diopside and α-iron, and thus isenthalpic decompression will lead to an increase in temperature.

Calculations of post-shock temperatures in silicates, assuming release along isentropes lying above the Hugoniot, lead to values that appear too low to account for some of the effects seen in recovery experiments, such as the change in refractive index observed in shocked silicate glasses (Gibbons, 1974). If release adiabat data do exist, they may be used in the calculation of post-shock temperatures (e.g., Gibbons and Ahrens, 1971; Ahrens and O'Keefe, 1972); this leads to much higher, and possibly more credible, release temperatures (as is shown in the comparison in Table 7-1), largely because the release paths lie below the Hugoniot (see Figure 7-1). However, no experimental tests of such calculations have been carried out for earth materials, and serious uncertainties exist in the post-shock temperatures of silicates of geophysical importance such as quartz and forsterite, even for material shocked to very modest pressure levels.

In view of the uncertainties that exist in the post-shock temperatures for silicates, their experimental measurement is important

Table 7-1

CALCULATED POST SHOCK TEMPERATURES
IN FUSED QUARTZ AND OLIGOCLASE,

using the Mie-Grüneisen Theory (A) or Release Adiabat Data (B)

Shock Pressure GPa	Post Shock Temperatures, °C			
	Fused Quartz		Oligoclase	
	A[1]	B[2]	A[3]	B[4]
10.0	0	80		
15.0	0	450		
18.0			27- 35	269-386
25.0	0	1220		
27.2			129-206	> 742
30.0	470	1480		
40.0	1860	2180		
41.7			327-395	>1031
50.0	3310	2820		

1. Wackerle (1962)
2. Gibbons and Ahrens (1971)
3. Ahrens et al. (1969)
4. Ahrens and O'Keefe (1972)

and could substantially increase the level of understanding of processes occurring under shock compression as well as providing valuable constraints on the thermal equation of state at high pressures.

Early successful experiments designed to measure post-shock temperatures in explosively shocked metals by Taylor (1963) and King et al. (1967) were carried out with a photo-multiplier tube and InSb infra-red radiation detector respectively. Taylor's experiments were on copper plates shocked to pressures in the range 90 to 170 GPa, and his measured residual temperatures agreed well with those predicted by McQueen and Marsh (1960) using the Mie-Grüneisen theory. King et al. endeavoured to extend the measurements to a lower pressure range and found good agreement between theoretical and measured temperatures for lead, but a large discrepancy for copper. Later experiments on copper (Von Holle and Trimble, 1976) confirmed that for pressures less than 80 GPa the measured residual temperatures were considerably higher than those calculated. Some of the difference, especially at low pressures, may be explained by the contribution of elastic-plastic work (e.g., Foltz and Grace, 1969), and the remainder may be due to non-hydrodynamic surface effects. These types of experiments were never really pursued because for moderate shock pressures in metals serious uncertainties in shock or post-shock temperatures did not appear to exist. More recently, attempts have been made to determine radiatively shock temperatures in metals at pressures around 50 GPa and temperatures close to the melting point (e.g., Urtiew and Grover, 1973). Experiments to determine the temperature distribution within shocked steel targets have also been carried out (Schneider and Stilp, 1977) using thermocouples

located at various points within the target. The temperatures they measured, which are by definition residual temperatures because of the slow, ∿50 ms, rise time of the thermocouples, decayed rapidly as a function of time, and as a function of distance from the centre of the impact, the maximum increase being ∿20°C. (However, because of the time-scales involved, this may not be a true post-shock temperature as calculated using the Mie-Grüneisen theory.)

Experiments on non-metals have largely been limited to the determination of radiative properties of materials under extremely high pressures. Some attempts have been made to measure actual shock temperatures (Kormer, 1968) either photographically or photo-electrically, but these are limited to transparent materials where the radiation from the shock front may be observed as it propagates through the material, eliminating the necessity of having a detector with a rise time similar to that of the shock wave. In particular, optical measurements in the visible region have been used to investigate the melting curve for alkali halides under pressures in the range 50 to 300 GPa (Kormer et al., 1965).

However, no attempts were made to expand the scope of the early experiments, such as those of Taylor and King et al., to include the measurement of post-shock temperatures in non-metals, even though large uncertainties exist for silicates. This was largely because the supposedly lower temperatures, coupled with the low sensitivity of available detectors, meant that experiments such as those of King et al. were not feasible. Recent improvements in detector technology have now made it possible to design a system capable of measuring post-

shock temperatures in silicates, and the availability of such data should help resolve the current uncertainties.

The difference between the residual temperatures calculated by different methods, is, for many materials, larger at low pressures where the elastic contributions and effect of phase changes are more important. Initial experiments were thus designed with the aim of investigating residual temperatures in silicates of geophysical interest shocked to pressures up to 30 GPa. The materials chosen were crystal quartz, Bamble bronzite (both of which undergo phase changes in this pressure range) and forsterite; for completeness, the metals used as driver plates in the experiments, aluminium-2024 and stainless steel-304, were also studied. Since the post-shock temperatures for the pressure range to be investigated were expected to be of the order of 100°C, the logical choice of instrument was an infra-red detector, which could be used to determine the brightness temperature of the back (free) surface of the material under shock. In addition, since silicates behave as fairly good black bodies in the infra-red beyond $\sim 5\mu$, with the exception of the silicate absorption band at $\sim 9\mu$, the radiative output of the sample is also maximised.

Once the post-shock temperatures have been determined experimentally, they may be evaluated in the light of various theories regarding their calculation. This should provide further insight into the nature of the thermal equation of state under shock conditions, and help in the interpretation of observations of shock metamorphism, and in the analysis of earth structure using Hugoniot data.

Chapter 8

THE EXPERIMENTAL TECHNIQUE

The method developed for experimental determination of post-shock temperatures involves the monitoring of radiation from the back (free) surface of a shocked sample with an infra-red radiation detector whose output may then be used to determine the brightness temperature of the sample. It is best described in two sections: the production of the shocked state, and the actual determination of the brightness temperatures. A schematic plan of the experimental lay-out is shown in Figure 8-1.

8.1. Production of Shocked State in the Sample Material

a. Experimental procedure.

In these experiments, a shocked state has been produced in the sample by the impact of a gun launched flyer plate. The technique is described in detail in Gibbons (1974), and has been used by a number of authors (e.g., Ahrens et al., 1971; Ahrens and Gaffney; 1971, King and Ahrens, 1976).

The gun used is a propellant gun, with a barrel ∿3.3 m long, and a ∿20 mm bore; it is capable of accelerating a typical projectile to speeds up to ∿2.5 km/s. The projectile consists of a metal (tungsten, stainless steel-304, aluminium-2024) flyer plate 15 mm in diameter and 2.5 mm thick pressed into the front of a polycarbonate (lexan) projectile about 25 mm long, and weighs from 7 to 16 grams depending on the flyer plate material. (In some cases, solid lexan projectiles, with thin copper foil discs glued to the front, were used to produce pressures less than ∿5 GPa.)

In all cases the propellant used was Bullseye Pistol powder, the

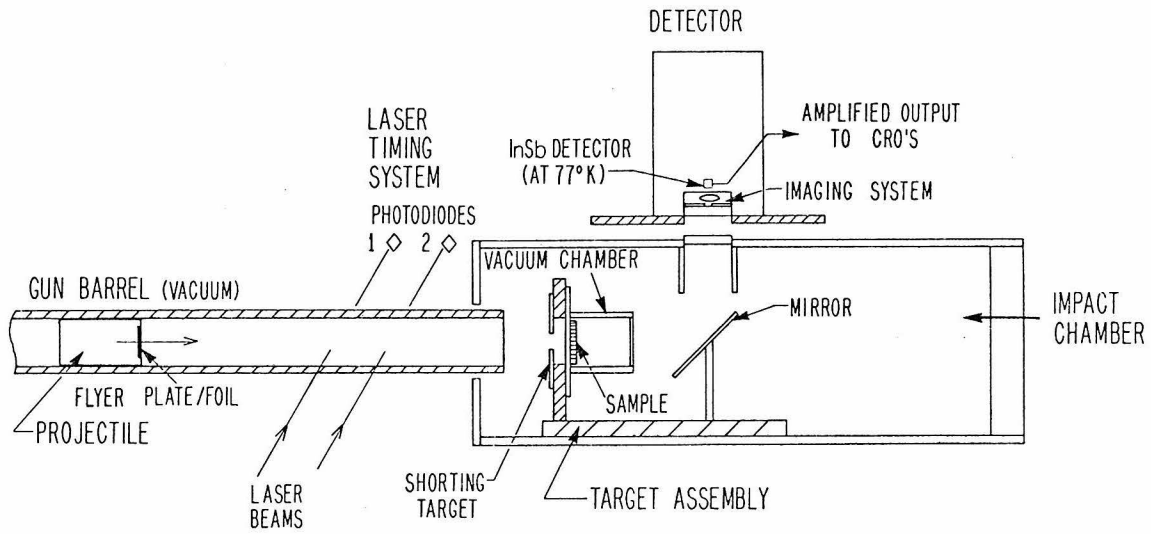

Figure 8-1. Schematic diagram of the experimental configuration. An oscilloscope recording the detector output at 50μs/div is triggered by the passage of the projectile past the first laser beam. A record having greater time resolution (5μs/div) is obtained from an oscilloscope triggered by the impact of the projectile with the shorting target.

amount varying from 1.75 to 14 g. The barrel was evacuated (to $\lesssim$5μ), both to increase the efficiency and to improve the quality of the timing traces. The projectile velocity is controlled by the amount of powder used: a graph of velocity as a function of the ratio of powder load to projectile mass (C/M) is shown in Figure 8-2. For a given flyer plate material, a good linear correlation exists between C/M and velocity, enabling the latter to be predetermined; this is an advantage since it allows temperature measurements to be made at regular pressure intervals, and measurement, in separate shots, of brightness temperatures at different wavelengths for the same pressure.

The velocity of the projectile is measured close to the end of the barrel using a laser timing system. In this, two laser beams (produced from a single laser using a beam splitter) are directed, perpendicular to the line of flight of the projectile, through windows in the barrel, and are then incident on two photo-diodes whose voltage output is monitored by a dual beam oscilloscope. The beams are separated by $\sim$6 cm, and this distance is measured prior to each shot using a micrometer gauge, with a vertical slide, designed to screw on to the end of the barrel. The slide is used to cut each laser beam in turn such that the amplitude of each photodiode signal is reduced to half its initial value; the difference between the two micrometer readings then gives the beam separation to .02 mm accuracy. When the front of the projectile passes the first laser beam, it causes the photodiode voltage to drop, triggering the oscilloscope sweep. The time interval between the points at which the two photodiode signals have dropped to half their initial level is measured from the oscilloscope trace and calibration

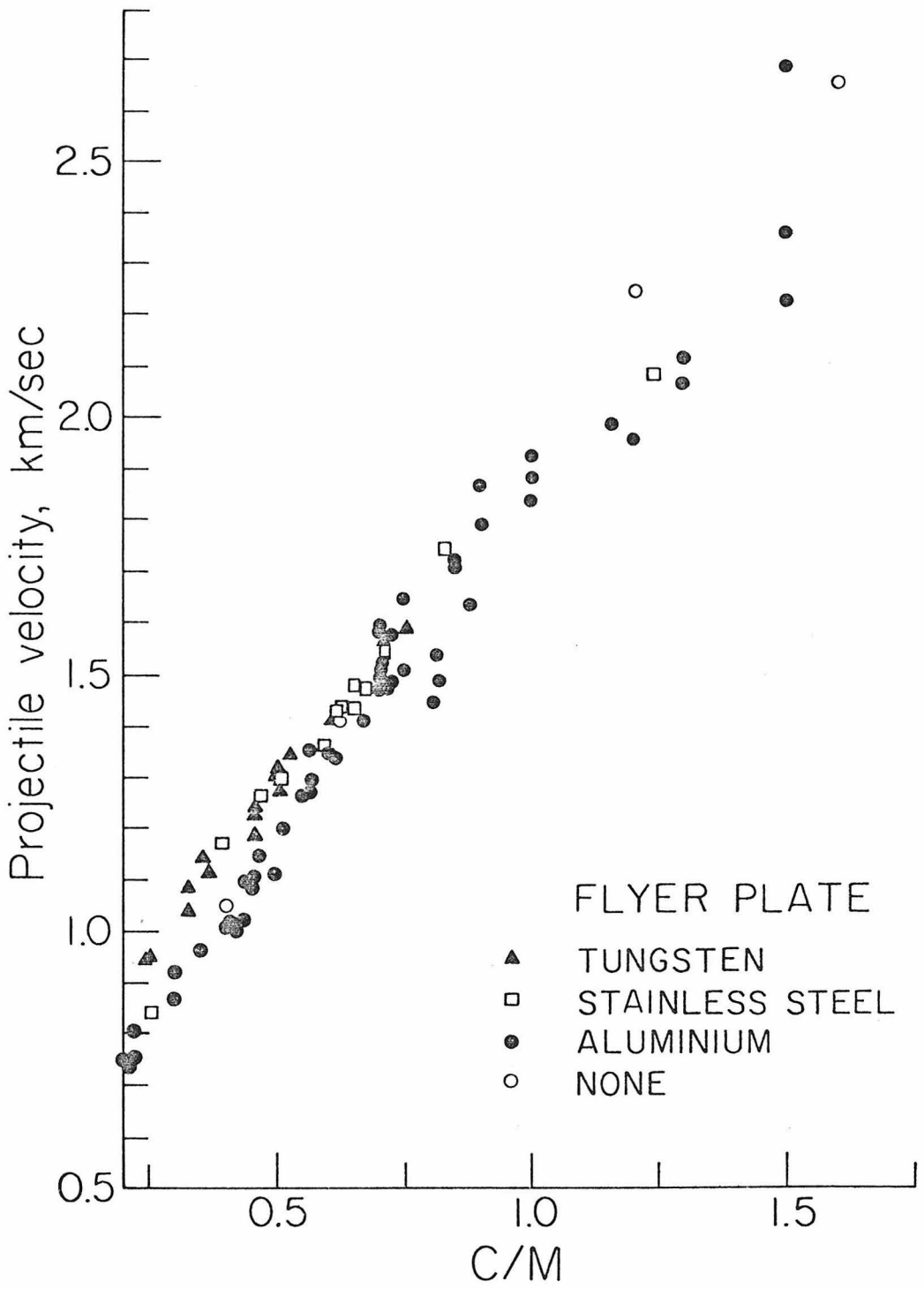

Figure 8-2. Plot of observed projectile velocity versus C/M ratio for different flyer plate materials. (C = weight of Bullseye powder, and M = weight of projectile.)

sweep (see Figure 8-3) and used to calculate the velocity. The timing accuracy is estimated at ±.5μs, and the velocity measurement is to ∿±.01 km/s.

After passing through the mylar window sealing the end of the barrel, the projectile makes contact across a shorting target and finally impacts the target assembly (see Figure 8-1). In order to reduce non-linear and non-planar shock effects, the target is carefully aligned, using a laser beam shining down the centre of the barrel, to maximise the planarity of the impact. The target assembly consists of a driver plate (1.5 mm aluminium-2024 or stainless steel-304), and a 3 mm thick silicate sample (15 mm in diameter) mounted on it by epoxy around the edges. (In the case of shots on metals, the driver plate is the sample.) The back of the sample is enclosed in a vacuum chamber, and the radiation from its free surface monitored by an infra-red detector calibrated for temperature determination.

Pressures reached in the sample are calculated using the measured Hugoniots of the flyer plate, driver plate, and sample materials, and the impedance match method described in detail below (see also Duvall and Fowles, 1963). Figure 8-4 shows the Hugoniots for the materials used in these experiments.

The accuracy of the pressure calculation depends on the precision of the velocity measurement and of the Hugoniot. In fact, the uncertainties in velocity are probably small compared with the scatter in the measured equation of state points, at least for natural materials such as crystalline quartz and Bamble bronzite, especially at pressures close to the Hugoniot elastic limit, which can vary from sample to sample, and

Figure 8-3. Typical photo-diode output records used in determining the projectile velocity. (a) is used to determine the signal amplitude for each beam. The distance between the points at which the two beams drop to half their initial amplitude in (b) is combined with the time calibration from (c) to give the projectile velocity. (Records from a shot with a tungsten projectile fired at 0.95 km/s, C/M = .252)

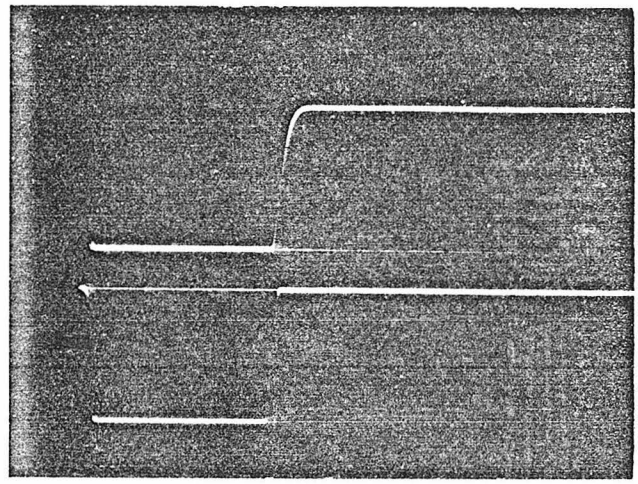

(a)

Pre-shot

5V/div.

20 μs/div.

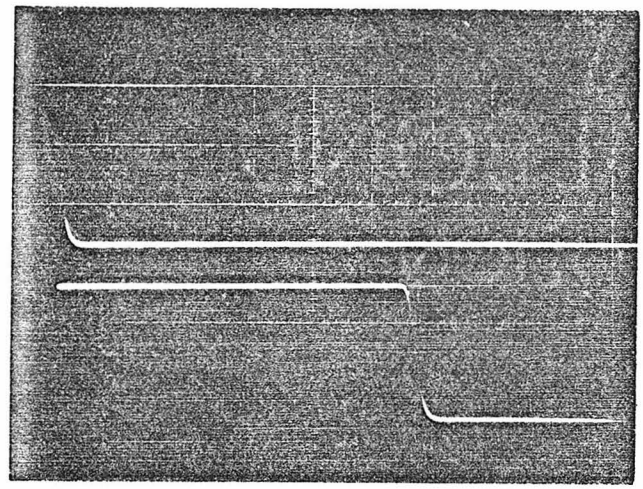

(b)

Timing record for shot

5V/div.

10 μs/div.

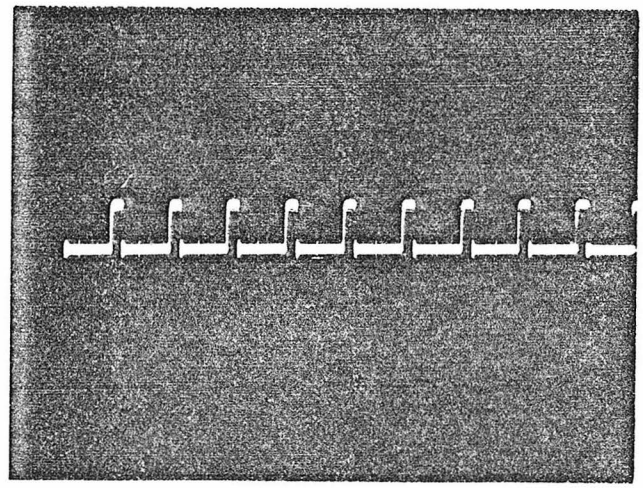

(c)

Time calibration

Frequency 100 kHz

10 μs/div.

Figure 8-3.

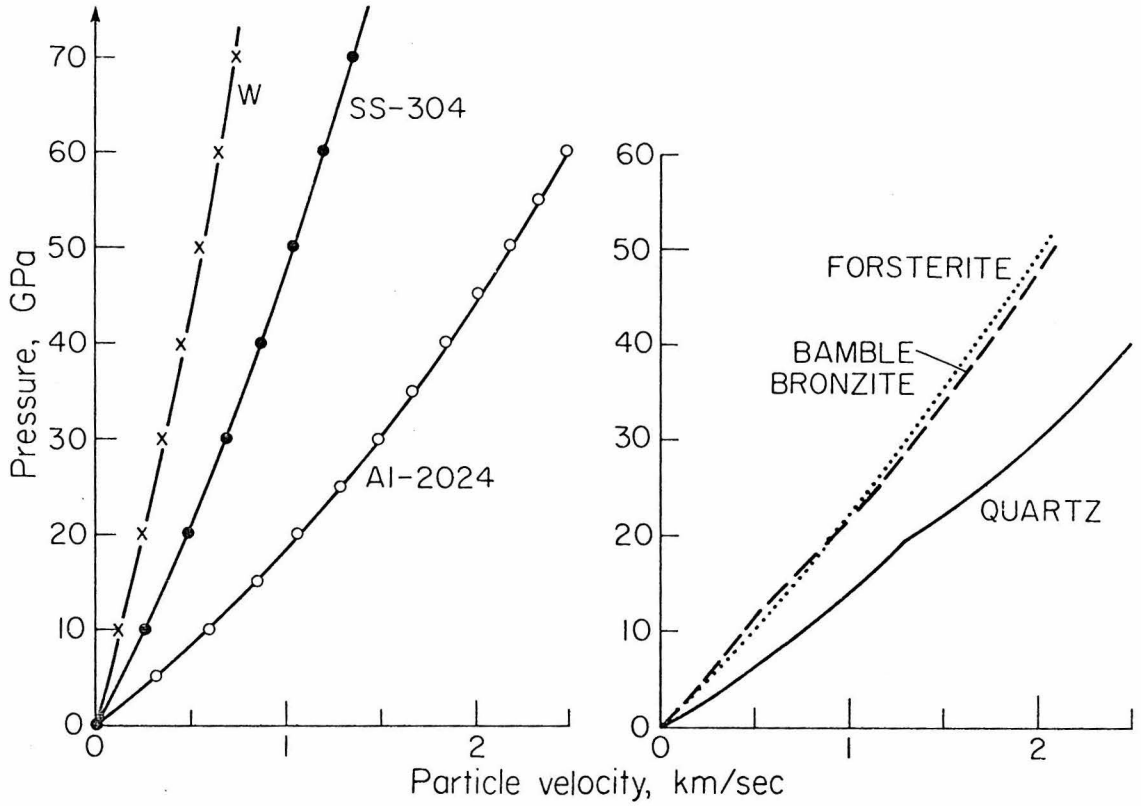

Figure 8-4. Hugoniots for the materials used in this study, plotted in the pressure-particle velocity plane.

to phase transitions. A likely estimate of the uncertainty in pressure would be ±.5 GPa in the metals, and ±.5 to 1 GPa in the other materials studied.

b. The impedance match method

For a plane shock wave travelling at velocity U through a material initial density ρ_o, compressed density ρ_1, and having a particle velocity of u_1 behind the shock, the conservation of mass may be expressed

$$\rho_o U = \rho_1 (U - u_1) \tag{1}$$

If the pressure on the unshocked medium is p_o, and on the shocked material p_1, the conservation of momentum leads to the relationship

$$p_1 - p_o = \rho_o U u_1 \tag{2}$$

Further, if the initial state has energy E_o, and the shocked state energy E_1, equating the work done to the gain in energy yields

$$p_1 u_1 = 1/2 \rho_o U u_1^2 + \rho_o U (E_1 - E_o) \tag{3}$$

Eliminating U and u_1, from (3) using (1) and (2) gives the Rankine-Hugoniot equation

$$E_1 - E_o = 1/2 (V_o - V_1) (P_1 + P_o) \tag{4}$$

where $V = 1/\rho$.

These equations may be generalised by superposing a uniform flow velocity U_o; this will allow consideration of the problem of transitions and interactions between dynamic states.

Equations (1) and (2) become

$$\rho_o (U - u_o) = \rho_1 (U - u_1) \tag{5}$$

$$p_1 - p_o = \rho_o (U - u_o) (u_1 - u_o) \tag{6}$$

Eliminating U from (5) and (6) gives the following relation between $p_1 - p_o$ and $u_1 - u_o$

$$u_1 - u_o = \pm\sqrt{(p_1 - p_o) (V_o - V_1)} \tag{7}$$

The positive sign represents states in which the material is accelerated from left to right, and the negative from right to left. In addition, transitions may occur through rarefactions which reduce the material to a lower pressure state.

When a plane shock wave is normally incident at a boundary between two materials, the pressure and particle velocity must be continuous at the interface. The dynamic state behind the reflected wave is the same for both media, and will lie at the intersection of the reflection Hugoniot for the first material and the Hugoniot of the second.

Figure 8-5 illustrates the determination of the shock state produced in a quartz sample, mounted on an aluminium driver plate, by the impact of a stainless steel flyer plate travelling at 2 km/s. Curves DB, DF and DJ are the Hugoniots for stainless steel-304, aluminium-2024 and quartz. The impact of the flyer plate produces a shock wave in the aluminium and a stopping shock in the steel. The latter state lies on the reflection Hugoniot for stainless steel passing through the projectile velocity u_p = 2 km/s, (i.e., a reflection of the Hugoniot about the line

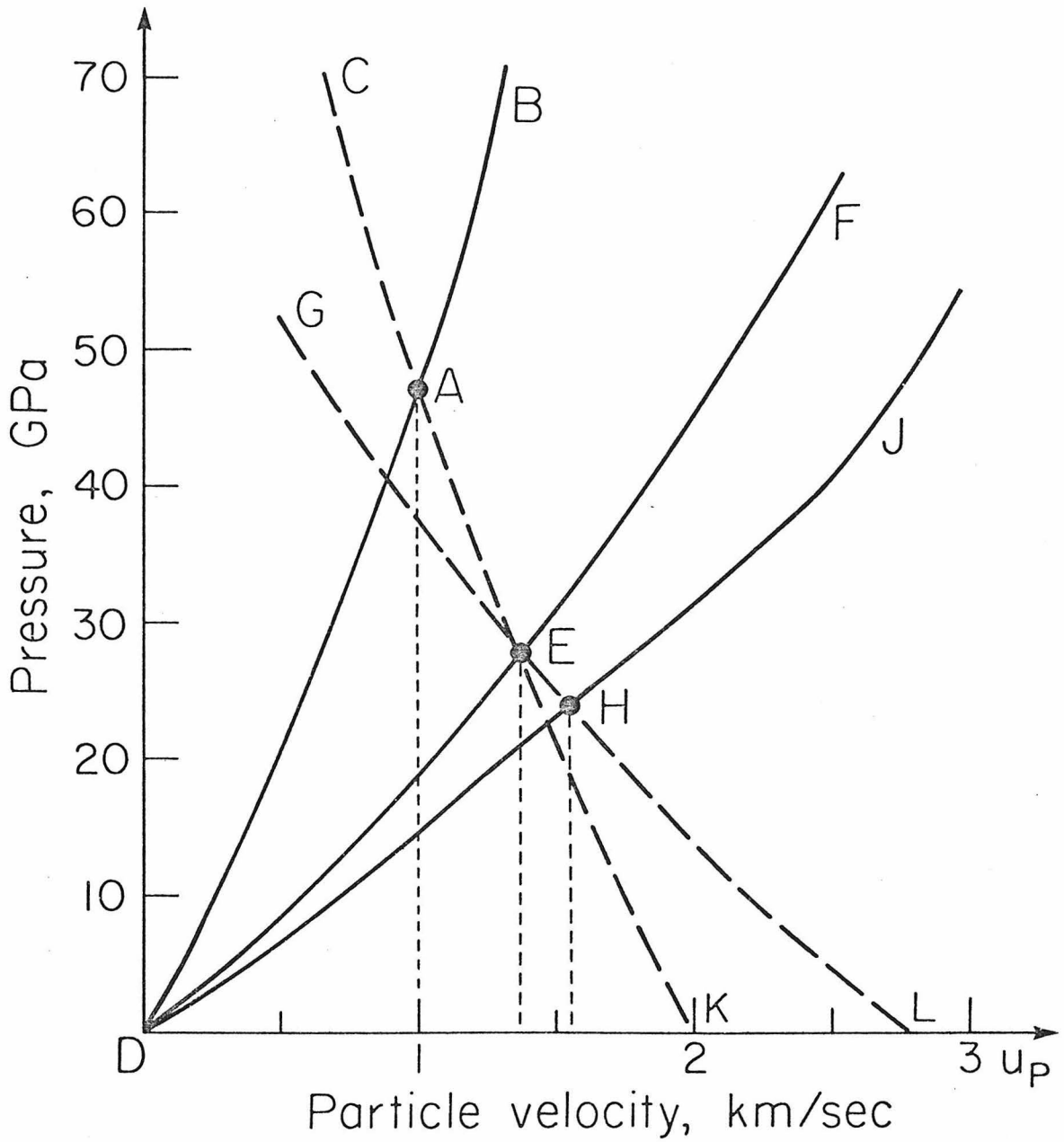

Figure 8-5. Impedance match solution for the impact of a stainless steel flyer plate on an aluminium driver plate bearing a quartz sample. For a detailed description, see text.

$u = u_p/2$ = 1 km/s), namely CAK in Figure 8-5. The former is given by the point of intersection of CAK and the aluminium Hugoniot DF, this is point E. Similarly, when the shock wave travelling through the aluminium impinges on the aluminium-quartz boundary, the resulting state must lie at the intersection of the aluminium reflection Hugoniot GEL and the quartz Hugoniot DJ. Thus the shock pressure in the quartz is the point H, or 24 GPa.

This illustrates the calculation of pressures in the case where flyer plate, driver plate and sample materials are different. If the flyer plate and driver plate materials are the same, then the shock state in the sample is given by the point of intersection of the reflection Hugoniot of the flyer/driver plate material about the line $u = u_p/2$ and the sample Hugoniot. The simplest cases are for aluminium impacted by an aluminium flyer plate, or stainless steel impacted by a stainless flyer plate, where the pressure is that corresponding to $u = u_p/2$.

8.2. Measurement of Temperature

As discussed in Chapter 7, the method developed for measurement of post-shock temperatures involves monitoring the radiation from the back (free) surface of the sample using an infra-red detector, and using the detector output to determine the brightness temperature of the surface. The detector is mounted above the impact chamber (see Figure 8-1), and monitors the back face of the sample via a mirror and optical system. The latter ensures that only the centre ($\sim$.8 cm dia.) of the sample is viewed, reducing the contribution from edge effects (also some-

what lessened by using a circular sample) and increasing the efficiency of the detection system. The detector is connected via an amplifier to two oscilloscopes. One is triggered by the passage of the projectile past the first laser beam of the timing system, and records the detector output at a rate of 50 μs/div. This provides a back-up record in case of failure of the higher time-resolution recording, and a means of checking that no temperature signals are generated prior to the passage of the shock wave through the sample assembly. (Note that it also provides another means of determining the projectile velocity.) The second oscilloscope is triggered by the contact of the flyer plate with the shorting target, which is approximately 75 mm in front of the driver plate, just prior to impact; this writes at 5 μs/div, and it is the record that is used in temperature determination. A typical record shows a sharp rise in signal corresponding to the arrival of the shock wave at the free surface of the sample, followed by a level portion corresponding to the residual temperature, and then a subsequent rise due to air shocks generated at the end of the sample chamber and the destruction of the mirror. Actual records will be discussed in detail in Chapter 9.

The detectors used in these experiments were InSb and HgCdTe; both are operated at 77°K and are enclosed in dewars cooled by liquid nitrogen. Response curves for these materials are shown in Figure 8-6; details of the principles of operation of these detectors, and their operational specifications, are given in Appendix A. In these experiments a filter was used to limit the bandwidth of the InSb detector to 4.5 to 5.75μ in order to minimise the possibility of radiation from the metal driver

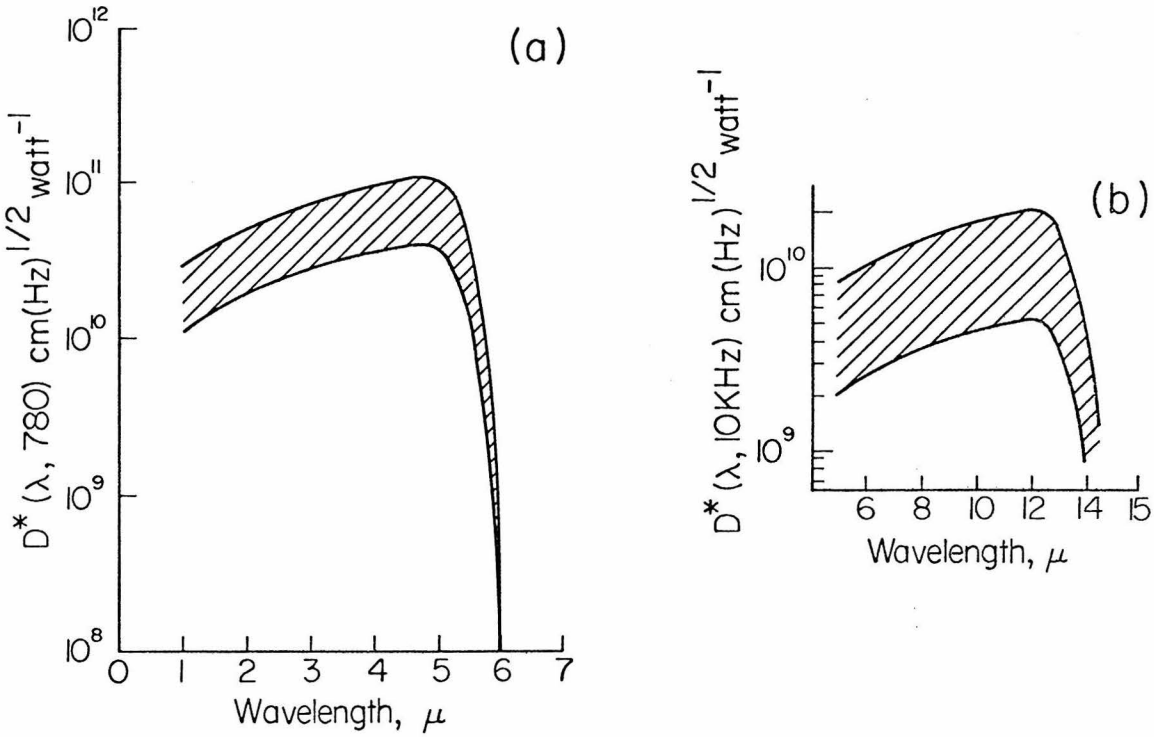

Figure 8-6. (a) Response curve for the InSb detector material. (b) Response curve for the HgCdTe detector material. Shaded areas indicate typical variations in detector sensitivity.

plate, or metal-sample interface, being transmitted through the sample and causing errors in the temperature determination. (Infra-red transmission scans for the non-metals studied are presented in Figure 8-7.) The InSb detector was used with a variable gain amplifier; the system rise time, which is essentially limited to $\sim$.25 μs by the chip itself, was $\lesssim$0.5 μs depending on the gain setting used. Although the HgCdTe is a faster material ($\lesssim$0.1 μs), the rise time of the detector-amplifier system was $\lesssim$.8 μs because a filter had to be used to reduce the large amount of high frequency noise which would otherwise have made accurate measurement of temperature impossible.

In order to convert the voltage record into a brightness temperature, the detector must be calibrated. This is best performed by heating the sample *in situ* to a known temperature, and recording the corresponding voltage output of the detector-amplifier system. This is easily done for metals, but would be very hard for the non-metals studied since they are extremely brittle and hard to heat in the experimental configuration without cracking. Instead, advantage was taken of the fact that they behave as fairly good black bodies beyond $\sim$4.5μ, with the exception of the silicate absorption band at $\sim$9μ, and a calibration curve obtained for a "black" body (graphite). Initial temperatures were determined by assuming that the material behaved as a black body; subsequently these values, which should in general be lower bounds, were corrected using measured values of the emissivity, where available. An emissivity of .8 would imply that the measured black body temperatures are $\sim$9% too low, and one of .5 values that are $\sim$35% low. A diagram of the apparatus used in detector

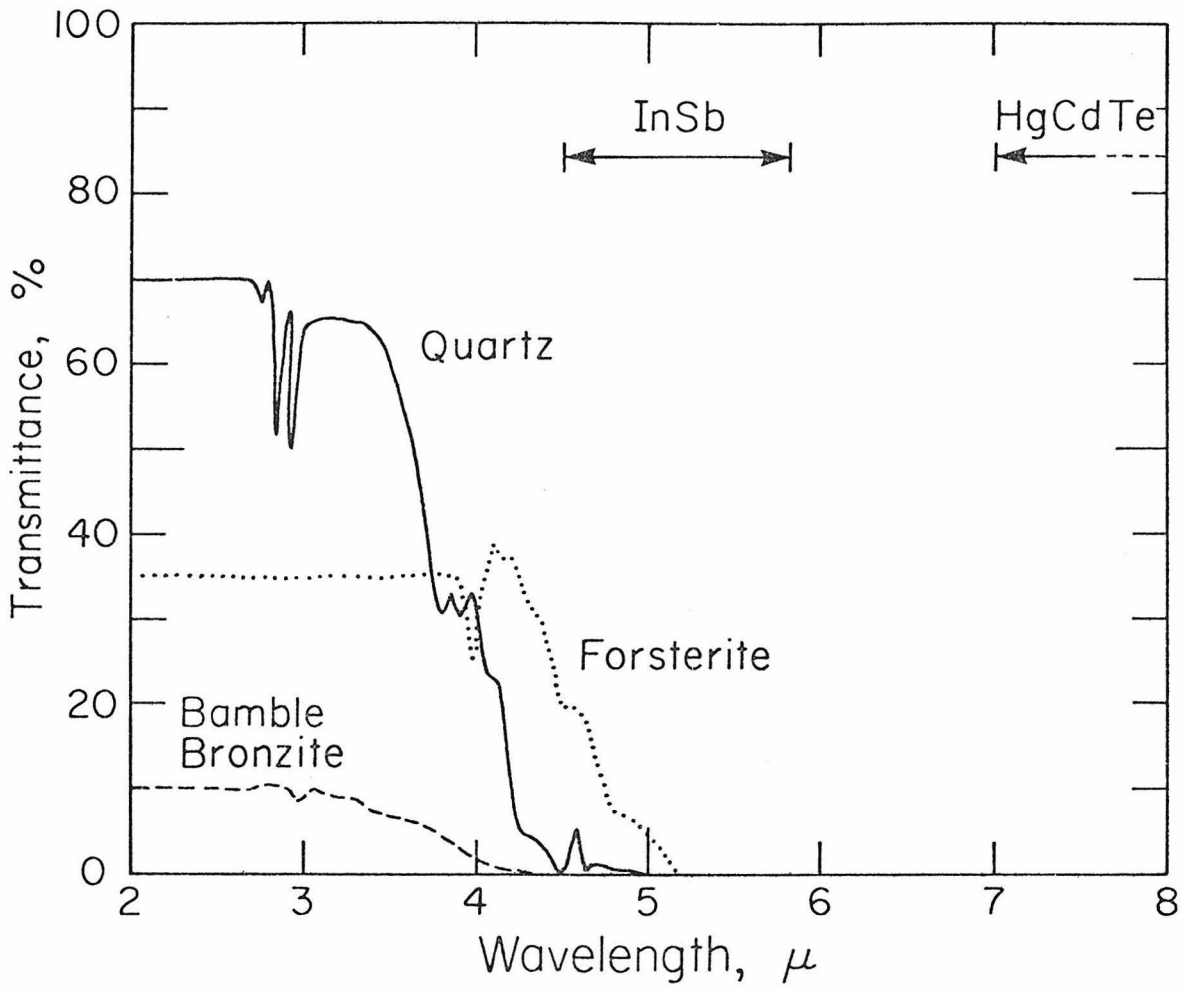

Figure 8-7. Infra-red transmission scans for the silicate materials studied. The operating range of the filtered InSb detector and the start of the HgCdTe band are also shown.

calibration is drawn in Figure 8-8: the "sample" is heated to a temperature T measured by the thermocouple by passing a current through the heating coil, and the corresponding detector output measured. Since the detector-amplifier systems are designed to operate at high frequencies, a simple static calibration is not possible, and modifications are necessary. The amplifier used with the InSb is a-c coupled, with a lower 3-db point of 1.35 kHz; this precludes the possibility of using a chopper to produce the required "dynamic" conditions. Instead, a d-c amplifier of known gain was constructed and used to determine the detector current as a function of temperature; the transfer function of the fast amplifier system was then used to convert this into the appropriate calibration curve. In the case of the HgCdTe system, the bridge circuit constructed for d-c operation proved too unstable for use in calibration, but as the lower 3 db point of the fast amplifier is 50 Hz, it was possible to use a chopper to obtain a dynamic calibration. The chopper used consisted of a six-bladed "fan" driven by a motor at $\sim$1000 rpm, giving a chopping frequency of $\sim$100 Hz; the detector output was displayed on an oscilloscope, and a photograph taken of the trace at each temperature point. The voltage was taken as the average amplitude of the square wave generated by the chopper.

Typical calibration curves are plotted in Figures 8-9 and 8-10, and Table 8-1 gives the power law fits to the curves. Both detectors gave extremely reproducible calibration curves, as is demonstrated by the two sets of points for aluminium in the case of InSb (these were obtained several weeks apart with a number of shots fired in between).

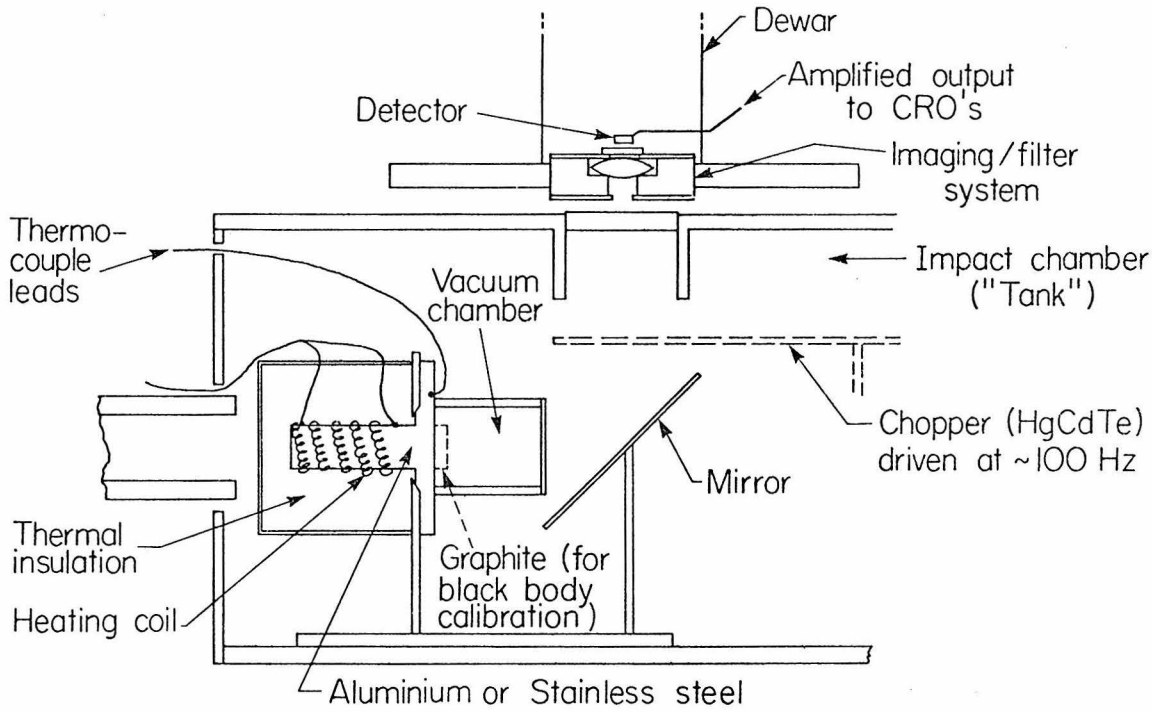

Figure 8-8. Schematic diagram of the calibration configuration. The chopper, shown in part, is only used with the HgCdTe detector.

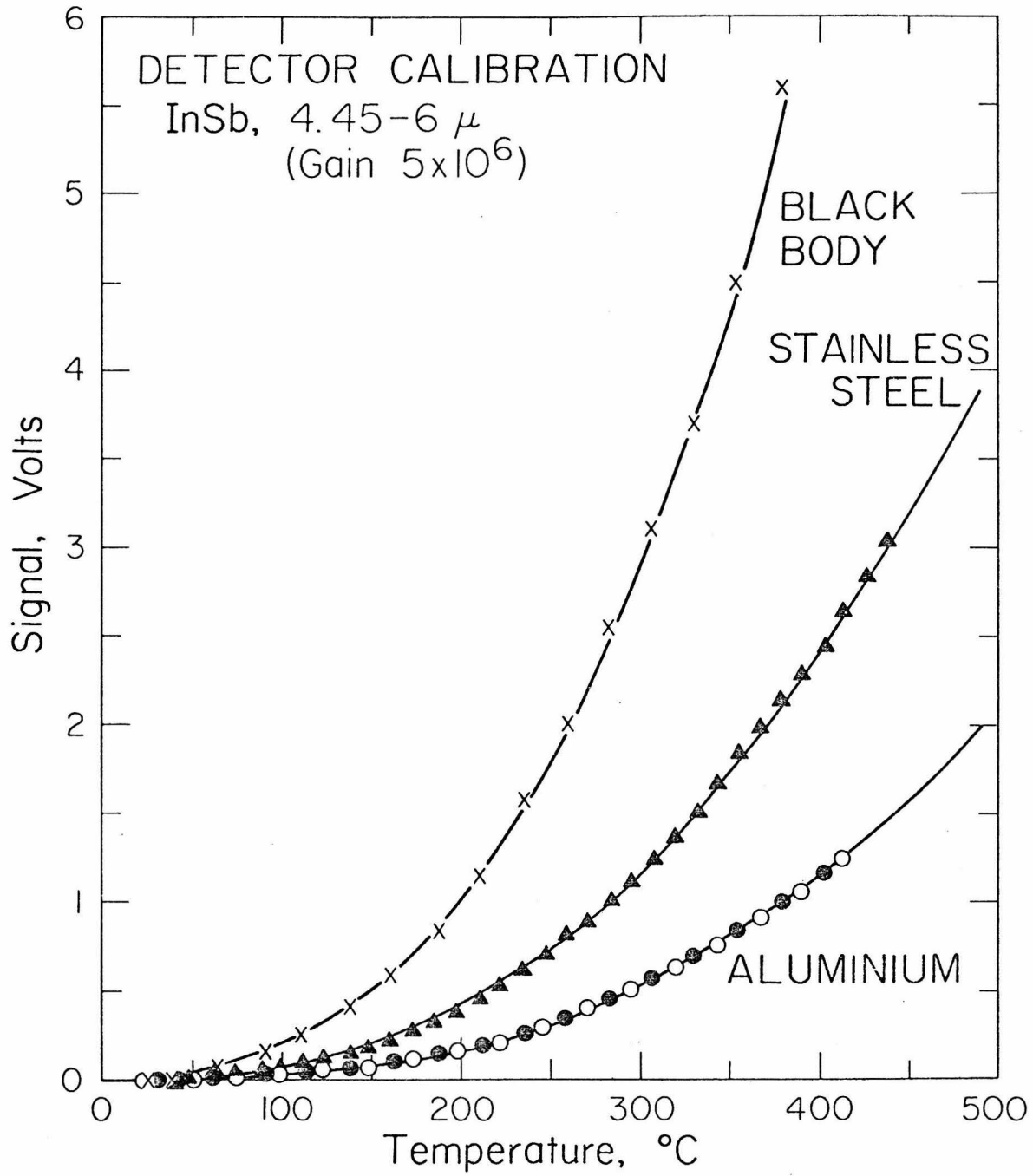

Figure 8-9. Calibration curves for the InSb detector, operating in the wavelength range 4.5 to 5.75μ. The open and solid circles in the aluminium curve are the results of two different calibration runs.

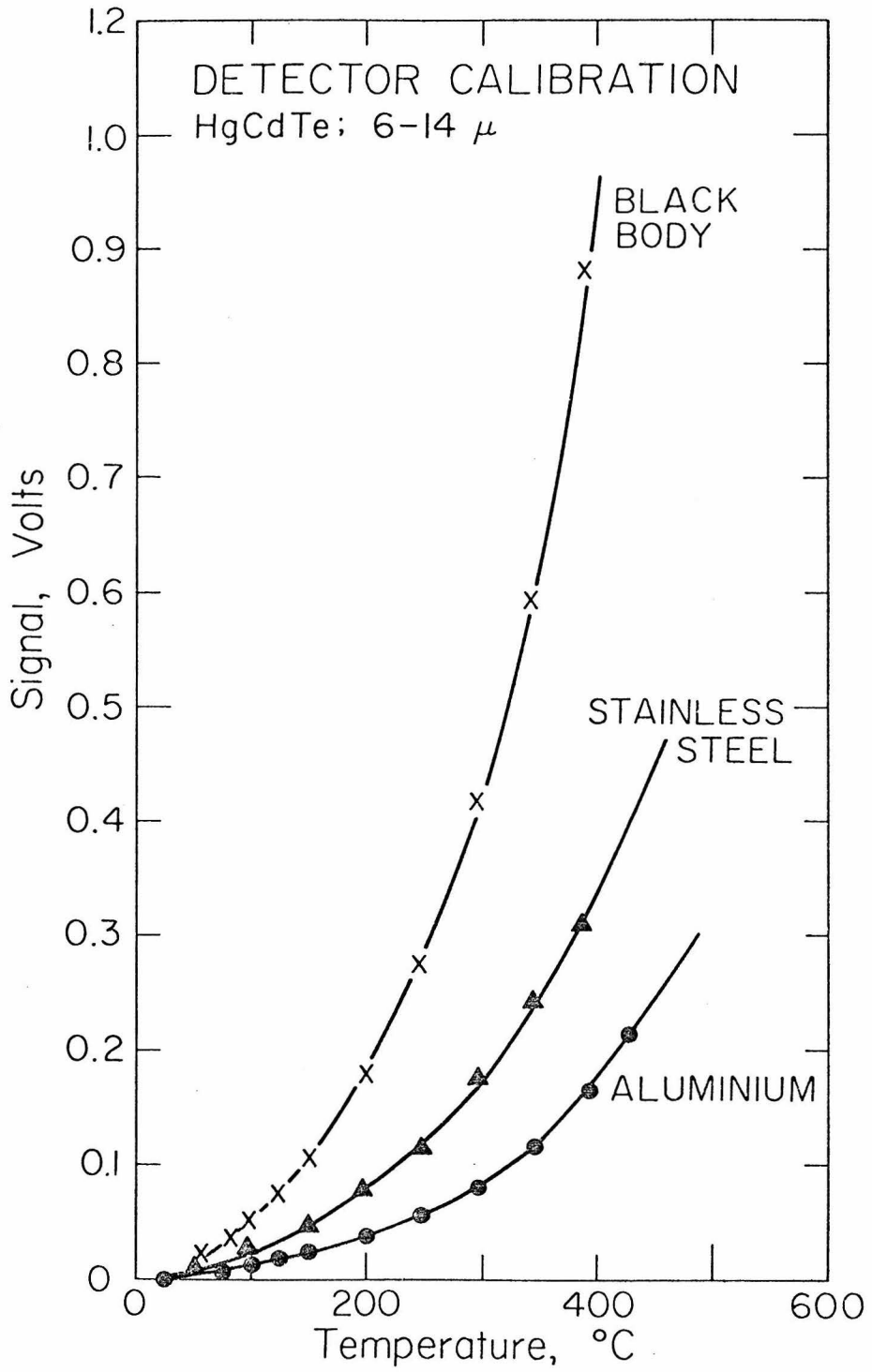

Figure 8-10. Typical calibration curves for the HgCdTe detector.

Table 8-1

POWER LAW FITS TO CALIBRATION CURVES

$S = a(T-24)^b \times 10^{-5}$; coefficient of determination r^2

	Black Body			Stainless Steel			Aluminium-2024		
	a	b	r^2	a	b	r^2	a	b	r^2
InSb	7.21	1.87	.99	2.21	1.93	.98	3.08	1.71	.95
HgCdTe	10.9	1.45	.97	10.05	1.32	.97	2.68	1.43	.98

Unfortunately, the HgCdTe had to be recalibrated on two occasions, once after the dewar had developed a vacuum leak and the detector had to be serviced, and once after the window material was changed from barium fluoride to the less brittle irtran-2. Consequently, whilst Figure 8-10 shows a typical set of calibration curves for the material, these may not be the actual ones used to derive the temperatures given in Chapter 9.

Having described the principles behind the temperature measurements, the sources of error should now be discussed. These can basically arise from two causes -- those related to the sample, and those originating from outside sources. Prime among the latter is contamination of the signal by radiation from air shocks which can be of extremely high temperature. Owing to the geometry of the apparatus these should not be important prior to the arrival of the shock wave at the free surface of the sample, and, indeed, no earlier signal rises were detected. The only air shock likely to affect the post-shock temperature measurement would be one generated at the back of the sample itself, which is (hopefully) eliminated by the sample vacuum chamber that is pumped down to $\lesssim 5\mu$. To reduce further possible radiation from residual gases within this chamber heated by compression due to the shock wave, the chamber was flushed out with helium prior to each shot. Radiation from later air shocks, such as that generated at the end of the sample chamber as the window breaks, is clearly visible on each record, and ultimately causes the detection system to saturate. If the samples were transparent, then radiation from the metal driver plate could add to the signal, but the rise should then precede the free surface arrival of the shock wave,

and this does not in general appear to be the case. Anyway, the emissivity of the metal is substantially lower than that of the sample, so this effect should be relatively small, and both detectors were chosen to operate at wavelengths where the samples are nearly opaque. (Forsterite does have a 20% transmittance at 4.5μ dropping rapidly to less than 5% at 5μ, and so may show minor effects due to transmitted radiation for the InSb detector.) Both the driver plate and the sample surface in contact with it were polished prior to mounting of the sample in order to minimise the "porous" surface interactions that could give rise to considerable heating (see e.g., Urtiew and Grover, 1974); this also reduces the likelihood of air being trapped in this interface, but this should be removed by the evacuation of the sample chamber. In order for the signal to be contaminated by radiation from the metal or the driver-sample interface, large changes must take place in the transmissivity of the sample under shock conditions; although changes have been reported in sapphire (Urtiew, 1974), these were <u>decreases</u> and at much higher pressures. It seems that this is not a likely source of error. Vibration of the detector-amplifier system could conceivably affect the output, but this was securely clamped in place, and such effects were generally not apparent; for some HgCdTe shots a negative signal of short duration (∿10 μs), obviously non thermal in origin, was observed prior to impact with the shorting target, but the output returned to the zero level before the free surface arrival.

Two main sources of errors associated with the sample behaviour under shock are changes in emissivity and the effects of non-uniform heating. The former may be investigated by comparing the brightness temperatures

obtained at different wavelengths, since the change would probably not be constant as a function of wavelength. Changes in emissivity may be related to phase changes, changes in surface properties and triboluminescence. In a recent work on residual temperatures in copper, Von Holle and Trimble (1976) determined temperatures by using the ratio of detector signals obtained at different wavelengths. They believed this would reduce the likelihood of error due to changes in emissivity and the effects of surface processes, and yield a relatively unbiassed estimate of the post-shock temperature. Unfortunately, for materials in which the emissivity is not a strong function of wavelength -- such as stainless steel and aluminium (see Figure 8-11) -- small errors in measurement of the detector output can lead to large changes in the ratio of the signals from the two detectors and totally unreasonable ratio temperatures, so that this technique has not proved useful. (The values of the emissivity obtained from the calibration curves were:

Al-2024 .125 (100°C) to .19 (400°C)

SS-304 . 38 (100°C) to .40 (400°C)

for the wavelength band 4.5 - 5.75μ, and

Al-2024 . 20 (100°C) to .19 (400°C)

SS-304 . 45 (100°C) to .37 (400°C)

for the range 7-14μ. The values for the aluminium suggest only a small amount of oxidation when compared with the curves in Figure 8-11(b), making allowances for the slight surface roughness. The values for the stainless steel are perhaps a little high; this is probably because of slight oxidation and surface roughness.)

The effect of non-linear heating may be more severe, and will be

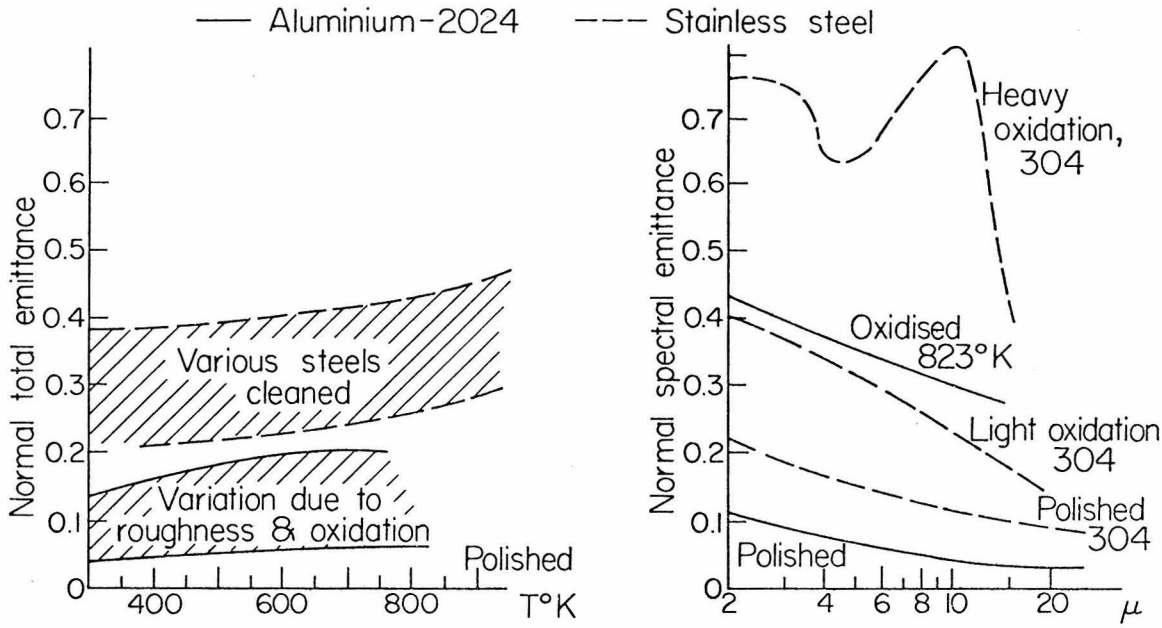

Figure 8-11. Variation of emissivity of aluminium-2024 and various steels, (values from T.P.R.C. Data Series 7, 1972).

discussed in detail with reference to the individual sample materials in a later chapter. Table 8-2 presents the results of some calculations in which it was assumed that 90% of the sample surface was at a temperature T, and the remaining 10% 100° or 200°C hotter. Having 10% of the surface 100°C hotter than the rest does not lead to severe overestimates of the mean temperature; indeed, the differences between the mean and measured temperatures are close to the accuracy of their determination. The differences are more serious for a 200° excess, especially for aluminium, but this is probably rather a large proportion of the surface to be so much hotter. If localised heating does occur, it may cause greater heating in a more limited region, but the bias in the temperature measurement will probably be no greater than that estimated in Table 8-2. The effect of surface processes such as jetting can also bias the temperature measurements; these will presumably be more important in metals where the optical depth is of the order of angstroms, than in silicates where it is microns. To reduce the likelihood of jetting, the sample surfaces were polished, but not to a high gloss as this would reduce the emissivity. (This is demonstrated for metals in Figure 8-11; the effect of surface roughness on the emissivity of silicates is more complex, but in polished quartz, the effect of the absorption peak at $\sim 9\mu$ is to lower the emissivity further than for a roughened plate (Lyon, 1965).)

Table 8-2

ESTIMATES FOR THE EFFECT OF NON-UNIFORM HEATING

90% of the sample surface at T, 10% at T + ΔT

Temperature T°C	Excess ΔT°C	Weighted Mean $\overline{T}$	Measured Temperature					
			In Sb			HgCdTe		
			Al	SS	BB	Al	SS	BB
50	100	60	70	70	65	70	75	70
50	200	70	115	110	100	85	100	90
100	100	110	120	115	110	120	120	110
100	200	120	155	145	143	130	135	130
150	100	160	170	165	160	165	165	165
150	200	170	200	190	175	185	183	183
200	100	210	215	210	215	215	215	215
200	200	220	240	235	232	245	235	235

Al = Aluminium-2024, SS = Stainless Steel-304, BB = Black Body

Chapter 9

MEASURED VALUES OF POST-SHOCK TEMPERATURES

In this chapter the results of measurement of post-shock temperatures in stainless steel 304, aluminium 2024, quartz, forsterite and bronzite will be presented, and factors that might affect the measurements discussed. In general, the measured values are considerably in excess of those predicted by theories based on the hydrodynamic irreversible work model; a discussion of the methods used in calculating Hugoniot and residual temperatures, and the implications of the observations, will follow in Chapter 10.

In all cases, the interpretation of the detector output is based on the assumption that the oscilloscope sweep at 5 μs/div is triggered at the moment of contact of the flyer plate with the shorting target (see Figure 8-1). This was checked both by analysing the timing of the signals seen on the back-up record triggered by the passage of the projectile past the first laser beam, and by using a delayed trigger on the oscilloscope. The assumption appears valid to within the accuracy of determination of $\sim$0.5 μs, which is close to the rise time of the detector. It is hoped to modify the target assembly so that in the future some kind of fiducial marks corresponding to the arrival of the shock wave at the driver plate-sample interface can be introduced into the detector record; however, this may involve using a different gun. Specific details of the shots fired in the course of this study will be found in Appendix B.

9.1. Observations for Stainless Steel-304 and Aluminium-2024

These metals were chosen for investigation because they are the materials used as driver plates in the shots on silicates, and the possibility of the contribution of radiation from the driver plate had to be considered. It is also interesting to compare the measured and theoretical temperatures in metals, where the theory was thought to be adequate, rather than in the silicates where large uncertainties in calculated temperatures exist.

Typical detector output records are shown in Figure 9-1: these are for the InSb detector, but the records obtained with the HgCdTe detector were essentially similar except for the longer rise time; the records were extremely reproducible. In general, the output shows a sharp, but low amplitude, rise corresponding to the free surface shock arrival, followed by a short level portion taken to correspond to the residual temperature. This is followed by a rapid rise to a peak occurring $\sim$7 μs after the free surface arrival, and subsequently the detector-amplifier system saturates upon arrival of radiation from an air shock generated at the end of the sample chamber. At the highest pressures, the separation of the initial level portion and the rise to the peak was indistinct; in these cases, the post-shock temperatures were determined from the output level 0.5 μs (InSb) or 0.75 μs (HgCdTe) after the free surface arrival. (These values correspond to the rise times of the detection systems.) In the shots using the HgCdTe detector, the system saturated prior to the arrival of radiation from the air shock, and the peak temperatures could not be determined

The temperatures determined in this manner are listed in Tables

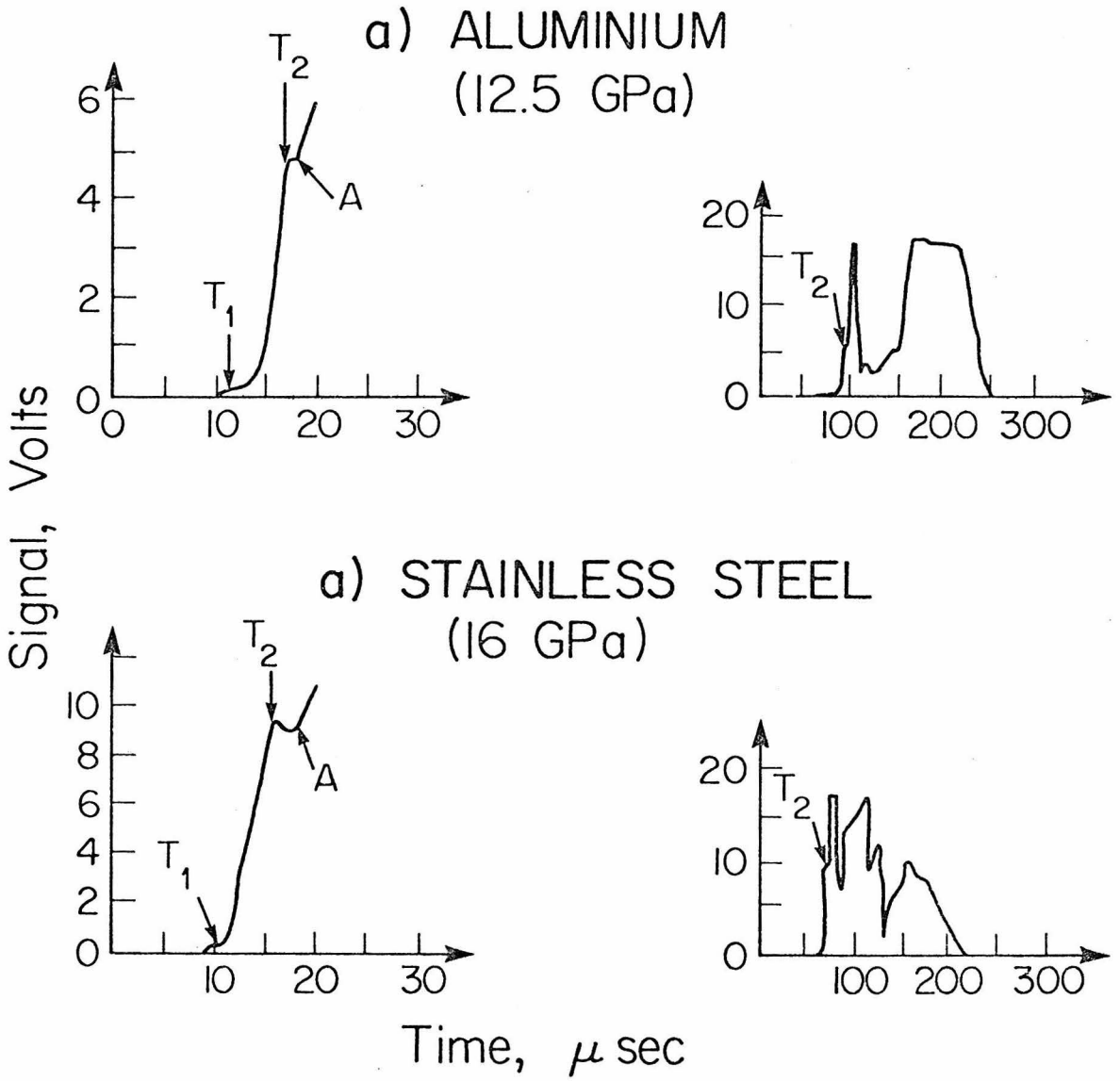

Figure 9-1. InSb detector output records for aluminium and stainless steel. T_1 = residual temperature, T_2 = peak temperature, A = air shock.

9-1 and 9-2; in general, the agreement between the values for the two wavelength ranges is good, with the difference not exceeding the estimated uncertainty in the measurement. The values of post-shock temperatures in stainless steel 304 were found to vary from 80°C at 11.5 GPa to 355°C at 50 GPa; these values may be compared with those calculated by McQueen et al. (1970) which ranged from 25 to 175°C. In aluminium-2024 the measured values went from 125°C at 10.5 GPa to 260°C at 33 GPa; the corresponding theoretical values are 35 to 218°C (McQueen et al., 1970). The values for steel may at first seem high when compared to the small amount of heating apparently observed in steel containers used in recovery experiments; however, these containers are not examined immediately, and the initial post-shock temperatures will quickly decay owing to thermal conduction. This is borne out by the observations of Schneider and Stilp (1977) who used thermocouples to measure the temperature within large steel targets as a function of time and distance from the centre of impact. The time resolution of their measurements was only 50 ms, and they found that the temperature decayed rapidly as a function both of time and of distance away from the impact. Since in the current experiments the temperature at the centre of impact is observed within 1 μs of the shock wave arriving at the free surface, the high observed temperatures are not necessarily inconsistent with the maximum increase of 18°C observed 1.2 cm from the impact centre by Schneider and Stilp.

The origin of the later peak, whose temperature could only be determined for the InSb experiments, is unclear, but it appears to be a material property rather than some effect common to all shots such as the compression of residual gas within the sample chamber. It

Table 9-1

MEASURED POST-SHOCK TEMPERATURES

IN STAINLESS STEEL-304

Temperature, °C

Pressure, GPa	InSb		HgCdTe		Peak
	SS	BB	SS	BB	(InSb)
11.5			80	60	
11.7	110	75			250
13.0	125	80			600
14.5			130	85	
16.0	145	100	145	95	830
23.0	195	130			1530
24.2			200	130	
43.0	325	230			
50.0	355	250			1820

SS = calibration using stainless steel

BB = black body temperature

Uncertainties in temperature: ±15° below 150°, ±10° above 150°.

T_o = 24°C

Table 9-2

MEASURED POST-SHOCK TEMPERATURES

IN ALUMINIUM-2024

Temperature, °C

Pressure, GPa	InSb		HgCdTe		Peak
	AL	BB	AL	BB	(InSb)
10.5	125	50			
11.5			140	65	
12.5	135	55			1250
15.0	150	60			
15.7			155	70	
18.5	175	75	185	80	1430
25.0			220	90	
27.0	230	105			2200
32.5	250	120			
33.0	360	127			3800

AL = calibration with aluminium

BB = equivalent black body temperature

Estimated uncertainties: ±20°C below 200°C, ±10°C above 200°C

T_o = 24°C

correlates well with pressure, shock, and free surface velocities for both stainless steel and aluminium, but the curves are separate for the two materials even if the temperature is estimated using the same calibration curve. It may be due to some form of localised frictional heating on break-up of the sample.

Discrepancies between measured and calculated temperatures have also been reported for other metals by several authors (e.g., Von Holle and Trimble, 1976), and some of the implications of this will be discussed in the next chapter. However, at this point it is reasonable to consider possible sources of error in the measurements. Since the optical depth is only angstroms, the behaviour of the surface layer is important: heating within this layer, such as discussed by Urtiew and Grover (1974), may lead to high temperatures unrepresentative of the bulk sample, especially if the heating is non-uniform. The surface is also an important factor controlling the emissivity, and roughening of the surface by the passage of the shock wave through it, and by such processes as jetting, could cause an increase in emissivity leading to an over-estimate of the temperature. For this reason, the corresponding black body temperatures, which are lower bounds on the residual temperatures, are also tabulated in Tables 9 -1 and 9 -2. They are still in excess of the calculated values for stainless steel, but are lower than the theoretical values for aluminium, which is not surprising as in the latter case the black body temperatures represent a five-fold increase in emissivity, which is highly unlikely.

The consistency of the results obtained in the two different wave-length bands suggests that the observed high temperatures may be real.

If this is the case, then the assumptions upon which the calculations are based must be reviewed. In particular, most calculations, such as those of McQueen et al. quoted here, ignore the effects of stress hardening (Smith, 1958) and non-hydrodynamic plastic work effects which have been observed in various metals including steel (Murr, 1975). The nature of the release path is also important, but poorly known.

From these experiments it appears that, in view of the low emissivity of the metals, the small signal corresponding to the post-shock temperature, and the low transmission coefficients of the silicate samples in the wavelength range studied, there should be no significant contribution to the temperatures measured for the silicates due to radiation from the driver plate.

9.2. Observations for Silicates

Post-shock temperatures were determined for quartz (natural single crystal, cut perpendicular to the c axis), forsterite (synthetic single crystal, cut perpendicular to the c axis) and Bamble bronzite. Typical oscilloscope records for the InSb and HgCdTe detectors are shown in Figures 9-2 and 9-3 respectively; once again, they were extremely reproducible, and the main features will be discussed separately for each material.

a) Corrections for emissivity

Initial estimates of post-shock temperatures in the silicate samples were based on the assumption that they behaved as black bodies in the wavelength range studied. For quartz in the range 5 to 8μ this is a

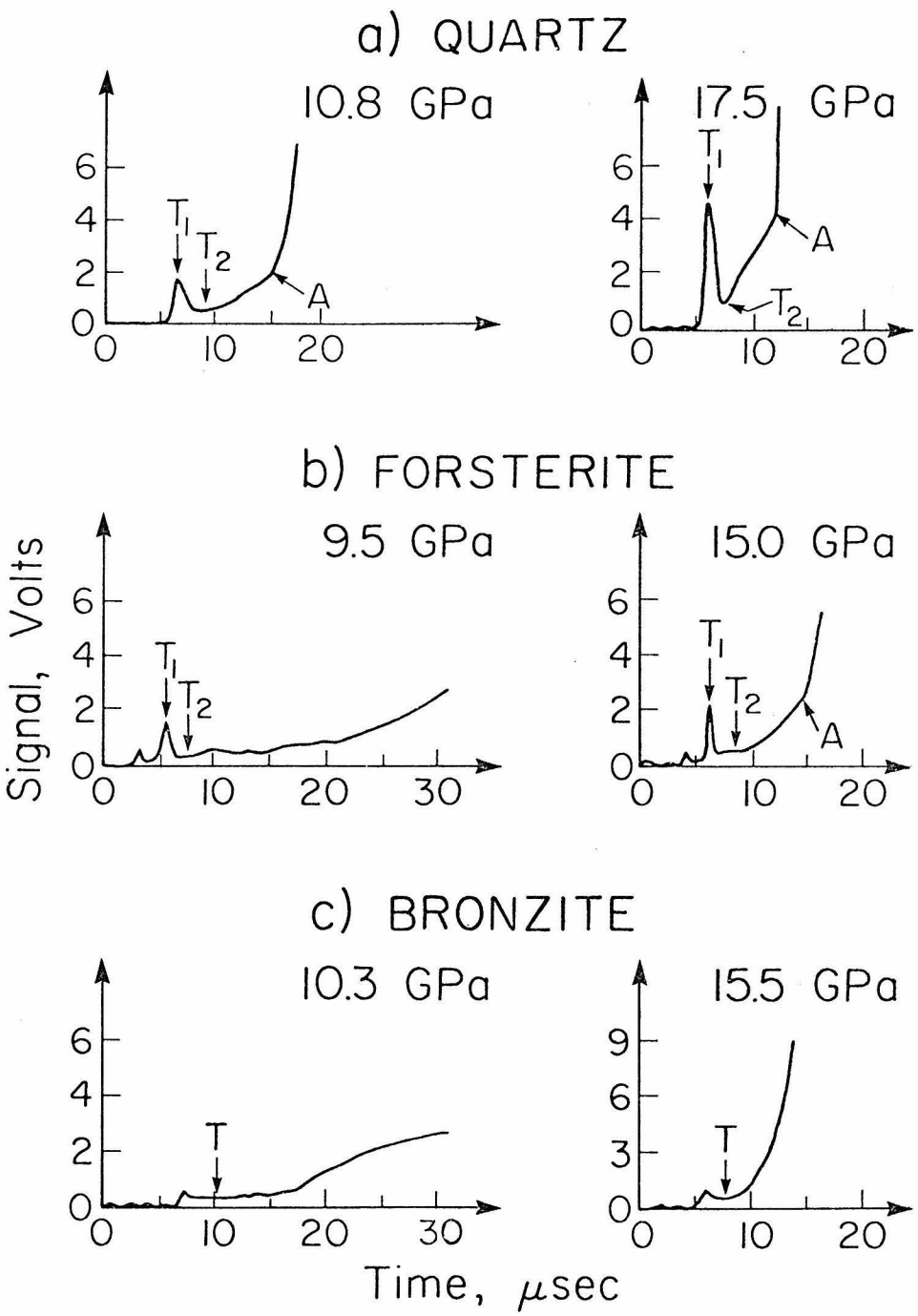

Figure 9-2. InSb detector output records for the silicates studied. T_1 = flash temperature, T_2 (or T) = residual temperature.

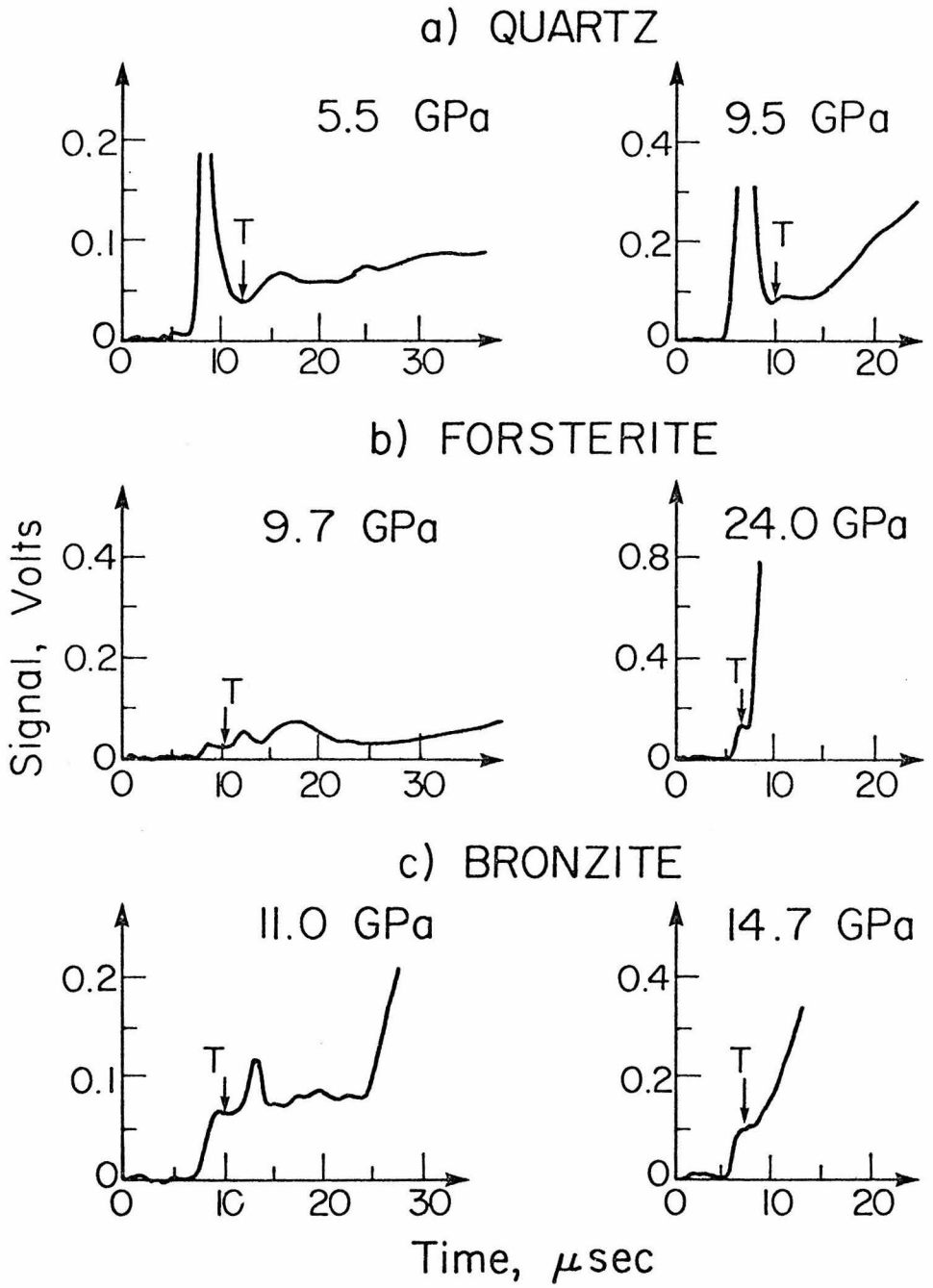

Figure 9-3. HgCdTe detector output records for the silicates studied. T = residual temperature.

reasonable approximation since the emissivity is greater than 0.9 (Touloukian and DeWitt, 1972), and is probably justified for the Bamble bronzite in the InSb range, since it does not transmit. However, the forsterite has a 20% transmittance at 4.5μ (dropping rapidly to less than 5% at 5μ), and the presence of the silicate absorption band at ∿9μ can cause a large drop in the emissivity. The latter effect is clearly visible in the comparison of black body and quartz emittance spectra at temperatures from 250 to 500°K presented by Lyon (1965).

Emissivities of silicate materials have been studied mainly with the objective of interpreting observed emission from the terrestrial planets in terms of their surface composition, and are thus available largely for rocks and powdered samples. In order to estimate the probable effect of the emissivity on the post-shock temperatures obtained, the values of the emissivity for quartz and dunite (primarily forsterite) listed in Table 9-3 were used. Note that the contrast between the emissivity minimum at the absorption peak and the maximum emissivity is controlled largely by the surface finish, although the maximum is fairly constant.

The detector output S may be expressed as

$$S = \int_{\lambda_1}^{\lambda_2} E(\lambda,T)D(\lambda)P(\lambda,T)d\lambda \qquad (1)$$

where $E = (\lambda,T) = E(\lambda)$ = emissivity (assumed independent of T)

$D(\lambda)$ = detector response, $P(\lambda,T)$ = Planck's function

λ= wavelength, T = absolute temperature.

This may be integrated numerically and used to derive the ratio of the signal obtained for a silicate at temperature T to that for a black body

Table 9-3

EMISSIVITIES FOR QUARTZ AND DUNITE

	Quartz		SiO_2[c]	Dunite
Wavelength, μ	Polished[a]	Rough[b]	(Crystalline)	Polished[a]
4.5	(.5)		.75	(.4)
5	.96		.90	.96
5.5	.97		.94	.96
6	.97		.93	.96
7	.98		.96	.96
8	.80	.85	.95	.96
9	.20	.62	.8	.98
10	.85	.85	.85	.85
11	.90	.93	.90	.64
12	.97	.96	.90	.88
13	.90	.96	.91	.92
14	.93		.93	.96
15	.96		.98	.98

a) Buettner and Kern (1965)

b) Lyon (1965)

c) T.P.R.C. Data Series 8 (1972) (Touloukian and DeWitt, eds.)

Values in parentheses are estimates.

at the same temperature. This correction factor is listed in Table 9-4: the values for bronzite were estimated from its absorption spectrum which has a broad peak between 8.5 and 12.5μ although the maximum absorption does not exceed 55%; in quartz the peak absorption, at ∿9.0μ, is almost 80%.

Since the post-shock temperatures are measured after the interaction of the shock-wave with the free surface, and that interaction will cause roughening of the surface, a correction factor derived for a rough surface might be more appropriate; however, the values listed in Table 9-4 for polished surfaces will be used since these should yield an upper bound on the temperature. Two additional factors should be taken into account: one is that the absorption peak may shift during shock compression (e.g., Goto et al., 1977), and broadening of the absorption bands for SiO_2 has been observed in samples recovered after shock compression to pressures up to 52 GPa (Mashimo et al., 1978). The second is the possibility of triboluminescence, or some other form of non-equilibrium radiation such as might be associated with a phase change; in these cases the emissivity may even exceed unity. Because of these uncertainties, the black body temperatures may well be more reasonable estimates of the residual values, with upper bounds set by the corrected temperatures.

(b) Quartz

The signals recorded using the InSb and HgCdTe detectors are extremely similar for quartz; the main features are a "flash" of short duration, which occurs at (or near) the time of arrival of the shock

Table 9-4

ESTIMATED SIGNAL CORRECTION FACTORS

$$\text{Correction factor} = \frac{\text{S silicate}}{\text{S Black body}} \text{ (values to nearest .05)}$$

	T = 400°K	T = 600°K
InSb		
Quartz (polished)	.90	.85
SiO_2 (crystalline)	.90	.90
Dunite (polished)	.85	.80
(Bronzite	.9	.9)
HgCdTe		
Quartz (polished)	.80	.80
Quartz (rough)	.90	.90
Dunite (polished)	.90	.90
(Bronzite	.85	.85)

wave at the free surface, a subsequent drop to a level "trough" (taken to represent the post-shock temperature) followed by a rise and eventual saturation due to radiation from air-shocks. At pressures below about 15 GPa the level portion after the initial peak is well defined, and it is this that is used to determine the residual temperature; however, at higher pressures the later "arrivals" tend to mask this, and the temperatures measured will in general be overestimates. (This is especially true for the slower HgCdTe detector, and probably accounts for the high measured temperature at 19.5 GPa.)

Temperatures determined for various shock pressures are listed in Table 9-5; with the exception of the 19.5GPa shot the residual values (both black body and corrected) are in quite good agreement for the two wavelength ranges, although the peak values are rather different. There appears to be a slight break in slope after the initiation of the phase change (at $\sim$14 GPa). One interesting feature is that quite high post-shock temperatures were measured for pressures below the Hugoniot elastic limit, which is 6.5 to 8.0 GPa (Wackerle, 1962); this observation is rather surprising since the elastic compression would be expected to be reversible.

The initial flash might be explained in a number of ways. If it only occurred for the InSb shots, it might be attributed to the transmission of radiation from the sample-driver plate interface, although as the transmissivity does not exceed 5% at these wavelengths it would represent an extremely high interface temperature; however, this explanation is ruled out since the flash is seen in the HgCdTe band where the quartz is opaque. Another possibility is that it represents

Table 9-5

MEASURED POST-SHOCK TEMPERATURES IN QUARTZ

Temperature, °C

	InSb			HgCdTe		
Pressure, GPa	Flash	BB	Corr.	Flash	BB	Corr.
5.0	235	80	87			
5.5				110	75	85
8.0	180	100	105			
9.5	225	120	125	320	115	127
10.8	245	155	162			
11.5	252	160	170			
15.0	340	177	187			
15.5*				--	160	180
17.5	377	185	195			
19.5				706	320	340
20.0	390	242	255			
21.5	425	250	265			

*This was a very faint record, and may not be reliable.

Uncertainties: ±10°C below 100°C, ±5°C above 100°C

T_o = 24°C

radiation from the shock front itself, although this seems improbable in view of the low time resolution of the detectors. Furthermore, if this were the case, the peak value would give a (low) estimate of the shock temperature, and the difference between it and the residual value could be used to estimate Grüneisen's parameter. The values obtained range from 27 to 2.17, while the thermodynamic Grüneisen's parameter for quartz is 0.7; this explanation would thus seem unacceptable. The most likely cause is triboluminescence, a phenomenon that has been documented in quartz by Nielson et al. (1961) who observed strong emission in the visible region of the spectrum from quartz shocked to similar pressures. In this case the black body temperature corresponding to the flash is unlikely to be significant.

The temperatures listed in Table 9-5 are in general somewhat higher than those calculated by Wackerle (1962) which were in the range 42 to 195°C for the same pressure range. (These values represent the values given by Wackerle corrected to an initial temperature of 24°C.) However, the agreement is surprisingly good at ∿15 GPa (177° measured versus 180° calculated) and the 50° discrepancies at the upper end of the pressure range may in part be due to the measured temperatures being overestimates, as discussed earlier. Wackerle's calculations did not take into account the possibility of elasto-plastic effects or the thermodynamic properties of the high pressure phase; later more complete calculations (e.g., Mashimo et al., 1978) yield somewhat higher temperatures in better agreement with the measured values.

In recovery experiments on quartz a number of localised adiabatic shear zones have been observed and it has been suggested (Grady, 1977)

that locally high temperatures in these zones may cause melting and contribute to the rapid loss of strength above the Hugoniot elastic limit. Such localised heating could lead to measured temperatures up to about 20°C higher than the bulk value, as described in Chapter 8.

(c) Forsterite

Forsterite was the only material studied where the detector output for the two wavelength ranges was markedly different. For the range 4.5 to 5.75μ the records are similar to those obtained for quartz, and are characterised by a "flash" at about the time of the free surface arrival, followed by a level portion and subsequent rise to saturation. In fact, for the shots at 9.5 and 15.0 GPa two peaks, separated by ∿2 μs were observed, the first apparently preceding the free surface arrival; the first peak was lower amplitude and for pressures in excess of 15 GPa only one peak was observed. Records obtained using the HgCdTe detector showed no peak, but simply a rise to a level portion similar to that seen for metals and bronzite. Triboluminescence has not been documented in forsterite, and would not be expected to occur only in a limited wavelength range. The most likely explanation for the change in signal is that the peaks represent transmitted radiation, since forsterite does have a transmission coefficient of up to 0.2 in the InSb range. If this is indeed the case, then the temperatures measured may tend to be slightly high as the driver plate and interface radiation will increase the signal.

The measured temperatures for forsterite are listed in Table 9-6; note that for pressures below the Hugoniot elastic limit (∿8.5 GPa; Ahrens and Petersen, 1969) there was no detectable rise in temperature

Table 9-6

MEASURED POST-SHOCK TEMPERATURES IN FORSTERITE

Temperature, °C

	InSb			HgCdTe	
Pressure, GPa	Flash	BB	Corr.	BB	Corr.
7.5	180	<50°	(no detectable rise)		
9.6*	237	105	115	65	77
15.0**	260	136	145		
18.0				105	112
20.2	285	140	152		
21.0				120	125
24.0				160	165
24.5	270	148	160		
28.0	300	156	167		

*Two peaks (175, 237°C) in InSb record; residual temperature corresponds to the difference between the levels after second and first peaks.

**Two peaks (135, 260°C); residual temperature estimated as before.

Estimated uncertainties: ±10°C below 100°C, ±5°C above 100°C

T_o = 24°C

and that the HgCdTe temperatures are lower, at least below 15 GPa. The latter observation is easily explained if there is some contribution to the InSb signal from transmitted radiation. Once again, the temperatures are much higher than expected (see Chapter 10); some of the additional heating may arise because the samples were up to 0.5% porous (density 3.222 to 3.215 gm/cm^3, as opposed to 3.224 gm/cm^3 reported by Kumazawa and Anderson (1969)). Although this does not cause a significant offset in the Hugoniot, compression of the gases present in the voids may lead to locally high temperatures.

(d) Bamble Bronzite ($(Mg_{0.86}Fe_{0.14})\ SiO_3$)

The records for Bamble bronzite were very similar for both wavelength ranges, and in fact resembled those obtained for metals in that there was no marked initial peak but simply a rise to a level portion used to determine the post-shock temperature, followed by a rise and eventual saturation. There was a slight peak observable in the InSb records; this is probably an artifact of the detector response, but could represent a lower limit on the shock temperature.

Temperatures determined for this material are listed in Table 9-7; the values are extremely similar for both wavelength ranges with the exception of the 25 GPa value. Between 20 and 25 GPa, the InSb temperature dropped by ∿25°C, whereas no corresponding drop was observed in the HgCdTe shots. The observed drop was probably due to the choice of sample: the Bamble bronzite is a natural single crystal which is permeated by fine cracks accounting for the 1% porosity reported by Gibbons (1974), and also contains some larger cracks. The presence of cracks can lead to high temperatures through localised heating,

Table 9-7

MEASURED POST-SHOCK TEMPERATURES IN BAMBLE BRONZITE

Pressure, GPa	Temperature, °C				
	Peak	BB	Corr.	BB	Corr.
6.0		$\lesssim$50° (no detectable rise)			
10.3	123	100	105		
11.0				110	120
14.8				145	160
15.5	185	147	157		
20.7	225	200	213		
21.5				185	200
25.0	200	175	185		
26.0				225	240

Uncertainties: ±10°C below 100°C, ±5°C above 100°C

T_o = 24°C

and the sample shocked to 25.0 GPa was the least cracked, so might be expected to reach lower temperatures.

The measured temperatures are much higher than would be calculated from conventional theories (see Chapter 10) although the discrepancy may in part be due to the cracking. As mentioned earlier, if the peak is representative of a lower bound on the shock temperature, then a lower bound on Grüneisen's parameter may be estimated assuming the release is adiabatic. For bronzite the values range from 3.4 at 10.3 GPa to 0.84 at 25.0 GPa (using the InSb data), compared to a thermodynamic value of 1.17 at zero pressure. Although the calculation is hard to justify, since the origin of the peak is uncertain, it is interesting to note that this type of variation would in fact yield higher calculated values of both shock and post-shock temperatures at lower pressures where the discrepancies between measured and calculated values are largest.

The relatively good agreement between calculated and measured temperatures for quartz, yet large discrepancies for forsterite and bronzite suggest that the latter may have some property in common to account for the extra heating. One possibility is the effect of the porosity; alternatively there may be some intrinsic difference in behaviour between framework and neso- or chain silicates.

Chapter 10

CALCULATION OF POST-SHOCK TEMPERATURES: COMPARISON OF OBSERVED AND THEORETICAL VALUES

10.1. Commonly Used Calculational Techniques

The most widely used method of calculating shock, and hence post-shock, temperatures, is probably that developed for metals by Walsh and Christian (1955). If the entropy S is expressed as a function of temperature T and volume v, then the change in entropy is given by

$$dS = \left(\frac{\partial S}{\partial T}\right)_v dT + \left(\frac{\partial S}{\partial v}\right)_T dv \tag{1}$$

Since $\left(\frac{\partial S}{\partial T}\right)_v = \frac{C_v}{T}$, where C_v is the specific heat at constant volume, and $\left(\frac{\partial S}{\partial v}\right)_T = \left(\frac{\partial P}{\partial T}\right)_v$, this expression may be rewritten

$$TdS = C_v dT + \left(\frac{\partial P}{\partial T}\right)_v dv \tag{2}$$

The energy conservation relation for the shock wave is

$$E_1 - E_0 = 1/2\ (P_1 + P_0)(v_0 - v_1) \tag{3}$$

where E and P are energy and pressure, and the subscripts 1 and 0 refer to the shock and initial states. The first law of thermodynamics may be written

$$TdS = dE + P\ dv \tag{4}$$

or, in integral form

$$\int_{S_1}^{S_0} [TdS]_{Hug} = E_1 - E_0 + \int_{v_0}^{v_1} [Pdv]_{Hug} \tag{5}$$

where the limits of integration refer to the initial and final shock

states and the integration is performed along the Hugoniot. Substituting for $E_1 - E_0$ from (3) and differentiating with respect to v_1 yields the relation

$$\frac{d}{dv_1}\int_{S_0}^{S_1}[TdS]_{Hug} = \frac{dP}{dv_1}\frac{(v_0 - v_1)}{2} + \frac{P_1}{2} = f(v_1) \qquad (6)$$

for a given Hugoniot. Combining this with (2) gives

$$\frac{d}{dv_1}\int_{S_0}^{S_1}[TdS]_{Hug} = C_v\frac{dT_1}{dV_1} + \left(\frac{\partial P}{\partial T}\right)_v T_1 = f(V_1) \qquad (7)$$

which has the solution

$$T_1(v_1) = To\ \exp\left(-\int_{v_0}^{v} b(v)dv\right) + \exp\left(-\int_{v_0}^{v} b(v)dv\right)\int_{v_0}^{v}\frac{f(v)}{C_v}\exp\left(\int_{v_0}^{v} b(v)dv\right)dv \qquad (8)$$

where $b = \frac{1}{C_v}\left(\frac{\partial P}{\partial T}\right)_v = \frac{\gamma}{v}$ where γ = Grüneisen's parameter. A common simplifying assumption is that b is independent of volume, in which case (8) reduces to the form actually derived by Walsh and Christian, namely,

$$T_1(v_1) = To\ \exp(b(v_0 - v_1) + \exp(-bv_1)\int_{v_0}^{v}\left[\frac{f(v)}{C_v}\exp(bv)\right]_{Hug}dv \qquad (9)$$

Equations (8) and (9) may be reduced to difference equations and solved iteratively along the Hugoniot. C_v may either be assumed constant or specified at each point; the Debye formulation is often used, where

$$C_v = 3R\frac{C_v^*}{3R}\left(\frac{\Theta_D(v)}{T}\right) \qquad (10)$$

and the volume dependence of the Debye temperature Θ_D is specified by

$$\Theta_D(v) = \Theta_D(v_0) \exp \{-\int_{v_o}^{v} \frac{\gamma(v)}{v} \, dv \} \qquad (11)$$

Temperatures T_s along an isentrope may also be derived from (7) which becomes

$$C_v \frac{dT_s}{dv_s} + \left(\frac{\partial P}{\partial T}\right)_v T_s = 0 \qquad (12)$$

which has the solution

$$T_s = T_o \exp \{\int_{v_0}^{v_s} \frac{\gamma(v)}{v} \, dv \} \qquad (13)$$

In particular, the post-shock temperature T_R is given by

$$T_R = T_1 \exp \{\int_{v_0}^{v_1} \frac{\gamma(v)}{v} \, dv \} \qquad (14)$$

In geophysical applications it is often assumed that the volume dependence of the Grüneisen parameter is given by

$$\gamma = \gamma_0 \left(\frac{v}{v_0}\right)^n \qquad (15)$$

and γ is usually assumed to be independent of temperature.

Two assumptions have been made throughout this derivation: firstly that an ordinary fluid-type equation of state is valid, which ignores the effects of rigidity or elasto-plastic work, and secondly that thermodynamic equilibrium exists in states behind the shock front. In addition, because of the form used for the energy conservation, equation (3), the treatment is strictly valid only where the shock state is reached by a single step and not in the two-wave region associated with the Hugoniot elastic limit or phase changes.

An alternative approach was described in detail by Ahrens et al. (1969).

The increase in internal energy ΔE_1 of a material shocked to a state with volume v_1 and pressure P_1 is given by equation (3) and is equated to the increase in internal energy resulting from isothermal compression at T_o from an initial volume to a final volume v_1 plus isovolumic heating to the shock temperature T_H. The energy increase along this path is given by

$$\Delta E_1 = \int_{v_0}^{v_1} \left(\frac{T\gamma C_v}{v} - P \right)_{T_o} dv + \int_{T_o}^{T_H} (C_v)_{v_1} \, dT \qquad (16)$$

where the temperature and volume dependence of the specific heat are described by the Debye Model. (The first term on the right hand side of (16) arises from the substitution of (2) into (4) with $dT = 0$.)

The pressure difference between the Hugoniot and the isotherm is given by

$$P_1 - P_T = b \int_{T_o}^{T_H} C_v \, dT \qquad (17)$$

where $b = \gamma/v$ is assumed constant. Hence the second term on the right hand side of (16) may be replaced by $\frac{P_1 - P_T}{b}$, giving

$$\Delta E_1 = \int_{v_0}^{v_1} \left(\frac{T\gamma C_v}{v} - P \right)_{T_o} dv + \frac{P_H - P_T}{b} \qquad (18)$$

Since ΔE_1 is given by (3), this equation may be solved for P_T, and T_H then determined from (17).

This formulation has the advantage that the effects of the Hugoniot elastic limit (P_e, v_e) and the two-wave structure resulting from it are readily included, for equation (3) may be written

$$\Delta E_1 = \frac{P_e(v_o - v_e)}{2} + \frac{(P_e + P_H)(v_e - v_H)}{2} \qquad (19)$$

It is also easily adapted for use in calculating shock temperatures in the high pressure regime for materials such as silicates which undergo phase changes. In this case the energy change ΔE_{PC} associated with the transition must be added to the change in internal energy associated with the isothermal compression followed by heating at constant volume

$$\Delta E_{HP} = \int_{v_o'}^{v_1'} (Tb'C_v' - P')_{T_o}\, dv + \int_{T_o}^{T_H} (C_v')_{v_1'} dT + \Delta E_{PC} \qquad (20)$$

where the primed quantities refer to the high pressure phase, and the value of ΔE_{HP} given by (3) is substituted as before.

Calculations of temperatures in the mixed phase region are considerably more complicated, but the Hugoniot state is assumed to be a mixture of both high and low pressure phases in thermal and mechanical equilibrium. The internal energy in the shock state is given by the Rankine-Hugoniot conservation equation (3) and is equated to the sum of the energy changes produced by the isothermal compression of both phases to P_H, the isobaric heating of both phases from T_o to T_H, and a transformational energy term. Two equations are derived which may be solved numerically for the mass fraction of transformed material and the Hugoniot temperature at a series of points on the mixed phase Hugoniot.

In all cases, post-shock temperatures are calculated from the shock temperatures assuming adiabatic expansion.

For cases where the release path is known, the residual temperature may be calculated directly, as described by Gibbons (1974). The energy in the Hugoniot state, given by (3), is equated to the change in internal energy due to the rise in temperature from the initial value T_o to the

residual value T_R plus the energy change along the release path. Thus

$$\Delta E = 1/2\ (P_1 + P_0)(v_0 - v_1) = \int_{v_1}^{v_R} [Pdv]_{release} + \int_{T_0}^{T_R} C_p\ dT \qquad (21)$$

The Hugoniot temperature may then be calculated from (15).

Having discussed some of the more commonly used methods for calculating shock and post-shock temperatures, one may now compare the results of these calculations with the observed values of post-shock temperature presented in Chapter 9.

10.2. Results for Aluminium and Stainless Steel

Since the Walsh and Christian approach was developed specifically for application to metals (in the absence of phase changes) where the Hugoniot elastic limits are low ($\lesssim$.2 GPa), the application of this technique should yield results in good agreement with the experimental observations. Figure 10-1 (a) and (b) show the values of shock (dashed lines) and post-shock temperature (solid curves) calculated for stainless steel-304 and aluminium-2024 using this approach; they are the same as those given by McQueen et al. (1970). Also plotted are the observed values, and, as can be seen, there is practically no agreement. In fact, the measured residual temperatures are, at low pressures, in excess of the calculated Hugoniot temperatures. Discrepancies between observed and theoretical residual temperatures in metals have also been reported by other workers (e.g., Von Holle and Trimble, 1976) using similar experimental techniques, and the question of the validity of the measurement arises. Certainly, the measured values may be too high because of

Figure 10-1. Observed and theoretical temperatures for shocked metals.
Solid symbols: observed (residual); InSb detector.
Open symbols: observed (residual); HgCdTe detector.

(a) Stainless Steel-304
— — — — calculated shock temperature (Walsh and Christian method)
———— calculated residual temperature (Walsh and Christian method)

(b) Aluminium-2024
— — — — calculated shock temperature (Walsh and Christian method)
———— calculated residual temperature (Walsh and Christian method)
— . — . — Elasto-plastic shock temperature (Foltz and Grace)
. . . . . Elasto-plastic theory, residual temperature.

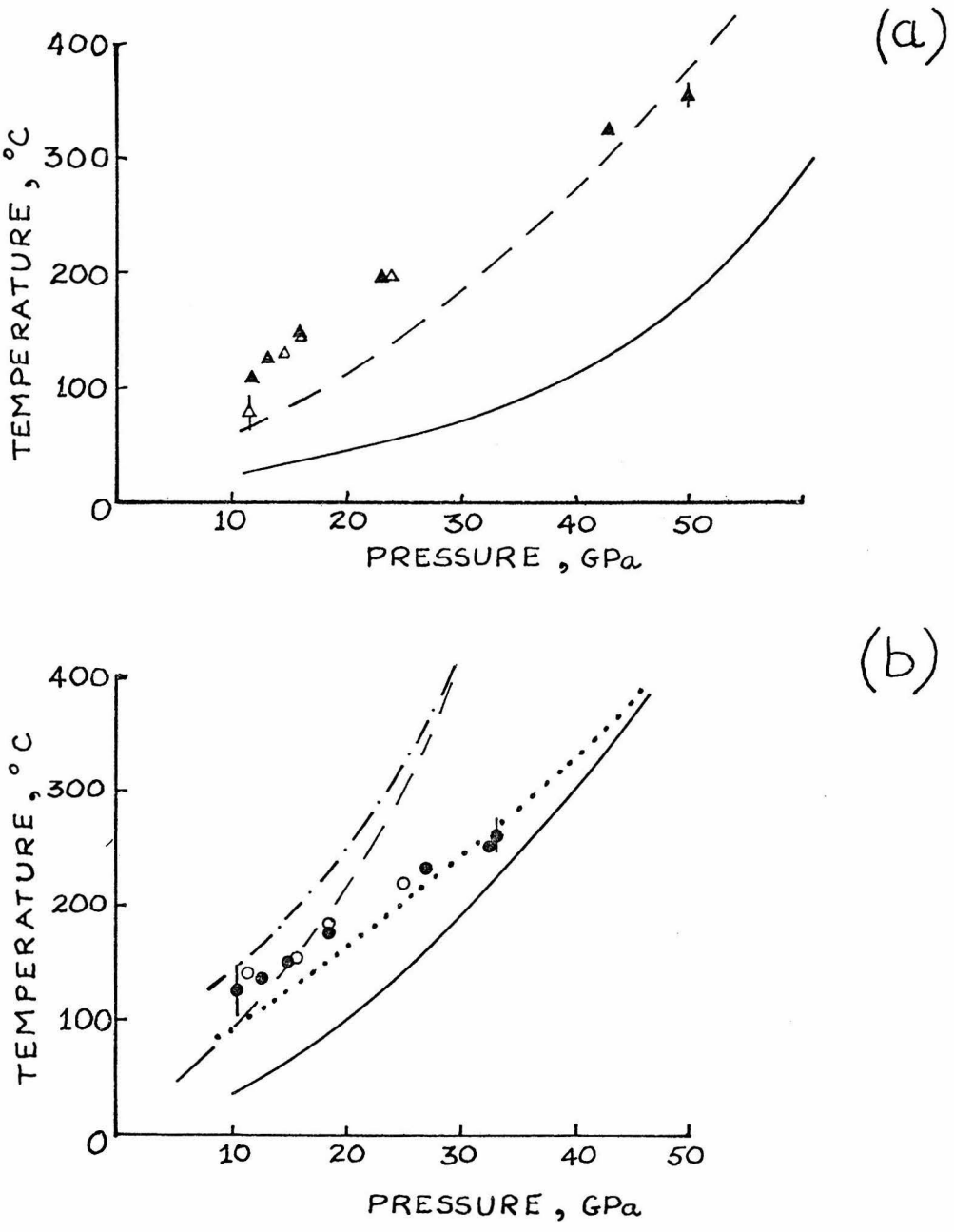
(a)
400
300
200
100
0
TEMPERATURE , °C
10
20
30
40
50
PRESSURE , GPa
(b)
400
300
200
100
0
TEMPERATURE , °C
10
20
30
40
50
PRESSURE , GPa

Figure 10-1.

surface processes or changes in emissivity -- though they are consistent in two wavelength ranges -- but the fact that they tend towards the theoretical values with increasing pressure suggests that the theory does not include some effect that dominates at low pressures. One obvious omission from the Walsh and Christian formalism is the effect of elasto-plastic work. Although the metals have low Hugoniot elastic limits, they retain some rigidity after yielding, and may undergo stress-hardening. The latter was reported by Fowles (1961), who demonstrated that an elasto-plastic equation of state should be used for aluminium shocked to pressures up to ∿15 GPa.

This concept was developed in detail by Lee and Liu (1967) and Lee and Wierzbicki (1967) and applied by Foltz and Grace (1969) to aluminium and copper. Briefly, the Rankine-Hugoniot law of conservation of energy is used in conjunction with a suitable material yield condition to derive a stress-temperature-strain relation characterising the response of the medium to a steady-state shock wave. A minor term appearing in the equations is the proportion of the plastic work W^P done by the shock front which is stored in the solid in the form of lattice imperfections. This is given by $(1-\gamma)W^P$, where the fraction $(1-\gamma)$ may either be taken as constant or allowed to decrease with increasing plastic work. The total amount of plastic work is related to the initial density of the material, ρ_o, the yield stress Y, which is assumed to be a linear function of the mean reduced temperature $\bar{\theta}$ ($\bar{\theta} = 1/2 \left[\frac{T + T_Y}{T_o}\right] - 1$, where T is the temperature, and the subscripts Y and O refer to the yield point and the reference state) and the elastic strain perpendicular to the direction of shock propagation e_2.

$$\rho_o W^P = 2Y (\bar{\theta}) \ln (1 + e_2) \qquad (22)$$

Using these relationships, the energy lost to permanent distortion of the crystal lattice may be evaluated. The actual calculations of the Hugoniot involve expanding the Helmholtz free energy per unit mass as a power series in the elastic extensions and temperature, where the coefficients are related to the elastic constants, thermal expansion and specific heat of the material, and then using this to determine the stress entropy and internal energy of the material. This treatment allows a direct calculation of temperature along the Hugoniot curve and incorporates the effects of material strength and finite anisotropic strain.

Foltz and Grace carried out the analysis for polycrystalline aluminium and copper; whilst their analysis may not be strictly valid for the aluminium alloy used in the present experiments, a comparison of their values for Hugoniot temperature (the dash-dot line in Figure 10(b)) and the measured residual temperatures is interesting. As can be seen, the calculated values are considerably in excess of the Walsh and Christian values at low pressures, but converge with them at higher pressures, which is precisely the behaviour observed in the measured residual temperatures. Although the release path is not certain, it has been proposed that for metals the release from shock pressure P_H occurs in two stages: first an elastic release (isentropic) to a pressure $P_H - 2Y$, where Y is the Hugoniot elastic limit, followed by plastic release parallel to the Hugoniot (see e.g., Fowles, 1961; Al'tschuler, 1965). The post-shock temperatures indicated by the dotted curve in Figure 10-1(b) were derived from Foltz and Grace's Hugoniot temperatures

assuming this form of release path with Y = 0.8 GPa. These values are in reasonable agreement with the experimental observations (which may be slightly high due to changes in emissivity).

Unfortunately, the analysis carried out by Foltz and Grace is not strictly valid for an alloy like stainless steel, and the constants required for the calculation are not really defined in this case. However, the relationship between the observed and Walsh and Christian values (Figure 10-1(a)) is similar to that observed for aluminium, and plastic deformation of the lattice has been observed in recovery experiments for pressures up to 50 GPa (e.g., Murr, 1975; Smith, 1958).

It is thus concluded that elasto-plastic work, which is not included in the Walsh and Christian formalism, causes significant heating at low pressures resulting in large differences between measured and calculated temperatures. However, at higher pressures ($\gtrsim$30 GPa for aluminium, $\gtrsim$50 GPa for stainless steel) the Walsh and Christian approach appears to predict values close to those measured experimentally.

10.3. Application to Silicates

Comparison of Hugoniot curves for silicates and metals reveals several notable differences: the silicates have high Hugoniot elastic limits (generally $\gtrsim$5 GPa) and undergo one or more phase changes which may begin at pressures as low as 14 GPa. In fact, because of the high Hugoniot elastic limit, the resulting two wave structure persists to high pressures and in those materials which begin to transform to high pressure phases at relatively low pressures (i.e., $\sim$14 GPa) the effects of dynamic yielding and the phase change may be hard to distinguish.

Another difference between these two classes of materials is their behaviour on yielding. Whereas metals retain some strength past the Hugoniot elastic limit and elasto-plastic work is important, the silicates appear to undergo a rapid and complete loss of material strength, as was documented in detail for quartz by Wackerle (1962). Since the two-wave structure due to the yielding in silicates persists to high pressures where it may be replaced by a two-wave structure due to a phase change, the Walsh and Christian approach is not valid and must either be modified or replaced by some other calculational technique such as that developed by Ahrens et al. (1969) and described in Section 10.1.

(a) Quartz

In his pioneering work on quartz, Wackerle (1962) circumvented the problem of the Hugoniot elastic limit by introducing an "equilibrium" Hugoniot obtained from a segmented linear fit to the plot of effective shock velocity U* against effective particle velocity u*, where U* and u* are given by

$$U^* = v_o[P/(v_o - v)]^{1/2} \tag{23}$$

$$u^* = [P(v_o - v)]^{1/2} \tag{24}$$

(These represent the true velocities only at high pressures where the two-wave structure no longer exists.) He then used this equilibrium Hugoniot and a modified form of the Walsh and Christian approach to calculate the shock and residual temperatures in quartz. His results are shown as the dashed and solid curves in Figure 10-2(a) (they have been corrected for an initial temperature of 24°C): the agreement between them and the observed post-shock temperatures is remarkably good except

Figure 10-2. Observed (black body) and theoretical temperatures for shocked quartz.
Observed black-body residual temperatures: triangles are "flash" temperatures; circles residual temperatures.
Solid symbols: InSb; open symbols: HgCdTe

(a) — — — Shock temperatures (Wackerle, 1962)
——— Calculated residual temperatures (Wackerle, 1962)
* Residual temperatures calculated using estimated release volume

(b) Heavy line: Calculated residual temperatures (Mashimo et al.)
— — — Shock temperatures, Hugoniot elastic limit 6GPa.
—·—·— Shock temperatures, Hugoniot elastic limit 8 GPa
——— Residual temperatures, Hugoniot elastic limit, 6 GPa.

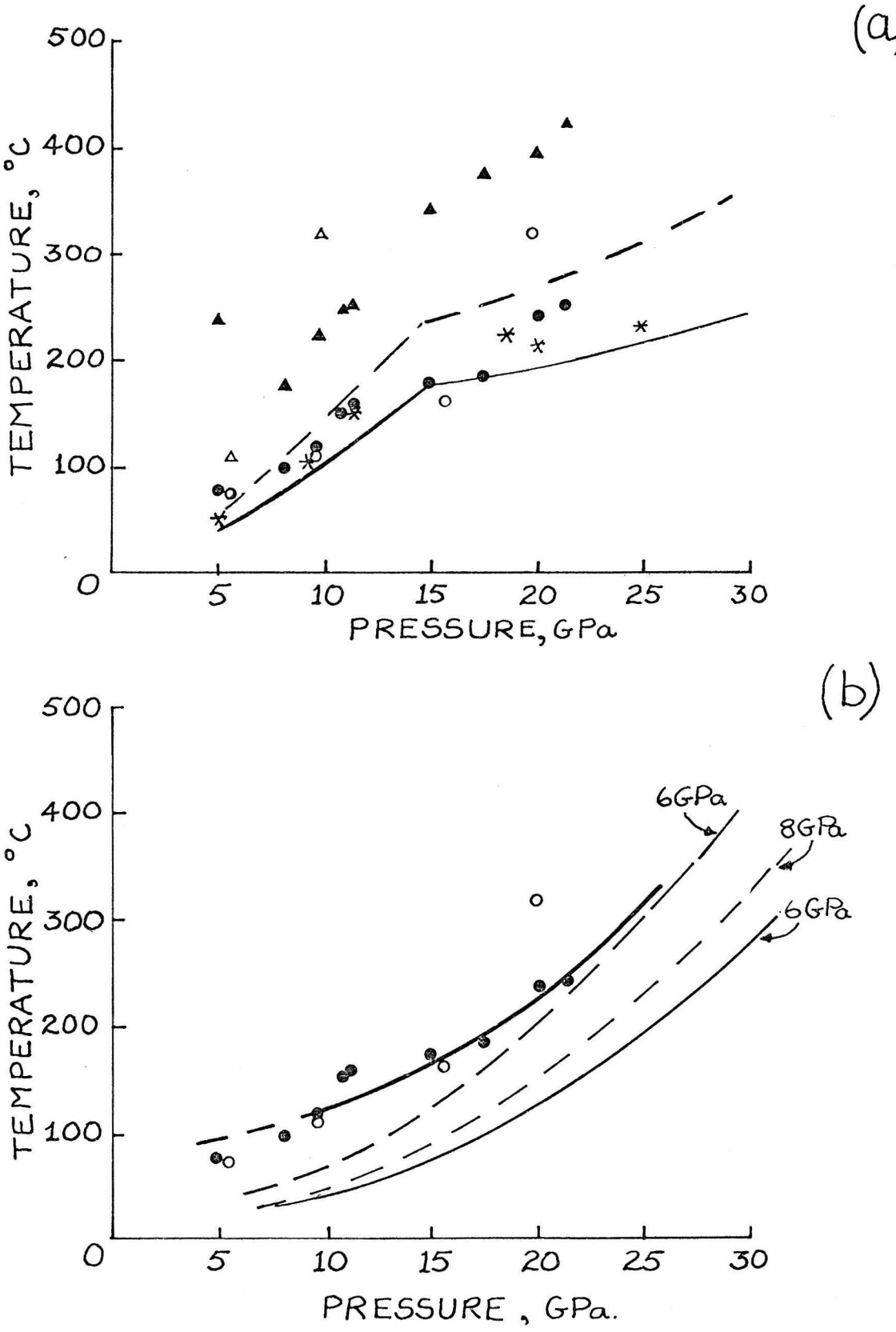
(a)
TEMPERATURE, °C
500
400
300
200
100
0
5
10
15
20
25
30
PRESSURE, GPa
(b)
TEMPERATURE, °C
500
400
300
200
100
0
6GPa
8GPa
6GPa
5
10
15
20
25
30
PRESSURE, GPa.

Figure 10-2.

for the lowest and highest pressure points. (The latter may be in error due to the detector response anyway.) As was discussed in Chapter 7, most calculations assume the release volume is either the same as (as in this case) or greater than the initial volume, when it may in fact be less. A smaller release volume results in higher post-shock temperatures because less energy is lost on release. Lyzenga and Ahrens (1978) derived a relationship between the minimum post-shock volume v_o' and the free surface and particle velocities, U_{fs} and u_p, for a Hugoniot state (p_1, v_1), namely

$$v_o' \geq \frac{(U_{fs} - u_p)^2}{p_1} + v_1 \qquad (25)$$

This was used with Wackerle's data to estimate the release volumes for pressures of 5.6, 9.0, 11.6 and 18.4 GPa, and these values used to recalculate the post-shock temperatures which are plotted as asterisks in Figure 10-2(a). Two additional points were calculated using measured release volumes from Grady et al. (1974). The agreement between these calculated values and the measurements is even better.

Mashimo et al. (1978) used release adiabat data to determine directly the residual temperatures in quartz in a manner analogous to that proposed by Gibbons (1974). Their results are plotted as the heavy curve in Figure 10-2(b): the agreement with the observations is excellent.

Figure 10-2(b) also shows the results of applying the method of Ahrens et al. (1969) which includes the effect of the Hugoniot elastic limit in the temperature calculations. The values of 6 and 8 GPa used for the elastic limit are the upper and lower bounds on the "free run" limit for z-cut quartz given by Wackerle. These temperatures are much

lower than the observed values, which are greater than the calculated shock temperatures even for the lower value of the Hugoniot elastic limit. (The discrepancy probably arises in the calculation of the isotherm.)

In all these calculations the effect of the quartz to stishovite phase change which begins at ∿15 GPa has been neglected except in so far as it changes the shape of the equilibrium Hugoniot or the release volume, although the properties of stishovite are well determined. The beginning of the mixed phase region is associated with the break in slope in Wackerle's curves (Figure 10-2(a)), and there appears to be a corresponding change in gradient in the data; however, with the present experimental system, the observations at pressures in excess of 20 GPa may not be very reliable for quartz, as explained in the last chapter. Calculations by Grady et al. (1974) indicate that at 20 GPa the phase transformation is ≤25% complete, and that it does not reach completion until ∿47 GPa. In calculations of post-shock temperatures the release path should also be understood, but the true nature of the release path from the mixed phase region is uncertain. Grady et al. suggest that it starts as unloading along a line of frozen concentration, but that at ∿8 GPa the high pressure phase may transform to a low pressure (amorphous) phase. In view of these uncertainties, and the lack of reliable observations further into the mixed phase region, calculations of temperatures assuming a mixture of high and low pressure phases were not pursued; however, it may be noted that the high pressure phase in general reaches a much higher temperature: Mashimo et al. calculated residual temperatures in stishovite of 730° at 20 GPa and

1170° C at 30 GPa.

(b) Forsterite

The forsterite used in this study was a synthetic single crystal having a porosity of $\lesssim$1%. Unfortunately the Hugoniot for this particular material has not been determined at pressures below ~50 GPa, but data are available for polycrystalline forsterite (McQueen, 1968) and for polycrystalline forsterite having an initial specific volume of 0.322 cm^3/g, or a porosity of ~4% (Ahrens et al., 1971). These two sets of observations serve to define a reasonable Hugoniot, and indicate that the present measurements were all in the low pressure regime; however, the Hugoniot may not be entirely correct, and no measurement of the Hugoniot elastic limit or release volume are currently available. In the calculation of post-shock temperatures using the technique of Ahrens et al.,(1969), values of 5 and 9 GPa were used for the elastic limit; the latter corresponds to the value for Twin Sisters dunite reported by Ahrens and Petersen (1971).

The available pressure volume data were used to derive equilibrium Hugoniots for the non-porous and porous samples in the manner used by Wackerle for quartz. The Walsh and Christian method was then used to calculate the Hugoniot temperatures; the final release volume was assumed, for both materials, to be the same as the initial volume of the non-porous sample, which will tend to yield a lower limit on the post-shock temperature. Temperatures were also calculated along a theoretical Hugoniot for single crystal forsterite, which was constructd from the Birch-Murnaghan adiabat using the constants given in Table 10-1 (for the details of this method see e.g., Davies, 1974). The theoretical

Table 10-1

SOME CONSTANTS RELEVANT TO THE CALCULATION

OF TEMPERATURES IN SHOCKED SILICATES

	ρ_o^{-1} cm^3/gm	γ_o	Θ_D[1] °K	$\bar{m}$	K_{os} GPa	K'_{os}
Quartz	.377	.703[2]	1050	20.03	37.7[2]	6.4[2]
Forsterite	.310	1.17[2,3]	900	20.12	126.7[3,4]	5.37[3]
Bronzite	.298[5]	.907	950	20.96	103.5[5]	9.59[5]
	.307	1.56[5]			105.0[7]	5.3[6]

γ_o = thermodynamic Gruneisen parameter

Θ_D = Debye temperature

$\bar{m}$ = mean atomic weight

K_{os} = zero pressure adiabatic bulk modulus

$K'_{os} = \left(\frac{\partial K_{os}}{\partial P}\right)_T$

1. Debye temperatures derived from fitting specific heat data from J.A.N.A.F. Tables.
2. Values from Anderson et al. (1968)
3. Kumazawa and Anderson (1969)
4. Graham and Barsch (1969)
5. Frisillo and Barsch (1972) $[(Mg_{0.8}Fe_{0.2})SiO_3]$
6. Chung (1971)
7. Kumazawa (1969)

Note: $\frac{\gamma}{v}$ was generally assumed constant.

Hugoniot fitted the observed data quite well above 15 GPa.

The results of the temperature calculations are shown in Figure 10-3; at this stage it should be noted that the 10 and 15 GPa measurements using the InSb detector are probably contaminated by radiation from the sample driver interface, as discussed in the previous chapter. The observed temperatures are considerably in excess of the values calculated for the non-porous polycrystalline forsterite using the equilibrium Hugoniot (curves A, A', Figure 10-3(a)), and are also greater than the values calculated for the theoretical Hugoniot (C, C') although there is some indication that the measurements tend towards the latter at high pressures. The values calculated for the "porous" equilibrium Hugoniot (B, B') are much higher than the observations except for the doubtful InSb points; this is not surprising since the samples were only ∿1% porous, and not 4%, but it does suggest that the measured temperatures might not be in great disagreement with theoretical values obtained from an appropriate equilibrium Hugoniot using actual release volumes.

Figure 10-3(b) shows the calculated shock temperatures derived using the method of Ahrens et al. for Hugoniot elastic limits of 5 and 9 GPa (curves E and F) and residual temperatures (E') obtained from the 5 GPa curve. These values are significantly lower than the observations below ∿20 GPa, but the observed values tend towards them at higher pressures; as long as the measured value is lower than the calculated Hugoniot temperature, the discrepancy may be explained largely in terms of the release volume. However, the fact that the observations are initially higher than the shock temperatures, but converge with the calculations

Figure 10-3. Observed (black body) and theoretical temperatures for shocked forsterite.
Triangles: "flash" temperatures; circles: residual temperatures.
Open symbols: HgCdTe; solid symbols: InSb.
Curves labelled in pairs, primed one is the residual temperature.

(a) A,A': polycrystalline forsterite; equilibrium Hugoniot
B,B': ~4% porous forsterite; equilibrium Hugoniot
C,C': theoretical Hugoniot

(b) D,D': theoretical Hugoniot; γ = 2.5 on compression, 1 on release.
E,E': actual Hugoniot, estimated Hugoniot elastic limit of 5 GPa.
F: Actual Hugoniot, estimated Hugoniot elastic limit of 9 GPa.

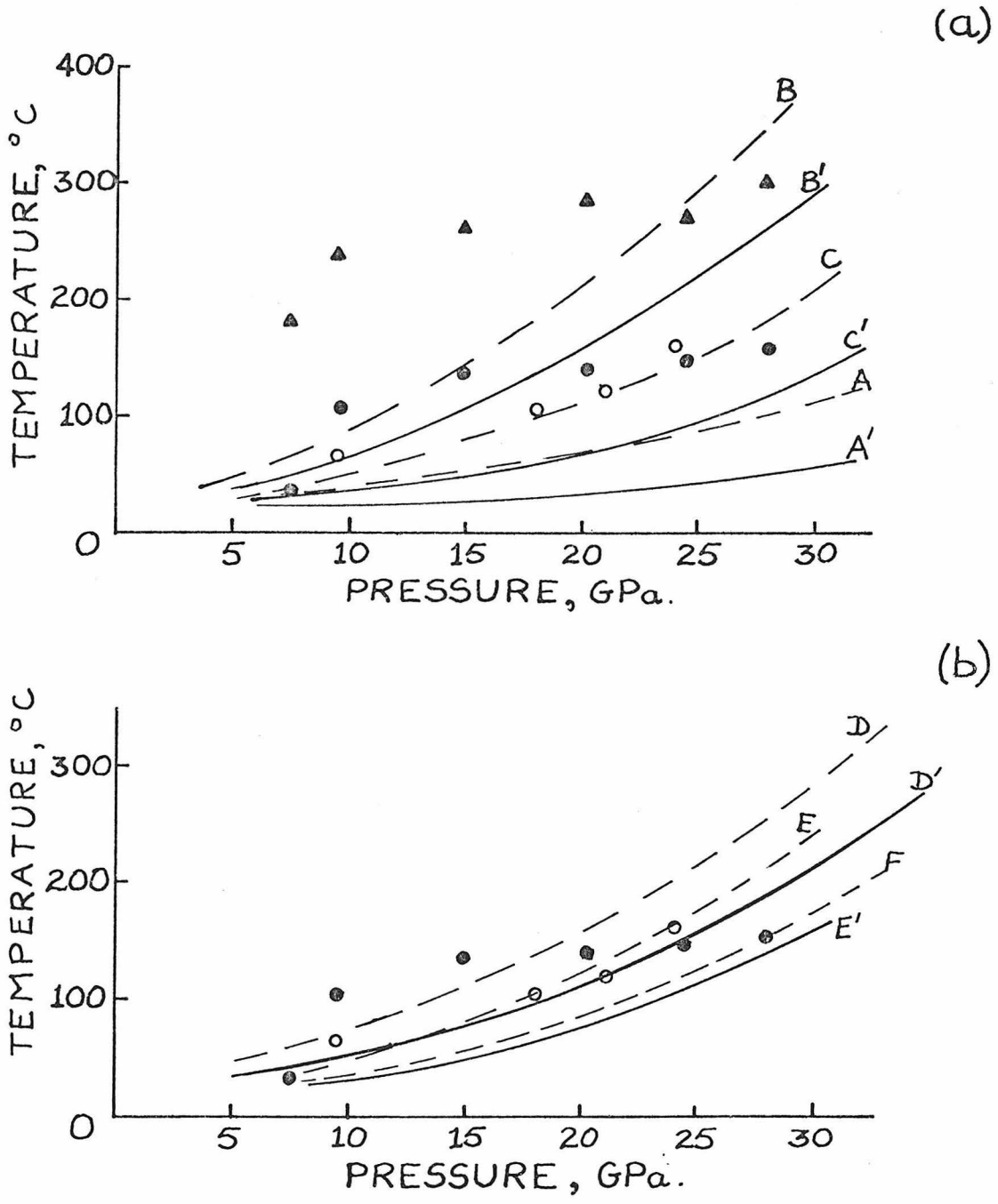
(a)
TEMPERATURE, °C
400
300
200
100
0
B
B'
C
C'
A
A'
5
10
15
20
25
30
PRESSURE, GPa.
(b)
TEMPERATURE, °C
300
200
100
0
D
D'
E
F
E'
5
10
15
20
25
30
PRESSURE, GPa.

Figure 10-3.

at high pressures is reminiscent of the behaviour observed in stainless steel and aluminium and ascribed to elasto-plastic effects. A detailed investigation of the process of dynamic yielding in forsterite would indicate whether such effects were possible here. It has been suggested (Ahrens et al., 1969) that strength effects are only significant in materials that do not undergo phase changes.

Calculations using the Walsh and Christian method were carried out to investigate the effects of varying the behaviour of Grüneisen's parameter, γ, and the Debye temperature Θ_D. (In the previous calculations it was assumed that γ/v was constant, and Θ_D independent of temperature, although the specific heats are fitted better if Θ_D does vary with temperature.) The Hugoniot temperatures are relatively insensitive to Θ_D, but are highly dependent on γ; however, if the same value of γ is then used to calculate the post-shock temperature, the latter varies very little. The curve D (Figure 10-3(b)) is the temperature on the theoretical Hugoniot for $\gamma = 2.5$, and D' is the residual temperature obtained from D but assuming $\gamma = 1$ on release. The agreement between D' and the observations is fairly good, and suggests this kind of approach may be valid. It does not have a good physical basis, although the shock and release processes are certainly different. In particular, the observations of release paths lying beneath the Hugoniot (e.g., Figure 7-1) and the apparent hysteresis in the shock and release process are not fully understood; they may be related to the behaviour of γ.

(c) Bamble bronzite

The dynamic compression of Bamble bronzite was studied by Ahrens and

Gaffney (1971) and recovery experiments were carried out by Gibbons (1974). Bamble bronzite consists of large natural single crystals which are closely described by the formula $(Mg_{0.86}Fe_{0.14})SiO_3$; the theoretical zero-pressure density is 3.308 gm/cm^3 whereas the density of the samples used by Ahrens and Gaffney varied from 3.276 to 3.298 gm/cm^3 indicating a porosity of from 1 to 3%. This porosity is manifest in the fine cracks that permeate the samples, which also contain some larger cracks. The variation in porosity probably accounts for the considerable scatter in the Hugoniot data, and the decrease in temperature between 20 and 25 GPa observed in the InSb measurements. The material has a Hugoniot elastic limit of 6.7 GPa and undergoes a phase change, probably to ringwoodite plus stishovite (Ahrens and Gaffney, 1971), which begins at $\sim$14 GPa and is not complete until $\sim$40 GPa. The properties of the high pressure phase are not well known, and the release paths from states in the mixed phase region have not been studied in detail; in this section the effect of the phase change will thus be neglected, although temperatures in the high pressure phase may be considerably higher than those in the low pressure phase.

An attempt was made to determine an equilibrium Hugoniot, as defined by Wackerle (1962), using the data of Ahrens and Gaffney for the Bamble bronzite, but the (U*, u*) points were so scattered that no obvious linear correlation existed, and the attempt was abandoned. Instead, theoretical Hugoniots were constructed from the Birch-Murnaghan adiabats using the constants of Table 10-1 and an initial specific volume of 0.304 cm^3/gm. Hugoniots were constructed for both values of γ (the differences arise from the different values of thermal

expansion and specific heat used in calculating γ), and a value of K'_{os} 5.3 was found to give a better fit to the observations, so was used throughout.

Figure 10-4(a) indicates the results for the theoretical Hugoniot with $\gamma = 0.907$. The curves A and A' are the calculated shock and residual temperatures, and are considerably lower than the observations. As in the last section, the behaviour of γ and Θ_D were varied, with no great improvement in the fit unless the release path had a smaller value of γ. In particular, curve B is the shock temperature for $\gamma = 2.5$ with the residual temperatures B' being calculated from B but assuming $\gamma = 1$ on release. The agreement between B' and the observations is somewhat better, especially at high pressures, but a Grüneisen's parameter of at least 3 during shock compression would be required to produce agreement at pressures less than 15 GPa. In this case the calculated release temperatures (assuming $\gamma = 1$) would be too high at pressures of $\sim$25 GPa, so a more complicated behaviour of γ would have to be postulated. This does not seem justified since the theoretical Hugoniot does not adequately describe the effects of varying sample porosity, and the high temperatures may be largely due to this; furthermore, the effect of the phase change has been neglected -- although this would provide some justification for changing the behaviour of the effective γ at 15 GPa. The temperatures calculated using the approach of Ahrens et al. (1969) with a Hugoniot elastic limit of 6.7 GPa and a smooth fit to the observed Hugoniot points are plotted as curves C and C'; these are in even worse agreement with the observations.

Figure 10-4(b) illustrates the results of using $\gamma = 1.57$; the

Figure 10-4. Observed (black body) and theoretical temperatures for Bamble bronzite.
Symbols as in Figure 10-3.

(a) A,A': theoretical Hugoniot, γ = .907.
B,B': theoretical Hugoniot, γ = 2.5 on compression, 1 on release.
C,C': actual Hugoniot, γ = .907, Hugoniot elastic limit of 6.7 GPa.

(b) D,D': theoretical Hugoniot, γ = 1.57
E,E': actual Hugoniot, γ = 1.57, Hugoniot elastic limit of 6.7 GPa.

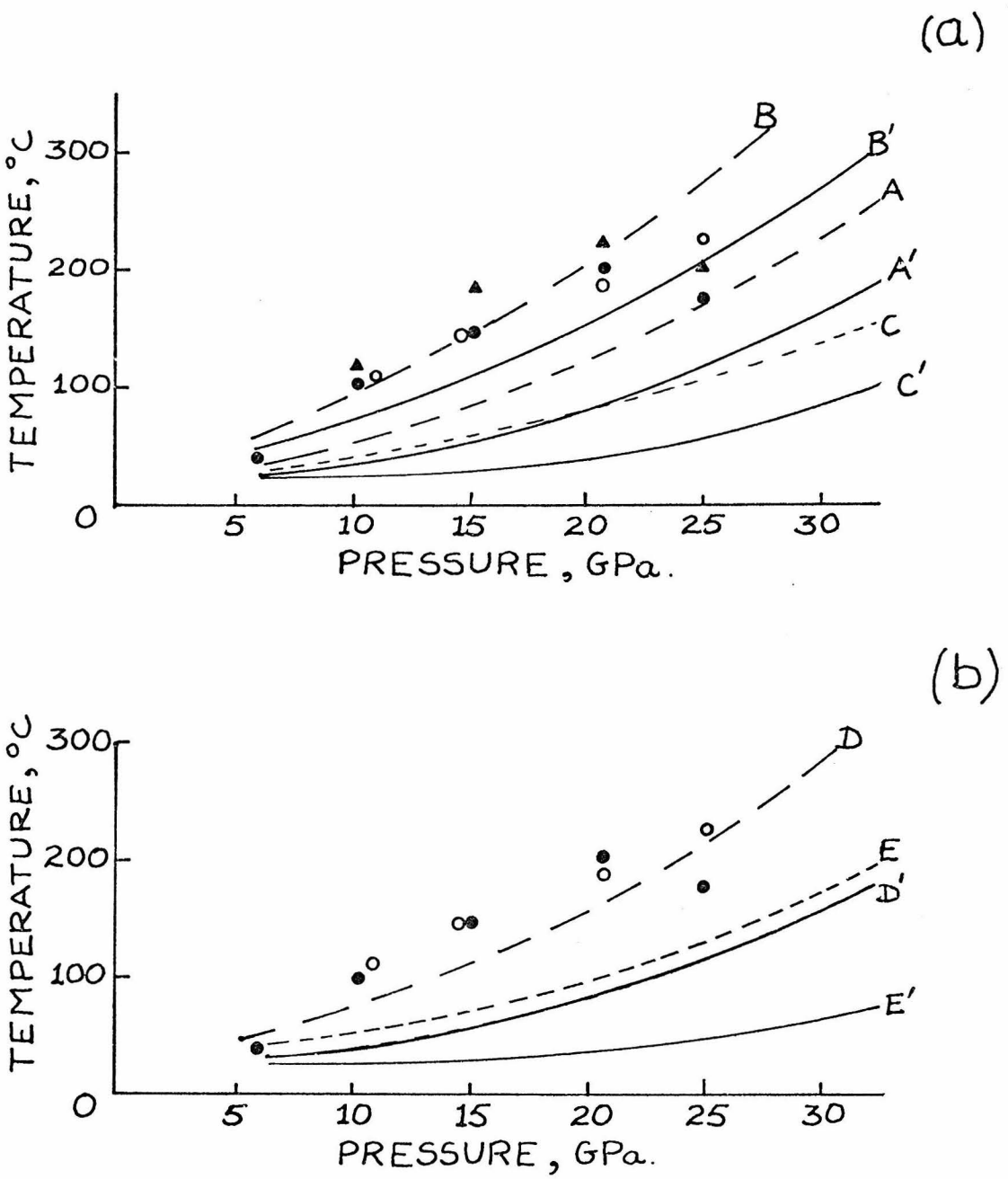
(a)
TEMPERATURE, °C
300
200
100
0
5
10
15
20
25
30
PRESSURE, GPa.
B
B'
A
A'
C
C'
(b)
TEMPERATURE, °C
300
200
100
0
5
10
15
20
25
30
PRESSURE, GPa.
D
E
D'
E'

Figure 10-4.

temperatures along the theoretical Hugoniot (D) are higher than those of curve A in Figure 10-4(a), but the release temperatures given by D' are little different from A'. The calculations including the Hugoniot elastic limits also yield higher shock temperatures (E), but the residual temperatures are much lower.

Recovery experiments by Gibbons (1974) revealed considerably crushing and fracturing caused by the shock loading, and fine deformational twin lamellae. Above 17.3 GPa some undulatory extinction was apparent, and at 22.6 GPa a very small amount of glass was detected on the fractures This suggests that the shock heating may be highly non-uniform, and the measured temperatures may thus be rather high.

Chapter 11

DISCUSSION

An experimental technique capable of measuring post-shock (brightness) temperatures in a variety of materials including metals and silicates has been developed. Initial experiments have produced reproducible results which are, in general, consistent at two wavelength ranges from 4.5 to 5.75μ and from 7 to 14μ. The reproducibility and consistency suggest that the measured temperatures are indeed representative of the residual temperatures in the shocked samples, although uncertainties still exist concerning the possible effects of changes in emissivity under shock conditions and of non-hydrodynamic surface processes.

It has been suggested (McQueen, 1977, personal communication) that the main significance of post-shock temperature measurements may lie in their relative values. This would mean that the rate of change of temperatures with shock pressure for a given material should be considered rather than the absolute values measured; some comparison of different materials might be possible, but only strictly in terms of changes in dT/dP. In this case, if the theory and observations are compatible, the measured and theoretical curves will be parallel. This is not in general the case in this study, where the measured temperatures often approach the calculated values at high temperatures, suggesting that there is some heating effect which is dominant at low pressures (which would probably not be true of non-linear heating in the surface layers).

Experiments on stainless steel and aluminium yielded measured values

that were considerably in excess of those predicted by the Walsh and Christian model (1955) at low pressures, but tended towards the latter at higher pressures. This was attributed to elasto-plastic effects, which are well documented in aluminium and yield temperatures in reasonable agreement with the measurements. Other workers, such as Von Holle and Trimble (1976) have reported discrepancies between measured and residual temperatures that persist to much greater pressures ($\sim$50 GPa) and apparently cannot be caused by elasto-plastic work; these have been ascribed to non-hydrodynamic surface heating. Surface effects are bound to affect measurements on metals where the infra-red optical depth is only $\sim 10^{-10}$ m, and may be, in part, responsible for the differences between theory and observation reported in this study. However, the agreement between the temperatures predicted by the elasto-plastic theory and the observations for aluminium is quite good, and it is hard to see why the effect of surface heating should be dominant at low pressures and not at higher ones. One effect that may influence the measurements of residual temperatures in aluminium is the ejection of material from the surface; this has been studied by Asay et al. (1976) for pressures of $\sim$25 GPa and is quite significant. A further study by Asay (1977) showed that material ejection was highly dependent on the rise-time of the shock wave, so the effect of material ejection on temperature measurement might be investigated by determining residual temperatures for different shock rise-times.

The measured temperatures obtained for the silicates were also quite consistent for the two wavelength ranges with the exception of the low ($\lesssim$15 GPa) measurements on forsterite using the InSb detector, where the

effect of the sample transmissivity is believed to have led to errors in the temperature determination. Agreement between observed and calculated temperatures in quartz is remarkably good when the equilibrium Hugoniot technique of Wackerle (1962) is applied. The fit is improved by using measured or estimated release volumes rather than the initial volume in the calculation of residual temperatures from the Hugoniot ones. The best match between experiment and "theory" arises when the post-shock temperatures are calculated directly from release adiabat data, and suggests that this technique should be used wherever possible in the calculation of residual temperatures.

Detailed release adiabat data were not available for forsterite or the Bamble bronzite, and, in fact, there is no good low pressure equation of state data currently available for forsterite; comparison of observed temperatures and those calculated in the optimal manner was thus not possible. The effects of uncertainties in the Hugoniot for forsterite and of porosity in both these materials may lead to errors in the determination of theoretical temperatures. Nevertheless, it appears that the Hugoniot temperatures implied by the measured residual values (assuming isentropic release) are higher than those calculated using the thermodynamic Grüneisen's parameter which is assumed to have a simple volume dependence. The effective value of γ on the Hugoniot is apparently required to be greater than the zero pressure thermodynamic value. An initial measurement of shock temperature in forsterite at $\sim$1 Mb also had a much higher value than calculated (Lyzenga, 1978, personal communication) and may be related to the observations in the low pressure regime. There are no good physical reasons for postulating a different γ for shock

compression from that for unloading; it is simply an ad hoc method of producing better agreement between theory and observations, and is certainly non-unique. However, the differences between observed and predicted release adiabats and the hysteresis observed in shock unloading suggest that some change in material properties may occur prior to release from the shock state. There is also limited evidence for some kind of elasto-plastic strength effect in forsterite.

The effects of surface heating on temperature measurement should be less severe in the silicates where the optical depth is microns. A more serious contribution may result from non-uniform shock heating which has been clearly demonstrated in silicates where such features as adiabatic shear zones (e.g., Grady, 1977) deformational twin lamellae and localised production of glass (e.g., Gibbons, 1974) have been observed. This non-uniform heating is believed to contribute to the complete loss of strength once the Hugoniot elastic limit is exceeded. Quartz was the only material where a temperature rise was observed at pressures below the elastic limit, so perhaps non-uniform heating also occurs in the elastic regime. Both forsterite and enstatite showed a rapid rise in temperature once the Hugoniot elastic limit was exceeded. (An additional feature complicating the measurement of post-shock temperatures in quartz is the initial "flash" which has been associated with triboluminescence.)

The good agreement between theory and observations for quartz yet apparent large discrepancies for forsterite and bronzite raises the question of inherent differences between these materials. Their behaviour on compression is certainly very different: quartz is much more compressible (and is also less dense initially). There is a possibility

that framework silicates (such as quartz) and chain silicates (such as bronzite) or neso-silicates (like forsterite) react differently under stress. The feldspars, which are also framework silicates, have similar initial densities to quartz and are also quite compressible (Ahrens et al., 1969); since release adiabat data are available for feldspars such as oligoclase, they are logical materials to investigate with the technique developed in this study in order to clarify this point.

No discussion has so far been presented of Waldbaum's (1971) suggestion that release from shock might be isenthalpic rather than adiabatic. Heating on release instead of cooling would certainly solve the problem of measured post-shock temperatures being higher than theoretical Hugoniot temperatures, but this hypothesis would not explain the convergence of measured and calculated values at high pressures. However, the assumption that the adiabatic release is in fact isentropic may not be strictly valid, although unless the real release path is known it is hard to correct for this effect.

Classifications of shock-metamorphism such as that of Stoffler (1971) are generally based on calculated values of shock and residual temperatures, and should be re-evaluated in the light of the present study. Stoffler based his classification on the calculations of Wackerle (1962) for quartz and Ahrens et al. (1969) for feldspars. The measurements of this study indicate that Wackerle's results are probably fairly reliable below ∿20 GPa, although it is important that they be corrected for the right initial temperatures and, where possible, for the actual release volume. They may also be rather low for pressures well into or above the mixed phase region. (The work of Mashimo et al. (1978), which

was in good agreement with the present study, indicates that Wackerle's values for both shock and residual temperature are low up to ∿70 GPa.) No measurements have been made for feldspars, but it may be noted that the calculational technique of Ahrens et al. (1969) yielded rather too low post-shock temperatures for all the materials studied here, and hence the values used by Stoffler may also be too low. The main implication of this study for impact metamorphism is that temperatures in forsterite and bronzite appear considerably higher than the theoretical values, especially for porous samples, and so the effects of impact metamorphism on basic rocks such as lunar basalt may differ from those expected on the basis of theory and lead to erroneous conclusions.

It was hoped that this study would yield some definite information on the behaviour of Grüneisen's parameter, which is critical for the reduction of shock wave data to the form needed for comparison with density-depth profiles within the earth. However, post-shock temperatures are not very sensitive to the behaviour of γ (unless it is different on shock compression and release) and appear more greatly influenced by the release path, in particular the release volume. There seems to be no need to postulate strange behaviour of γ for quartz to ∿25 GPa, although the high observed values of residual temperatures in forsterite and enstatite suggest that conventional calculations of shock temperature, at least below ∿25 GPa, are inadequate for these materials. This implies that the use of shock wave data in this pressure range to infer the properties of silicates within the earth's mantle may be subject to considerable error. The development of static high pressure apparatus capable of producing pressures in excess of this value has made the use of shock

wave data largely redundant except for inferring the constitution of the deepest mantle, and the present work does not yield any information on the behaviour of the high pressure phases of the minerals studied.

Future development of this technique will include adapting it so the whole sample assembly is *in vacuo*; this should allow better resolution of the post-shock temperatures especially at higher pressures where the destruction of the vacuum chamber is currently a problem. A system for introducing fiducial marks corresponding to the time of entrance of the shock wave into the sample is also planned, which should eliminate any remaining uncertainties in the time of occurrence of the various temperature rises. It is also hoped to improve the time resolution of the HgCdTe detector by building a less noisy, more efficient amplifier, which should reduce the system rise-time to $\sim$0.1 μsec.

BIBLIOGRAPHY

Ahrens, T. J., D. L. Anderson and A. E. Ringwood, Equations of state and crystal structures of high-pressure phases of shocked silicates and oxides, Rev. Geophys., 7, 667-707, 1969.

Ahrens, T. J. and E. S. Gaffney, Dynamic compression of enstatite, J. Geophys. Res., 76, 5504-5513, 1971.

Ahrens, T. J., J. H. Lower and P. L. Lagus, Equation of state of forsterite, J. Geophys. Res., 76, 518-528, 1971.

Ahrens, T. J. and J. D. O'Keefe, Shock melting and vaporization of lunar rocks and minerals, The Moon, 4, 214-249, 1972.

Ahrens, T. J. and C. F. Petersen, Shock wave data and the study of the earth in The Application of Modern Physics to the Earth and Planetary Interiors, S. K. Runcorn, ed., 449-461, Wiley-Interscience, 1969.

Ahrens, T. J., C. F. Petersen and J. T. Rosenberg, Shock compression of feldspars, J. Geophys. Res., 74, 2727-2746, 1969.

Al'tschuler, L. V., Use of shock waves in high pressure physics, Sov. Phys. Usp., 8, 52-91, 1965 (English Trans.).

Anderson, O. L., E. Schreiber, R. C. Liebermann and N. Soga, Some elastic constant data on minerals relevant to geophysics, Rev. Geophys., 6, 491-524, 1968.

Asay, J. R., Effect of shock-wave rise time on material ejection from aluminium surfaces, Sandia Laboratories Report SAND77-0731, 1977.

Asay, J. R., L. P. Mix and F. C. Perry, Ejection of material from shocked surfaces, App. Phys. Lett., 29, 284-287, 1976.

Buettner, K. J. K. and C. D. Kern, The determination of infrared emissivities of terrestrial surfaces, J. Geophys. Res., 70, 1329-1337, 1965.

Chung, D. H., Equations of state of pyroxenes in the (Mg, Fe)SiO_3 system, E⊕S Trans. Am. Geophys. U., 52, 919, 1971 (abstract).

Davies, G. F., Limits on the constitution of the lower mantle, Geophys. J. R. astr. Soc., 38, 479-503, 1974.

Duvall, G. E. and G. R. Fowles, Shock waves, Chapter 9, in High Pressure Physics and Chemistry, Volume II, R. S. Bradley, ed., Academic Press, London, 209-291, 1963.

Foltz, J. F. and F. I. Grace, Theoretical Hugoniot stress-temperature-strain states for aluminum and copper, J. Appl. Phys., 40, 4195-4199, 1969.

Fowles, G. R., Shock wave compression of hardened and annealed 2024 aluminum, J. Appl. Phys., 32, 1475-1487, 1961.

Frisillo, A. L. and G. R. Barsch, Measurement of single-crystal elastic constants of bronzite as a function of pressure and temperature, J. Geophys. Res., 77, 6360-6384, 1972.

Gibbons, R. V., Experimental effects of high shock pressure on materials of geological and geophysical interest, Ph.D. Thesis, California Institute of Technology, 1974.

Gibbons, R. V. and T. J. Ahrens, Shock metamorphism of silicate glasses, J. Geophys. Res., 76, 5489-5498, 1971.

Goto, T., G. R. Rossman and T. J. Ahrens, Absorption spectroscopy in solids under shock compression, Proc. 6th AIRAPT International High Pressure Conference, Boulder, Colorado, 1977 (in press).

Grady, D. E., Processes occurring in shock wave compression of rocks and minerals, in High Pressure Research: Applications in Geophysics, M. H. Manghnani and Syun-Ibi Akimoto, eds., Academic Press, New York, 359-435, 1977.

Grady, D. E., W. J. Murri and G. R. Fowles, Quartz to stishovite: wave propagation in the mixed phase region, J. Geophys. Res., 79, 332-338, 1974.

Graham, E. K., Jr. and G. R. Barsch, Elastic constants of single-crystal forsterite as a function of temperature and pressure, J. Geophys. Res., 74, 5949-5960, 1967.

J.A.N.A.F. Thermochemical Tables, Nat. Stand. Ref. Data Ser., Nat. Bur. Stand. (U.S.), 37, 1141 pp., 1971.

King, D. A., and T. J. Ahrens, Shock compression of ilmenite, J. Geophys. Res., 81, 931-935, 1976.

King, P. J., D. F. Cotgrove and P. M. B. Slate, Infra-red method of estimating the residual temperature of shocked metal plates, in Behaviour of Dense Media under High Dynamic Pressures, J. Berger, ed., Gordon and Breech, 513-520, 1968.

Knopoff, L. and J. N. Shapiro, Comments on the interrelationship between Gruneisen's parameter and shock and isothermal equations of state, J. Geophys. Res., 74, 1439-14 , 1969.

Kormer, S. B., Optical study of the characteristics of shock-compressed condensed dielectrics, Sov. Phys. Usp., 11, 229-254, 1968.

Kormer, S. B., M. V. Sinitsyn, G. A. Kirillov and V. D. Urlin, Experimental determination of temperature in shock-compressed NaCl and KCl and of their melting curves at pressures up to 700 Kb, Sov. Phys. J.E.T.P. 21, 659-700, 1965.

Kruse, P. W., L. D. McGlauchlin and R. B. McQuistan, Elements of Infrared Technology, Wiley and Sons, New York, 1962.

Kumazawa, M., The elastic constants of single-crystal orthopyroxene, J. Geophys. Res., 74, 5973-5980, 1969.

Kumazawa, M. and O. L. Anderson, Elastic moduli, pressure derivatives and temperature derivatives of single-crystal olivine and single-crystal forsterite, J. Geophys. Res., 74, 5961-5972, 1969.

Lee, E. H. and D. T. Liu, Finite-strain elastic-plastic theory with application to plane-wave analysis, J. Appl. Phys., 38, 19-27, 1967.

Lee, E. H. and T. Wierzbicki, Analysis of the propagation of plane elastic-plastic waves at finite strain, J. Appl. Mech., 34, 931-936, 1967.

Lyon, R. J. P., Analysis of rocks by spectral infrared emission (8 to 25 microns), Econ. Geol., 60, 715-736, 1965.

Lyzenga, G. A. and T. J. Ahrens, The relation between the shock-induced free surface velocity and the post-shock specific volume of solids, J. Appl. Phys., 49, 201-204, 1978.

Mashimo, T., K. Nishii, T. Soma, A. Sawaoka and S. Saito, Some physical properties of amorphous SiO_2 synthesized by shock compression of α-quartz, Preprint, 1978.

McQueen, R. G., Shock wave data and equations of state, in Seismic Coupling, G. Simmons, ed., Advanced Research Projects Agency Meeting, 1968.

McQueen, R. G. and S. P. Marsh, Equations of state for nineteen metallic elements from shock-wave measurements to two megabars, J. Appl. Phys., 31, 1253-1269, 1960.

McQueen, R. G., S. P. Marsh and J. N. Fritz, Hugoniot equation of state of twelve rocks, J. Geophys. Res., 72, 4999-5036, 1967.

McQueen, R. G., S. P. Marsh, J. W. Taylor, J. N. Fritz and W. J. Carter, The equation of state of solids from shock wave studies, Chapter VII, in High-Velocity Impact Phenomena, R. Kinslow, ed., Academic Press, 293-417, 1970 (see also Appendix C, D, E, pp. 518-520, 521-529, 530-568).

Murr, Lawrence E., Interfacial Phenomena in Metals and Alloys, Addison Wesley, pp. 326, 348, 349, 1975.

Nielson, F. W., W. B. Benedick, W. P. Brooks, R. A. Graham and G. W. Anderson, Electrical and optical effects of shock waves in crystalline quartz, in Colloques Internationaux du Centre National de la Recherche Scientifique, No. 109, Les Ondes de Détonation, 391-414, 1961.

Schneider, E. and A. Stilp, Measurement of temperature distributions within steel targets impacted by hypervelocity projectiles: method and preliminary results, Paper presented at the 7th International Congress on Instrumentation in Aerospace Simulation Facilities, RMCS, Shrivenham, England, September, 1977.

Shapiro, J. N. and L. Knopoff, Reduction of shock-wave equations of state to isothermal equations of state, J. Geophys. Res., 74, 1435-1438, 19 .

Smith, C. S., Metallographic studies of metals after explosive shock, Trans. Metall. Soc. of AIME, 212, 574-589, 1958.

Stoffler, D., Progressive metamorphism and classification of shocked and brecciated crystalline rocks at impact craters, J. Geophys. Res., 76, 5541-5551, 1971.

Stoffler, D., Deformation and transformation of rock-forming minerals by natural and experimental shock processes. 1. Behaviour of minerals under shock compression, Fortschr. Miner. 49, 50-113, 1972.

T.P.R.C. Data Series: Thermophysical Properties of Matter; Y. S. Touloukian, and C. Y. Ho, eds., vol. 7, Thermal radiative properties of metallic elements and alloys; vol. 8, Thermal radiative properties of non metallic elements and compounds, IFI/Plenum, New York, 1972.

Takeuchi, H. and H. Kanamori, Equations of state of matter from shock wave experiments, J. Geophys. Res., 71, 3985-3994, 1966.

Taylor, J. W., Residual temperatures in shocked copper, J. Appl. Phys., 34, 2727-2731, 1963.

Touloukian, Y. S. and D. P. DeWitt, Thermal radiative properties, non-metallic solids, T.P.R.C. Data Series, 8, Plenum Press, 1972.

Urtiew, P. A. and R. Grover, Radiation temperature in solids under shock loading, Fifth Symposium on Temperature, its Measurement and Control in Science and Industry, Nat. Bur. Stand., 4, 677-684, 1973 (Am. Inst. Phys.).

Urtiew, P. A., Effect of shock loading on transparency of sapphire crystals, J. Appl. Phys., 45, 3490-3493, 1974.

Urtiew, P. A. and R. Grover, Temperature deposition caused by shock interactions with material interfaces, J. Appl. Phys., 45, 140-145, 1974.

Von Holle, W. G. and J. J. Trimble, Temperature measurement of shocked copper plates and shaped charge jets by two-colour IR radiometry, J. Appl. Phys., 47, 2391-2394, 1976.

Wackerle, J., Shock compression of quartz, J. Appl. Phys., 33, 922-937, 1962.

Waldbaum, D. R., Temperature changes associated with adiabatic decompression in geological processes, Nature, 232, 545-547, 1971.

Walsh, J. M. and R. H. Christian, Equation of state of metals from shock wave measurements, Phys. Rev., 97, 1544-1556, 1955.

APPENDIX A

OPERATIONAL DETAILS FOR THE INFRA-RED RADIATION DETECTORS USED

(a) Mode of operation

The basic principle behind the use of semiconductors as radiation detectors is the interaction of incident radiation with the detector material to produce electrical energy. For some materials the photon energy is sufficient to free an electron completely from the semiconductor; this is known as the photo-electric effect. In other materials, absorption of the photon energy produces an internal photo-effect by creating a free electron or a free hole or both. The latter materials are then classified as photoconductive, where the signal detection depends on measuring the change in conductivity generated by the incident radiation, photovoltaic, if the carriers are produced at some point where a potential barrier exists that separates the charges and produces a voltage, or photo-electromagnetic, when the charges are separated by the action of a magnetic field. A detailed description of infra-red detector technology is given in Kruse et al. (1962).

The InSb detector used operated in a photovoltaic mode: radiation incident on the p-n junction produces electron-hole pairs, which are then separated by the internal electric field such that the n-region becomes negatively and the p-region positively charged. The ends of the semiconductor are short circuited by an external conductor, causing a current to flow through the circuit as long as radiation falls on the junction. The HgCdTe detector operates in the photoconductive mode.

The most commonly quoted detector characteristic is the detectivity D*, which is defined as follows. The radiation power capable of producing a signal voltage equal to the noise voltage is known as the noise equivalent power P_N, and is given by

$$P_N = \mathcal{I} A_D \left(\frac{V_N}{V_s}\right) \frac{1}{(\Delta f)^{1/2}} \qquad (1)$$

where $\mathcal{I}$ = rms irradiance falling on a detector of area A_D, $\frac{V_N}{V_s}$ = ratio of the rms noise voltage in the bandwidth Δf to the rms signal voltage. Since most detectors have a value of P_N that is directly proportional to the square root of the detector area, an area independent quantity known as the detectivity D* is defined as

$$D^* = \frac{A_D^{1/2}}{P_N} = \frac{(\Delta f)^{1/2}}{A_D^{1/2}} \cdot \frac{V_s}{V_N} \qquad (2)$$

The detectivity is usually quoted as a specific temperature and centre frequency, with a reference bandwidth of 1 Hz; its units are $cmHz^{1/2}/watt$.

(b) Characteristics of the detectors used

The InSb detector and preamplifier used in this study were purchased from the Santa Barbara Research Centre. The detector was a circular chip 1 mm in diameter, having a detectivity of 5×10^{10} $cmHz^{1/2}/watt$ when operated at 77°K. The fast matched preamplifier consisted of a current mode operational amplifier with a feedback resistance of 1 kΩ and a non-inverting voltage mode post-amplifier; this stage had a gain of 500. The upper and lower 3db frequencies were 20 MHz and 1.35 kHb respectively, although the system rise time of ∿0.1 μs is controlled by the detector chip itself. For use in measuring post-shock temperatures an additional amplifier with variable gain (from 1000 to 30,000) was

designed by Mr. Wayne Miller and built by Mr. Victor Nenow; the circuit diagram for this amplifier is shown in Figure A-1.

The HgCdTe detector, which had an area of 2×10^{-2} cm^2 and a detectivity of 6.94×10^9 $cmHz^{1/2}/watt$, was used with a matched amplifier having a gain of 1000; both were purchased from the Santa Barbara Research Centre. The amplifier consisted of an a-c coupled voltage mode amplifier plus a 499 Ω load resistor and circuitry to produce the bias current of 10 ma required by the detector; its upper and lower 3 db frequencies were 10 mHz and 50 Hz respectively. The rise time of the detector-amplifier system is ∿.05 μs; however, for operation at low signal levels it was found to produce an unacceptable level of very high frequency noise, and so had to be operated with a filter which raised the rise time to ∿0.75 μs.

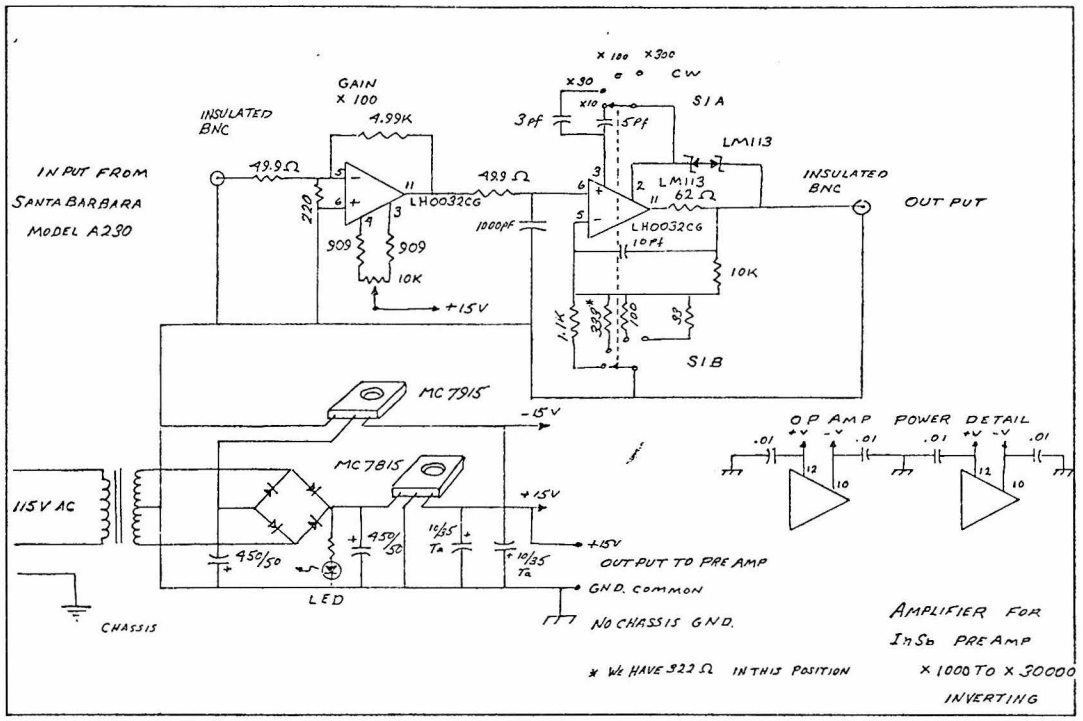

Figure A-1. Circuit diagram for InSb post-amplifier.

APPENDIX B

DETAILS OF SHOTS FIRED IN THIS STUDY

Table B-1

Experimental Details of the Shots

Detector	Flyer Plate	Velocity, km/s	Pressure, GPa
STAINLESS STEEL-304:			
HgCdTe	AL	0.95	11.5
InSb	AL	0.97	11.7
InSb	AL	1.15	13.0
HgCdTe	AL	1.22	14.5
InSb	Lexan	2.75	16.0
HgCdTe	AL	1.35	16.0
InSb	AL	1.70	23.0
HgCdTe	SS	1.17	24.2
InSb	W	1.51	43.0
InSb	W	1.70	50.0
ALUMINIUM-2024:			
InSb	AL	1.26	10.5
HgCdTe	AL	1.35	11.5
InSb	AL	1.42	12.5
InSb	Lexan	2.90	15.0
HgCdTe	SS	1.26	15.7
InSb	AL	2.00	18.5
HgCdTe	SS	1.43	18.5
HgCdTe	W	1.59	25.0
InSb	W	1.67	27.0
InSb	W	1.95	32.5
InSb	W	1.98	33.0

Table B-2

Experimental Details of Shots on Silicates

Detector	Flyer Plate	Driver Plate	Velocity, km/s	Pressure, GPa
1. QUARTZ				
InSb	AL	AL	0.76	5.0
HgCdTe	AL	AL	0.81	5.5
InSb	Lexan	AL	2.10	8.0
HgCdTe	AL	SS	1.48	9.5
InSb	AL	SS	1.49	9.5
InSb	AL	AL	1.35	10.8
InSb	AL	AL	1.47	11.5
InSb	AL	AL	1.88	15.0
HgCdTe	SS	AL	1.36	15.5
InSb	W	SS	1.20	17.5
HgCdTe	W	SS	1.32	19.5
InSb	W	AL	1.54	20.0
InSb	W	SS	1.42	21.5
2. FORSTERITE				
InSb	AL	AL	.74	7.5
InSb	AL	AL	1.02	9.6
HgCdTe	AL	AL	1.02	9.6
InSb	AL	AL	1.47	15.0
HgCdTe	AL	AL	1.58	18.0
InSb	AL	AL	1.99	20.2
HgCdTe	SS	SS	1.23	21.0
HgCdTe	W	SS	1.23	24.0
InSb	W	SS	1.25	24.5
InSb	W	SS	1.41	28.0
3. BAMBLE BRONZITE				
InSb	AL	SS	0.75	6.0
InSb	AL	AL	1.08	10.3
HgCdTe	AL	AL	1.15	11.0
HgCdTe	AL	AL	1.51	14.8
InSb	AL	AL	1.57	15.5
InSb	SS	AL	1.47	20.7
HgCdTe	SS	SS	1.48	21.5
InSb	W	SS	1.28	25.0
HgCdTe	W	SS	1.31	26.0